High-Sensitivity PET using Optimised Continuous Cylindrical Shell Nanocomposite and Transparent Ceramic Scintillators

Keenan Wilson

School of Electrical and Data Engineering

University of Technology Sydney

A thesis presented for the degree of

Doctor of Philosophy

November 25, 2020

Certificate of Authorship / Originality

I, Keenan Wilson declare that this thesis, is submitted in fulfilment of the requirements for the award of Doctor of Philosophy, in the School of Electrical and Data Engineering at the University of Technology Sydney.

This thesis is wholly my own work unless otherwise referenced or acknowledged. In addition, I certify that all information sources and literature used are indicated in the thesis. This document has not been submitted for qualifications at any other academic institution.

This research is supported by the Australian Government Research Training Program.

Abstract

Positron emission tomography (PET) systems typically employ 2D or 3D arrays of discrete monocrystalline rectangular prismatic scintillators, arranged in a ring around the imaging object. As PET systems have evolved towards higher spatial resolution and sensitivity, the number of crystals has increased while the dimensions of the crystals have decreased, leading to ever-increasing costs and complexity - particularly in total-body PET. At the same time, the need for optical isolation between crystals limits packing efficiency and hence achievable sensitivity. The chief alternative to discrete-crystal PET - monolithic scintillators with external photodetector arrays - introduces its own challenges, since producing large, high quality scintillator crystals is expensive and technically challenging.

Two new classes of scintillator have recently emerged as alternatives to monocrystalline scintillators for gamma detection - nanocomposites, which combine scintillating nanoparticles with an organic polymer binder - and transparent ceramics. Both are cheaper and easier to manufacture than monocrystalline scintillators, and can be more easily formed into complex shapes - however, they are also less transparent and, in the case of nanocomposites, less dense. Neither has previously been employed in PET systems to any significant degree.

In this work, a new PET system design is proposed which exploits the properties of these new scintillators. Instead of discrete crystals or flat monolithic slabs, the scintillator is formed into a continuous cylindrical shell, tiled on the inner and outer surfaces with silicon photomultiplier photodetectors. The design aims to achieve high sensitivity and competitive spatial resolution compared to similar discrete-crystal PET systems.

Five nanocomposite and four transparent ceramic scintillators are evaluated, and an optimisation method developed to maximise the probability of locating in-

teractions between 511 keV photons and the scintillator within a given tolerance. A technique for localising the endpoints of the lines of response in a monolithic cylindrical shell is developed and evaluated for the best materials of both types. A coincidence detection method based on deconvolution and spatio-temporal partitioning of photon clusters is developed and evaluated. Finally, a simulated PET scan of several point sources inside the optimised scanner is performed, and images reconstructed using analytic and iterative algorithms; spatial resolution and sensitivity are evaluated.

The promising results obtained in this work establish the feasibility of the proposed design and confirm that the design objectives can be achieved. The design offers a markedly different design envelope to conventional PET, and suggests a new pathway to lower-cost total-body PET.

Dedication

For my wife, Yukti.

Acknowledgments

First and foremost I wish to thank my supervisor, Dr. Daniel Franklin at The University of Technology Sydney. It goes without saying that without your guidance and drive this project would not have been possible. I truly appreciate the sheer amount of time, effort and caffeine you have contributed. I want to also thank my co-supervisor, A/Prof Mehran Abolhasan for keeping me on the right track over the years. Special thank you to Dr. Mitra Safavi-Naeini at ANSTO for her many insights and contributions to our work. Thank you to A/Prof Justin Lipman and Dr. Negin Shariati for accommodating me in their lab; it was such a great place to work and I really enjoyed my time there. I want to also show my gratitude to UTS for not only their financial support, but for the structural support within the university, which has carried me to this point. Thank you to Dr. Matt Gaston and ARCLab; without these resources, this work would literally not have been possible. I also greatly appreciated receiving financial support from ANSTO and AINSE for conference funding. My time at UTS would not have been the same without Roumani Alabd. Thank you, not only for your contribution to this work, but also for your friendship. All the best for your own PhD!

On a personal note, I would like to thank my family (Wilsons and Srivastavas) for their love, guidance and especially patience. I especially want to thank my wife, Yukti for her love, never ending support and belief in me.

Keenan Wilson

Sydney, Australia, 2020.

Contents

List of Figures

List of Tables

Chapter 1

Introduction

Positron emission tomography (PET) is a widely-used nuclear medical imaging modality with broad clinical, biological and human health research applications. In contrast to imaging techniques such as 2D X-ray imaging, X-ray computed tomography (CT), some variants of magnetic resonance imaging (Structural MRI and Diffusion-based MRI), which produce a structural map of the imaging object, PET is a *functional* imaging modality, which elucidates biological *processes* (as opposed to *structures* in close to real time). PET is commonly used for cancer diagnosis and treatment planning, where it delineates regions of tissue with elevated metabolism (indicating rapid and abnormal cellular growth). It is also a critical tool in biological research, since by choosing an appropriate radiotracer, a wide variety of different biological processes can be quantitatively evaluated in living animals.

PET images are either acquired over a period of up to around 30 minutes to obtain a single static three dimensional image, or acquired in temporal frames with durations of seconds to minutes to create 4-dimensional spatio-temporal images, which map the uptake, distribution and excretion of positron-emitting radiotracers inside the body. Examples of PET applications include measurement of blood flow, respiration, metabolism, and receptor density and activation in the brain. This wealth of information is invaluable both for clinical diagnosis and the development of treatment plans for cancer, and also in the research sphere for studies involving small and large animals - especially the preclinical evaluation of new drugs.

During PET imaging, a compound known as a *radiotracer*, which includes a short-lived positron-emitting radioisotope such as ^{18}F, ^{15}O or ^{11}C, is injected into

the patient. The choice of compound depends on the target of interest - for example, when PET is used for cancer imaging, the most common radiotracer is an analogue of glucose, ^{18}F-fluorodeoxyglucose (FDG), which functions almost identically to normal glucose in the body. During the scan, the radiotracer circulates through the bloodstream, and some fraction interacts biochemically with the target tissue (in FDG for example, via an intracellular metabolic trapping process). The resulting physical concentration distribution of the radiotracer therefore corresponds to the extent to which it is trapped within the target cells. PET is an exceptionally sensitive imaging modality. While other modalities can provide functional information in a living subject, no imaging technique can approach the sensitivity of PET for molecular imaging; it is able to determine concentrations of radiopharmaceuticals at the nmol or even pmol range, allowing for non-invasive imaging, monitoring of disease and elucidation of biological pathways.

The radioisotope undergoes β^+ decay (concentrated at, but not exclusive to the target cells), and the emitted positron travels a short distance before annihilating with an electron to convert 100% of their combined rest mass into a pair of 511 keV gamma photons, radiating away from the point of annihilation in almost exactly opposite directions (the slight acollinearity is due to the non-zero pre-annihilation momentum of the positron and electron). The emitted antiparallel gamma photons simultaneously travel away from the point of annihilation, and due to their high energy, the majority will exit the body without scattering. These photons may be detected by an external photon detector array.

Due to the near-antiparallel direction of emission of the annihilation photons, the detection of two near-simultaneous 511 keV photons enables a *line of response* (LOR) to be drawn between the points of detection. The fundamental assumption in PET is that for most of these coincidences, a decay has occurred somewhere along this line (or close to it), since the positron only travels a short distance from the point of radionuclide decay before annihilating (less than 1 mm on average in the case of ^{18}F). By accumulating many of these LORs over time in a *sinogram* (a 3D or 4D histogram of the orientation and position of the LORs in cylindrical coordinates of $(R, \theta, \phi(t))$, where θ and ϕ are the transaxial azimuth and elevation of the LOR and R is the minimum distance of the LOR from the z-axis), a unique

mathematical representation of the radiotracer distribution can be constructed. A number of different algorithms, such as filtered backprojection (FBP) or maximum likelihood expectation maximisation (MLEM) may then be used to transform this sinogram from projection space into an image domain representation of spatial (or spatio-temporal) distribution of the radiotracer. Several additional corrective steps are then applied to compensate for attenuation, scatter, random (false positive) coincidences and the non-uniform sensitivity of the detector geometry to different potential lines of response (normalisation).

The number of gamma photons available for potential detection is limited by the maximum radiotracer dose which can safely be administered to the patient, and the half-life of the radiotracer. It is therefore very import to have a highly sensitive detector system that is capable of detecting as many of these photons as possible, since this is directly related to the quality of the resulting image (in particular, it determines the achievable signal to noise ratio). The high energy of these photons makes detection challenging; direct detection sensitivity in semiconductor detectors (e.g. reverse-biased silicon diode detectors) is extremely low due to the low density and low effective atomic number (Z_{eff}) of common semiconductor materials and the limited thickness of such detectors (around 1 mm is the maximum feasible thickness which can be achieved). Instead, the normal approach in PET is to use a *scintillator*, most commonly a high density inorganic crystal with small amounts of certain rare-earth dopants, to absorb some or all of the energy of the gamma photon (depending on the mode of interaction) and re-emit the energy as a shower of lower-energy optical photons [1]. These photons can be detected and counted easily using semiconductor photodetectors, and the total energy deposited by the gamma photon interaction estimated from the number of detected optical photons. Generating accurate lines of response with full angular coverage requires that the positron-emitting object be surrounded by a ring (or multiple parallel rings) of scintillation detectors.

Improving the performance of PET systems for clinical and biological research applications is a major research problem, driven largely by the need for higher quality images, and improved cost-effectiveness. Most current PET systems have an absolute sensitivity for coincidence detection of the order of a few percent only [2,

3], which limits the achievable signal-to-noise ratio of the system. More recently, there has been growing interest in total-body PET, in which the axial field of view extends to encompass the entire body simultaneously (as opposed to whole-body PET, in which the patient's whole body is progressively scanned via successive axial translations through a short ring of detectors) [3, 4]. While this substantially improves sensitivity by virtue of the improved solid angle coverage around the imaging object, it comes at an enormous cost due to the huge number of tiny scintillation crystals and photodetectors required. However, at present, this is the most popular strategy for increased detection sensitivity in PET.

Silicon photomultipliers (SiPMs) have become a more viable option in PET recently, due to improving responsiveness and probability of detection; adding an alternate solution to the sensitivity problem - improving timing resolution (when coupled with fast, high density and bright Lutetium based scintillators). Time-of-flight PET, as it is known, can improve effective system sensitivity gain by measuring the temporal difference between detections of the two annihilation photons. The position of the original annihilation event may then be localised to within a certain range along the LOR and the noise reduced along those particular voxels (i.e. boosting SNR).

Spatial resolution in PET is limited by a number of factors, including the size of the scintillator crystals, photon acollinearity and positron range (although the latter can be largely corrected using image deconvolution methods). Shrinking the scintillator crystals only works up to a point, beyond which efficient coupling of the individual crystals to photodetectors becomes impractical due to the interstitial reflective coatings needed. Scintillation detectors are also inherently expensive and difficult to manufacture, as a result scintillator crystal itself accounts for a large proportion of the overall cost of the scanner [5, 6, 4]. An alternative approach is to use monolithic scintillator slabs coupled to photodetector arrays to analytically estimate the location of the point of interaction within the slab. Monolithic slabs have a higher spatial coverage compared to regular block scintillation detectors and are capable of measuring the depth of interaction (which in turn improves timing resolution [7, 8]). However, the production of large crystals of uniform quality from high-performance scintillator materials is challenging and very expensive.

Furthermore, accurate localisation is challenging when the interaction occurs near the boundary of the rectangular slabs, and algorithms capable of handling this well (typically based on neural networks) are computationally expensive.

New approaches which seek to simultaneously address the problems of achieving high spatial resolution and high sensitivity without greatly inflating the cost of a scanner would clearly be of enormous value in the field of PET, and would expand the availability and utility of this important imaging modality both for clinical and biological applications. **This work proposes and, via simulation, evaluates a solution to problems of PET sensitivity and spatial resolution, while simultaneously keeping the system cost-effective, by exploiting the properties of new nanocomposite and transparent ceramic scintillator materials to enable the construction of a radically new PET scanner geometry based on an extension of the monolithic scintillator concept to its ultimate conclusion: a continuous cylindrical shell with no internal boundaries**. Our design couples this cylindrical shell with a double-sided array of silicon photomultiplier detectors, tiled on both the inner and outer surfaces of the shell, such that the entire cylindrical volume would act as a single monolithic scintillation detector.

While this geometry offers many advantages compared to conventional scanner designs, including the potential for very high sensitivity and spatial resolution, the design presents a number of major technical challenges, including optimising the geometry based on the properties of the specific scintillator materials, and the need for new methods for detecting coincidences and locating the endpoints of the lines of response in the scanner. This Thesis aims to develop methods which address each of these challenges, culminating in a proof-of-concept image reconstruction based on a full simulation of an optimised scanner design.

1.1 Research Objectives and Overview

The overall aim of this work is to develop the methods needed to implement a continuous cylindrical shell PET scanner using nanocomposite or transparent ceramic materials, and evaluate the performance of a simulated scanner based on this design

concept, including the development of a complete pipeline for transforming list-mode data to a corrected 3D image.

The specific research objectives of this Thesis are:

1. To develop methods for objectively comparing the performance of different nanocomposite and transparent ceramic scintillator materials, including development of accurate simulation models for different materials and the development of appropriate performance metrics which are relevant to PET performance, and evaluate this for a range of promising nanocomposite and transparent ceramic scintillator materials;

2. To develop a technique for optimising the thickness of the cylindrical scintillator shell to maximise the performance metric defined above for a given scintillator, and find this optimised thickness for each of the evaluated scintillator materials;

3. To adapt an existing approach for localising the point of interaction in a flat monolithic scintillator to a continuous cylindrical shell;

4. To design a method for coincidence detection suitable for use in the proposed scanner design; and

5. To implement a simulated scanner using one of the best-performing materials, optimised according to the developed performance metric, simulate several simple phantom and/or point source models and evaluate its sensitivity and spatial resolution.

Each chapter of the Thesis will solve important engineering design questions, contributing to the overall aim.

Chapter 2 provides a comprehensive review of literature which is relevant to the overall aim. This includes a broad overview of current PET systems and the physical interactions taking place within them. The photodetectors, scintillation materials and system architecture are discussed in detail, including a review of the root causes of system limitations and how they might be addressed. Finally, image reconstruction theory is explored, including analytic and iterative algorithms, for use in quantifying an output. The literature review is the first step in identifying

why the system limitations are present, what has already been done to address them and how we might approach a new solution to the sensitivity and spatial resolution problems.

Chapter 3 aims to make a determination of *which nanocomposite or transparent ceramic materials might be suitable for use in the proposed system.* Since Rayleigh scattering is a limiting factor for the optical transparency of the nanocomposites / ceramics, it is also important to *find the optimal thickness for the scintillator slab*; finding the maximum probability of gamma detection for a desired position estimation accuracy. Each scintillator material has been simulated as a simple monolithic block detector with dual-sided readout, using Monte Carlo-based methods over a range of scintillator thicknesses, with an analytic algorithm used to determine the point of interaction. Importantly, this chapter defines a critical performance metric for monolithic scintillators based on the probability with which an interaction can be localised to within a specified tolerance. This metric is then used to optimise the scintillator thickness for each of the evaluated materials. A detailed statistical analysis of the spatial error distributions and fraction of Compton and photoelectric events is performed for each optimised scintillator, and the best-performing nanocomposite and transparent ceramic materials are identified.

This chapter resulted in the following publications:

- **Keenan J. Wilson**, Roumani Alabd, Mehran Abolhasan, Mitra Safavi-Naeini, and Daniel R. Franklin. Optimisation of monolithic nanocomposite and transparent ceramic scintillation detectors for positron emission tomography. *Sci Rep* 10, 1409 (2020).

- **K. Wilson**, IEEE, R. Alabd, IEEE, and D. R. Franklin. Optimisation of Monolithic Nanocomposite and Ceramic Garnet Scintillator Thickness for PET. Poster presentation at 2018 IEEE Nuclear Science Symposium and Medical Imaging Conference (NSS/MIC), Sydney, Australia.

Possible geometries for the fully monolithic, continuous cylindrical shell PET architecture are presented in Chapter 4. Two geometries are presented, using materials which were identified to be the most suitable from the previous chapter; GLuGAG:Ce and LaF_3:Ce-polystyrene, each with a shell thickness equivalent to the

optimal thickness for a median euclidean distance error of <5 mm. The main aim of this chapter is to *demonstrate that this geometry is potentially feasible for PET, and successfully generating lines of response from coincident detections*, which may then be used in image reconstruction algorithms. A novel methodology for localisation of gamma pairs and generation of a line of response is described and a statistical analysis of the error in measurement of the LORs are presented, as well as an initial measurement for sensitivity of the scanner. Sensitivity is presented as the fraction of annihilation events which yield usable LORs.

This work resulted in the following publication:

- **Wilson, K.J.**, Alabd, R., Abolhasan, M., Franklin, D.R. and Safavi-Naeini, M., 2019, July. Localisation of the Lines of Response in a Continuous Cylindrical Shell PET Scanner. In *2019 41st Annual International Conference of the IEEE Engineering in Medicine and Biology Society (EMBC)* (pp. 4844-4850). IEEE.

Due to the radical differences between the proposed scanner architecture and conventional pixellated scanners, existing methods for coincidence detection cannot be applied. Chapter 5 presents *a methodology for coincidence detection by segmenting the scanner into sub-regions, accumulating events in each as a set of time-domain signals, and deconvolving them by the scintillator impulse response to correct for pulse pile-up, and then performing spatio-temporal cluster analysis to identify probable coincidence events.* The results are broken down into the fraction of true coincidences detected and compared to the fraction of false positives and false negatives for different types of interactions.

This work has resulted in the preparation of the following paper for submission to *Physics in Medicine and Biology*:

- **Wilson, K.J.**, Alabd., R, Safavi-Naeini, M., Franklin, D.R., Efficient spatio-temporal deconvolution-based pulse pile-up correction for coincidence detection in monolithic-scintillator PET systems, *To be submitted to Physics in Medicine & Biology*

Chapter 6 presents a reconstruction of an image of a number of simulated point sources placed inside the field of view, using LORs generated by the scanner and

the methods described in the previous two Chapters. The aim is to firstly *determine whether or not the scanner can actually produce a reasonable image* and secondly, *measure the spatial resolution of the point source image* by measuring the full width at half maximum of the line profile through each point source. Post-processing for randoms correction and attenuation corrected normalisation of the image is also demonstrated.

An extended version of the this chapter is currently in preparation as a paper for submission to *IEEE Transactions on Medical Imaging*:

- **Wilson, K.J.**, Alabd., R, Safavi-Naeini, M., Franklin, D.R., Characterisation of a Simulated Continuous Cylindrical Shell PET Scanner with Nanocomposite and Ceramic Scintillators, *To be submitted to IEEE Transactions on Medical Imaging.*

Finally, Chapter 7 summarises the results and implications of this work, and provides recommended directions for continuation of this work in the future.

1.1.1 Additional Research Contributions

A number of additional research publications and presentations are listed below:

- Alabd, R., Safavi-Naeini, M., **Wilson, K.J.**, Rosenfeld, A.B. and Franklin, D.R., 2018. A simulation study of BrachyShade, a shadow-based internal source tracking system for HDR prostate brachytherapy. *Physics in Medicine & Biology, 63*(20), p.205019.

- R. Alabd, **K. Wilson**, D. R. Franklin. Source Tracking in a Scattering Medium via Fast Hierarchical Pattern Matching. Oral presentation at 2018 IEEE Nuclear Science Symposium and Medical Imaging Conference (NSS/MIC), Sydney, Australia.

- A. M. Ahmed, A. Chacon, **K. Wilson**, D. Franklin, K. Bambery, A. Rosenfeld, S. Guatelli, M. Safavi-Naeini. Sparse time-of-flight in-beam PET for quality assurance in particle therapy. Poster presentation at 2019 IEEE Nuclear Science Symposium and Medical Imaging Conference (NSS/MIC), Manchester, United Kingdom.

Chapter 2

Literature Review

2.1 Positron Imaging

Positron emission tomography (PET) is a well-established nuclear medical imaging modality which is seeing clinical use in oncology, neurology and cardiology, as well as a number of research applications such as the monitoring of disease therapies and drug effectiveness. Imaging is based on the capture of radiation from an internal energy source in the form of an injected radio-labelled tracer. When the radiotracer is injected into the body, it undergoes decay, releasing positrons which combine with nearby electrons in what is known as an *annihilation event*; a complete mass to energy conversion in accordance with Einstein's famous equation, $E = mc^2$, producing two 511 keV gamma photons, travelling in opposing directions from the point of interaction (See Figure 2.1).

A ring of high density, high effective atomic number scintillation detectors encompassing the field of view, are used in the detection of these high energy gamma photons. An event is stored only if both gamma photons are detected within specific timing and energy windows; known as a *coincidence detection*. The original annihilation event is known to lie somewhere along a *line of response* between the two detectors where the scintillation interactions occurred and these stored lines of response are subsequently used in the reconstruction of the original image, using either analytic or iterative reconstruction algorithms.

The predetermined time frame is known as a coincidence window and exists because there will always be some variation in the detection time of the two photons.

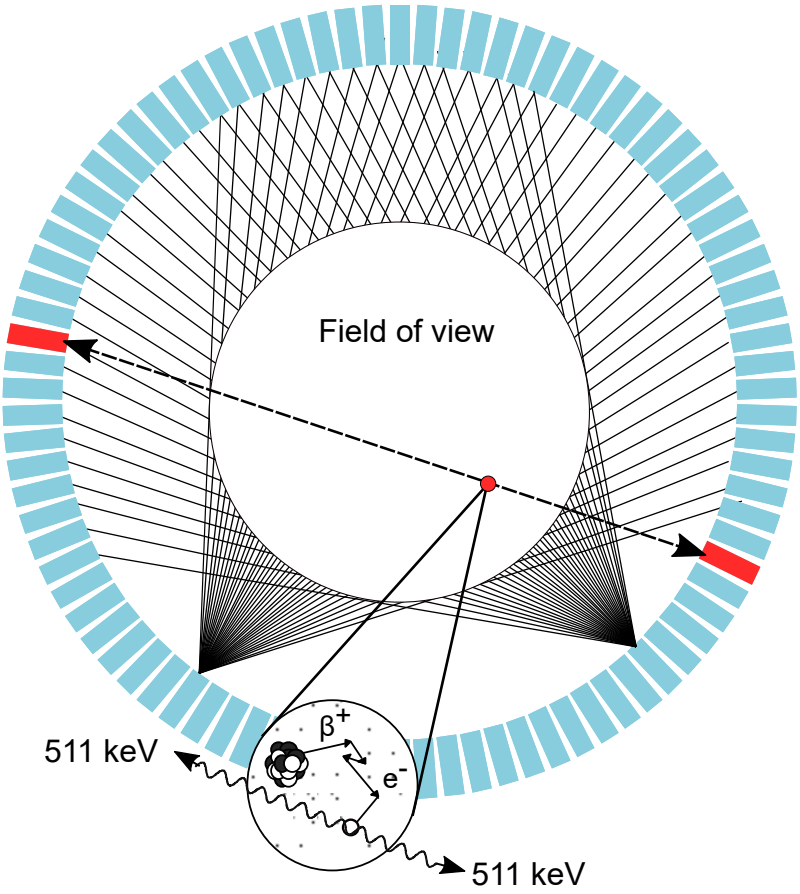

Figure 2.1: The radiotracer decays to produce a positron which, upon travelling a short distance inside the patient, annihilates with an electron and produces two 511 keV gamma photons emitted in approximately opposite directions. The detection of these two gamma photons is said to be a "true" event if they are detected by two detectors which are set up to be "in coincidence" (indicated by the lines across the field of view). [9]

This arises due to a number of reasons; primarily, because the event is extremely unlikely to occur in the precise centre of the detectors, the flight paths will be different lengths and will therefore arrive at different times. Also, the circuitry used to detect the photons will be slightly different in each case and hence will have different signal transit times for each. Otherwise, the characteristics of the detection system will be responsible for timing resolution; including scintillation decay time, light yield and photodetector response time. The coincidence timing window is typically 6-12 ns and the uncertainty in the time stamp of each detection is generally 1-2 ns [10]. In addition to the timing window the line of response must also lie within a valid acceptance angle for the scanner and the energy of the

detection must be within a particular energy window, in order to demonstrate that the annihilation photon has not undergone Compton scattering inside the patient. Because of the large number of annihilation events taking place, it is crucial that the detection system has sufficient spatial, temporal and energy resolution to determine that annihilation photon pairs are indeed part of the same event.

2.1.1 Types of Detected Events

Coincidence events satisfying requirements for the acceptance angle, timing and energy thresholds are not always desirable events; some proportion of these will be scattered, or the coincidence will originate from two separate annihilation events, leading to incorrect LORs. Terminology for these events will be discussed below. See Figure 2.2 [11] for further clarification.

True Events

Events which are largely unaffected by scattering or separate annihilation events, resulting in a correct LOR are termed *true events*.

Scatter Events

After an annihilation event, one (or both) of the gamma photons may be Compton scattered by the patient, the scanner gantry itself or objects outside the field of view, to then be picked up as an event by the detector. Scattering will result in the loss of some energy and will usually be filtered out with an energy window; removing the events which are outside the photopeak. The scatter fraction is generally constant for the object being imaged and the radioactivity distribution.

Random Events

In certain cases, if two separate annihilation events occur at the same time, they may be incorrectly identified as a coincidence, if a single gamma photon is detected from each event (with the others undetected). This may likely lead to the incorrect LOR. The rate of random events (R) in the system is related to the rate of decay of the radiotracer, which is modelled to some degree by the relation

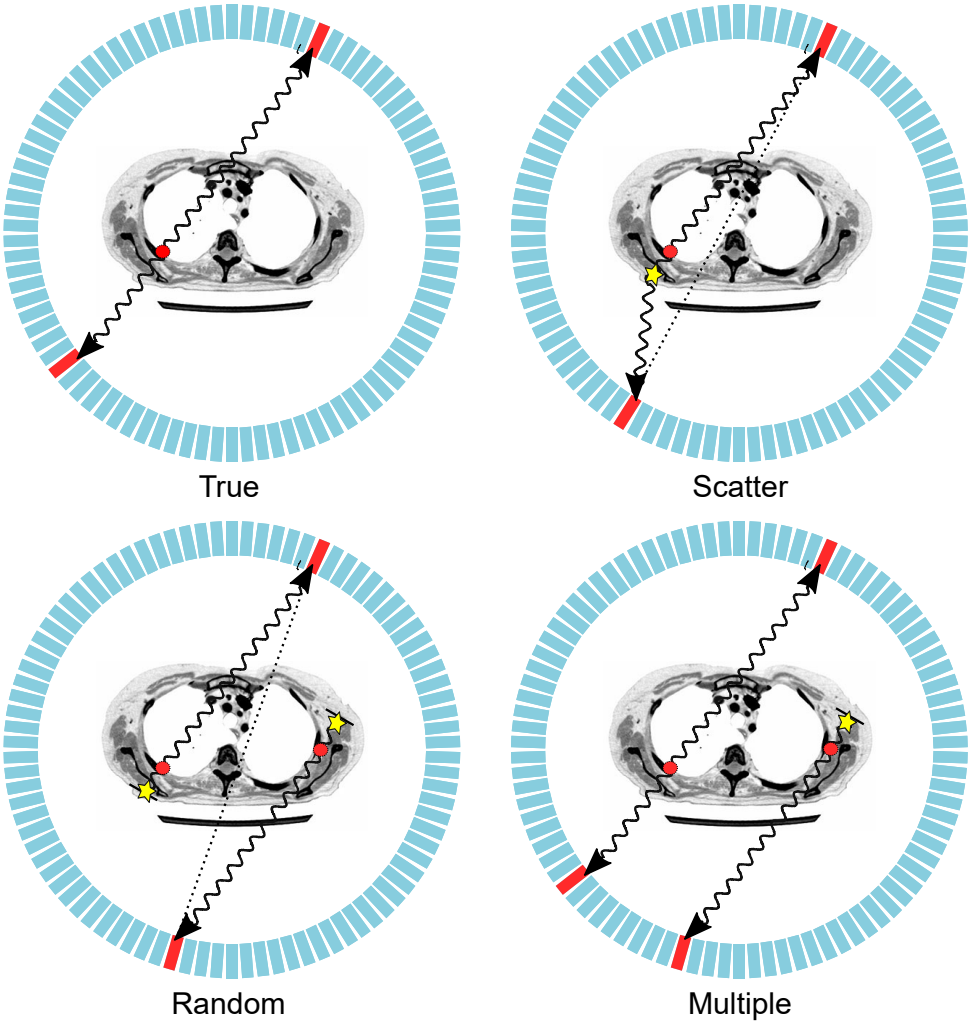

Figure 2.2: Types of events occurring in a PET scanner which may trigger a coincidence detection. Scatter, random and multiple events will cause degradation of the reconstructed image and so need to be controlled [11].

$$R_{ab} = 2\tau N_a N_b \tag{2.1}$$

Where 2τ is the width of the coincidence timing window and N is the single event rate incident upon detectors a and b ($N_a \approx N_b$) [11].

Multiple Events

If multiple annihilation events occur, resulting in more than two singles within the coincidence timing window, then all of them are discarded. There is generally no way to be completely sure which of the singles make up the coincidence. This will obviously become more prevalent with a high count rate or larger timing windows.

2.1.2 Photon Interactions with Matter

Electromagnetic radiation, when passing through matter, will either penetrate it completely or undergo some type of interaction. There are four types of interactions which are often seen for the photon energies present in nuclear medicine. The probability of each particular interaction is dependent upon the energy of the photon and the atomic number of the material.

Photoelectric Effect

The incoming gamma photon energy is *completely* transferred to an atomic electron. Part of the energy overcomes the binding energy of the electron, the rest is converted to kinetic energy as the electron is ejected.

Incoherent (Compton) Scattering

In cases where high energy photons interact with loosely bound orbital electrons (with low binding energy), only some of the energy is transferred to the electron; sufficient enough to eject it. The rest remains with the original photon, itself scattered in a new direction θ_c. The scattering relationship is given by

$$E_\gamma^{'} = \frac{E_\gamma}{1 + \frac{E_\gamma}{m_0 c^2}(1 - \cos\theta_c)} \tag{2.2}$$

Where E_γ is the original energy of the photon, $E_\gamma^{'}$ is the energy after scattering, θ_c is the angle of scatter, m_0 is the rest mass of an electron and c is the speed of light.

Figure 2.3 shows the the relationship between scattered angle and energy, but also the differential scattering cross-section (for a 511 keV photon), which is proportional to the angular probability distribution [12]. We can see then that there is a larger probability of a small scattering angle, meaning that most Compton scattered events will be *forward scattered*.

Pair Production

The photon interacts with the entire nucleus and is converted to a positron-electron pair. The threshold energy for this interaction is 1.022 MeV (equal to 2 electron

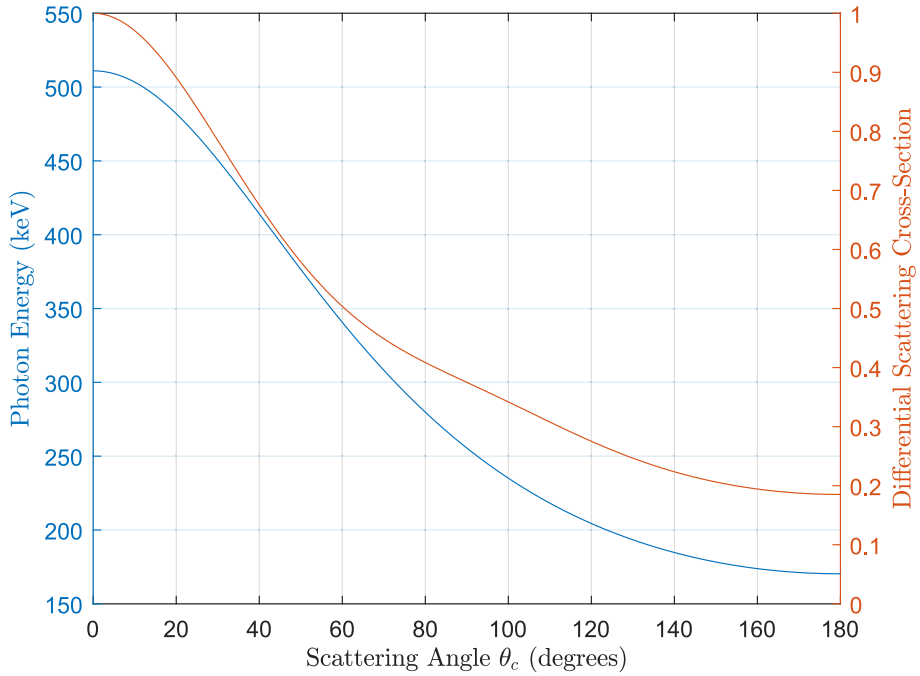

Figure 2.3: Angular probability distribution (broken line) given by the Klein-Nishina equation [12] and resultant energy (solid line) for Compton scattered annihilation photons [11].

rest masses), so is unlikely to occur in PET.

Coherent (Rayleigh) Scattering

For lower energy photons interacting with the nucleus, the energy transfer to the atom can be neglected since is has a relatively large rest mass. The momentum change is very small, resulting in a small change in direction for the photon. This also extends to interactions with very small particles, which will be covered in greater detail in chapter 3; where optical photon interactions with nanoparticles are discussed.

2.2 PET Radiotracers

Since positron emitting radiopharmaceuticals have such short half-lives (see Table 2.1 below), the modality has only quite recently been realized as a viable option clinically. In particular the discovery in the usefulness of fluorine-18 labelled 2-

Radioisotopes	Half-life	β^+ energy (MeV)		Range in water (mm)	
		Average	Maximum	Average	Maximum
^{11}C	20.4 min	0.385	0.960	1.1	4.1
^{13}N	9.96 min	0.492	1.19	1.5	5.1
^{15}O	123 sec	0.735	1.72	2.5	7.3
^{18}F	110 min	0.250	0.635	0.6	2.4
^{62}Cu	9.74 min	1.315	2.94	5.0	11.9
^{64}Cu	12.7 hr	0.278	0.580	0.64	2.9
^{68}Ga	68.3 min	0.836	1.9	2.9	8.2
^{82}Rb	78 sec	1.523	3.35	5.9	14.1
^{124}I	4.18 days	0.686	1.5	2.3	6.3

Table 2.1: Some common positron emitting radiotracers currently used in PET imaging. Adapted from [15] and [11].

fluoro-2-deoxy-D-glucose (FDG) as a metabolic tracer, with a relatively longer half-life has pushed the industry to accept full-time PET operation in many hospitals around the world.

The first three entries into Table 2.1 are elements that are very common in biological systems and are very useful in tracing biological processes. There are many different radiotracers based on these particular isotopes. While Fluorine does not really fit into this category, it has the useful property of being able to replace a hydrogen atom (or in the case of FDG a hydroxyl in the glucose molecule [13]).

The first four isotopes in Table 2.1 have the additional benefit of producing only a single positron. Some of the heavier elements will actually produce additional gamma photons in addition to the positron, which in some cases may interfere with scintillation cameras, sometimes even registering as false coincidences [14].

2.2.1 Metabolism

FDG is the premier radiotracer used for imaging metabolic processes and is specifically used to measure the speed of metabolism of glucose, the main application of which is in the detection of cancer and monitoring cancer spreading throughout

the body. If the body is in a fasting state (which it is during the PET scan), then the majority of bodily tissue will consume fatty acids rather than glucose, with the exception of the brain and some other organs. Cancer cells also have a high glucose metabolism and will uptake and accumulate significant portions of the tracer at their location within the body. The reason why we don't simply use radioactive glucose in this situation is because it is quickly metabolised into lactate and returns to normal circulation inside the body.

There are some additional isotopes which may become commercially available as other options for measuring metabolic processes in the future. For example ^{11}C acetate, which is able to trace the speed of oxidative metabolism (in the brain and myocardium - the muscular wall of the heart) and also ^{11}C palmitic acid which is able to trace the metabolism of the fatty acids (again, in myocardium) [16].

2.2.2 Blood Flow and Regional Perfusion

Blood flow and regional perfusion are slightly different in their definitions; blood flow is the amount of blood (in ml) to be supplied to a particular tissue or organ in a specific time period. Perfusion is the blood flow, per unit mass (in ml/min/g).

There are a number of radiotracers which are used to measure these, the two most common being ^{82}Rb chloride and ^{13}N ammonia, both of which are used in myocardial perfusion. Respectively, the $^{82}Rb^{+}$ cation or the $NH{-}4^{+}$ ion will substitute for a K^{+} ion in the red blood cells, to then be carried to the myocardium. In addition, the $NH{-}4^{+}$ ion can actually be taken up by the myocardium itself and become trapped, when it interacts with glutamine to form glutamate [17]. The rubidium tracer will need to be transported to the myocardium through a Na^{+}/K^{+} pump.

Similar to ^{13}N ammonia, ^{62}Cu-labelled pyruvaldehyde bis(N4-methyl)thiosemicarbazone (PTSM) has a mechanism where it will be rapidly taken up by cells and then trapped as it becomes metabolically altered. It is used mainly for tracing blood flows in myocardium and tumour tissue. Other tracers which are present in the research arena include Oxygen-15 water, which is freely diffusible across membranes and has minimal physiological effect on the target tissue or organ. For this reason it is often used in brain and myocardium blood flow studies [15].

2.2.3 Tumour Proliferation

Malignant tumours (cancers) grow very rapidly and as a result will consume significantly more nucleotides during DNA synthesis, particularly they are a large consumer of thymidine phosphate. By using radiotracers which target this action, we can observe the growth of a particular cancer. ^{11}C thymidine and ^{18}F labelled 3'-fluoro-3'-deoxythymidine (FLT) have both been used for this purpose, though the former does have a relatively short half-life and is affected by the metabolism of the blood. FLT is much more metabolically stable and is better suited to tracing. During the DNA synthesis process, after FLT has been phosphorylated and incorporated into DNA, it will become metabolically trapped by the cancer cells.

We can also monitor the proliferation of cancerous tumours by examining the rate of protein synthesis. This process is reliant upon amino acids, which have been successfully labelled with radiotracer [18]. Examples are ^{11}C-L-methionine, 6-^{18}F fluoro-L-meta-tyrosine (FMT) and 1-amino-3-^{18}F fluorocyclobutane-1-carboxylic acid (FCCA), which have shown good potential for imaging brain tumours.

2.2.4 Positron Energy

When the positron decays from a particular radionuclide, it will be ejected with a kinetic energy that is within a spectrum of energies unique to that particular radionuclide. As may be seen in Table 2.1, the range of the positron is proportional to its kinetic energy. For example, ^{18}F has a relatively low energy positron (average 250 keV), which will only travel a short distance (average 0.6 mm in water) before interacting with a random electron and undergoing annihilation. However, a positron ejected from ^{82}Rb, with an average kinetic energy of 1.523 MeV, will on average travel 5.9 mm in water before interacting with an electron. This property is an important consideration when choosing a radiotracer because it will affect the overall spatial resolution of the system. A higher positron energy and range will have a higher probability of the reconstructed image being susceptible to blurring.

2.3 PET Detectors

Accurate detection of annihilation gamma rays is key to correctly imaging the injected radiotracer. Many different types of detectors have been explored for application in PET systems, though generally there is a common aim to achieve certain ideal properties [19, 20].

2.3.1 Detector Properties

Stopping Power

Stopping power refers to the probability that the incident gamma photons will be absorbed by the detector; this property is dependent upon the density (ρ) and effective atomic number (Z_{eff}) of the materials used. The effective atomic number is given by (2.3), where f_n is the fraction of the total number of electrons in element n in the compound and Z_n is the atomic number of element n [21]. The power m depends on gamma radiation energy; for 100-600 keV photons this varies from 3-3.5 [10].

$$Z_{eff} = \sqrt[m]{f_1 Z_1^m + f_2 Z_2^m + ... + f_n Z_n^m} \tag{2.3}$$

A detector with high stopping power effectively means it will have a high sensitivity with less scattering effects (which may introduce depth of interaction errors into the system). Conversely, a high stopping power may allow for more compact detector design, if required.

Energy Resolution

Refers to the precision of measuring the energy of the incident gamma ray and the ability to distinguish between other interactions with different energies. This is particularly important because we need to distinguish between hits which have been Compton scattered (lower energy) and regular hits on the detector. The energy resolution (R) is defined as the full width at half maximum (FWHM) of the photopeak (ΔE), given as a percentage of the photopeak energy (E_γ).

$$R(\%) = \frac{\Delta E}{E_\gamma} \times 100 \tag{2.4}$$

Timing Resolution

Timing resolution refers to uncertainty in the timing of a coincidence detection, due to statistical fluctuations in the signal (due to movement of electrons, electron hole-pairs or scintillation photons) or electronic noise in the circuitry associated with the timing chain (e.g. the photomultiplier tube (PMT), the constant fraction discriminator (CFD), and the time to digital converter (TDC) [22]). For a pair of detectors, this uncertainty is described by a Gaussian distribution, where the timing resolution is the FWHM of the curve.

Good timing resolution will reduce statistical noise from random coincidences and, in time-of-flight PET, enable more precise localisation of the positron annihilation along the line of response. In scintillation-based detectors, the timing resolution is dependent on the rise and decay times of the optical emission from the scintillator material itself, as well as jitter in the photodetector response.

Spatial Resolution

Spatial resolution refers to the ability of the detector system to distinguish between point sources that are in very close proximity. If we are to image a source that is much smaller than the resolution of the system, then there will be a blurring of the image, known as the spread function. Depending on the type of source, this may either be a point spread function (for a point source) or a line spread function (for a line source). This can usually be approximated as a Gaussian function, where the spatial resolution is defined as the FWHM. Spatial resolution may be affected in part by the properties of the detectors; including width, spacing, stopping power, depth of interaction and angle of incident gamma rays. (Of course there are some other causes not related to the detectors, such as positron range, non-collinearity of gamma rays, number of angular samples and image reconstruction parameters as well) [23, 24].

Cost

While not specifically a property of a detector, it is still ideal (commercially at least) for a detector system to be cheap. This is mostly a product of the materials used or degree of difficulty of the manufacturing processes.

2.3.2 Semiconductor Detectors

Semiconductor detectors operate via direct detection of the incident radiation; upon absorption, the radiation causes excitation of the valence electrons in the material and the formation of electron-hole pairs. When electrodes are placed either side of the semiconductor material and an electric field is applied, these electron hole pairs flow toward the cathode and anode respectively, causing a current pulse which may be measured. The magnitude of the pulse is proportional to the number of electron-hole pairs and hence energy deposited by the radiation.

This is perhaps the most energy efficient mode of detection for gamma rays, though the semiconductor materials used for this application must be extremely dense, high purity and (desirably) operational at room temperature. For these reasons, traditional semiconducting materials such as silicon and germanium are typically unsuitable for gamma ray detection; they are relatively low density, meaning they will have low stopping power, but also suffer from thermally induced noise current when operated (and stored) at room temperature.

Two particular materials which have been identified as having properties suitable in PET imaging are Cadmium telluride (CdTe) and cadmium zinc telluride (CZT) [25]. These were both found to have exceptional properties for useful application in gamma ray detection; excellent stopping power (due to high ρ and Z_{eff}), good energy and spatial resolution and stable performance at room temperature. Though as with all semiconductor materials, purity is often a problem during fabrication. Impurities in the material will often impede electron flow and hence reduce the effectiveness of the detector significantly. Growing large volumes of CdTe or CZT is usually very difficult and extremely expensive and for this reason these detectors are usually not employed in fully body PET imaging systems. Though they can be used in smaller systems requiring very high spatial resolution; for example, targeted scans or small animal systems used in pre-clinical research.

2.3.3 Scintillation Detectors

Unlike the semiconductor detector, scintillation detectors operate via indirect detection of gamma photons. The high ρ, high Z_{eff} volume of scintillator material is used to absorb the high energy incident gamma photons and convert their energy into

a shower of lower energy optical photons, which may be efficiently detected by an optically coupled photo-detector, such as a photomultiplier tube (PMT), avalanche photodiode or silicon photomultiplier (SiPM). The signal is then amplified and converted to an electrical signal for coincidence processing.

Figure 2.4 describes the scintillation process as electrons move between energy states in the crystal; upon interaction, the energy deposited by the gamma photon excites electrons in the valence band of the crystal to overcome the energy gap (E_g) and move into the conduction band. Since this state is unstable, electrons decay back to the valence band, releasing energy in the form of optical scintillation photons. This process is known as luminescence and generally, the scintillation photons produced are in the ultraviolet wavelength range and are emitted isotropically from the point of interaction [11]. By doping the crystal with impurities, it is possible to raise the ground state of the electrons at the impurity sites, to just above the valance band and also produce excited states just below the conduction band, effectively reducing the energy gap. This is of interest because we know from the Plank-Einstein relation

$$E = h\nu \tag{2.5}$$

The quantum energy (E) will be proportional to frequency (ν) and hence inversely proportional to wavelength (since h = Plank's constant). This means that by doping the scintillation crystal it is possible to manipulate the wavelength of the scintillation photons; producing an output in the visible range, which may be more efficiently detected by photodetectors at room temperature. Usually, the amount of dopant in the crystal will only be a small percentage, so as to keep photon reabsorption in the dopant to a minimum.

Scintillation detectors are currently used in almost all clinical PET systems. While they do not have the energy efficiency or sharpness in energy resolution of the semiconductor examples mentioned previously, generally scintillators have comparable (and in some cases superior) density and Z_{eff}, translating to excellent stopping power. Additionally, the scintillators themselves are grown as single crystals using either of the Czochralski, Kyropoulos or Bridgman-Stockbarger methods [26, 27], which involve complex fabrication processes using very high temperature furnaces

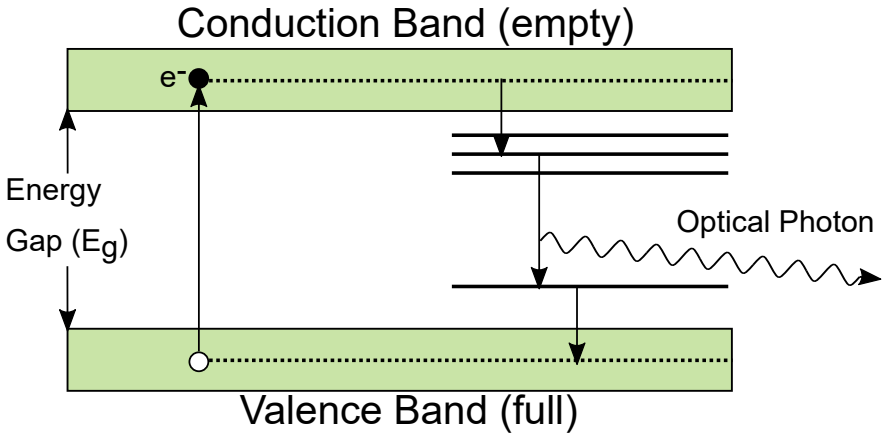

Figure 2.4: Shows the excitation of a valence electron to the conduction band in a scintillation crystal. Upon moving back to the stable state, optical photons are produced which can be detected by PMTs or photodiodes [11].

for extended periods. Although these processes can be quite costly and purity is still a concern, the production yield is generally much better then for CdTe or CZT, translating to an overall lower cost.

2.3.4 Photomultiplier Tube

Most current commercial detector systems use solid-state photodetectors (SiPMs) for readout, though PMTs are still in use, both in legacy systems and novel research-based scanners [28]. PMTs have demonstrated responsiveness to single photon interactions, they have very good energy (15-25% - coupled to LSO arrays [29, 30]) and timing resolution (475 ps - again coupled to LSO [31]).

The structure of the PMT may be seen in Figure 2.5 - it consists of a photocathode at the entrance window (which will be coupled to a volume of scintillator material) and an electron multiplier arrangement, set in a vacuum inside a glass tube. Scintillation photons incident on the photocathode may produce a photoelectron (via the photoelectric effect), which is guided by a focusing grid to the nearest dynode. The dynode is able to attract this primary photoelectron via an applied positive potential, relative to the photocathode (usually 200-400 V [10]). The dynodes are coated with materials having similar characteristics to the photocathode and upon interaction with the incident photoelectron, release multiple secondary photoelectrons. Each successive dynode has a linear increase in potential difference,

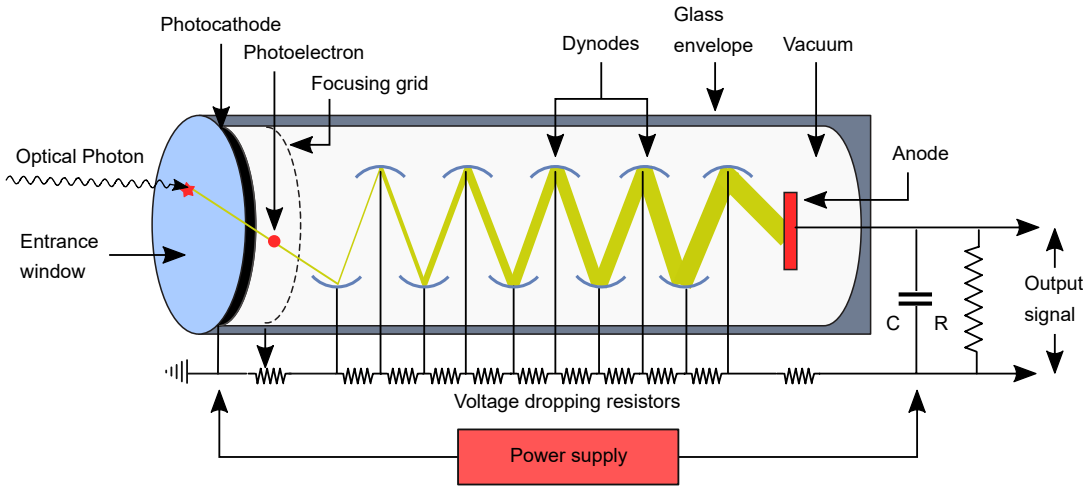

Figure 2.5: Components and basic operating principles of a photomultiplier tube (PMT) [10].

producing a multiplier effect to increase the amount of photoelectrons exponentially as they are directed toward the anode. It is here that they are collected and output as current pulse.

The multiplication factor (m) is dependent upon the energy of the primary photoelectron, which is itself dependent upon the potential difference between each element (by definition potential energy is the product of charge and Voltage: $U_E = qV$). The total gain at the anode is given by

$$gain = m^n \tag{2.6}$$

Where n is the number of dynodes. PMTs have quite high gain in practice; typically 10^6-10^7 [29], which in turn provides a very good signal to noise ratio for the system. Typically though, the quantum efficiency (QE) of the detector is not very strong (the ratio of the number of generated photoelectrons to the number of incident scintillation photons, expressed as a percentage); the typical QE for a PMT is approximately 20-30% [32].

For traditional full-body PET systems PMTs perform well, though trends in the commercial space have tended towards hybrid modality scanners; where functional PET imaging is combined with the anatomical imaging capabilities of CT and MRI. PMTs are not ideal in this regard, especially with the latter modality, where the large magnetic fields involved interfere with internal electron movement of the PMT. In

the research field, there is strong interest in developing novel, targeted PET designs using considerably smaller geometries, where the overall bulk of these detectors becomes a problem.

2.3.5 Avalanche Photodiode

The first hybrid PET/MRI system capable of simultaneous acquisitions was made commercially available in 2010 by Siemens Healthcare [33] - the PET detector system is based on avalanche photodiodes (APD), due to their insensitivity to magnetic fields. Their size has also led to incorporation into several small animal PET systems [29, 34, 35, 36].

The operation of an APD is very similar to a regular PIN photodiode (a layered p-type, intrinsic, n-type semiconductor configuration), with the difference that it has an additional layer / structure; a p-n junction. There are many types of structures for an APD, one of which may be seen in Figure 2.6; where P^+ denotes the positively doped region, N^+ the negatively doped region and P^- the intrinsic or depleted region. The region P is a lightly doped p-region (the avalanche layer), which forms the p-n junction.

When scintillation photons penetrate through into the intrinsic region of the detector, the interactions create electron-hole pairs (similar to the direct detection semiconductor detector). A very large reverse bias (several volts per μm) is applied across the regions, which results in an especially large electric field at the p-n junction. Electrons drifting toward the p-n junction become greatly accelerated by this electric field and gain sufficient energy to ionize further electrons when a collision occurs with the crystal lattice. Similarly, these new electrons are also accelerated by the electric field and cause further impact ionization - effectively producing a gain for the output pulse. The internal gain of a typical APD is approximately 10^2-10^3 [29], which is significantly less than a PMT.

APDs have some obvious strengths in their compact design and resistance to magnetic fields. They also have a comparable energy resolution to the PMT (16.2 % @ 511 keV, room temperature [35]) and a very high quantum efficiency ($>$ 80 % [37], typically in the 500-600 nm range). Though there are still some drawbacks; typically the signal will have a relatively slow rise time compared to a PMT, meaning

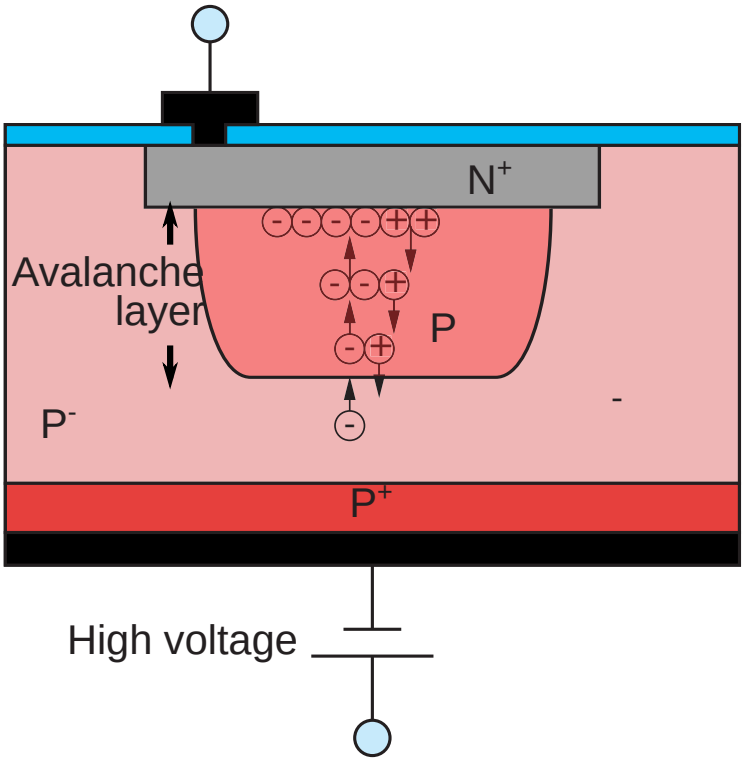

Figure 2.6: Components and basic operating principles of an avalanche photodiode (APD) [39]. Shows doping of semiconductor layers and gain occurring in the avalanche layer.

that APDs will exhibit slower timing resolution (∼26-43 ns [38]) and are generally unsuitable for TOF PET. There is also some concern with pulse fluctuations as the stability of the gain is a function of both the applied bias voltage and the operating temperature. Both must be adequately controlled when used in imaging systems. In some cases cooling may be required to achieve adequate SNR.

In normal operation mode the APD does not have the gain required for a response to single photons, though if the reverse bias is increased significantly, then this may be accomplished. This is known as Geiger mode and APDs operating in this particular configuration are known as single-photon avalanche photodiodes (SPAD). In this mode the gain is increased to reach parity with the PMT (10^6-10^6) and becomes completely independent of the energy of the incident radiation. The SPAD is the basis of the next evolution in semiconductor detectors - the silicon photomultiplier (SiPM).

2.3.6 Silicon Photomultiplier

The SiPM detector is analogous to a large array of very small (10-100 μm) SPADs connected in parallel, over a pixel surface area of only ∼1-3 mm. Owing to the small volume of the SPAD, the depletion layer is also typically very small (∼0.7 μm [29]) and hence the operating voltage (bias voltage) is much smaller than for the APD. Each SPAD is paired with its own quenching resistor; each unit is known as a microcell and can number between 500-10000 per pixel (depending on the size of the pixel surface area). The SiPM, like the SPAD, has the ability to detect single photons, though because of its structure it is able to introduce some energy proportionality for multiple interactions; each microcell can independently register an interaction and may be output as the sum of their currents (analogue mode), or by simply counting the pulses (digital mode).

When a scintillation photon interacts with a microcell, an excessive current is released via Geiger avalanche across the microcell. The quenching circuit is set up passively, with resistors in series to each SPAD - this is here for two reasons; firstly to stop the current output signal and ready the microcell for the next detection and secondly, to control the current so as not to destroy the circuitry. The avalanche current causes a voltage drop across the resistor, reducing the bias across the semiconductor below the breakdown voltage; effectively halting the avalanche process. There will then be some recovery time associated with the microcell recharging back to the bias voltage, in preparation for the next interaction [40].

The SiPM significantly improves upon the capabilities of the APD, making it the detector of choice in current and future PET systems, especially hybrid PET / MRI systems [41, 42]. The properties of all three detector types are summarised in Table 2.2. SiPMs have characteristics very much similar to the traditional PMT used in current PET systems; the gain, energy resolution and timing resolution are all comparable. The quantum efficiency though is somewhat misleading and for this reason most research papers and manufacturers quote *probability of detection efficiency* (PDE), which is itself partially based on the quantum efficiency.

$$PDE = QE \times FF \times P_g \tag{2.7}$$

Where FF is the fill factor; a ratio of the active area of the microcells to the total

area of the SiPM and accounts for the dead space present between micropixels. Is intrinsically linked to the geometrical design of the microcell array; typical values range from 20-80% [29, 43, 44]. P_g is the probability of an electron-hole pair causing an avalanche event and is dependent upon the location of the interaction (and hence primary electron-hole pair) and the electrical field shape [45] - typical values range between 0.5-1 [29, 46]. Generally, the combination of these factors leads to an overall PDE of much less than 100 %, especially for shorter wavelengths (since QE is strongly wavelength dependent). Usually this will be in the vicinity of 30-40%, though has been reported as high as 55% at 420 nm [23, 47, 48] - interestingly still higher than PMTs.

TOF PET is a very active area of research at present and SiPMs have proven to be aligned to this goal [7]. There are certain traits which are being explored further to improve the intrinsic timing resolution. Improving the PDE is one avenue; higher detection probability means that there is a higher chance that the very first scintillation photons will be detected. Reduction in the SiPM capacitance is another avenue; a large SiPM capacitance increases both the rise and decay times of the pulse. This is actually tied to the size of the microcell surface area, though simply decreasing the size of the microcells presents a compromise in PDE, as the proportion of dead space between pixels will be increased. Progress is being made on new fabrication techniques which are being used to reduce the gap between microcells, while minimising the amount of optical crosstalk (this is itself a problem, as a photon detection can effectively be doubled by neighbouring microcells) [23, 48, 49]. SiPMs are already very competitive, if not superior to both PMTs and APDs, despite their relatively short time in the field - further improvement of their performance as well as reductions in fabrication cost will mean it is only be a matter of time before other photodetectors are completely supplanted.

2.3.7 Detector Designs

Block Scintillation Detectors

Modern PET systems in the current clinical environment incorporate a block scintillation detector design. Traditional scintillation detectors have aimed to locate the position of the annihilation photon by restricting the scatter of scintillation photons

Properties	PMT	APD	SiPM
QE (%)	20-30	>80	>80
PDE(%)	30 @320 nm	74 @600 nm	55@ 420 nm
Single Photon Response	Yes	No	Yes
Gain	10^6-10^7	10^2-10^3	10^6-10^7
Temp. Dependence	Low	High	Medium
B Field interaction	Yes	No	No
Energy Resolution (%)	15-25	16.2	19-25
Timing Resolution (ns)	0.475	26-43	0.24

Table 2.2: A comparison of typical photodetector properties.

within a small volume. In this case, the spatial resolution is therefore proportional to the size of the detector. The block detector reduces the size of the crystal elements by cutting the block into a grid array and then filling the gap with highly reflective material to stop optical photons being transmitted to neighbouring elements.

Before the block detector was introduced each detector element would have it's own PMT, but costs could quickly blow out if this method were continued whilst trying to reduce detector size. The solution was to use a number of PMTs for each block (for example using a 2×2 array of PMTs for a block of 8×8 crystal elements), then using Anger logic to locate the position of the annihilation event. This system has been further improved by using *quadrant sharing*, which uses larger sized PMTs to overlap adjacent blocks allowing the number of PMTs to be further reduced. More recent systems have incorporated digital SiPMs rather than PMTs.

Problems with this design still remain though; there is still an element of inter-crystal light scatter, especially for high resolution systems where crystal size is very small (on the order of 1 cm length by 1 mm×1 mm face). There is also a compromise between having good depth of interaction (DOI) information (short crystals) or high sensitivity (long crystals). There are some designs that have attempted to address this, but generally there will be a cost involved as other performance parameters are reduced [50]. Figure 2.7 shows a number of alternative designs which use depth encoding to address the DOI issue, though in most of these designs (all except for (d) - the monolithic detector, and (a) in some cases [51, 52]) estimation of the position

of interaction is somewhat limited; being localised to only two possible depths. A high DOI uncertainty leads to what is known as *parallax error* or DOI blurring in the acquired images; the LOR may be drawn incorrectly from the inner face of the scintillator material, rather than the actual position. This problem becomes more pronounced the further the LOR is from the central axis of the detector, meaning that there will be non-uniform spatial resolution across the field of view.

The subfigures in Figure 2.7 provide depth encoding via a number of methods; (a) simply by stacking two (or more) crystal / photodetector units and reading each layer independently [53, 54, 55], (b) dual-end photodetectors which provide DOI information by analysing the difference in light intensity at each end (simultaneously) [56, 57, 35, 58], (c) Phoswich configurations which use layers of crystals with different decay characteristics and determine DOI via pulse shape discrimination [59, 60, 61], (d) monolithic crystals which use statistical modelling of light maps incident on the detector surface [62, 50, 63, 64, 65], or (e-f) dual-layer crystals with offset positions or mixed shapes, which have different light output profiles [66, 67]. More recently, other solutions to depth encoding have emerged which utilize a light guide at the entrance face of the scintillator crystal. These light guides mimic a dual-sided detector readout by redirecting light travelling away from the photodetector back towards it, along non-primary elements [68, 69, 70].

The sensitivity of the system is reduced because of the dead space introduced by the reflective material between detector elements. And although it is not related to performance, the cost of manufacture will increase for smaller sized crystals, due to the complexity and scale of machining needed.

Monolithic Scintillation Detectors

One particularly interesting solution to DOI blurring is monolithic scintillators. These use the light intensity and spread of scintillation photons on the photodetector pixels to estimate the position of the scintillation event and unlike the block detector, the spatial resolution is not dependent on the size of the crystal. They also have improved gamma photon capture efficiency, and have good spatial and energy resolution [72, 73, 62].

Many different methods have been proposed to determine the point of interac-

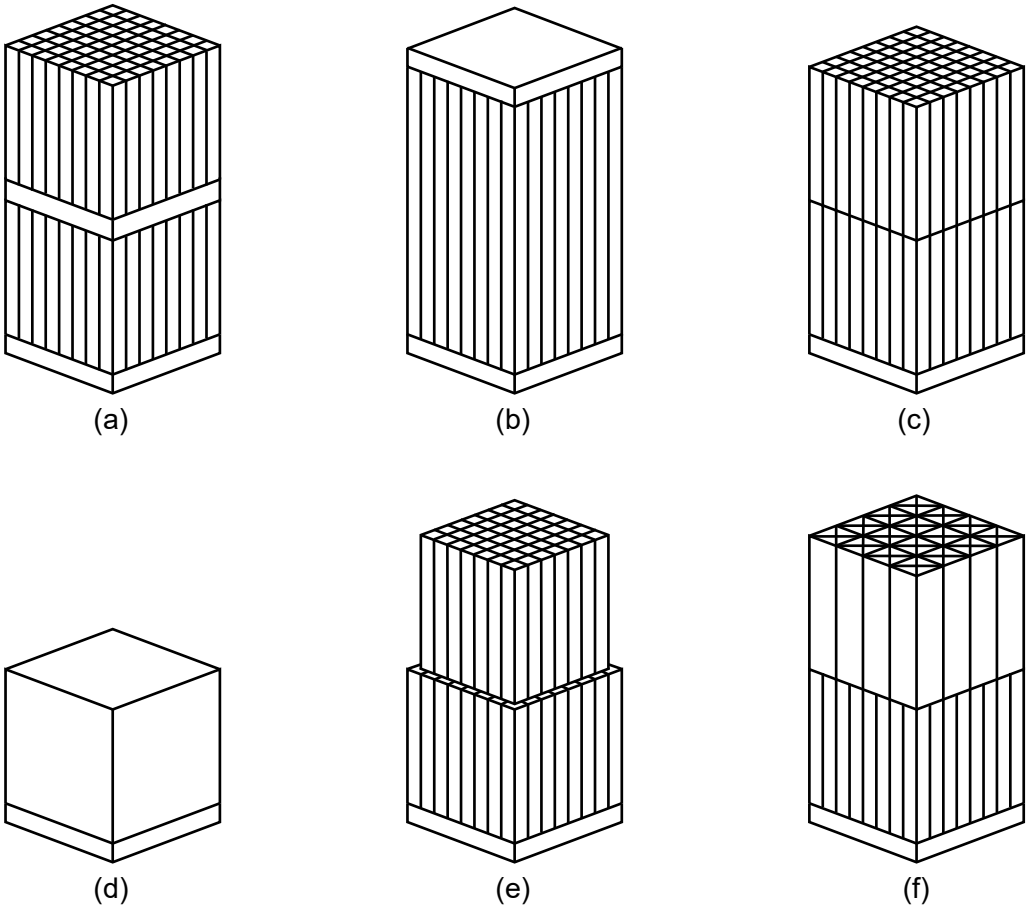

Figure 2.7: Detector designs seeking to improve upon the DOI capabilities of the block detector. (a) Dual-crystal photodetector(s) layers. (b) Single-crystal layer with photodetectors at each end. (c) Phoswich design with two types of scintillation materials. (d) Statistical positioning with a monolithic crystal block. (e) Dual-layer crystals with offset positions. (f) Dual-layer crystals of mixed shapes. [71].

tion between an incident gamma photon and a monolithic scintillators based on analysis of the distribution of optical photons detected on one or more surfaces of the monolithic slab.

Statistical algorithms such as maximum likelihood (ML) [74, 75], chi-squared (χ^2) [72] or k-nearest-neighbour kNN [72, 62, 76] have been used to fit the optical photon distribution, as measured by the optical photodetector, to a set of previously-measured reference profiles, and thereby estimate the 3D point of interaction within the crystal. These algorithms have been shown to work well; however, the calibration of the localisation systems (i.e. the production of the reference profiles) requires either laborious experimental measurements or extensive Monte Carlo simulations,

since a large number of events must be recorded over a range of known positions and angles of incidence. This work would also need to be repeated for monolithic slabs with different dimensions or material properties.

An alternative to the statistical methods is to fit an analytic function to the observed optical photon distribution, using an optimisation algorithm which aims to minimise the mean squared error between the observed distribution and the analytic model [63, 77]. Where an exact analytic model is difficult or impractical to derive due to complex optical properties of the material or the presence of high levels of Rayleigh scatter, neural networks may offer superior performance as they can intrinsically account for non-linearities in the relationship between the observed photon distribution and the point of interaction in the slab, particularly near slab boundaries. [78].

The optical photon distribution observed at the detector surface may be affected by internal reflections from the sides of the slab, and may be truncated near its edges and corners, which will impair the performance of analytic-model-based position determination algorithms unless incorporated into the model. Covering the non-detector faces of the scintillator slab with an absorptive coating, such that optical photons reaching the edges of the slab will be absorbed rather than reflected, allows the model to be simplified, at the cost of some sensitivity. Such coatings are known to degrade energy resolution to some extent; however, this can be mitigated if the scintillator has a high scintillation yield [72, 77].

The optical photon distribution which will be observed depends on the nature of the interaction of the gamma photon with the scintillator. For cases where the photon is photoelectrically absorbed, all of the optical photons will be emitted from a single point, with the number of optical photons proportional to the energy of the gamma photon. A similar outcome will result from Compton interactions where the scattered photon escapes from the scintillator slab; in this case, the number of photons emitted at the point of interaction will be proportional to the difference in energy between the incident and scattered photon. These two cases will be the easiest to localise due to the simplicity of the interaction; the scintillation event may be treated as an isotropic point source [77, 78]. In a scattering medium, it is necessary to also introduce an attenuative factor due to the imperfect transparency

of the material [79]. This is described by (2.8)

$$J = \frac{\varepsilon}{4\pi R^2} e^{-kR} \tag{2.8}$$

where J is the flux density of optical photons at distance R from a source emitting ε photons following a scintillation event. The scatter-induced losses are modelled by k.

In the event of multiple points of energy deposition within the scintillator (for example, a Compton interaction followed by photoelectric absorption of the scattered photon), the optical photon distribution becomes much more diffuse, and accurately fitting an analytic model to the observed optical photon distribution becomes a much more difficult problem. If individual pulses can be discriminated, it may be possible to estimate each location where energy was deposited in the scintillator. For PET, only the first of these is important, since this will define the endpoint of the line of response. This is most likely to be the shallowest observed scintillation event.

2.3.8 Alternative Detector Configurations

Typical PET scanners used in the clinical environment feature 4-5 full rings of block scintillation detectors, surrounding the patient. The axial field of field of view is typically 15-25 cm [2]. Several groups have attempted to expand the axial or solid angle coverage of PET scanners to improve the sensitivity of the system and hence the image signal to noise ratio. Cherry et. al. are developing perhaps the most high profile system regarding this: the "EXPLORER" project is a long axial "total body" system, capable of imaging the entire body at once [4].

Other attempts to improve the solid angle coverage include the development of full body truncated spherical systems [80], or partial spherical or polyhedral systems for targeted brain scans[81, 82]. Though most of these designs have proven difficult to construct and have remained theoretical studies.

Systems consisting entirely of monolithic scintillation detectors [65] reduce the amount of dead space, while simultaneously improving DOI estimation. A small animal system featuring a continuous cylindrical slab of LYSO scintillator has been constructed [83], which has been shown to achieve good spatial resolution and sensitivity. Though the method of construction has been achieved by boring a hole in

the centre of a single crystal ingot, so scalability may prove challenging.

Increasing the geometric coverage of the scanner will positively influence the signal-to-noise ratio, spatial resolution and reduce scan time (or alternatively the radiation burden on the patient). Generally though, an increase in component cost scales with the increase in coverage [23].

2.3.9 Time-of-Flight PET

In recent years there have been significant advances in the timing resolution of PET detectors, thanks to the discovery of fast scintillation materials (such as LSO, LYSO and $LaBr_3$) and the advancement of photodetectors (especially SiPMs) [84, 7]. In modern PET systems, timing resolution has reached below the nanosecond range, with detectors now able to distinguish between singles events which are hundreds of picoseconds apart. The measured time difference (Δt) between the two singles correlates to the position (Δx) of the annihilation event with respect to the central axis of the ring structure (see Figure 2.8), according to the equation [85]

$$\Delta x = \frac{c\Delta t}{2} \tag{2.9}$$

Theoretically, if coincidence timing were exactly precise, it would be possible to pinpoint the exact location of the annihilation event and there would be absolutely no need for image reconstruction. In reality, a fast timing resolution is able to reduce the size of the LOR to a probable range. The time difference (Δt) is blurred by variance $\sigma^2_{\Delta t}$, which corresponds to a blurring of the estimated position by $\sigma^2_{\Delta t}$ (this variance is show in Figure 2.8).

More certainty in the position of the annihilation event, along the LOR translates to less influence from random and scatter events and an overall improvement of the signal-to-noise ratio [23, 86]. Also beneficial, is an increased accuracy of the attenuation map and the possibility of generating an attenuation map based on emission data [87, 88, 89, 90, 91].

Time-of-flight detectors, which also use depth encoding to provide DOI information, can actually improve the timing resolution further by adding a timing correction to the signal, accounting for the propagation time of scintillation photons through the medium [7, 92]. Monolithic scintillation detectors have an additional

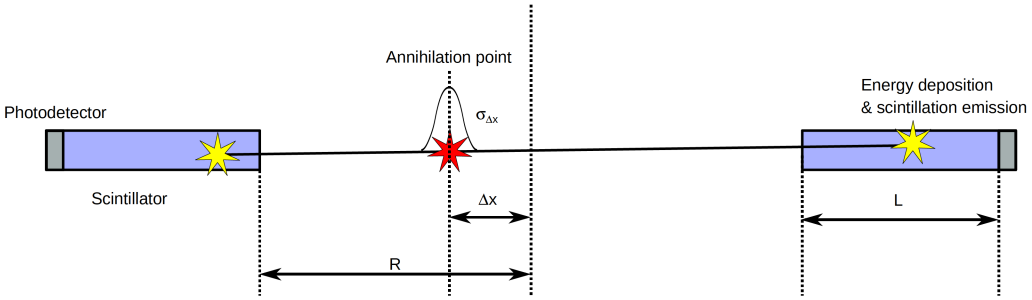

Figure 2.8: Time-of-flight PET concept. The difference in arrival time (Δt) of each single can be correlated to the position of the annihilation event (Δx) via (2.9). The shaded region indicates a blurring of the position estimation by variance $\sigma^2_{\Delta x}$, since the timing is not exact [85].

advantage with regard to timing information; they use multi-pixel sampling of the scintillation pulse. Seifert [93] has shown that rather than using a single time stamp from the first scintillation photon striking a single pixel, more accurate timing information is possible by using multiple time stamps from the initial part of the pulse. Some monolithic scintillation detectors have been demonstrated to have sub-200 ps crystal response time [8].

2.4 Scintillation Materials

2.4.1 Scintillator Properties

Following on from the detector properties covered in the previous section, scintillators often have specific properties which relate to their overall performance. The basis of most of these is in their efficiency and speed of conversion from initial interaction to readable output signal. A comparison between scintillator crystals may be seen in Table 2.3.

Scintillation Yield

This is the *estimated* amount of optical photons produced per keV of energy absorbed (sometimes specified in MeV). In a PET system, gamma photons are approximately 511 keV, so the estimation would be multiplied by this amount. A High photon yield improves spatial resolution, meaning it will be easier for the

Scintillator	Density (gcc)	Yield (/keV)	Decay (ns)	Peak λ (nm)	R (%)	Z_{eff}	Hygro	Refs.
NaI:Tl	3.67	45	230	415	7.1	50	Yes	[94, 10]
BGO	7.13	8	300	490	11	73	No	[95, 10]
LSO:Ce	7.4	27	40	420	7.9	66	No	[96]
LYSO:Ce	7.1	34	41	397	8.1	65	No	[97]
GSO:Ce	6.7	12.5	56	430	7	59	No	[96]
LuAp:Ce	8.34	11.4	16.5	365	9.3	65	No	[95]
$LaBr_3$:Ce	5.1	63	16	380	2.6	46	Yes	[98]
LaF_3:Ce	5.9	4.5	30	330	16	-	Yes	[94]
YAG:Ce	4.57	24	88	550	11.1	32	No	[99]
Plastic*	1.03	10	2	Various	-	12	No	[10]

Table 2.3: Some common scintillation materials used in PET detectors. * Indicates typical values — there are many different types of plastic scintillators. Energy resolution (R) is measured at a reference energy of 662 keV. Some scintillators are identified by their acronyms: $Bi_3Ge_4O_{12}$ (BGO), Gd_2SiO_5:Ce (GSO:Ce), Lu_2SiO_5:Ce (LSO:Ce), $LuAlO_5$:Ce (LuAP:Ce), $Lu_{1.8}Y_{0.2}SiO_5$:Ce (LYSO:Ce)

.

exact location of the hit to be determined. This is especially useful in PET systems where the scintillation photons are spread between multiple photo-detectors, or in monolithic scintillation detectors where a high photon yield translates to high statistical accuracy [77].

Decay Time

Refers to the amount of time required for light photons to be produced by the scintillator. A fast decay time is necessary for timing precision (and is a requirement for TOF PET) and also ensures that events do not "pile up" on top of one another, causing dead time in the detector. A good scintillator is able to process events at high count rates, while reducing the amount of random coincidences. As a general rule of thumb, for a scintillator decay time τ, the maximum event rate that the scintillator can handle is $\frac{1}{2\tau}$ [10].

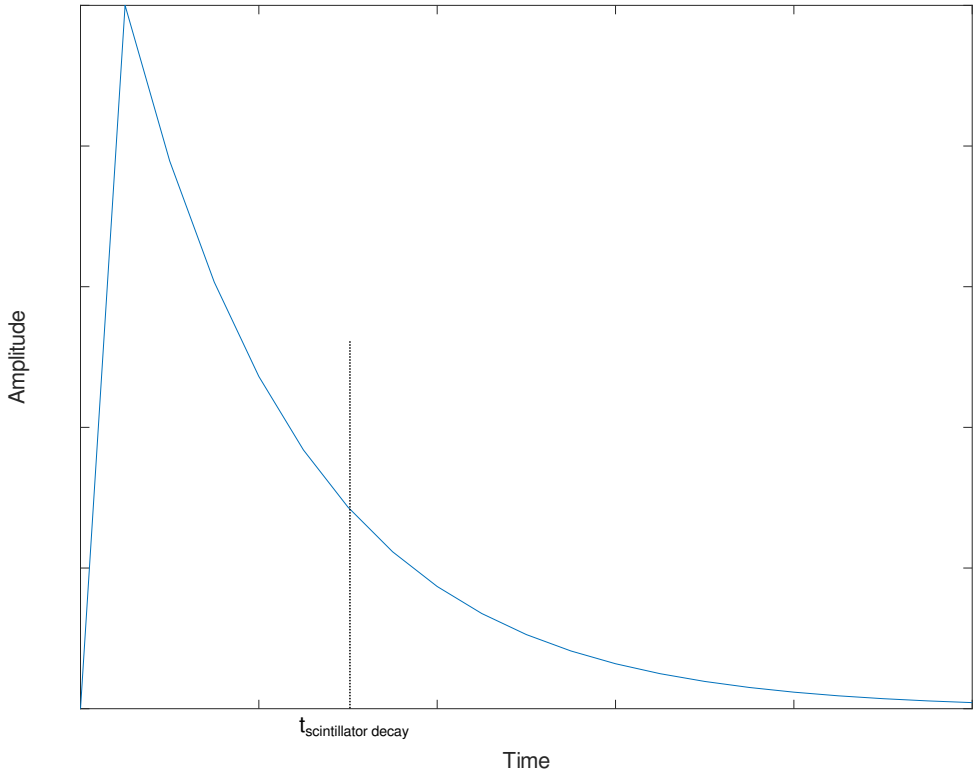

Figure 2.9: Typical scintillator pulse shape. [85].

It is also important to note that for systems dependant upon very precise timing resolution (i.e. TOF PET), the rise time of the scintillator is also a very important consideration. Time stamping of a coincidence event will generally happen when optical photon detection reaches above a certain threshold, which is achieved during the rising portion of the pulse (see Figure 2.9). Fast crystals, such as LSO, LYSO and $LaBr_3$, tend to have both fast rise and decay times.

Emission Wavelength

The frequency spectrum of the scintillation photons should be matched to the spectral efficiency of the photodetector. For example, a typical photomultiplier tube with a bi-alkali photocathode has an optimal spectral peak between 350 nm – 475 nm. If the peak is too far below 350 nm (i.e. UV range), then there is a chance that the scintillation photons will be absorbed into the glass in the entrance of the photodetector.

Index of Refraction

This parameter is important for coupling light from the scintillator to the photodetector. Ideally, the refractive index of the scintillator needs to match the refractive index of the glass on the photodetector to reduce internal reflections. This is also relative to the emission wavelength of the scintillation photons.

Optical Attenuation Length

This is somewhat different to the stopping power mentioned previously in the section on detector properties. For high energy gamma photons, a material possessing a low attenuation length (high stopping power) is desirable, so there is maximum probability of the photon interacting with the material (this depends on ρ and Z_{eff}). In the optical range however, the reverse is true. Scintillators with a long optical attenuation length are preferred for better energy resolution, or in the case of monolithic detectors; to more accurately execute positioning algorithms.

The attenuation length (λ) is defined as the length of penetration (y) where the irradiance ($I(y)$) has dropped to $1/e$ of the incident irradiance (I_0). Often material datasheets will specify an attenuation or absorption coefficient (α), rather than an attenuation length - though this is just the inverse (i.e. $\lambda = 1/\alpha$). (2.10) shows the relation in terms of the attenuation coefficient [100]

$$I(y) = I_0 e^{-\alpha y} \tag{2.10}$$

It should easily be seen that for $y = 1/\alpha$, the irradiance has dropped to e^{-1} of I_0. In addition to these properties it is most desirable for scintillators to be rugged, cheap to manufacture and non-hygroscopic (meaning it will not absorb water molecules).

There are many different types of scintillation materials which have been used in PET systems, though in almost all cases these will be inorganic crystals, owing mostly to superior stopping power and scintillation yield (despite expensive and time consuming fabrication processes). Plastic scintillators, such as polystyrene, polyvinyltoluene (PVT) or polymethylmethacrylate (PMMA) with an added fluor can produce acceptable yield and exceptional timing resolution for PET applications, they are also easily shaped and cheap to produce. However, the stopping power is

much too low comparatively and they are particularly susceptible to damage from high energy gamma photons [101].

2.4.2 Nanocomposite Scintillators

Nanocomposite scintillators are a relatively new class of materials for radiation detection applications. They consist of a mixture of nanometre-scale (most commonly inorganic) scintillating particles, uniformly mixed with a transparent polymer or other organic matrix. The matrix can either be non-scintillating, such as oleic acid (OA), or a polymer scintillator, such as polystyrene (PS) or polyvinyltoluene (PVT). Because the gaps between scintillator nanoparticles are filled with a material with a refractive index closer to that of the scintillator than air (or vacuum), scattering is limited and light transmission is improved compared to the use of a compressed bulk powder [102]. Nevertheless, no matrix material has a refractive index which perfectly matches that of the nanocrystal; therefore, scattering remains a significant performance-limiting factor, particularly in comparison to monocrystalline scintillator materials. For hygroscopic materials, the matrix offers the additional advantage of providing a degree of protection for the nanoparticles against moisture ingress. Some examples of nanocomposites which may be feasible for PET have been summarised in Table 2.4.

Accurately modelling the optical and physical properties of a nanocomposite is considerably more complex than for a homogeneous material. Scattering may be approximated as Mie scattering, but since the particle size is normally much smaller than the nanocrystal scintillator's emission wavelength, it may be assumed that each particle will see an approximately uniform electric field. Therefore, scattering can be approximated as purely Rayleigh to a high degree of accuracy [94].

Most useful nanoscintillator particles will be of a size such that scattering is essentially purely Rayleigh (i.e., satisfying the criteria $m \cdot x < 1$, where $m = n_p/n_m$ is the ratio of the refractive index of the scintillator particles to that of the matrix, and $x = 2\pi r/\lambda$ and $\lambda = \lambda_0/n_m$ where λ_0 is the peak emission wavelength of the scintillator [105]). If this condition is satisfied, then the transmission of scintillation

Nanoparticle	$LaBr_3$:Ce	Gd_2O_3	LaF_3:Ce	LaF_3:Ce	YAG:Ce
Matrix	PS	PVT	OA	PS	PS
Load (% Vol.)	19	4.6	34	50	50
Peak λ (nm)	380	550	334	334	550
Yield (ph/keV)	63	22	4.5	4.5	20.3
R (% @662 keV)	2.6	11.4	16	16	11.1
Decay (ns)	16	17	30	30	87.9
ρ (g/cm^3)	1.81*	1.34*	2.59*	3.47*	2.81*
n (@peak λ)	1.69*	1.56*	1.52*	1.65*	1.72*
α (cm^{-1})	2.00*	0.09*	2.05*	0.15*	0.95*
Refs.	[98, 103]	[21, 103]	[104, 94, 103]	[104, 94, 103]	[99, 103]

Table 2.4: Physical and optical properties of a range of proposed nanocomposite materials. Most properties listed are found from the literature; several parameters, marked with an $*$, have been estimated from the volume fractions listed, assuming a 1 cm thick slab with 9 nm diameter nanoparticles. R is the loading factor. PS is polystyrene; PVT is polyvinyl toluene; OA is oleic acid.

photons may then be calculated via (2.11) [94, 21, 106, 107]:

$$T = \frac{I}{I_0} = exp\left\{-4\pi^4 \frac{d^3 \bar{L} f_p n_m^4}{\lambda^4} \left(\frac{m^2-1}{m^2+2}\right)^2\right\} \tag{2.11}$$

Where I/I_0 is the ratio of the output light intensity (I) to the emission light intensity (I_0), d is the diameter of the nanoparticle, f_p is the volume fraction of particles, $\bar{L}$ is the average path length and λ is the wavelength of the scintillation photons. This expression assumes that the diameter of nanoparticles is uniform, there is no agglomeration of particles in the matrix, also that the photons emitted during scintillation are of exactly the same wavelength.

In practice, none of these assumptions is strictly accurate. Particle agglomeration is of particular concern where the nanocomposite loading factor is high, potentially creating additional scattering losses [108]. If there is some overlap between the absorption spectrum of the matrix and the luminescence spectrum of the nanoscintillator, self-absorption of scintillation photons may occur; some polymer matrix materials are known to exhibit this behaviour, especially in the UV region

[21, 109]. Despite these limitations, (2.11) provides a good approximation of optical transmission of scintillation photons for the majority of nanocomposite materials.

The refractive index of the nanocomposite (n_c) is a function of the nanoparticle loading factor - in fact, much research has been conducted into the problem of using inorganic nanoparticles to effectively tune the refractive index of an organic material. Generally, an *effective medium* model based on Maxwell-Garnett theory (or variants of it) can be used to estimate the composite refractive index using an additive linear approximation, as shown in (2.12) [110, 111, 112]

$$n_c = n_m f_m + n_p f_p \tag{2.12}$$

Where n_m and n_p are the refractive indices of the matrix and nanoparticles respectively and f_m and f_p represent the fractions of each material, by volume. It is important to note that while a large number of inorganic-organic nanocomposite scintillator materials are known to follow this linear relationship between volume fraction and overall refractive index, others do not. There are a number of different factors which affect the refractive index; unfortunately, there is no general theoretical model which can be applied to all combinations of materials. Instead, it is often necessary to employ empirical methods. For instance, a TiO_2-polystyrene nanocomposite synthesised by Rao et. al [113] is best described by a quadratic equation. The authors hypothesise that strong chemical bonding between the two materials changed the polarisability of the polymer, resulting in the observed behaviour. Other factors which can impact upon the refractive index include the diameter of the nanoparticles; for PbS-gelatine, there was a significant drop in refractive index compared to the bulk material when the mean diameter of the nanoparticle component was less than 25 nm [112]. Also, if a surfactant coating with a lower refractive index than the nanoparticle is applied to improve the uniformity of the nanocomposite, it may significantly contribute to the overall volume [114] and hence alter the refractive index.

Using (2.11) and (2.12), it is possible to get a sense of the desirable properties for suitable bulk scintillator and matrix materials. Ideally, closely matching scintillator and matrix refractive indices, small nanoparticle size (< 10 nm), long emission wavelength and non-overlapping emission and absorption spectra will help to max-

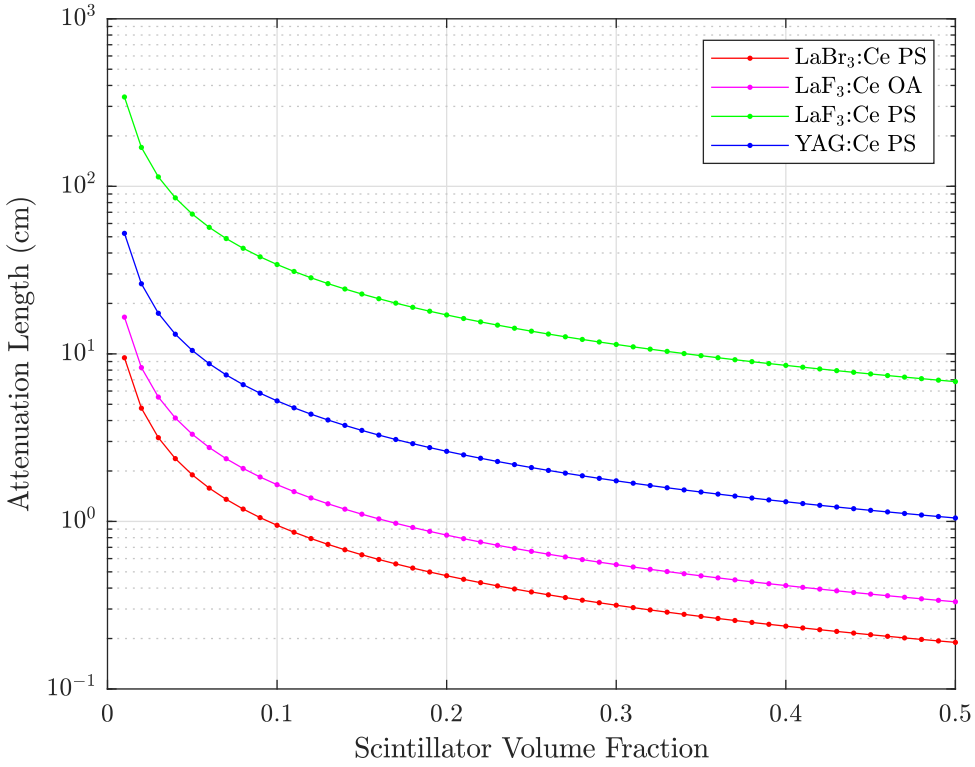

(a) Calculated optical attenuation length from Rayleigh scattering, using (2.11).

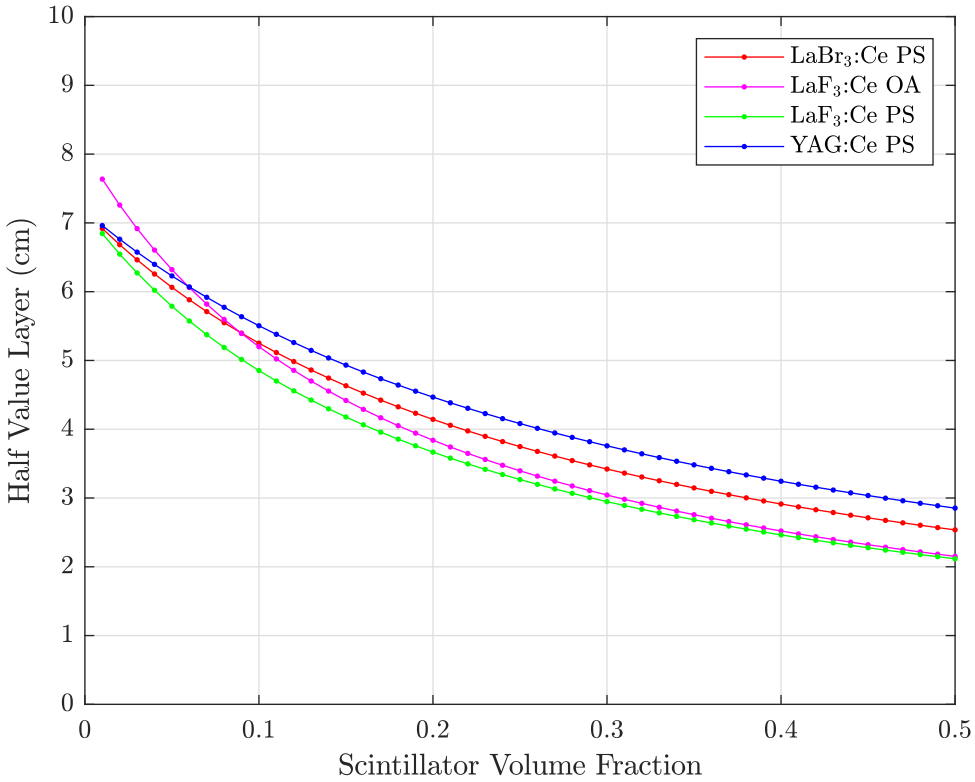

(b) Calculated gamma HVL thickness as a function of scintillator loading factor.

Figure 2.10: (a) All nanoparticles are assumed to be spherical and uniformly distributed, with a constant diameter of 9 nm (for comparison). (b) Calculated using data from the National Institute of Standards and Technology [103].

imise transmission of the scintillation light. For the bulk scintillator material, high light yield per MeV of incident photon energy, good energy resolution, and a short time constant are also desirable for most applications.

In addition to these desirable properties, the nanocomposite needs to exhibit a high linear attenuation coefficient so as to maximise its sensitivity to high-energy gamma radiation. This requires the nanocomposite to have as high a density and effective atomic number as possible. Since these properties are generally quite low for the matrix material, it is necessary to use a high-ρ, high-Z_{eff} bulk scintillator material at a high loading factor. Unfortunately, a high loading factor also has the effect of reducing the optical transmittivity of the nanocomposite. This can be more easily seen in Figure 2.10(a), which uses (2.11) to calculate the optical attenuation length of for a number of potential nanocomposite materials, and Figure 2.10(b), which compares the half-value layer (HVL, sometimes referred to as half value thickness, defined as the thickness required to reduce the intensity of incident gamma radiation by 50%) for each material as a function of loading factor (volume fraction of scintillator).

2.4.3 Transparent Ceramic Scintillators

Doped synthetic garnet materials, such as yttrium aluminium garnet (YAG) and lutetium aluminium garnet (LuAG) have been been used for decades in monocrystalline forms in photonics applications such as optically pumped lasers. Monocrystalline synthetic garnet scintillators have also been proposed for use in a variety of medical imaging applications such as PET due to their high density, high scintillation yield and good optical transparency. Recent progress in fabrication techniques has enabled the synthesis of certain garnets as optically transparent polycrystalline ceramics. Such ceramics retain many of the properties of the equivalent monocrystalline material (in particular, the high density and linear attenuation coefficient), and may offer a higher scintillation yield in some cases [115]). The principal benefit of multicrystalline transparent ceramics is easier and more cost-effective fabrication, and the flexibility of being able to form the precursor powder into arbitrary shapes and structures prior to sintering - a near-impossibility with single-crystal materials.

The optical and scintillation properties of transparent ceramics are heavily in-

Ceramic	GYGAG:Ce	GLuGAG:Ce	GAGG:Ce	LuAG:Pr
Peak λ (nm)	550	550	530	310
Yield (ph/keV)	50	48.2	70	21.8
R (%)	4.9	7.1	4.9	4.6
1st Decay (ns)	100	84	90	21.4
2nd Decay (ns)	500	148	194	771
ρ (g/cm^3)	5.8	6.9	6.63	6.73
n (@peak λ)	1.82	1.92	1.90*	2.03*
α (cm^{-1})	0.10	2.00	3.13*	2.86*
refs.	[119, 120, 121]	[118, 84]	[115, 122]	[117, 122]

Table 2.5: Properties of several transparent ceramic scintillator materials proposed for radiation detection applications. Properties listed with * have been calculated, while those with * were obtained from literature pertaining to the equivalent monocrystalline form of the material.

fluenced by the specific manufacturing process used. Usually, the ceramic is formed by the sintering method, where a precursor material is calcinated and milled into nanoparticles (∼100-200 nm) before being pressed into a green body (unfired ceramic) and sintered at around 1500-1700°C [116, 117]. The resulting solid may then undergo hot isostatic pressing (HIP) to reduce porosity, followed by annealing and polishing to create a highly transparent solid [118, 119]. The atmosphere in which the sintering and annealing steps are performed has a significant effect on the transparency of the resulting ceramic, and its propensity to exhibit afterglow effects [120]. The properties of several examples of ceramic garnet scintillators are listed in Table 2.5.

Compared to the Czochralski, Kyropoulos or Bridgman-Stockbarger methods used to grow large single-crystal scintillators, the process of creating transparent ceramic scintillators is much more amenable to the production of complex geometries and scaling up to large volumes. Growth of high-quality defect-free monocrystalline scintillators with consistent characteristics requires extremely high, uniform and well-regulated temperatures and atmospheric conditions. Additionally, the maximum dimensions of monocrystalline scintillators are limited by both the maximum

dimensions of the ampoules (in the Bridgman-Stockbarger method) and by the difficulty in maintaining a stable, uniform thermal gradient across a wide crystallisation zone [26, 27]. The ability of the ceramics to be pressed into different moulded shapes eliminates most of these problems, and the lower temperatures involved mean that material losses are able to be more easily controlled since there is no risk of evaporation of the melt.

One of the most significant challenges of producing ceramic garnet scintillators is achieving high optical transparency in the finished product. Cherepy et al. proposed a method to reduce the residual porosity of the ceramic with hot isostatic pressing, greatly improving optical transparency [121]. Optical properties are also improved through the selection of high purity precursor materials with cubic / isotropic crystal structures (i.e. no birefringence), which reduces optical scatter caused by grain boundaries and secondary phases [121].

2.5 Image Reconstruction

A major underlying problem with PET is that the radiotracer distribution inside the patient cannot be directly imaged. Instead, the image must be reconstructed by first taking the measured LOR data and then applying an algorithm to convert 1D projection data (or list-mode data) into a 2D or 3D image. There are two broad groups of algorithms used for image reconstruction: analytic image reconstruction, which is based on a mathematical analysis of the Radon transform, or iterative reconstruction which is based on least squares or expectation maximization algorithms converging to an image.

2.5.1 Data Storage

Sinograms

In image processing, it is generally accepted to describe lines in the image space in terms of normal parameterisation [123], so the LORs used for the projection data $p(s, \phi)$ will often be defined as shown in Figure 2.11. The parallel LORs at a singular projection angle ϕ (the angle subtended by the normal to the LOR with respect to the x-axis), are shown as the dashed lines a distance s from the origin; described in

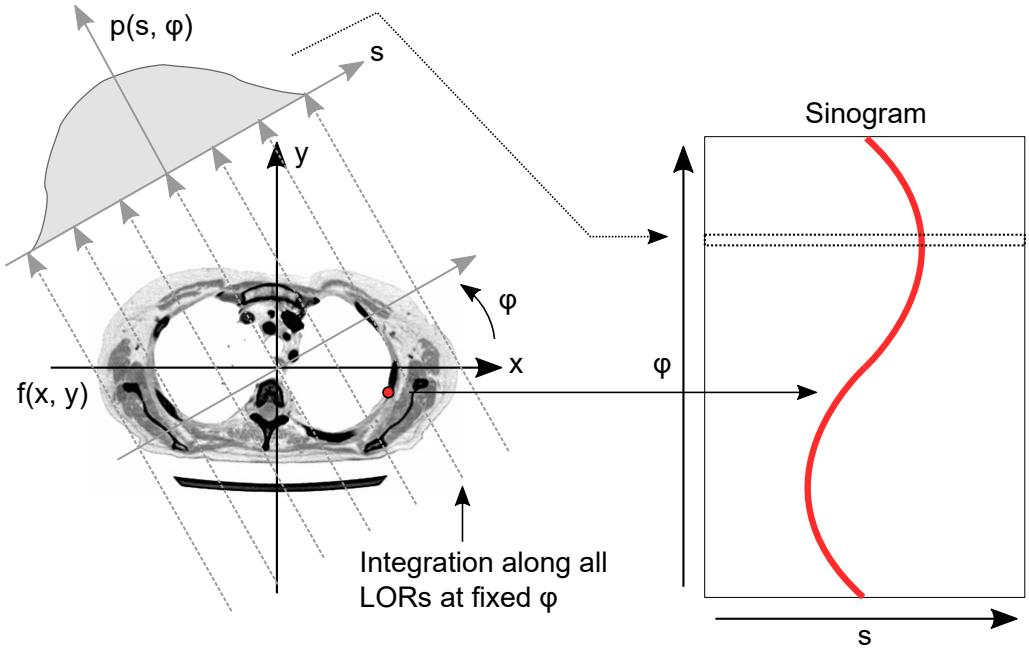

Figure 2.11: Construction of a sinogram from projection data [125]. The dashed lines are measured lines of response from a particular projection angle. The Radon transform is then used to obtain a 1D intensity distribution, which is then stored in the sinogram as a function of distance and projection angle.

this coordinate system by the equation

$$x\cos\phi + y\sin\phi = s \tag{2.13}$$

The projection $p(s,\phi)$ is obtained by taking a line integral along each LOR, to give an intensity profile at that particular angle. This operation is known as the (2-D) Radon transform [124], or the x-ray transform and is written as

$$p(s,\phi_k) = \int_{-\infty}^{\infty}\int_{-\infty}^{\infty} f(x,y)\,\delta(x\cos\phi + y\sin\phi - s)\,dx\,dy \tag{2.14}$$

Where $f(x,y)$ is the object being imaged; in this case the radiotracer distribution inside the patient. Essentially, integration across the object only occurs when the argument of the delta function $(x\cos\phi + y\sin\phi)$ is equal to zero (i.e. for a particular s value corresponding to a measured LOR). In Figure 2.11 represents a continuous function, though in real world applications, the projections will be discretised as they are dependent upon discrete LORs. It is therefore more appropriate in this case to describe the projections as double sum equations, rather than integrals.

Each of these projections are then stored in a sinogram, as shown in Figure 2.11. Each row of the sinogram corresponds to a particular projection, with each point along the s plane represented by a particular intensity value. This is then repeated for each projection angle until the entire 180° range of measurements are covered (the LORs extend in both directions, so measurements $> 180°$ will be redundant). Each point of the object's radiotracer intensity distribution is represented as a sinusoid.

List Mode Data

An alternative to sinogram storage is list mode data collection. Rather than plot each projection on a graph, each capture is simply listed as an entry into a data file. The advantage of this methodology is that parameters other than position may be recorded at the same time. It is especially useful to record energy and timing information of coincidences, for simplicity in filtering scattered photons and random coincidences, through the application of energy and timing windows. In fact, this methodology has produced improvements in spatial and temporal accuracy [87, 126, 127]. Additionally, timing information may be used for TOF PET. This method does require a large amount of storage space however, especially for data capture in high resolution, high sensitivity systems, where each event requires a separate data entry. As hard drive storage naturally is becoming cheaper and faster, this should be less of a problem moving forward.

2.5.2 Filtered Backprojection

Analytic image reconstruction attempts to find the solution to the *inverse Radon transform*, for each projection. The result of simple backprojection will look like a "smearing" of the projection across the 2-D image space, with each of the projection intensity values being spread uniformly over the image pixels which lie along the LOR at that particular angle. As each of the backprojections are overlaid onto the pixels, they will overlap, causing a blurring of the image from oversampling. This effect is commonly known as $1/r$ blurring, where r represents the distance from the object of interest.

The blurring may be understood by looking first at how the projection data relates back to the final image. The central section theorem tells us that the 1D

Fourier Transform (FT) of a projection at angle, ϕ, will equal the cross section of the 2D FT of the image at the same orientation [9]. Therefore, the 2D FT of the image will have a superposition of all 1D FT projection data and will be oversampled about the centre (looking like spokes on a wheel). A Fourier analysis reveals that a filter function is required for correction. The image $f(x, y)$ of the radiotracer distribution of the original object may be described as

$$f(x,y) = \int_0^{\pi} \int_{-\infty}^{\infty} |\nu_s| P(\nu_s, \phi) e^{j2\pi s\nu_s} \, d\nu_s \, d\phi \tag{2.15}$$

The inner integral in (2.15) is therefore simply the inverse Fourier transform of $P(\nu_s, \phi)$ multiplied by a filter function with frequency response $|\nu_s|$. This is called *filtered backprojection*. Reconstructing the entire image from these filtered back projections requires integration of all filtered backprojections over the range $0 < \phi < \pi$.

In practice, the process for filtered backprojection is as follows [128]:

- Take the 1D Fourier transform of each projection $p(s, \phi)$ to give $P(\nu_s, \phi)$.
- Multiply $P(\nu_s, \phi)$ by the filter function $|\nu_s|$.
- Take the 1D inverse Fourier transform.
- Integrate over the range $0 < \nu_s < \pi$ to get a reconstruction of $f(x, y)$ (simple backprojection).

The filter function $|\nu_s|$ we are talking about here is a ramp function, which is actually not absolutely integrable; as the integral would tend towards infinity. Also, because $|\nu_s| = 0$ at $\nu_s = 0$, some information may be lost at this point of the algorithm. Often this value will be scaled or a simple guess to account for this. A number of functions have been developed to address these issues, perhaps the most basic of which is the"Ram-Lak" filter [129], which is essentially a ramp function that has been band limited to the maximum frequency measurable in a projection (see Figure 2.12). That is, we use a *windowed* filter function.

The maximum frequency of the filter is known as the Nyquist frequency and may be easily determined if the pixel size is known for a particular detector. Because the

acquisition data are discrete, the maximum number of peaks possible in a projection would be in a situation in which peaks and valleys occur in every alternate pixel [130]. The Nyquist frequency can then be determined by the simple formula

$$\text{Nyquist Frequency} = \frac{0.5 \text{ cycles}}{\text{pixel size (cm)}} \tag{2.16}$$

If sampling is coarser than the Nyquist rate, then too many of the higher spatial frequencies may be cut out leading to image artefacts, known as *aliasing*.

2.5.3 Backproject Then Filter

Another technique which attempts to remove $1/r$ blurring is the Backproject Then Filter algorithm (BPF). This is similar to FBP, but the filter is applied at a different stage in the process; whereas in FBP the filter is applied before backprojection, in BPF it is applied after.

This can overcome some of the added complexity of FBP in terms of necessary rebinning and interpolation, but generally the images are poorer in quality and the process is more computationally intensive. This is primarily caused by the backprojection process generating an image that is beyond the original matrix size; the 2D blurred image must be truncated to the size of the original, losing data in the process [131]. Using 2D Fourier transforms with a cone filter may also produce periodic convolution, causing wrap around effects [132]. For these reasons FBP has proven to be much more popular for implementing image reconstruction.

The algorithm for BF is as follows:

- Reconstruct the image using simple backprojection.
- Take the 2D Fourier transform of the backprojected image.
- Multiply by the filter function $|\nu_s|$
- Take the 2D inverse Fourier transform.

2.5.4 Types of Filters

Filtered Back-Projection and Backproject then Filter are both highly susceptible to high frequency noise and unfortunately the Ram-Lak filter will only accentuate this.

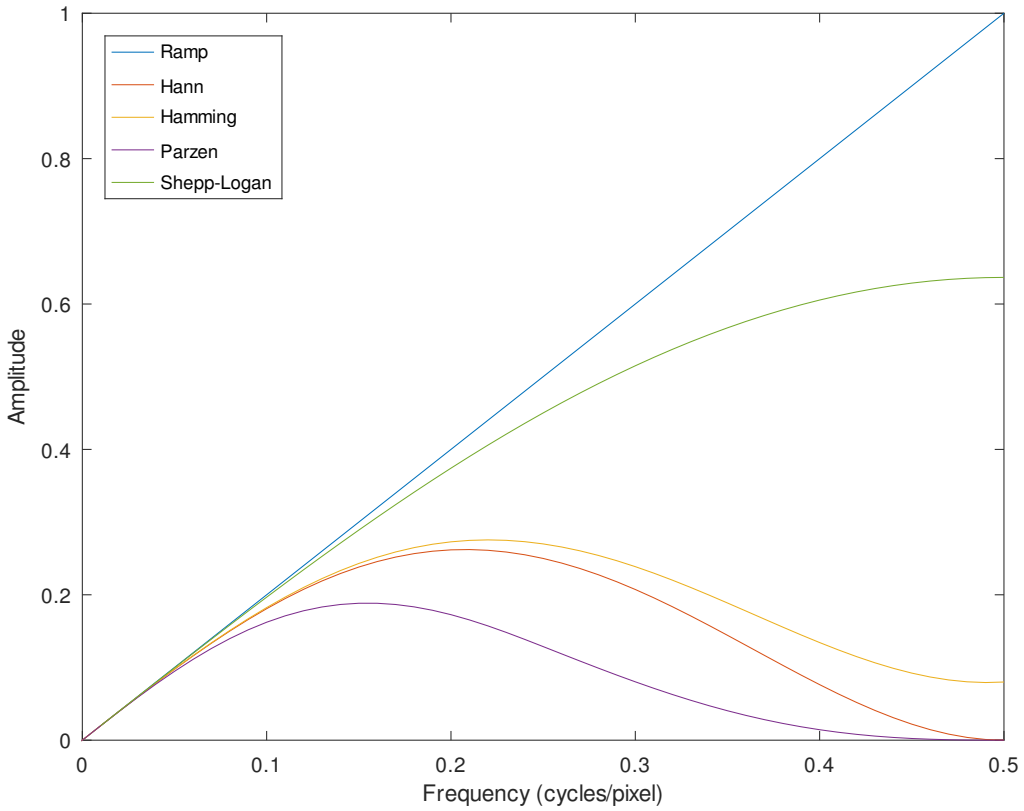

Figure 2.12: Some common examples of band-limited filter functions used in Filtered Back-Projection image reconstruction. [130]

The sharp boundaries at the edges of the filter also causes the spatial domain filter kernel to become oscillatory and introduces ringing artefacts into the reconstructed image [131]. Attempting to reduce the influence of these issues on the image has led to a number of different filter functions being used, many of which are based on the Ram-Lak and multiplied with another function. For example, the "Shepp-Logan" filter is the Ram-Lak filter multiplied by a sinc function.

Figure 2.12 shows a number of different low-pass filters, which aim to reduce the high frequency noise and ringing artefacts associated with the ramp function. There is somewhat of a trade-off between filtering the noise (smoothing the reconstructed function) and spatial resolution; obviously, the more data that is suppressed, the more detail is lost from the reconstructed function. So, the Parzan filter will be very good at smoothing the function (i.e. improving the SNR) at the cost of spatial resolution, while the Shepp-Logan will have a much softer impact on these factors.

We are able to vary the properties of each of these filters somewhat further by varying the cutoff frequency (ν_c); the lower the value of ν_c, the more noise can be

removed (again, at the expense of spatial resolution). This is important in certain cases where ν_c needs to be adjusted for particularly noisy data, such as the imaging of obese patients, or low count density studies [130].

There is no one particular function that excels for all applications and this is the reason why there are still so many filters used for nuclear medicine. Investigations into a methodology for determining filter choice and cutoff frequency, based on desired image properties have been conducted [133], but have unfortunately not proven to be suitable. The choice of filter function and the associated cut-off frequency are still chosen empirically based on a small number of sample images.

2.5.5 3D Image Reconstruction

Until this point, consideration has only been made for image reconstruction in a single detector ring. In practice, PET scanners will often use several rings of scintillation detectors. Image reconstruction in this case may be performed in 2D mode; using attenuating plates called septa to separate detector rings, ensuring that only direct LORs are captured. Images may then be "stitched" together afterwards along the axial dimension. This mode is acceptable for image reconstruction, though a significant portion of data is lost to the septa.

Removing the septa and exposing detectors to oblique angle detections, may complicate the process somewhat, though if handled correctly, can potentially improve the sensitivity of the scanner and improve the SNR. Two processes and their variations will be discussed.

Rebinning Algorithms

Rebinning algorithms are used to take the oblique angle data (from different axial rings) and sort them into sinograms for each transaxial slice, allowing 2D reconstruction algorithms to be used for each detector ring. The simplest method is Single Slice Rebinning (SSRB) [134], which assigns the oblique angle LOR to the sinogram at it's midpoint. This does result in position dependent image blurring for objects which are displaced from the central region of the scanner and for larger apertures [135], so further variations have been developed.

Multi-Slice Rebinning (MSRB) [136] is similar to SSRB, though rather than

rebinning to the sinogram of a single axial slice, MSRB will use a stack of consecutive sinograms, then axially filter to reduce blurring. MSRB improves accuracy of the reconstruction, though has some susceptibility to noisy data and is computationally more costly. Lastly, perhaps the most useful algorithm, is Fourier Rebinning (FORE) [137], which uses an approximation between the oblique and direct sinograms in Fourier space. Because this is only an approximation, computational processing is somewhat reduced compared to exact method 3D reprojection algorithms.

3D Reprojection

3D FBP is achieved similarly to what has been previously described for 2D image reconstruction, though using a Colsher Filter [138] in place of the ramp filter, for dealing with 2D parallel projections. The problem with this method in a real system is in the truncation of the oblique angle projection data at each end of the scanner.

To account for this, the 3D reprojection (3DRP) algorithm [139] is used before attempting 3D FBP. It is known that the 2D FBP of direct projections have sufficient data for a full reconstruction of the image (the oblique data is redundant), so this may be used to provide an estimate for the missing data. By calculating the line integrals along the estimated image, the projections from the missing LORs can be merged with the rest of the measured data. The entire process is outlined as [140, 128]:

- Reconstruction of direct projections using 2D FBP (outlined in 2.5.2)
- Forward projection from image estimate to construct missing line integrals.
- Take the Fourier transform of each 2D parallel projection.
- Multiply by the Colsher filter.
- Inverse 2D Fourier transform.
- Backproject

The 3DRP algorithm is the best performing analytic reconstruction method in terms of image quality, though does require significant computational resources for the estimation of missing projection data [135].

2.5.6 Iterative Image Reconstruction

Iterative reconstruction is a methodology that has gained significant traction in the clinical environment in recent years, due to its ability to account for the noise structure in the observed data. The images produced are generally superior to those produced by analytical reconstruction methods, since they are based on a more realistic model of the system. The main drawback is that the algorithms used are much more complex and require a great deal more processing power, hence why they are becoming feasible in modern computing systems.

The iterative method seeks to work toward an outcome to the image reconstruction problem by first estimating a solution, then successively improving the estimation by repeatedly comparing it to the measured data. Commonly, the first estimate is the forward projection of either a uniform matrix of 0 or 1 (depending on whether the algorithm is additive or multiplicative) [141]. This forward projection will result in a sinogram, which may then be compared (as a ratio) to the measured sinogram on a pixel-by-pixel basis. The result is then used as the new estimate to then again be compared to the measured data, continuing for a set number of iterations, or until the image comes within some tolerated error.

There are five necessary components needed for iterative image reconstruction [142] [128]:

1. **A vector of the measured data (m)** - obtained by finding the lines of response.

2. **A vector of parameters (n)** - representing an estimation of the radiotracer distribution in the image domain, as pixels (2D) or voxels (3D). This is the image we wish to find.

3. **The system matrix (A)** - relates the measured data (m) to the unknown image vector (n). The system matrix will actually model the *mean of the data vector*, $< m >$ (so noise is removed).

4. **An objective function** - Provides a measure of the agreeability of the parameters with the measured data. The objective function is a definition of the "best" image, usually expressed mathematically as a cost function. In

PET image reconstruction this is usually either a variation of a least squares function (can be either weighted, with or without a penalty term) or, more commonly in iterative reconstruction, maximum likelihood or maximum a posteriori (MAP). The last case is interesting, in that initial conditions desired in the final image are provided as a priori information, which will guide the iterative reconstruction process to an image with the desired features. Often this may be structural information (gained from MRI or CT scans), smoothness or boundary parameters. A weighting in the objective function balances the a priori term with the measured data.

5. **An Algorithm** - To achieve an optimisation of the cost function and produce the best image estimate.

2.5.7 The System Matrix

The system matrix is the link between our estimate of the parameters (i.e. our estimate of the values of our pixels or voxels in image space) and the mean of the measured data. This relationship is shown by

$$< m >= q = An \tag{2.17}$$

Where vector q is the mean value of the measured data, A is the system matrix and vector n is the estimated parameters. Unfortunately the size of the system matrix is often extremely large (often $> 10^8$ elements) and it's dimensions are irregular (for an image of $N \times N$ dimensions, the system matrix $A = aN \times N^2$, where a is the number of projection angles) [143], hence it is computationally impractical to solve 2.17 analytically. Instead, we multiply the estimated set of parameters to the system matrix and compare the output to the actual measured data, then adjust the parameters accordingly.

Each element of the system matrix a_{ij} corresponds to the probability that an emission from pixel (or voxel) j will be detected along the unique LOR between detector pair of index i. Each row of the system matrix will therefore correspond to image vectors, from each line of response through the field of view. Similarly, each column of the system matrix corresponds to the system response (i.e. the sinogram

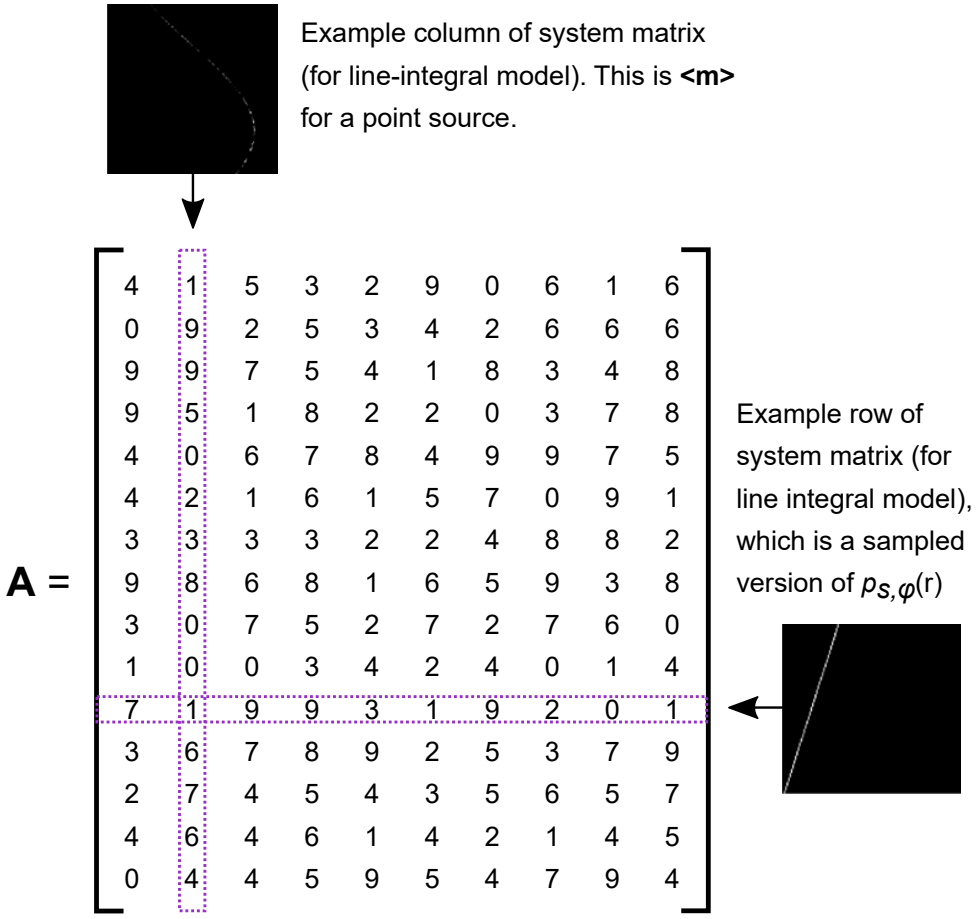

Figure 2.13: The columns of the system matrix directly relate to the mean measured data for a point source, that is, each sinogram is rearranged from a matrix to a vector. The rows of the system matrix correspond to each of the sinogram bins, which are obtained by considering line integrals through the FOV. Each column has the same number of elements as the measured data, and each row has the same number of elements as the number of parameters to estimate. [146].

with mean data $< q >$) for a particular point source emitter. Figure 2.13 shows this in more detail.

In practice, constructing the system matrix can be accomplished in a number of ways; either using an analytic model, using a Monte Carlo simulation [144], or actually measuring point sources at various locations in the field of view and mapping each result [145].

2.5.8 Iterative Algorithms

There are two main classes of iterative algorithms: statistical and algebraic. Algebraic algorithms such as ART [147] are based around solving systems of linear equations to iteratively correct each pixel on a projection ray. ART and its variants have seen a small amount of use in PET, though by far the most common algorithms in use are the statistical algorithms, which are based on the maximum likelihood expectation maximisation (ML-EM) algorithm and it's many variations. For this reason, the statistical algorithms will be the main focus.

Maximum Likelihood Expectation Maximisation

The maximum likelihood expectation maximisation (ML-EM) algorithm, introduced by Shepp and Vardi [148], uses a Poisson model for the data which is indicative of the random nature of nuclear decay. The cost function in this case is of course the maximum likelihood function, which converges to a solution based on expectation maximisation. The well known equation may be written in matrix form as [148, 149, 135]

$$n^{k+1} = \frac{n^k}{A^T 1} A^T \frac{m}{An^k + b} \tag{2.18}$$

This expression describes how the next estimate of the image, n^{k+1}, is based on the current estimated parameters, n^k. The process flow in Figure 2.14 can aid in the explanation.

- An initial estimate c^0 is made (which is generally a matrix of constant value).
- Forward project by applying the system matrix (An^k).
- Add a background term, consisting of scatters and randoms (b).
- Compare the estimated data to the measured data ($\frac{m}{An^k + b}$).
- Backproject using the transpose of the system matrix (A^T).
- Multiply by the current estimate to get the next image update (normalised by the term $A^T 1$, where 1 is a constant vector of all elements set to one).

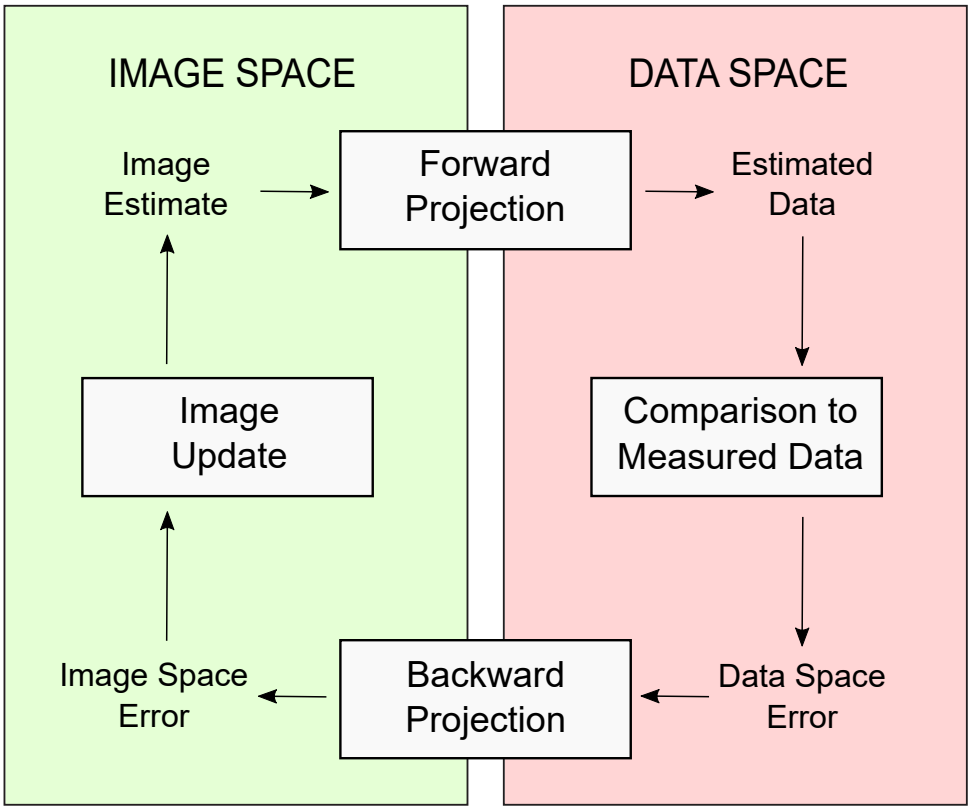

Figure 2.14: Iterative reconstruction algorithm flow diagram. [150].

Ordered Subsets Expectation Maximisation (OS-EM)

OS-EM [151] is a variation of the ML-EM algorithm which splits the projection data into subsets. This is usually a case of dividing the sinogram data depending on azimuthal angle. With each iteration of the algorithm having only a fraction of the data to process, a solution is found faster, relative to the number of subsets used.

The speed increase of OS-EM over ML-EM comes at the cost of non-convergence to the ML-EM image and there is some variance in the solution between different subsets of the data. This is usually an acceptable compromise as ML-EM takes a long time to reach convergence on a solution and is usually stopped before doing so. For this reason, OS-EM is widely used.

Maximum A Posteriori

One method of removing high frequency noise components is to add a priori information to the objective function; information that is known (or desired) about the object, guiding it to converge to an image with the desired parameters [152, 153].

This is similar to implementing a penalty term in each iteration, to influence the smoothness or edges of the images. Anatomical information from hybrid PET/MRI or PET/CT may also be used to guide the structure of the image [154, 155], which overcomes a loss in spatial resolution. These methods add a lot of complexity to the reconstruction and are often unused in the clinical environment due to the difficulty in choosing the correct parameters.

2.5.9 Image Reconstruction Software

STIR

The Software for Tomographic Image Reconstruction (STIR) library [156] is an open source software (written in C++), focused on 3D PET iterative image reconstruction, though 3D analytic algorithms are also supported. The software has been made available since 2000, originating from the PARAPET project and is some of the most widely used reconstruction software within the field. STIR includes libraries for image and projection data manipulation, file format conversions as well as the algorithms for reconstruction. Both sinograms and list mode data are supported. The current stable version of the library is v3.0.

CASToR

Customizable and Advanced Software for Tomographic Reconstruction (CASToR) [157] is a much more recent software package (written in C++) for iterative image reconstruction with PET, SPECT and CT. Includes tools for general image processing and data processing, including a conversion of ROOT data to the CASToR format. Analytical algorithms are not yet implemented. The current stable version is v2.1.

MIRT

The Michigan Image Reconstruction Toolbox (MIRT) [158] is a collection of open source algorithms written in Mathwork's MATLAB language. Included are a number of iterative and analytic algorithms for PET, SPECT, x-ray, CT and MRI.

2.6 Conclusion

This chapter presents an overview of PET operation and the many areas of active research within the field. Of particular interest are the different approaches to improve sensitivity, spatial resolution and signal-to-noise ratio of the image. The first route is to employ faster scintillation materials and photodetectors to improve the timing resolution, the second is to improve the geometrical coverage of the scanner - both of these likely require an increase in the cost of componentry.

A potential solution is to use lower cost nanocomposite or transparent ceramic scintillation materials, to shape a scanner which is geometrically efficient; a monolithic continuous cylindrical shell architecture. Silicon photomultipliers seem the obvious choice for coupling to the shell; they are physically small enough to be used both outside and inside the ring and have superior detection capabilities compared to PMTs or APDs (mass production should also see an improvement in cost).

This geometry leads to several important design questions. For an optically translucent material, what is the optimum thickness at which to make the shell? It is assumed that detections may be lost if the scattering is too great. There are also many different materials available - which of these has the superior performance for this application? Before reaching full image reconstruction, methods for determining coincidence detection and generating lines of response must also be explored.

Chapter 3

Monolithic Nanocomposite and Transparent Ceramic Scintillation Detectors for use in Positron Emission Tomography

3.1 Introduction

Detection and characterisation of high-energy photons is an inherently challenging task due to their highly penetrating nature. Semiconductor detectors are unable to directly detect such photons with high efficiency, due to the limited detector thickness, low density and low effective atomic number of most semiconductor materials [32]. To increase the probability of detecting high energy photons, in most applications it is necessary to optically couple an optical photodetector to a *scintillator*. When a high-energy photon interacts with a scintillator, the energy deposited is absorbed by atoms in the scintillator (commonly cerium, europium or thallium) and re-radiated as multiple lower-energy photons, typically in the optical range, which are easily detected by the photodetector. Many scintillator materials now exist, including some with very high stopping power due to their very high density and effective atomic number. The best of these also provide high light output, high energy resolution and fast decay time, and emit wavelengths which are well-suited to detection by solid-state silicon detectors or photomultiplier tubes.

Good scintillator materials are nearly transparent at the emission wavelength, and so can be made as thick as desired to achieve the required detection probability. The overwhelming majority of high-performance scintillator materials in use today are inorganic crystals, which offer high stopping power and good light output at wavelengths compatible with solid-state detectors and photomultiplier tubes. While they offer many excellent scintillation properties, crystal scintillators are intrinsically challenging to manufacture, requiring lengthy growth periods at very high and carefully regulated temperatures [26, 27]. Although some materials can be grown to quite large crystal sizes, they are generally brittle and difficult to cut or machine to anything other than relatively simple shapes (such as polyhedral blocks or occasionally cylinders); some materials which have many good optical and scintillation properties are also hygroscopic, requiring careful protection of the crystal to avoid degradation.

For applications requiring position sensitivity, the dominant approach is to optically couple discrete scintillator crystals to individual photodetector pixels in an optical photodetector array to form a detector block. Naturally, the most common crystal shape for this application is a rectangular prism. High-resolution and long axial field of view PET systems may utilise many tens of thousands of such crystals; if the scanner is capable of discerning depth of interaction, these crystals may be present in multiple layers. In a discrete-crystal PET system, each crystal is normally optically isolated from the others, and covered with a reflective coating on five of its six sides. Assembling the arrays needed for a large PET system rapidly becomes more difficult as the crystal size decreases and the scanner dimensions increase, with the scintillator arrays representing a substantial fraction of the cost of the scanner [5, 6, 4]. Furthermore, since a cylindrical shell cannot be divided into a finite number of equal-sized rectangular prisms without introducing gaps, sensitivity varies with respect to the angle of rotation around the central axis. This problem is even worse for PET systems which are intended to have a spherical or D-shaped geometry.

For PET, an alternative to arrays of discrete scintillator crystals is for each detector block to use a monolithic slab of scintillator material coupled to a pixellated photodetector array. The distribution of optical photons arriving at the detector can then be used to estimate the point of interaction within the crystal. This signifi-

cantly complicates the task of coincidence detection, but offers the major advantage of simplified manufacturing compared to the discrete-crystal model. Monolithic scintillators are normally fabricated as rectangular prisms. However, growing large crystals of uniformly high quality remains technically challenging, and the materials are still not easily fabricated into non-rectangular shapes.

Two new classes of materials have recently emerged as lower-cost alternatives to single-crystal scintillators, particularly where complex shaping of the scintillator is required: nanocomposites [102] and transparent ceramics [159]. Nanocomposites are a uniform mixture of inorganic scintillator nanocrystals and a polymer binder or matrix, which itself may also be a scintillating material. Although the nanocomposite has a lower density and effective atomic number (and hence stopping power) compared to the single-crystal solid form of its inorganic scintillator component, these parameters are still significantly higher than those of pure polymer scintillator materials. Other important parameters, such as optical photon yield and wavelength, are also similar (but not identical) to those of the bulk material. On the other hand, transparent ceramic/garnet scintillators are chemically related to existing single-crystal scintillator materials, but with a polycrystalline structure. Many of the desirable properties of comparable single-crystal scintillators are retained (in particular, high stopping power and light output), however, they can be fabricated more rapidly at much lower temperatures, and formed into complex shapes much more easily than monocrystalline scintillator materials.

A common shortcoming of both nanocomposites and transparent ceramic scintillators is their lower optical transparency compared to single-crystal scintillators. In the case of nanocomposites, the difference between the refractive indices of the nanocrystal scintillator and the matrix polymer leads to Rayleigh scattering and reduced transmittivity. A similar problem also exists to some extent in ceramic garnet scintillators due to the presence of grain boundaries in the material. Slabs of single-crystal scintillator material can be made as thick as necessary to achieve the desired sensitivity, due to the low optical attenuation of the material. However, this is not the case for either nanocomposites or ceramics, as beyond a certain optimal thickness, scattering and attenuation degrade the optical signal to the point where it is no longer useful in providing an accurate estimate of the point of interaction

within the scintillator. Therefore, determining the optimal thickness for the scintillator is an important design question for those wishing to utilise these materials in PET systems and other radiation detection applications. In this context, *optimal* refers to that thickness which maximises the number of photons whose point of interaction can be estimated within a specified threshold of accuracy. Too thin, and the probability of detection will be too low; too thick and many of the optical photons may be absorbed before reaching the optical photodetector, resulting in an inaccurate position estimation.

This work proposes a general method for determining optimal thickness of a monolithic scintillator slab, given the physical properties of the scintillator material, based on cubic spline interpolation between results obtained from a set of Monte Carlo simulations. The method is demonstrated by applying it to provide a quantitative comparison between a range of promising nanocomposite and transparent ceramic scintillators. Section 3.2 discusses the specific methods to be used in this work and introduces the proposed thickness-optimisation technique; Section 3.3 presents results comparing scintillator performance with two fixed thicknesses plus the optimal thickness for each material, and discusses the key implications. Finally, the outcomes of this research are summarised in Section 3.4.

3.2 Materials and Methods

In this section, a Monte Carlo-based approach to the optimisation of monolithic scintillator slab thickness for a given material is described. The method is applicable to any material with accurately characterised physical and optical properties. Simulations are performed using version 8.0 of the Geant4 Application for Tomographic Emission (GATE), which extends the well-known Geant4 Monte Carlo framework to enable complex simulations of the interaction of radiation and matter to be constructed via text-based descriptions of geometry and materials [160, 161, 162].

3.2.1 Performance Metric and Optimisation Algorithm

In scintillator-based imaging systems such as PET, the probability of detecting an emitted photon is limited by thickness of the scintillator and the radiation length in

the scintillator material at the wavelength (or wavelengths) of interest. For imaging systems based on *monolithic* scintillators, detection probability must be defined more specifically, also taking into account the *accuracy* of detection - that is, the probability that the location of a the first energy-depositing interaction within the scintillator can be estimated to within a certain tolerance of the true location inside the scintillator. Using this metric, "optimal thickness" of a large rectangular slab of scintillator material may be defined as **the thickness which enables the greatest fraction of incident photons to be localised to within a specified distance of the true point of interaction**. It is reasonable to expect that such an optimum exists; if the scintillator is too thin, detection efficiency will be very low due to the small number of primary photons which will interact with it (although they can be localised very precisely within the slab), while if it is too thick, the optical attenuation of the scintillator will cause too many of the scintillation photons to be absorbed for accurate determination of the point of interaction, and the probability of multiple Compton scatter events (which manifest as a multi-point emission within the scintillator) increases.

To determine the optimal monolithic scintillator thickness for each material, for a given gamma photon energy, a series of GATE simulations of a given scintillator material are performed with different slab thicknesses. An exhaustive evaluation may be performed for a range of potential thicknesses; however, for most materials this is not necessary. The optimal thickness may be determined by the following procedure:

1. Choosing the desired threshold of detection accuracy suitable for the proposed application;

2. Simulating photon interactions with the scintillator with a small number of thicknesses;

3. Applying the chosen location-determination algorithm to the observed optical photon maps on both sides of the scintillator;

4. Determining the probability of being able to estimate the first point of interaction of the incident gamma photons to within the chosen threshold for each simulation; and

5. Apply cubic spline interpolation between the measured points and determine its maximum from the first derivative.

This approach will work with any position estimation algorithm, such as several of those described in Section 2.4. In this work, we utilise an error-minimisation method to fit the location and emission intensity parameters of a simple analytic model to the observed patterns of photon emission on both the front and back side of the scintillator.

3.2.2 Simulation Parameters

To evaluate the chosen performance metric and develop a model for its optimisation, a series of GATE simulations were performed, using the basic geometry in Figure 3.1. The depth of the scintillator slab (in the z dimension - for a PET scanner, this would be the radial dimension) was varied - between 5 mm and 35 mm in steps of 5 mm for the transparent ceramics, and between 10 mm and 70 mm in steps of 10 mm for the nanocomposites. Each simulation consisted of 20000 primary photons.

3.2.3 Detector Geometry

The geometrical design of the scintillation detector (3.1) is very similar to the monolithic detector model previously described in [163] and simulated in Geant4 and GATE [164]. In this study, the scintillator volume of width×height×depth = 20 mm×20 mm×t; Figure 3.1 shows an example where $t = 10$ mm.

The detectors are arranged in a double-sided readout (DSR) configuration, a design which supports accurate localisation of the point of interaction over a wider range of scintillator thicknesses compared to either front-only or back-only readout systems [62]. This is particularly important for the lower density nanocomposite materials discussed here. The detectors themselves are modelled as a simple silicon photodiode; the pixellated detector planes are coupled to the scintillator via thin layers of Meltmount and epoxy (0.05 mm and 0.1 mm respectively), while the exterior surface is covered by a 1 mm polymer/metal layer representing the electronics in the detector. Non-detector faces of the scintillator are covered with non-reflective

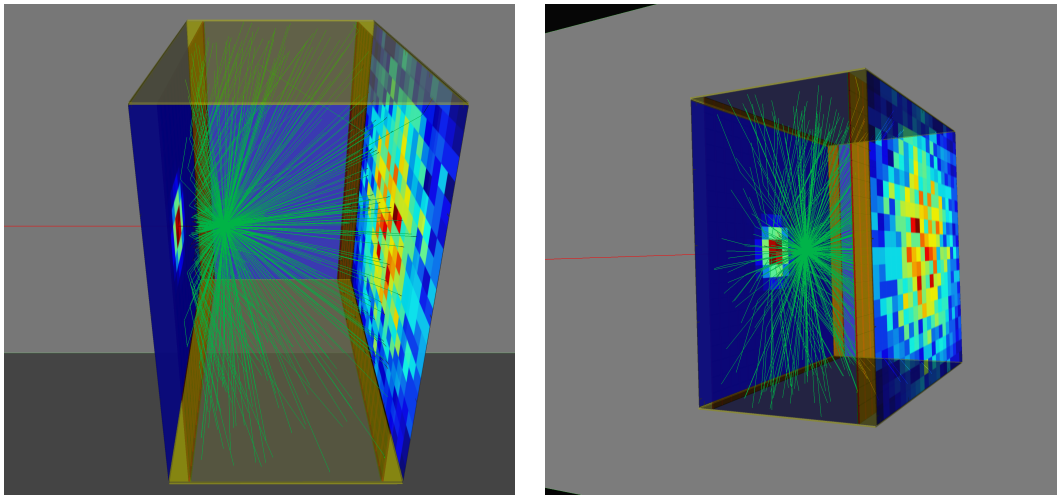

(a) (b)

Figure 3.1: A single photoelectric interaction, captured using a dual photodetector configuration with a 10 mm thick GYGAG:Ce scintillator slab. The incoming γ photon (red) interacts with the scintillator (blue) and emits a shower of 550 nm optical photons (shown in green). Note that the only a small fraction of the optical photon paths are shown for clarity. Subfigures (a) and (b) provide two different views of the same interaction.

black paint. Detector pixels are 1 mm×1 mm (with zero assumed dead space).

3.2.4 GATE Parameters

The following parameters were used with GATE version 8.0 and Geant4 version 10.2.2.

System

A GATE *optical system* is implemented for accurate optical tracking of the scintillation photons and modelling the relevant physics, including optical attenuation, scattering and surface properties.

Physics

GATE uses the Geant4 low background experiment (LBE) physics list, as it is recommended for simulations incorporating optical photon transportation and scintillation processes [165]. Compton scattering and photoelectric processes have been added

for gamma photon interactions, along with all processes relating to optical interactions, including bulk absorption, Rayleigh scattering, Mie scattering and boundary processes.

Surface Properties

The UNIFIED model was used to define the optical surface properties of the interfaces between materials. To simulate the absorptive black paint covering the scintillator material, the *ground-front-painted* finish was used; the reflectivity is set to zero so that optical photons are not internally reflected. The optical roughness of surfaces can be specified by altering the σ_α value (defined as the standard deviation of the Gaussian distribution of micro-facets around the average surface normal); however, it has previously been shown that for the scintillator-Meltmount-detector interfaces, this parameter has a minimal influence on the accuracy of estimation of the point of interaction due to the large size of detector pixels relative to the micro-facets [62, 166]. Therefore, this parameter has been set to $\sigma_\alpha = 0.1$ (corresponding to a polished surface). The interface between the detector and the Meltmount layer has been specified as *perfect-apd*, which assumes perfect flatness and 100% efficiency.

Source

The source is a simple monochromatic 511 keV photon gun. Since the focus of this work is providing a mechanism to compare optimal thicknesses of different scintillator materials, rather than the localisation algorithm itself, all photons are directed at the centre of the scintillator slab, parallel to the z axis. For optimal thickness determination, 20000 primary (γ) photons have been fired at the detector for each evaluated combination of scintillator thickness and material. For determination of spatial error and analysis of scatter composition, 200000 primary (γ) photons were used.

3.2.5 Nanocomposite Loading

Figure 2.10(a) and 2.10(b) demonstrate that for nanocomposite materials, optical transmittivity and stopping power are both strongly influenced by the scintillator loading fraction; however, the effects are in opposition to one another. Higher

loading (i.e. a higher fraction of nanoscintillator compared to the matrix material) results in a higher average density and effective atomic number (and hence stopping power); however, optical attenuation is increased, limiting the benefits of a high loading factor since many of the scintillation photons are scattered and/or absorbed before they can be detected.

To ensure that enough scintillation photons can be detected for an accurate estimate of the point of interaction to be determined, a reasonable approach to choosing an appropriate loading factor is to balance the optical attenuation length equally against the gamma radiation attenuation length. If a DSR detector configuration is being used with this approach, the thickness of the scintillator which satisfies this criterion is doubled compared to a single-sided readout design (i.e. for DRS, the maximum distance away from any detector is only half of the scintillator thickness). The scintillator loading volume fraction may be found by considering Figure 2.10(a). For example, a 2 cm thick nanocomposite detector made from LaF_3:Ce nanoscintillator material in an oleic acid matrix (with double-sided readout) would require a 1 cm optical attenuation length (half the length of the scintillator) to satisfy the condition. A 1 cm attenuation length for LaF_3:Ce is equal to approximately 17% scintillator loading by volume.

Alternatively, if a specific attenuation length is required - for example, 50% attenuation of 511 keV gamma photons (the half value layer or HVL) - then a suitable loading factor and thickness can be computed such that the gamma radiation attenuation length equals the optical attenuation length. In the case of a single-sided detector, the point of intersection of the curves in Figure 2.10(a) and 2.10(b) can be found; for the DSR configuration, the optical attenuation length only needs to be equal to half of the HVL. This may be more easily seen in figure 3.2, which shows both of these plots overlaid for LaF_3:Ce OA. The scintillator volume fraction satisfying the condition in this case is $\sim$5%, at the point of intersection. All of the loading factors used in the simulations are shown in Table 3.1.

3.2.6 Scintillation Event Position Determination

Estimation of the most likely coordinates of the first point of interaction for each (interacting) primary event is performed in Matlab through analysis of the "Hits"

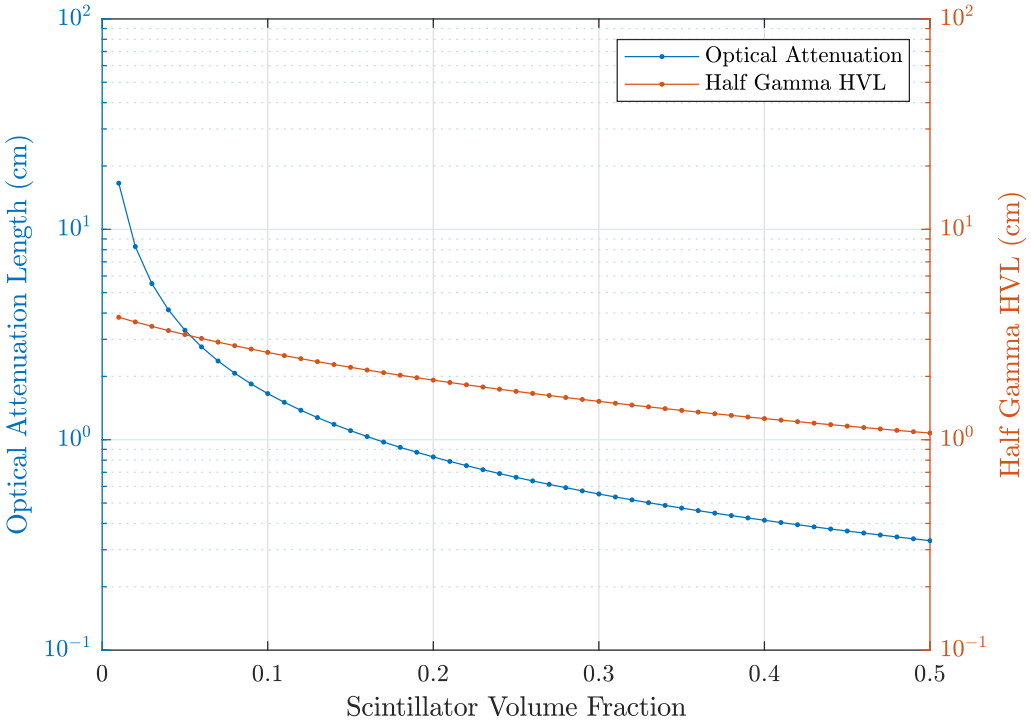

Figure 3.2: Overlaid plots of optical attenuation and HVL / 2 for LaF_3:Ce oleic acid. The point of intersection between these curves is used to determine appropriate scintillator loading factor for the nanocomposite; in this case, the point of intersection occurs at ∼5%.

Nanoparticle	$LaBr_3$:Ce	Gd_2O_3	LaF_3:Ce	LaF_3:Ce	YAG:Ce
Matrix	PS	PVT	OA	PS	PS
1 cm load (%)	19	4.6	34	50	50
2 cm Load (%)	9	4.6	17	50	50
HVL Load (%)	3	4.6	5	50	28
T. Opt. (%)	7	4.6	12	50	37

Table 3.1: A summary of the loading factors by % volume, used in these simulations. Calculated as described, using figures 2.10(a) and 2.10(b). The loading factor for optimal thickness (denoted T. Opt.) was chosen based on a 3 cm thick slab, using the same methodology.

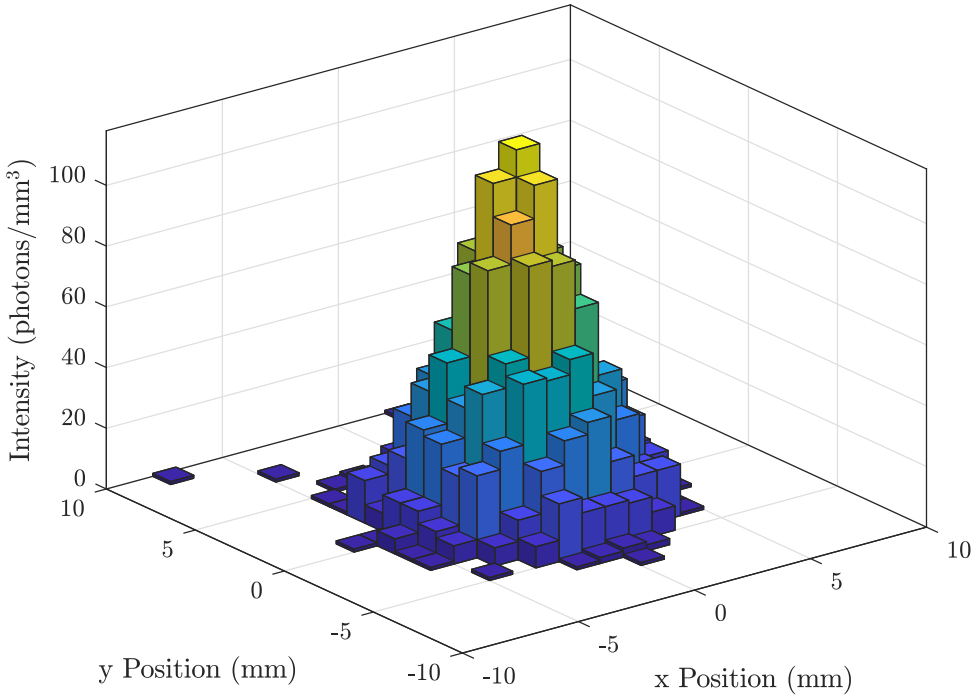

(a) Detected photons (front)

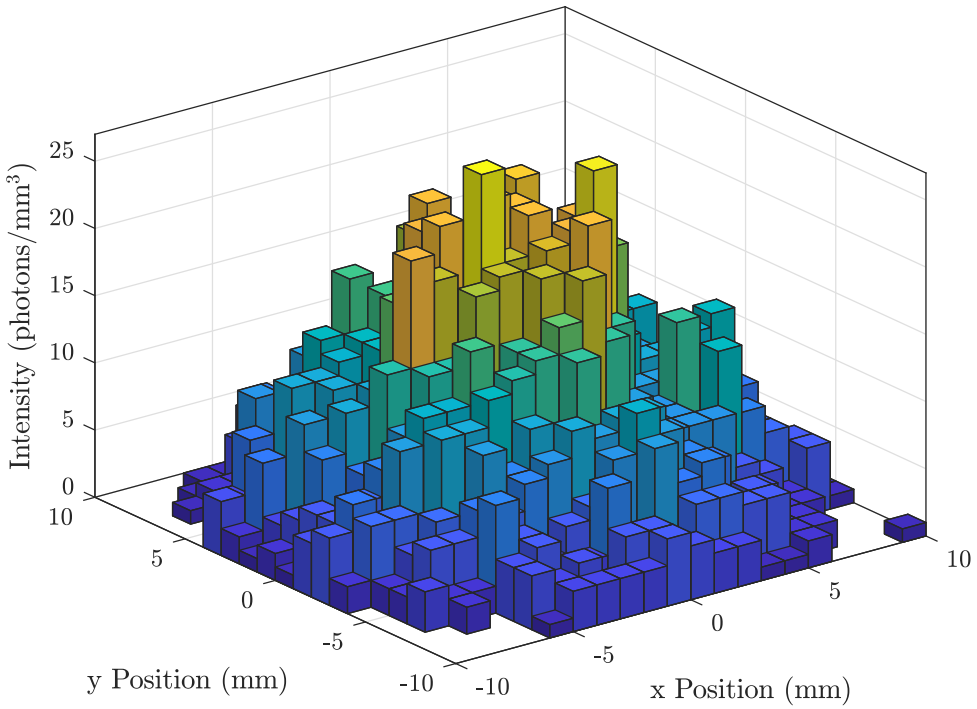

(b) Detected photons (back)

Figure 3.3: An analytic model of the expected photon map is jointly fitted to the photon distributions observed on both the front and back of the scintillator. The calculated parameters for the function are then used to estimate the position of interaction of the initial gamma photon and the number of scintillation photons emitted.

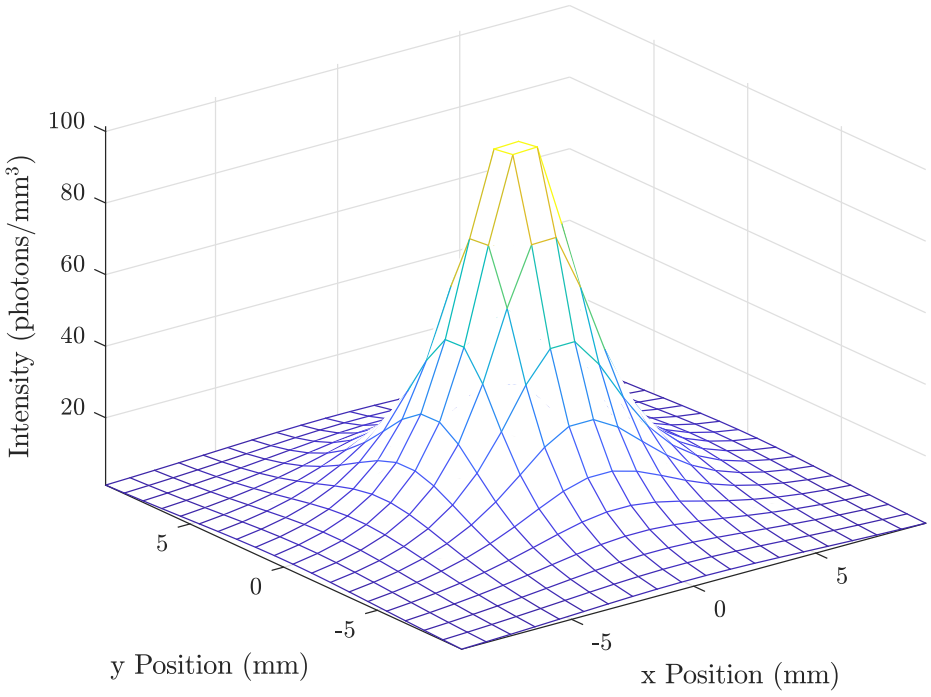

(c) Fitted model (front)

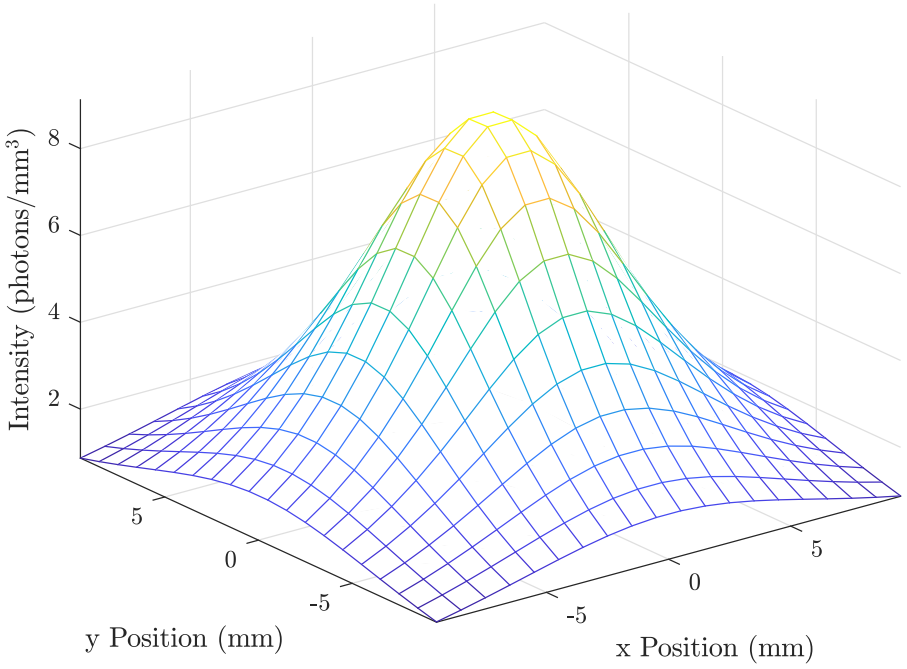

(d) Fitted model (back)

Figure 3.3: (Continued from previous page). The optical photon distribution on the front and back detector and shown in Figure 3.3(a) and 3.3(b) respectively, while Figure 3.3(c) and 3.3(d) show the analytic functions fitted to these distributions using (3.1) and (3.2).

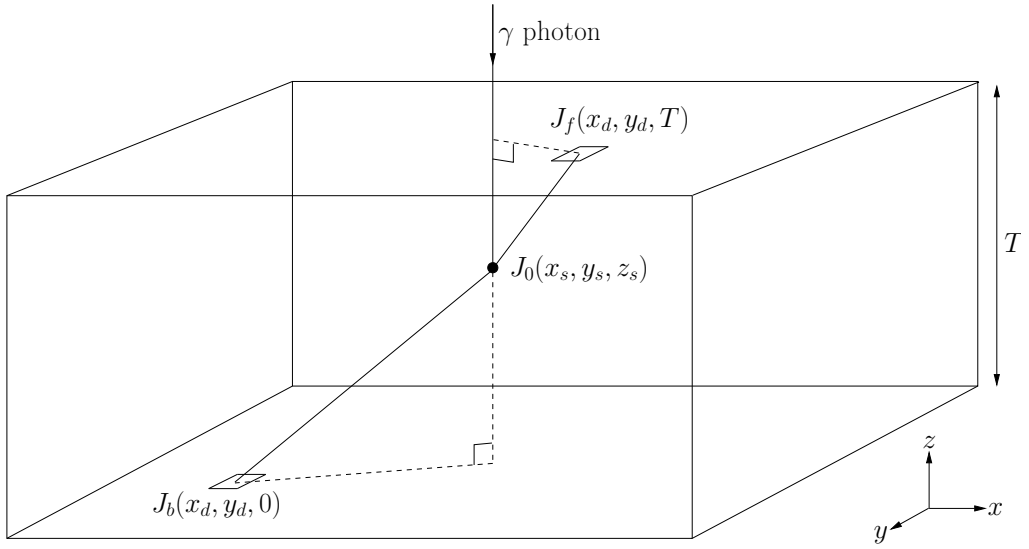

Figure 3.4: The incident γ photon strikes the scintillator slab at point (x_s, y_s, z_s), with intensity J_0. The optical photon intensity detected on pixels (of dimensions $\Delta x \times \Delta y$) at position (x_d, y_d) on the back and front faces of the detector are given by J_b (3.1) and J_f (3.2) respectively.

list-mode data recorded during the simulation. This file records the location of all photon interactions with the scintillator and detector (both gamma and optical photons). The true 3D points of interaction with the scintillator, as well as the number of photoelectric, Compton and Rayleigh scatter events which occur inside the scintillator material for each interacting primary (γ) photon are logged, together the 3D coordinates at which any scintillation photons interact with the detector surface. The time of each interaction and deposited energy are also logged. An example of the detected photon distributions is shown in Figure 3.3(a) and 3.3(b).

Detected optical photons are isolated into those associated with an individual primary via a timing window (chosen to suit the time constants of each scintillator material). The optical photon distributions on the surface of each detector are binned into 1 mm$\times$1 mm pixels.

A parametric model of the predicted photon distribution (as a function of location within the scintillator slab) is derived from (2.8), and fitted to the discrete photon map via the Levenberg-Marquardt minimisation algorithm. The geometry is described in Figure 3.4. For a scintillation event occurring at position (x_s, y_s, z_s), the number of photons arriving at a pixel of dimensions $(\Delta x \times \Delta y)$ located at (x_d, y_d)

on the back face is given by:

$$J_b(x,y) = \frac{J_0 z_p \Delta x \Delta y e^{-\frac{\sqrt{(x_s-x_d)^2+(y_s-y_d)^2+z_s^2}}{\lambda}}}{4\pi\left((x_s-x_d)^2+(y_s-y_d)^2+z_s^2\right)^{\frac{3}{2}}} \tag{3.1}$$

where J_0 is the number of emitted scintillation photons, and λ is the radiation attenuation length. Similarly, on the front face (i.e. the first face through which the incident photon passes), the expected number of photons arriving at the same pixels is given by:

$$J_f(x,y) = \frac{J_0 (T-z_p) \Delta x \Delta y e^{-\frac{\sqrt{(x_s-x_d)^2+(y_s-y_d)^2+(T-z_s)^2}}{\lambda}}}{4\pi\left((x_s-x_d)^2+(y_s-y_d)^2+(T-z_s)^2\right)^{\frac{3}{2}}} \tag{3.2}$$

where T is the thickness of the scintillator slab.

To account for total internal reflection within the scintillator slab, J_b is set to zero anywhere outside a circle of radius

$$R_b = z_s \frac{n_{mm}}{n_s^2 - n_{mm}^2} \tag{3.3}$$

where n_{mm} is the refractive index of Meltmount (the optical coupling compound) and n_s is the scintillator's refractive index. Similarly J_f is set to zero outside of a circle of radius

$$R_f = (T-z_s) \frac{n_{mm}}{n_s^2 - n_{mm}^2} \tag{3.4}$$

An example of the fitted analytic model is shown in Figure 3.3(c) and 3.3(d).

3.2.7 Materials

Scintillator properties were taken from the literature where possible (see Table 2.4 and 2.5) or, for the case of the nanocomposites, calculated via the methods described in Section 2.4 (see (2.11) and (2.12)). Several of the optical and physical properties, including the density, refractive index and optical absorption length are dependent upon the loading factor of the nanoscintillator relative to the binder. The scintillation spectrum is assumed to be monochromatic at the peak emission wavelength, so refractive index and absorption length are single values (calculated for the peak wavelength).

The silicon and epoxy layers use the default parameters found in the GATE material database, while Meltmount has been created using the chemical composition described by Van der Laan et al. [164].

As a reference material, equivalent simulations were also conducted using Lu_2SiO_5 (LSO), which is a well known scintillation material, common in many PET systems.

3.3 Results and Discussion

3.3.1 Calculation of the Optimal Scintillator Thickness

The relationship between scintillator thickness and the number of events detected is shown in Figure 3.5 and 3.6 for the nanocomposite and transparent ceramic scintillators, respectively. These plots include separate curves for detections whose estimated point of interaction has been correctly detected within spatial error limits of 1 mm, 2 mm, 3 mm, 4 mm, 5 mm and all detections regardless of accuracy; ΔD is the total spatial error ($\Delta D = \sqrt{\Delta x^2 + \Delta y^2 + \Delta z^2}$). The location of the maxima of each of these curves is summarised in Table 3.2.

Of the nanocomposite materials evaluated, LaF_3:Ce-polystyrene offers the maximum probability of detection for $\Delta D \geq 3$ mm, and is only slightly worse than YAG:Ce-PS at $\Delta D \leq 2$ mm; in all cases, this sensitivity is achieved by LaF_3:Ce-polystyrene with a much thinner slab of scintillator than for the other materials. This is chiefly due to the high loading factor (and hence high density and Z_{eff}) relative to the other nanocomposite materials. As previously discussed, however, the loading factor cannot be increased without compromising the transmittivity of the nanocomposite. YAG:Ce-polystyrene offers a fair compromise between sensitivity and accuracy of interaction localisation. It has the highest probability of detection (of the nanocomposites) for $\Delta D \leq 1$ mm and $\Delta D \leq 2$ mm and offers sensitivity which is comparable to LaF_3:Ce-PS for $\Delta D \leq 3$ mm.

With their high density and Z_{eff}, the transparent ceramics offer a much higher probability of detection at any given slab thickness compared to the nanocomposite materials. As with the nanocomposites, the key differences between the different ceramic materials related to detection efficiency and accuracy of position estimation are their emission wavelengths and their optical transmittivity. GAGG:Ce, GLuGAG:Ce and LuAG:Pr all have similar attenuation coefficients at 511 keV, however GYGAG:Ce has by far the highest optical transmittivity, allowing a higher proportion of the the scintillation photons to reach the detectors. While GYGAG:Ce

achieves the highest overall probability of detection, the thickness required for this to occur is ≥45 mm and a high proportion of events are localised with an error $\Delta D > 5$ mm. As for the nanocomposites, a higher scintillator thickness increases the impact of coherent optical photon scattering, making it increasingly difficult for the localisation algorithm to accurately estimate the point of interaction. The benefits of high optical transparency are therefore limited if density and Z_{eff} are such that a very thick slab of scintillator is required, since although a large fraction of photons will be detected, their point of interaction cannot be accurately localised.

GLuGAG:Ce provides the highest probability of detection for all finite ΔD limits. This is the most dense material while being marginally more transparent than GAGG:Ce and LuAG:Pr. If the scanner is to be optimised for accuracy rather than sensitivity, an optimal thickness for GLuGAG:Ce would be approximately 20 mm, yielding detection of about 46% of photons to within 1 mm of their true point of interaction, and 62.5% of photons within 5 mm. On the other hand, increasing the scintillator thickness to around 27.5 mm will increase the latter figure of merit to 67.5% while reducing the former to around 43% - demonstrating that further increases in scintillator thickness will capture more photons, but with progressively decreasing accuracy. The maximum sensitivity of GAGG:Ce and LuAG:Pr are somewhat lower, peaking at around 48% and 60% of incident photons, respectively (for events localised to within 5 mm of the true location).

In summary, while all transparent ceramic scintillator materials significantly outperform the evaluated nanocomposite materials, there may be price points at which certain nanocomposite materials offer sufficient performance to justify their use in a PET scanner design.

3.3.2 Analysis of Photoelectric vs Compton Interactions

The probability of photoelectric, single and multiple Compton interactions in each scintillator type is shown in Tables 3.3, 3.4, 3.5 and 3.6 for 1 cm, 2 cm, half-value layer thickness and optimal thickness monolithic slabs. LSO has been used as a benchmark scintillator for comparison with these materials, as may be seen in Tables 3.3, 3.4 and 3.5, which show the percentage and composition of events detected for scintillators of 1 cm, 2 cm and the HVL of each material, respectively.

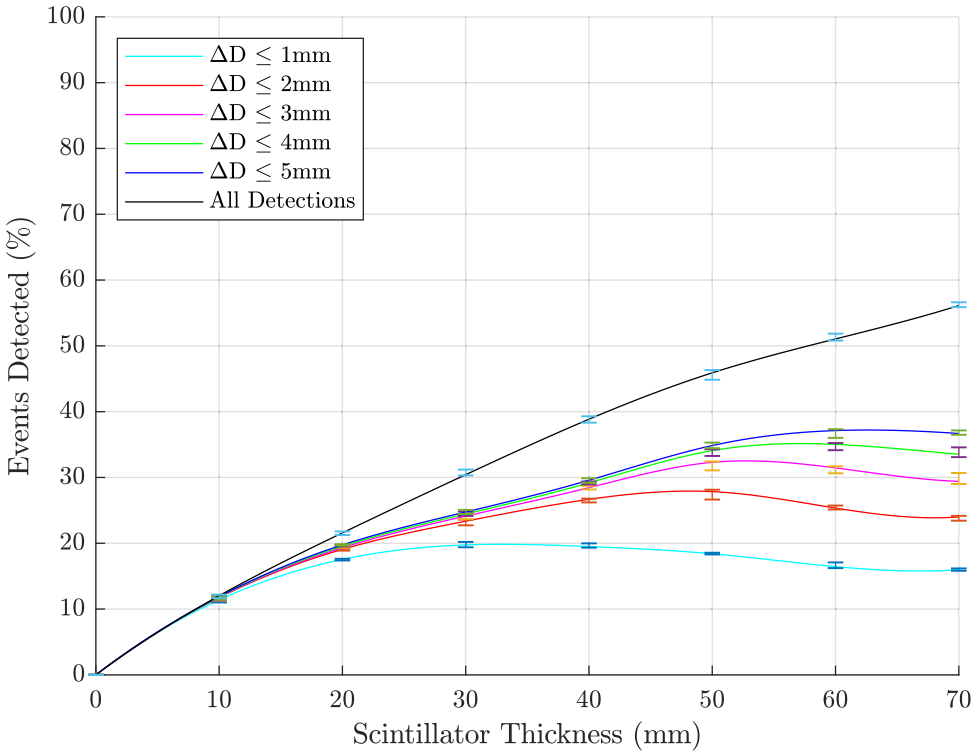

(a) Gd_2O_3 PVT (4.6 % loading)

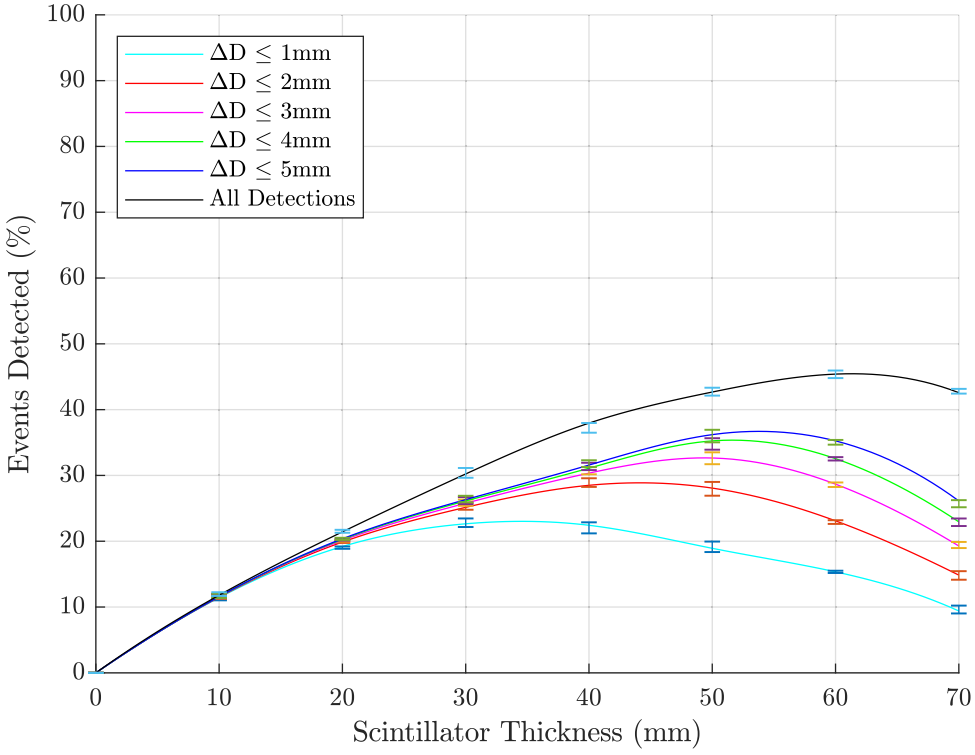

(b) $LaBr_3$:Ce PS (7 % loading)

Figure 3.5: Percentage of events detected to a specified accuracy of 1 mm, 2 mm, 3 mm, 4 mm, 5 mm and all detections as a function of scintillator thicknesses for nanocomposite materials. Median values with interquartile ranges are shown.

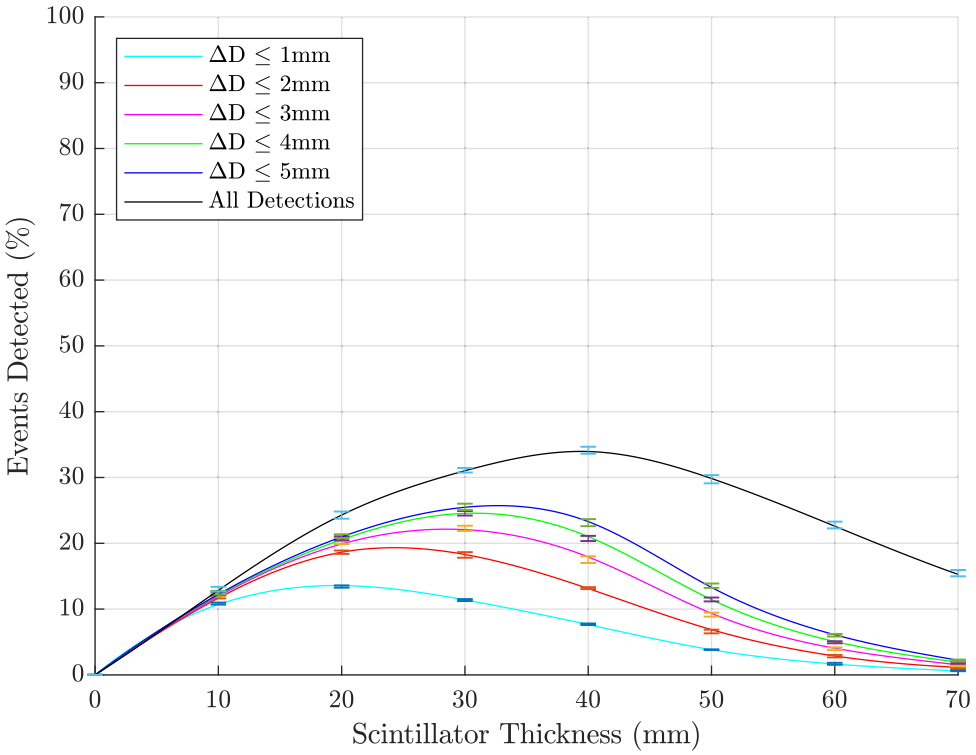

(c) LaF_3:Ce OA (12 % loading)

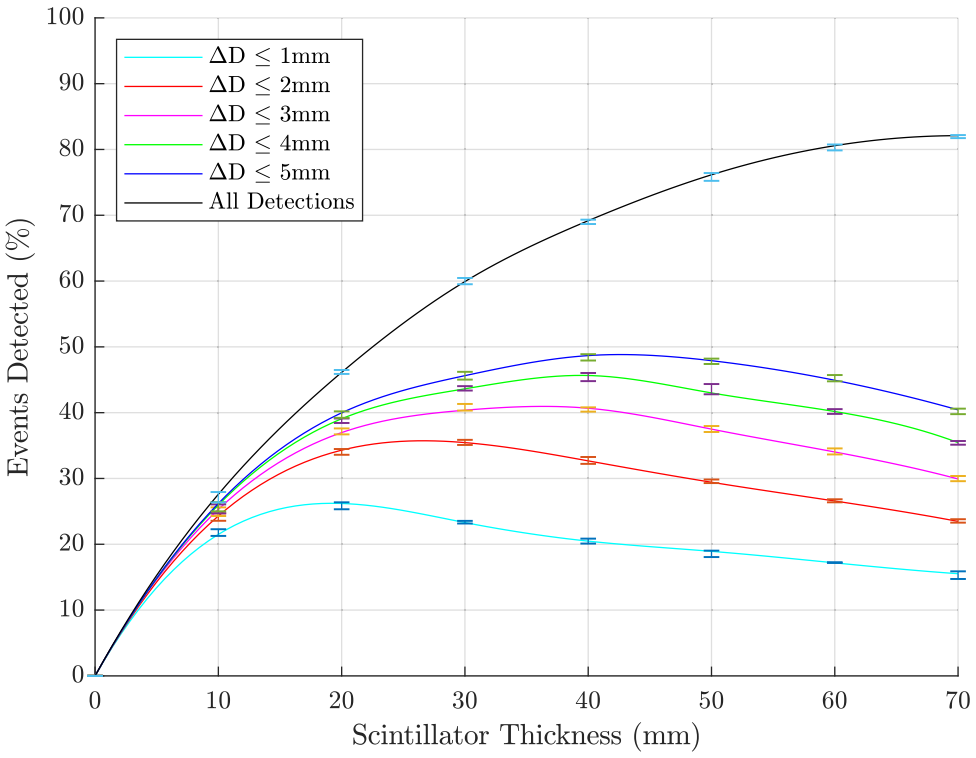

(d) LaF_3:Ce PS (50 % loading)

Figure 3.5: (Continued from previous page).

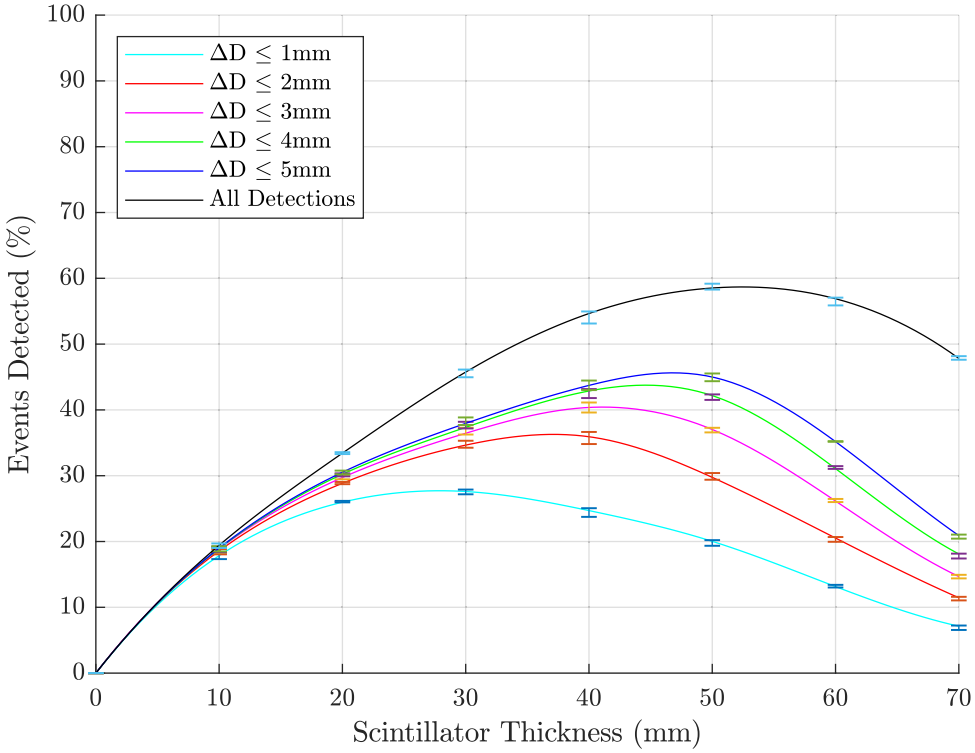

(e) YAG:Ce PS (37 % loading)

Figure 3.5: (Continued from previous page).

Scintillator	**ΔD ≤ 1 mm**		**ΔD ≤ 2 mm**		**ΔD ≤ 3 mm**		**ΔD ≤ 4 mm**		**ΔD ≤ 5 mm**		**All Detections**	
	T. Opt. (mm)	P. D. (%)	T. Opt. (mm)	P. D. (%)	T. Opt. (mm)	P. D. (%)	T. Opt. (mm)	P. D. (%)	T. Opt. (mm)	P. D. (%)	T. Opt. (mm)	P. D. (%)
Gd_2O_3 PVT	32.91	19.84	48.18	27.93	52.71	32.52	57.18	35.15	62.61	37.21	-	-
$LaBr_3$:Ce PS	34.56	23.02	44.13	28.88	49.33	32.67	51.61	35.36	53.78	36.70	61.33	45.45
LaF_3:Ce OA	19.58	13.58	24.26	19.33	28.50	22.15	30.78	24.58	32.66	25.73	39.42	33.97
LaF_3:Ce PS	19.21	26.23	26.61	35.73	36.35	40.95	39.41	45.66	42.60	48.83	-	-
YAG:Ce PS	27.91	27.72	37.12	36.28	41.13	40.43	44.61	43.76	46.79	45.63	52.43	58.69
GAGG:Ce	12.58	37.17	13.57	42.66	13.85	45.04	13.91	46.73	13.98	47.95	14.53	54.46
GLuGAG:Ce	19.25	46.33	25.25	56.48	26.70	62.37	27.39	65.71	27.54	67.82	28.08	79.94
GYGAG:Ce	29.78	44.13	31.13	52.78	40.54	59.09	41.68	63.67	42.63	66.75	-	-
LuAG:Pr	15.69	42.28	18.31	51.26	18.78	55.50	18.81	58.08	18.96	59.95	19.52	69.09

Table 3.2: Optimum scintillator thickness (denoted T. Opt.) and corresponding probability of detection (P. D.) within a limit of 1, 2, 3, 4, 5 and all detections. ΔD is the total error in position estimation for the point of interaction, for both nanocomposite and transparent ceramic scintillator materials.

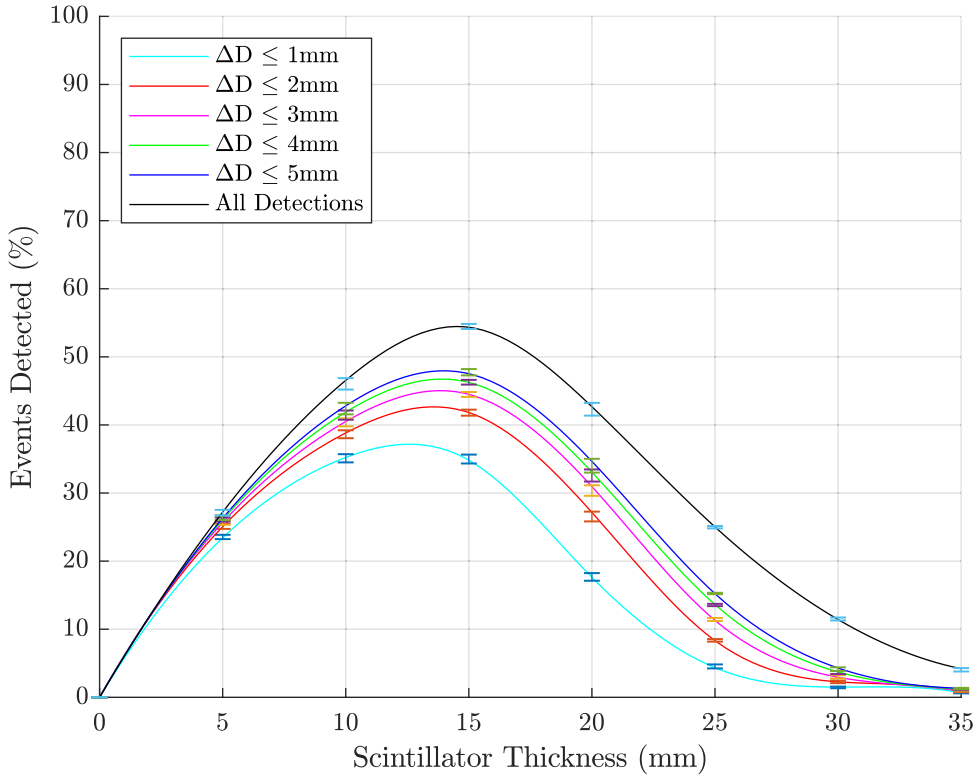

(a) GAGG:Ce

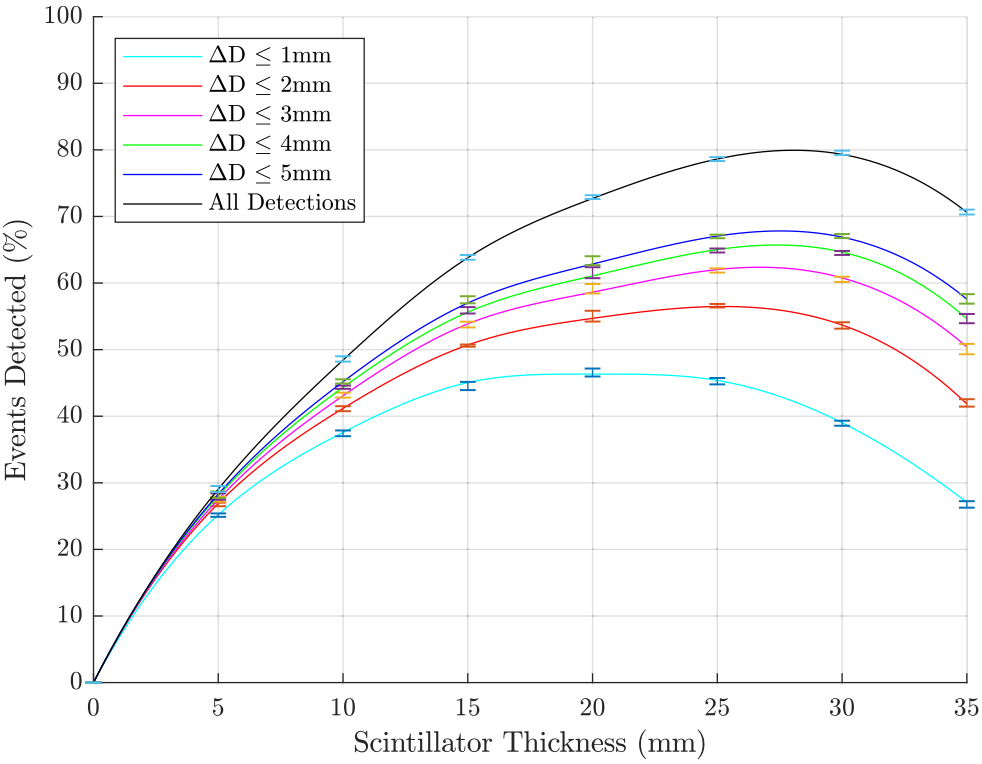

(b) GLuGAG:Ce

Figure 3.6: Percentage of events detected to a specified accuracy of 1 mm, 2 mm, 3 mm, 4 mm, 5 mm and all detections as a function of scintillator thicknesses for transparent ceramic materials. Median values with interquartile ranges are shown.

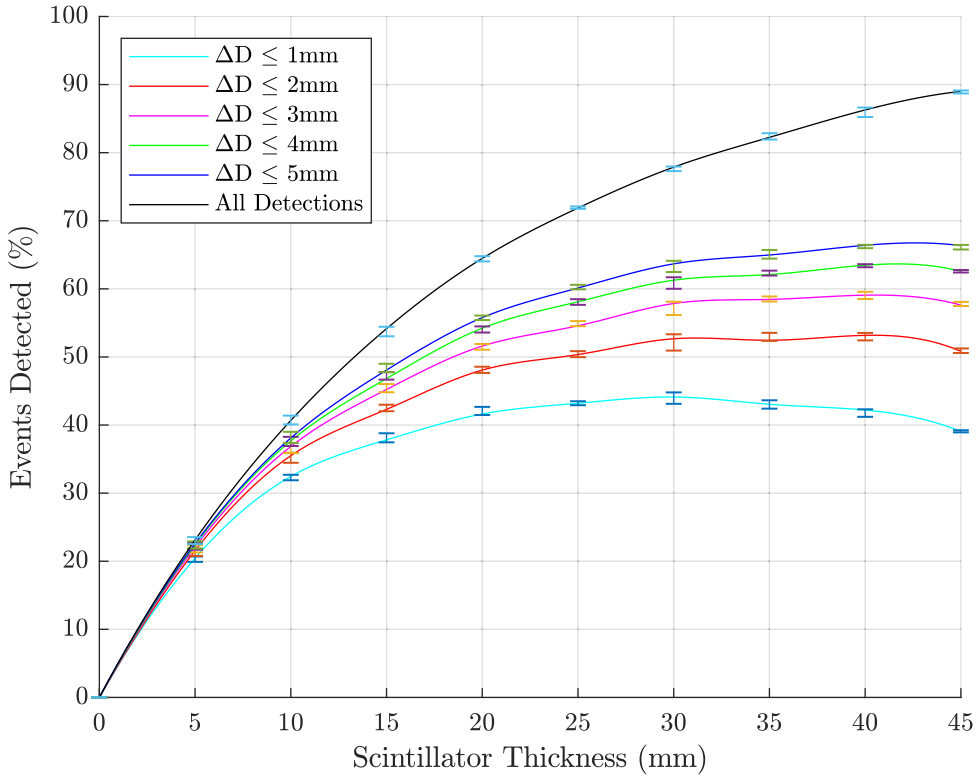

(c) GYGAG:Ce

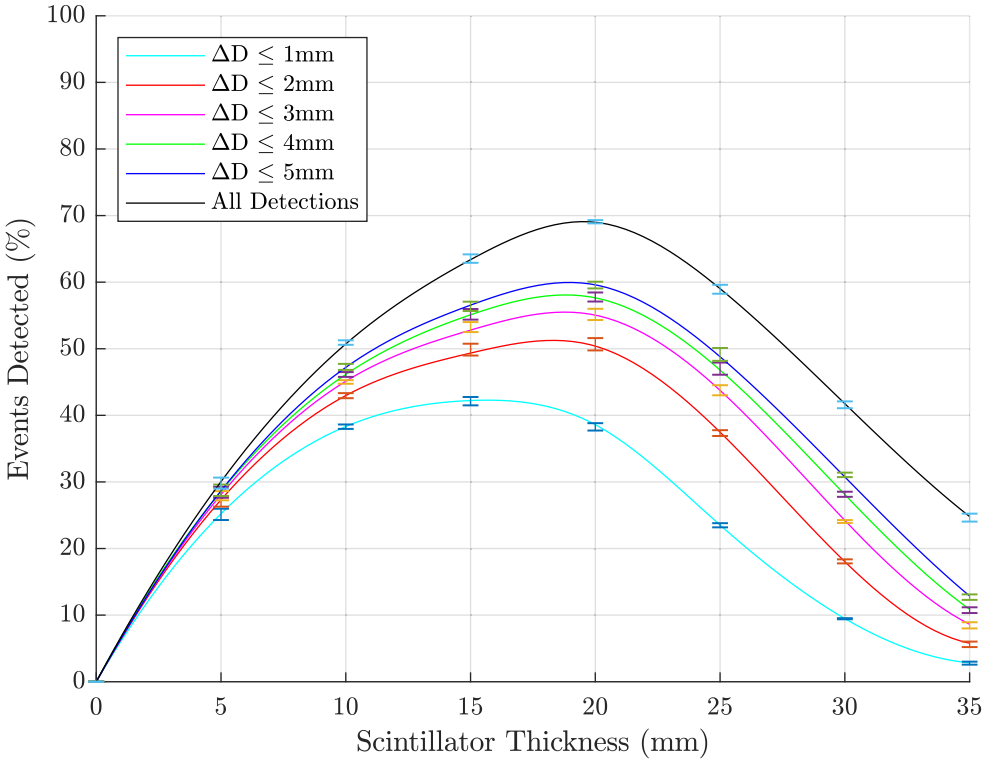

(d) LuAG:Pr

Figure 3.6: (Continued from previous page). Note that the x-axis is slightly longer for GYGAG.

The analytic function used for estimating the location of the point of interaction assumes that all interactions are photoelectric. In reality, many interactions involve one or more Compton (incoherent) scatter events, which potentially results in more than one point of energy deposition within the scintillator slab. Since energy is lost in each Compton interaction, the probability of photoelectric absorption increases with each subsequent scatter. The result is a more spread-out (and, in general, irregular) projection of optical photons on the detector surface following a multi-interaction event compared to a simple photoelectric interaction or a Compton interaction where the scattered photon does not undergo any further interaction with the scintillator.

The cross-sections determining the probability of interaction via photoelectric absorption and Compton scattering are complex functions of the electronic structure of the atoms in the photon path. Photoelectric absorption cross-section is approximately proportional to the 4th or 5th power of Z_{eff} and proportional to the 3.5th power of wavelength. By contrast, Compton cross-section is approximately proportional to the density of the material and wavelength. At 511 keV, the dominant process is Compton scattering for both nanocomposite and ceramic scintillators, although a substantial minority of photons are absorbed photoelectrically in both cases (much more so for the ceramics). The majority of cases for the evaluated scintillator materials listed in Tables 3.3-3.6 involve either purely photoelectric interactions, single or double Compton scatter events (more heavily weighted towards photoelectric and single-Compton events in the case of the ceramic materials).

The high loading factor of LaF_3:Ce-PS makes it the best-performing nanocomposite in terms of the proportion of photoelectric interactions. All of the transparent ceramic materials offer performance which is much more similar to the benchmark performance of the LSO than even the LaF_3:Ce-PS nanocomposite, both in terms of the total proportion of events detected and the percentage of these interactions which are photoelectric. In terms of scattering composition, LuAG:Pr has characteristics most similar to the LSO with only $\sim$4% difference in the number of photoelectric interactions recorded, though GLuGAG:Ce and GAGG:Ce still have respectable numbers ($\sim$10% and 13% difference respectively). GYGAG:Ce has less then half the photoelectric count of LSO, again due to a lower density. Interestingly, LuAG:Pr has the highest percentage of events detected at 1 cm scintillator

thickness, but as this is increased to 2 cm all other ceramics have a higher rate of increase (with GLuGAG:Ce increasing the most).

Multi-interaction events degrade the accuracy of the fitting algorithm, which assumes all energy is deposited at a single location. Fortunately, since the fraction of photon energy deposited is related to the angle of scatter, the magnitude of this degradation is smaller than at first may appear. If the first interaction deposits a large fraction of the gamma photon's energy, the angle of scatter will also be large - but the reduction in photon energy reduces the mean free path length of the scattered photon compared to the initial 511 keV gamma photon. Therefore, the resulting optical photon distribution will be dominated by the first point of interaction, with only a minor impact on the position of the endpoint of the line of response. If the amount of energy deposited at the first point of interaction is small, the angle of scatter will also be small. Therefore, subsequent interactions will follow a trajectory through the scintillator which is not very different to that of the original photon. If the next interaction is photoelectric (which is now more likely as the photon energy has been reduced), the resulting line of response will only deviate slightly from the true line of response (and will be slightly pulled back towards the true LOR by whatever energy was deposited at the first point of interaction). The largest error introduced by such events will be in the radial direction (depth). The intermediate case - an initial or secondary Compton scatter which deposits some non-trivial amount of energy, followed by further multiple Compton interactions, results in the largest errors in the placement of the line of response.

3.3.3 Spatial error

The mean and median errors in each dimension of the estimated positions of gamma photon interactions (where the ground truth is defined as the first point of interaction in the scintillator slab) together with their interquartile ranges (central 50% of errors) and standard deviations are summarised in Tables 3.7-3.10, for scintillator thicknesses of 1 cm, 2 cm, the HVL thickness and optimal thickness, respectively. These results include all event types (both pure photoelectric events and events including one or more Compton scatters). Monocrystalline LSO has again been used as a benchmark scintillator for comparison with each of the materials.

Scintillator	Photoelectric/Compton scatter composition						Total events detected (%)
	PE (%)	C1 (%)	C2 (%)	C3 (%)	C4 (%)	C5+ (%)	
Gd_2O_3 PVT	1.58	87.98	9.37	0.91	0.14	0.02	11.70
$LaBr_3$:Ce PS	2.47	84.04	11.63	1.62	0.22	0.02	15.17
LaF_3:Ce OA	6.55	76.00	14.46	2.51	0.41	0.07	20.81
LaF_3:Ce PS	9.75	71.17	15.41	3.05	0.56	0.07	27.02
YAG:Ce PS	1.89	78.67	15.47	3.23	0.62	0.12	21.68
GAGG:Ce	26.95	53.13	15.73	3.51	0.57	0.11	45.12
GLuGAG:Ce	24.34	55.14	16.33	3.55	0.57	0.07	48.50
GYGAG:Ce	14.08	61.98	18.33	4.57	0.86	0.17	40.14
LuAG:Pr	30.09	52.47	14.16	2.84	0.39	0.04	49.79
LSO	34.85	49.36	13.11	2.34	0.31	0.03	55.57

Table 3.3: Distribution of photoelectric and Compton-scattered interactions for a 1 cm thick scintillator slab, expressed as the percentage of events of this type which are detected out of the total number of primary photons incident on the detector. CN denotes N Compton scatter interactions prior to either final photoelectric absorption or escape from the scintillator. Monocrystalline LSO is also included as a reference benchmark.

Scintillator	Photoelectric/Compton scatter composition						Total events detected (%)
	PE (%)	C1 (%)	C2 (%)	C3 (%)	C4 (%)	C5+ (%)	
Gd_2O_3 PVT	1.34	83.90	12.56	1.90	0.22	0.07	21.29
$LaBr_3$:Ce PS	1.11	83.99	12.72	1.84	0.28	0.06	22.08
LaF_3:Ce OA	3.32	77.77	15.57	2.76	0.49	0.10	26.09
LaF_3:Ce PS	9.84	64.15	19.87	4.96	0.95	0.23	45.09
YAG:Ce PS	1.86	71.85	19.76	4.95	1.21	0.37	37.82
GAGG:Ce	30.41	41.14	20.79	6.15	1.28	0.23	41.18
GLuGAG:Ce	24.33	49.12	19.88	5.39	1.06	0.21	71.59
GYGAG:Ce	14.14	54.38	22.75	6.84	1.56	0.34	62.65
LuAG:Pr	31.20	45.98	17.76	4.18	0.77	0.10	67.50
LSO	34.86	45.00	15.95	3.53	0.58	0.08	78.85

Table 3.4: Distribution of photoelectric and Compton-scattered interactions for a 2 cm thick scintillator slab.

Scintillator	Photoelectric/Compton scatter composition						Total events detected (%)	Thickness HVL (mm)
	PE (%)	C1 (%)	C2 (%)	C3 (%)	C4 (%)	C5+ (%)		
Gd_2O_3 PVT	0.92	77.69	17.49	3.19	0.60	0.12	39.56	53.10
$LaBr_3$:Ce PS	0.14	79.93	16.77	2.65	0.43	0.08	40.30	64.40
LaF_3:Ce OA	0.28	81.42	15.45	2.47	0.33	0.05	26.92	64.90
LaF_3:Ce PS	10.06	63.76	19.99	4.98	1.01	0.21	46.25	21.20
YAG:Ce PS	1.11	71.55	20.98	4.92	1.10	0.33	43.26	39.50
GAGG:Ce	26.91	53.04	15.80	3.52	0.64	0.08	46.64	10.60
GLuGAG:Ce	24.34	55.14	16.33	3.55	0.57	0.07	48.50	10.00
GYGAG:Ce	14.39	58.90	20.06	5.30	1.11	0.24	48.52	13.10
LuAG:Pr	30.13	52.73	14.02	2.74	0.34	0.04	47.30	9.29
LSO	35.14	50.59	12.04	1.96	0.26	0.02	48.10	7.99

Table 3.5: Distribution of photoelectric and Compton-scattered interactions for a scintillator thickness equal to the half value layer for each scintillator material.

Scintillator	Photoelectric/Compton scatter composition						Total events detected (%)	Thickness Opt. (mm)
	PE (%)	C1 (%)	C2 (%)	C3 (%)	C4 (%)	C5+ (%)		
Gd_2O_3 PVT	0.79	76.72	18.51	3.24	0.60	0.14	43.23	62.61
$LaBr_3$:Ce PS	0.32	79.76	16.65	2.71	0.45	0.10	40.57	53.78
LaF_3:Ce OA	1.20	79.75	15.83	2.64	0.48	0.09	30.84	32.66
LaF_3:Ce PS	11.51	55.73	23.62	7.08	1.69	0.38	60.21	42.60
YAG:Ce PS	1.64	68.30	22.42	5.76	1.42	0.46	50.43	49.79
GAGG:Ce	22.17	52.64	19.34	4.81	0.90	0.14	53.03	13.98
GLuGAG:Ce	25.15	46.13	21.07	6.17	1.23	0.24	78.38	27.54
GYGAG:Ce	15.30	47.61	25.34	8.83	2.36	0.56	79.72	42.63
LuAG:Pr	31.61	46.25	17.24	4.08	0.71	0.11	67.61	18.96

Table 3.6: Distribution of photoelectric and Compton-scattered interactions for a scintillator thickness equal to the optimal thickness for each scintillator material.

Scintillator	x error (mm)				y error (mm)				z error (mm)				Total error (mm)			
	Med.	Mean	IQR	SD	Med.	Mean	IQR	SD	Med.	Mean	IQR	SD	Med.	Mean	IQR	SD
Gd_2O_3 PVT	1×10^{-5}	4×10^{-3}	0.1	0.5	-3×10^{-4}	-3×10^{-3}	0.1	0.5	-1×10^{-1}	-6×10^{-2}	0.2	0.7	0.2	0.4	0.2	0.9
$LaBr_3$:Ce PS	-5×10^{-4}	-7×10^{-4}	0.1	0.6	-3×10^{-4}	-3×10^{-4}	0.1	0.6	-1×10^{-1}	-4×10^{-2}	0.1	0.9	0.2	0.5	0.2	1.2
LaF_3:Ce OA	1×10^{-3}	3×10^{-3}	0.3	1.0	-2×10^{-3}	-6×10^{-4}	0.3	1.0	-1×10^{-1}	6×10^{-2}	0.4	1.3	0.5	1.0	0.6	1.6
LaF_3:Ce PS	-6×10^{-4}	-4×10^{-3}	0.3	1.0	8×10^{-4}	3×10^{-3}	0.3	1.0	-1×10^{-1}	3×10^{-2}	0.3	1.2	0.4	0.9	0.5	1.6
YAG:Ce PS	-4×10^{-4}	-6×10^{-3}	0.1	0.6	4×10^{-5}	-2×10^{-3}	0.1	0.6	-1×10^{-1}	6×10^{-3}	0.4	1.0	0.3	0.6	0.3	1.2
GAGG:Ce	2×10^{-5}	-4×10^{-3}	0.2	1.2	-3×10^{-4}	-2×10^{-3}	0.2	1.2	-1×10^{-1}	1×10^{-1}	0.4	1.4	0.3	1.0	0.6	1.9
GLuGAG:Ce	-2×10^{-4}	-2×10^{-3}	0.1	1.1	-4×10^{-4}	2×10^{-3}	0.1	1.1	-1×10^{-1}	2×10^{-1}	0.4	1.4	0.3	1.0	0.6	1.8
GYGAG:Ce	-7×10^{-5}	1×10^{-3}	0.1	1.1	-8×10^{-5}	1×10^{-3}	0.1	1.0	-1×10^{-1}	1×10^{-1}	0.3	1.3	0.3	0.9	0.5	1.8
LuAG:Pr	2×10^{-5}	4×10^{-3}	0.2	1.1	-5×10^{-4}	4×10^{-4}	0.2	1.1	-1×10^{-1}	2×10^{-1}	0.5	1.4	0.4	1.1	0.7	1.8
LSO	-3×10^{-4}	-7×10^{-3}	0.1	1.1	9×10^{-5}	1×10^{-3}	0.1	1.1	-1×10^{-1}	3×10^{-1}	0.4	1.4	0.3	1.0	0.7	1.8

Table 3.7: Mean and median errors in the estimation of the point of interaction within a 1 cm thick scintillator slab, in each dimension and overall. Standard deviations and interquartile ranges (the spread of the middle 50% of errors) are also listed.

The mean and median errors in each dimension are very small for all materials at thicknesses of 1 and 2 cm, indicating that the localisation method introduces minimal bias. The spread of error in x and y is smaller than the depth dimension, with the difference becoming much more pronounced for thicker scintillator slabs due to two factors: the increased probability of multiple interactions, and increased Rayleigh scattering and attenuation prior to optical photon detection.

Figure 3.7 and 3.8 show a set of scatterplots showing position estimation distribution error in each dimension and in total as a function of depth for optimised slabs of LaF_3:Ce-PS and GLuGAG:Ce, respectively (Note that the threshold of the colour scale is only approximately $\sim$10 % of the absolute maximum bin count, to show greater detail in lower count bins). For these materials, the majority of errors in each dimension are within $< \pm 1$ mm, with the majority of interactions occurring within 5 mm of the detector surfaces. The outliers mostly corresponding to multi-interaction events. The greatest lateral error (x and y) occurs around the half-thickness of the scintillator slab, since this point is the furthest from either front or back detector and therefore most susceptible to scatter and attenuation. The higher density of the ceramic results in a larger fraction of events being detected close to the front surface compared to the nanocomposite, resulting in an overall superior performance for this material. These general observations also apply to the other nanocomposite and ceramic scintillators.

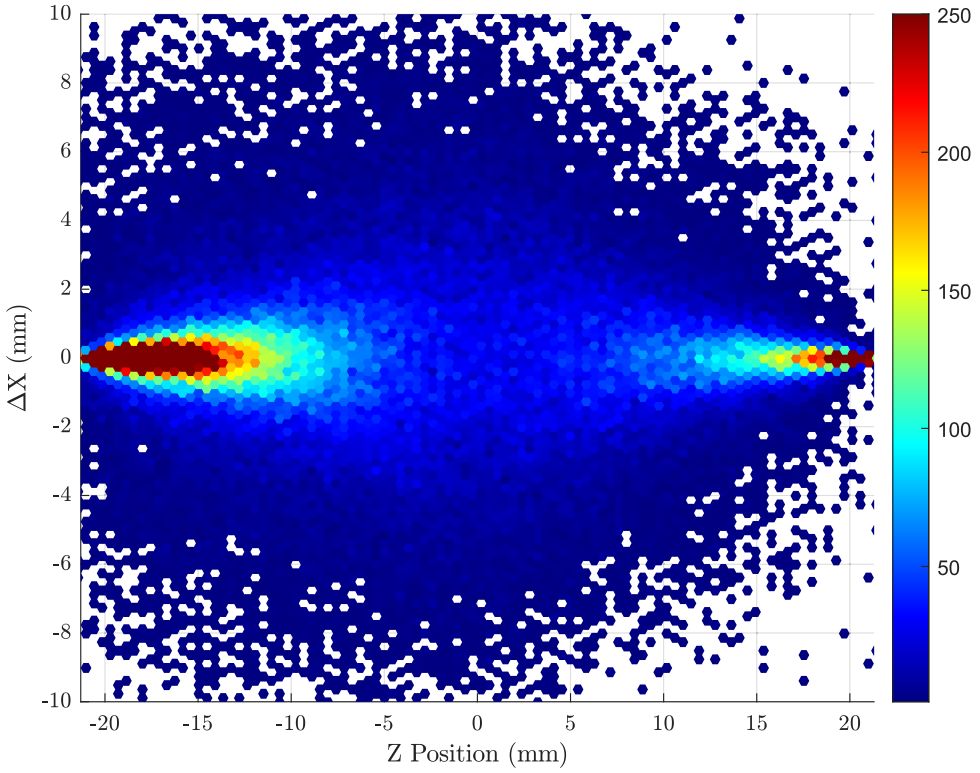

(a) x

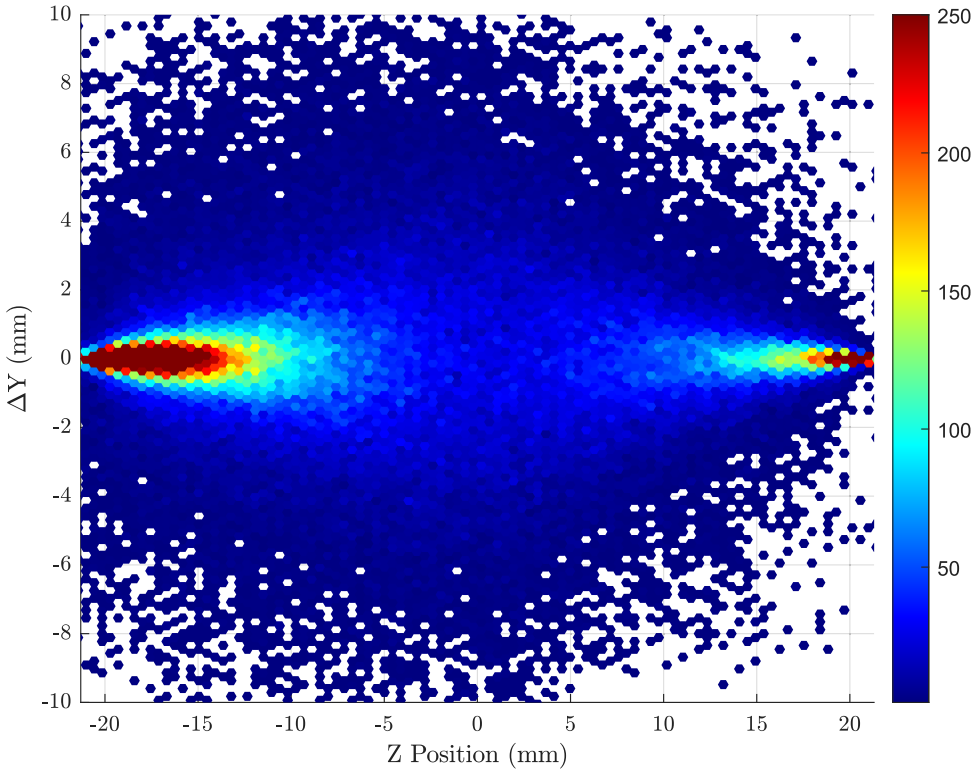

(b) y

Figure 3.7: Distributions of error in position estimation in each dimension as a function of depth for a LaF_3:Ce-PS monolithic scintillation detector, at the calculated optimal thickness. Figure 3.7(d) shows the distribution of total Euclidean error.

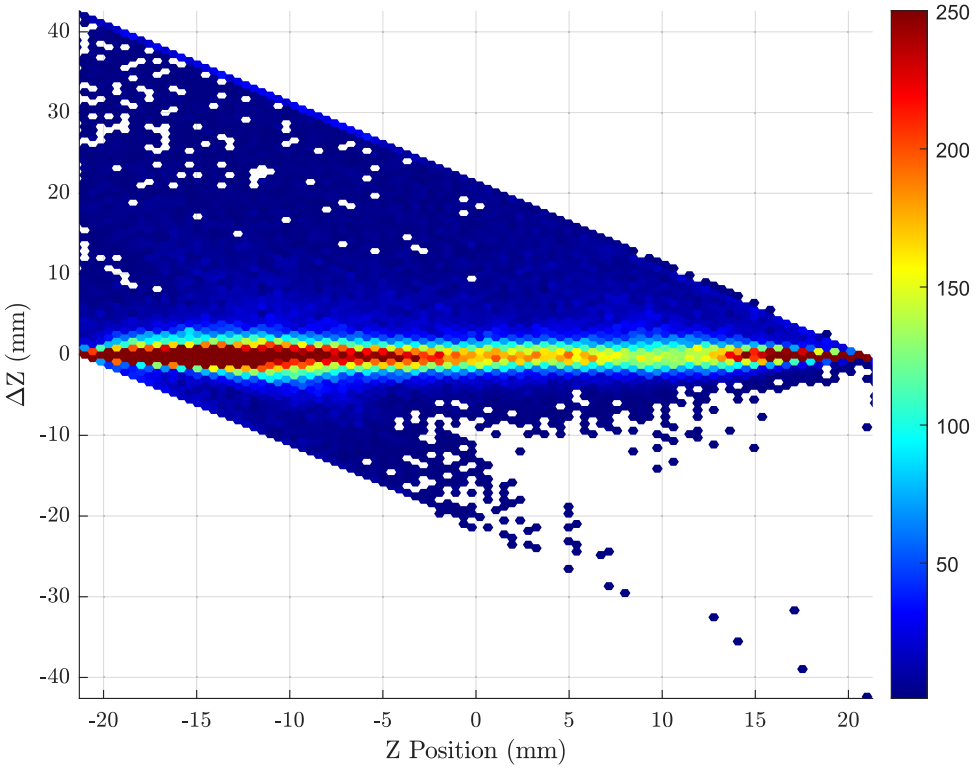

(c) z (depth)

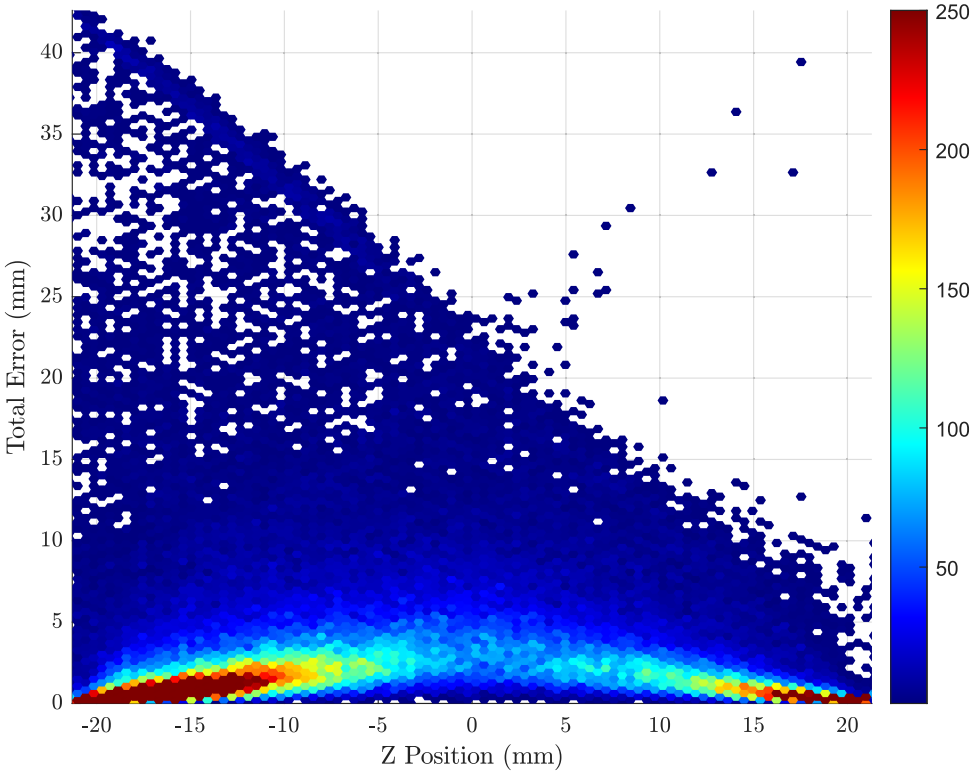

(d) Total error

Figure 3.7: (Continued from previous page).

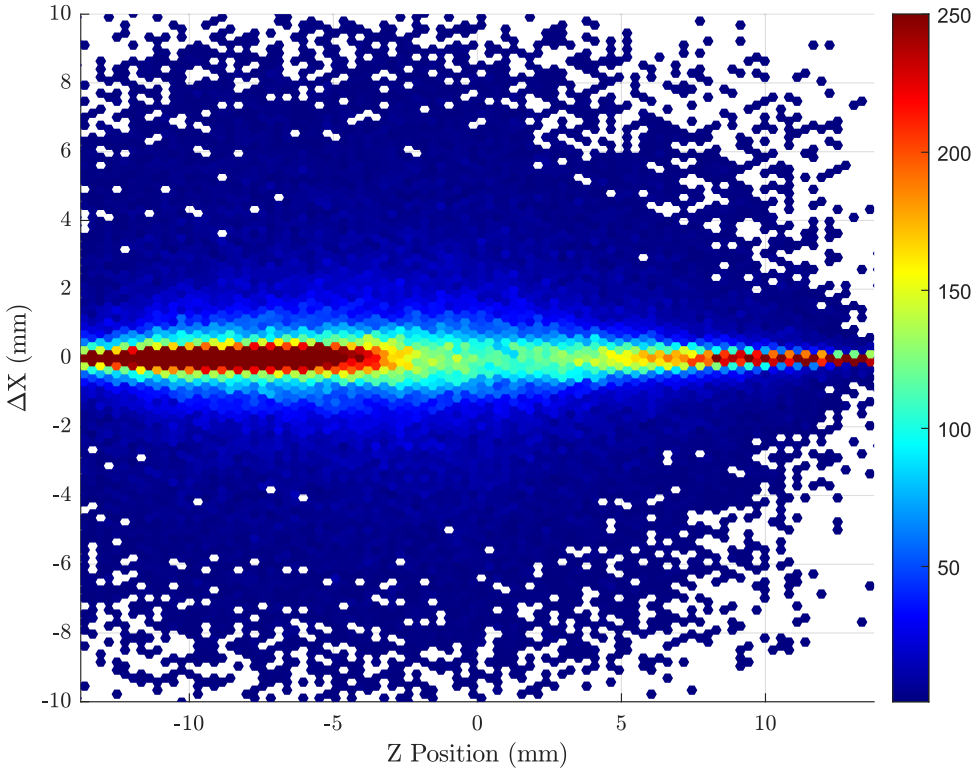

(a) x

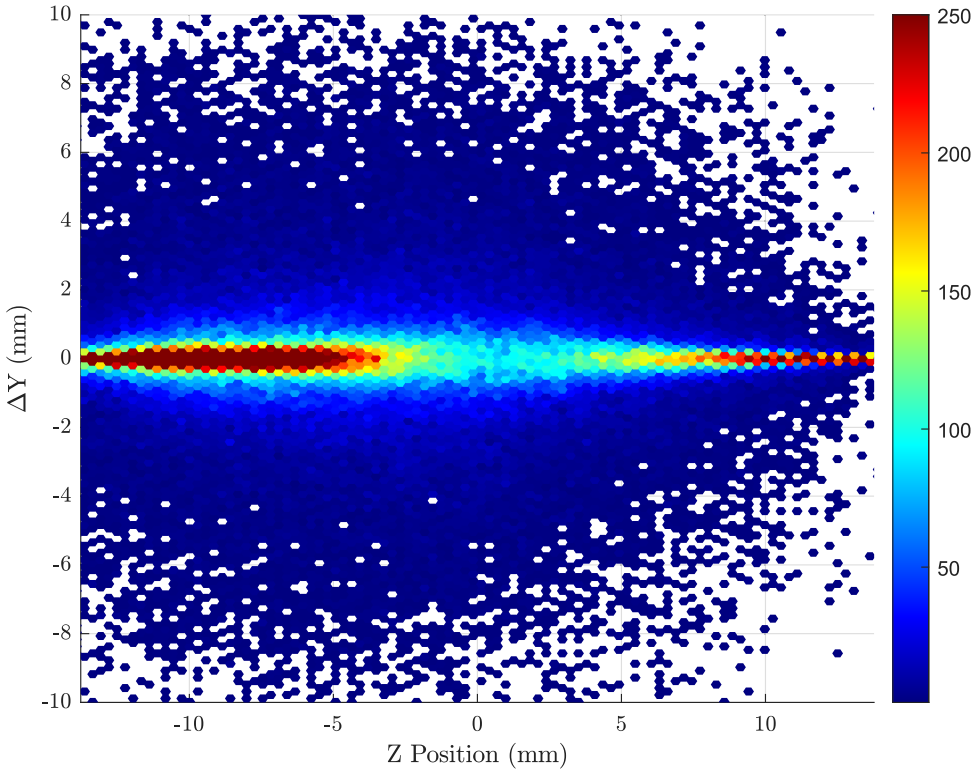

(b) y

Figure 3.8: Distributions of error in position estimation in each dimension as a function of depth for a GLuGAG:Ce monolithic scintillation detector, at the calculated optimal thickness. Figure 3.7(d) shows the distribution of total Euclidean error.

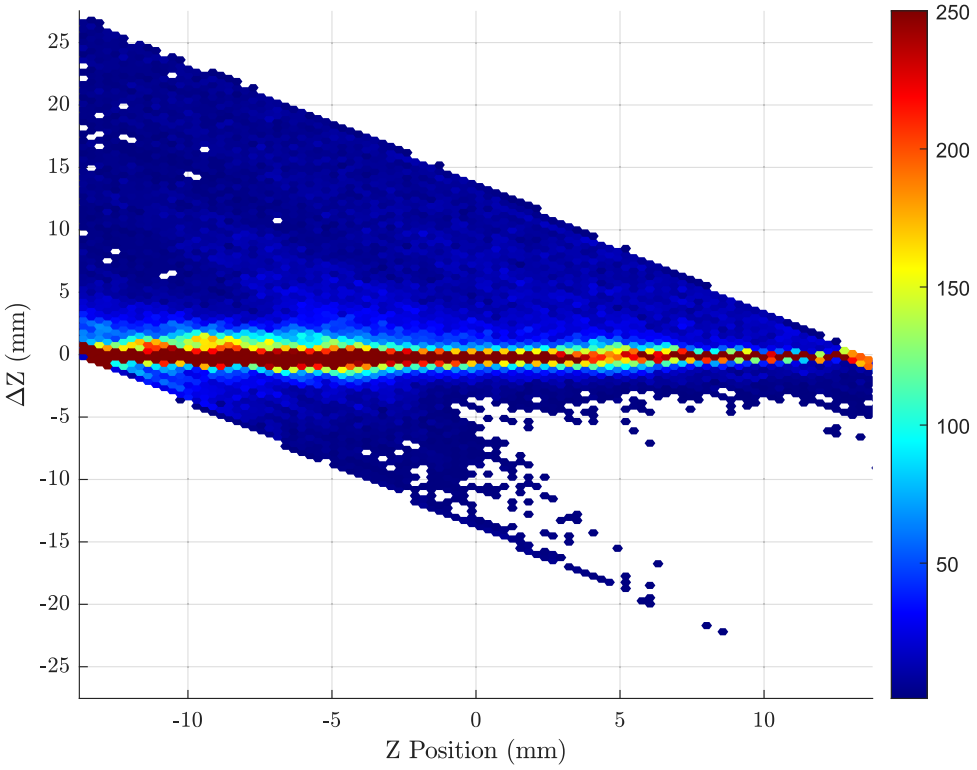

(c) z (depth)

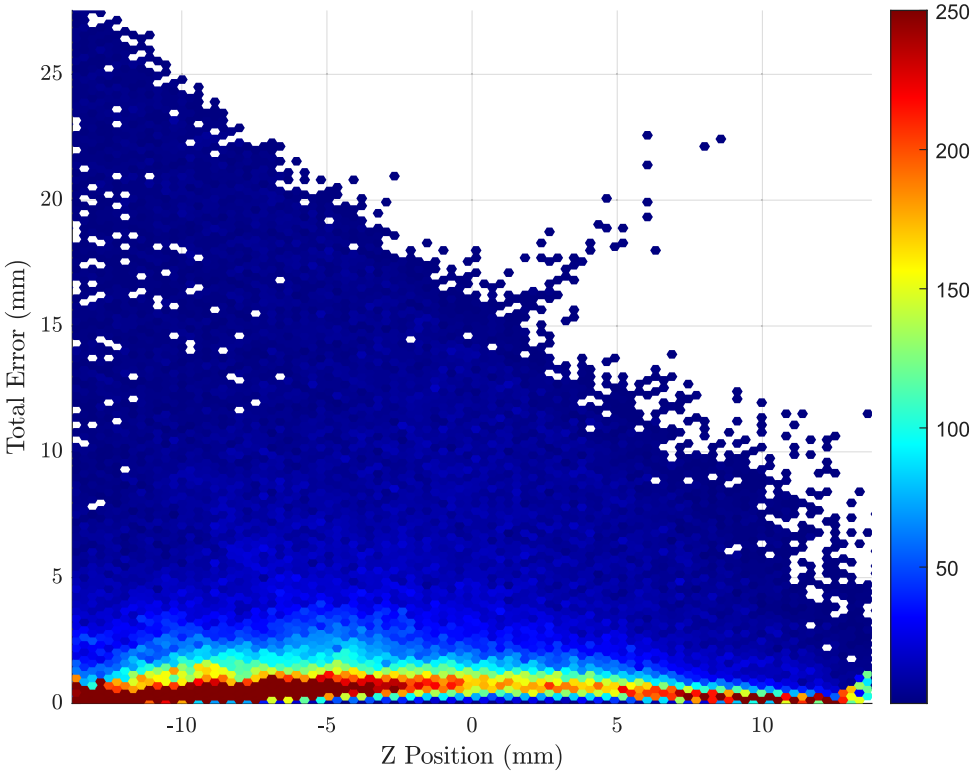

(d) Total error

Figure 3.8: (Continued from previous page).

Scintillator	x error (mm)				y error (mm)				z error (mm)				Total error (mm)			
	Med.	Mean	IQR	SD	Med.	Mean	IQR	SD	Med.	Mean	IQR	SD	Med.	Mean	IQR	SD
Gd_2O_3 PVT	4×10^{-4}	4×10^{-3}	0.3	0.8	-4×10^{-4}	-6×10^{-3}	0.3	0.8	-1×10^{-1}	0.3	0.3	2.3	0.4	1.0	0.4	2.4
$LaBr_3$:Ce PS	-2×10^{-4}	1×10^{-3}	0.2	0.8	-1×10^{-4}	-7×10^{-4}	0.2	0.8	-1×10^{-1}	0.2	0.2	1.9	0.3	0.8	0.3	2.1
LaF_3:Ce OA	-2×10^{-4}	-7×10^{-3}	0.6	1.4	2×10^{-3}	-2×10^{-3}	0.6	1.4	-1×10^{-1}	0.5	0.8	2.8	0.9	1.8	1.3	2.9
LaF_3:Ce PS	-1×10^{-4}	2×10^{-3}	0.6	1.4	-2×10^{-5}	-2×10^{-3}	0.6	1.4	-9×10^{-2}	0.6	0.7	3.0	0.8	1.9	1.4	3.1
YAG:Ce PS	1×10^{-5}	4×10^{-3}	0.3	1.0	-1×10^{-3}	-1×10^{-3}	0.3	1.0	-1×10^{-1}	0.4	0.9	2.4	0.6	1.4	1.0	2.5
GAGG:Ce	6×10^{-4}	1×10^{-2}	0.8	1.9	9×10^{-4}	1×10^{-2}	0.8	1.9	-2×10^{-2}	0.8	1.4	3.4	1.2	2.7	2.7	3.5
GLuGAG:Ce	6×10^{-5}	-4×10^{-3}	0.4	1.5	-3×10^{-4}	-4×10^{-3}	0.4	1.5	-9×10^{-2}	0.7	0.8	2.8	0.6	1.9	1.6	3.1
GYGAG:Ce	2×10^{-4}	3×10^{-3}	0.3	1.5	-1×10^{-4}	-4×10^{-3}	0.3	1.5	-1×10^{-1}	0.7	0.6	2.9	0.4	1.8	1.6	3.2
LuAG:Pr	-7×10^{-4}	-3×10^{-3}	0.5	1.5	-4×10^{-4}	3×10^{-4}	0.5	1.5	-6×10^{-2}	0.7	1.0	2.7	0.8	2.0	1.6	2.9
LSO	1×10^{-4}	2×10^{-3}	0.3	1.4	2×10^{-4}	-2×10^{-3}	0.3	1.4	-9×10^{-2}	0.9	0.8	2.8	0.4	1.8	1.6	3.0

Table 3.8: Mean and median errors in the estimation of the point of interaction within a 2 cm thick scintillator slab, in each dimension and overall. Standard deviations and interquartile ranges (the spread of the middle 50% of errors) are also listed.

Scintillator	x error (mm)				y error (mm)				z error (mm)				Total error (mm)			
	Med.	Mean	IQR	SD	Med.	Mean	IQR	SD	Med.	Mean	IQR	SD	Med.	Mean	IQR	SD
Gd_2O_3 PVT	-1×10^{-3}	-2×10^{-3}	0.8	1.7	2×10^{-3}	1×10^{-2}	0.8	1.7	-1×10^{-1}	1.3	0.9	6.8	1.2	2.9	2.1	6.7
$LaBr_3$:Ce PS	4×10^{-4}	2×10^{-3}	0.7	1.7	5×10^{-4}	-2×10^{-3}	0.7	1.7	-1×10^{-1}	0.5	0.9	4.1	1.2	2.3	2.3	4.2
LaF_3:Ce OA	4×10^{-3}	6×10^{-3}	2.3	3.3	3×10^{-4}	4×10^{-3}	2.4	3.3	-4×10^{-2}	1.7	4.0	9.3	4.3	6.8	7.1	8.1
LaF_3:Ce PS	-1×10^{-3}	5×10^{-4}	0.6	1.5	-2×10^{-4}	-6×10^{-3}	0.6	1.5	-1×10^{-1}	0.7	0.8	3.3	0.8	2.1	1.5	3.4
YAG:Ce PS	-7×10^{-4}	-2×10^{-3}	0.6	1.4	-8×10^{-4}	-2×10^{-3}	0.6	1.4	-1×10^{-1}	0.6	0.8	4.0	0.9	2.0	1.4	4.0
GAGG:Ce	-2×10^{-6}	5×10^{-4}	0.2	1.2	-2×10^{-4}	-2×10^{-4}	0.2	1.2	-1×10^{-1}	0.2	0.4	1.5	0.3	1.1	0.7	1.9
GLuGAG:Ce	-2×10^{-4}	-2×10^{-3}	0.1	1.1	-4×10^{-4}	2×10^{-3}	0.1	1.1	-1×10^{-1}	0.2	0.4	1.4	0.3	1.0	0.6	1.8
GYGAG:Ce	-1×10^{-4}	-3×10^{-4}	0.2	1.2	2×10^{-4}	-6×10^{-3}	0.2	1.2	-1×10^{-1}	0.3	0.4	1.8	0.3	1.2	0.8	2.2
LuAG:Pr	5×10^{-4}	2×10^{-3}	0.2	1.0	-3×10^{-4}	1×10^{-3}	0.2	1.0	-1×10^{-1}	0.1	0.5	1.3	0.4	1.0	0.6	1.7
LSO	3×10^{-4}	3×10^{-3}	0.1	1.0	-1×10^{-4}	-8×10^{-4}	0.1	1.0	-1×10^{-1}	0.1	0.3	1.1	0.3	0.9	0.5	1.5

Table 3.9: Mean and median errors in the estimation of the point of interaction within a scintillator slab with thickness equal to the half-value layer (HVL), in each dimension and overall. Standard deviations and interquartile ranges (the spread of the middle 50% of errors) are also listed.

Scintillator	x error (mm)				y error (mm)				z error (mm)				Total error (mm)			
	Med.	Mean	IQR	SD	Med.	Mean	IQR	SD	Med.	Mean	IQR	SD	Med.	Mean	IQR	SD
Gd_2O_3 PVT	2×10^{-4}	7×10^{-3}	1.0	2.0	1×10^{-3}	6×10^{-3}	1.0	2.0	-1×10^{-1}	0.9	1.2	5.7	1.6	3.0	2.9	5.7
$LaBr_3$:Ce PS	-6×10^{-4}	-4×10^{-3}	0.7	1.6	4×10^{-4}	5×10^{-3}	0.7	1.6	-1×10^{-1}	0.4	1.0	3.7	1.2	2.3	2.3	3.7
LaF_3:Ce OA	-2×10^{-3}	2×10^{-4}	1.2	2.1	9×10^{-4}	2×10^{-3}	1.2	2.1	-7×10^{-2}	0.7	1.5	4.2	1.7	3.1	2.7	4.2
LaF_3:Ce PS	1×10^{-3}	1×10^{-3}	1.2	2.1	4×10^{-6}	4×10^{-5}	1.2	2.1	-7×10^{-2}	1.1	1.6	5.3	1.8	3.4	3.2	5.1
YAG:Ce PS	2×10^{-4}	6×10^{-3}	0.8	1.7	-7×10^{-4}	-6×10^{-3}	0.8	1.7	-1×10^{-1}	0.7	1.1	4.5	1.3	2.7	2.4	4.4
GAGG:Ce	4×10^{-4}	2×10^{-3}	0.3	1.4	-6×10^{-4}	-8×10^{-3}	0.3	1.4	-1×10^{-1}	0.3	0.6	2.0	0.5	1.5	1.1	2.4
GLuGAG:Ce	-2×10^{-4}	-1×10^{-3}	0.6	1.7	5×10^{-4}	-1×10^{-3}	0.5	1.7	-7×10^{-2}	1.0	1.1	3.6	0.8	2.3	2.0	3.7
GYGAG:Ce	-1×10^{-4}	-4×10^{-3}	0.7	1.8	-7×10^{-5}	2×10^{-3}	0.7	1.8	-8×10^{-2}	1.5	1.3	5.8	1.0	3.2	2.8	5.7
LuAG:Pr	9×10^{-4}	8×10^{-3}	0.5	1.5	7×10^{-4}	-9×10^{-5}	0.5	1.4	-6×10^{-2}	0.6	0.9	2.6	0.7	1.9	1.5	2.8

Table 3.10: Mean and median errors in the estimation of the point of interaction within a scintillator slab with thickness equal to the calculated optimal thickness, in each dimension and overall. Standard deviations and interquartile ranges (the spread of the middle 50% of errors) are also listed.

3.4 Conclusion

A general method for optimising the thickness of a monolithic scintillator detector via Monte Carlo simulations was developed and demonstrated with a range of nanocomposite and transparent ceramic scintillator materials. The optimisation criterion which is maximised is the probability of detecting and localising the position of gamma interactions with the scintillator volume to within a specified margin of error. The method enables the optimisation process to be tuned according to the required minimum acceptable localisation accuracy, and can be adapted to a variety of monolithic scintillator localisation techniques beyond those discussed in this work. Importantly, this work demonstrates that for monolithic scintillator materials, determination of 'optimal thickness' is more complex than considering only the linear attenuation coefficient of the scintillator material.

Of the evaluated materials, the most promising nanocomposite scintillator for PET is LaF_3:Ce-polystyrene, which is largely due the high loading factor which can be achieved without compromising its optical transparency at the scintillation emission wavelength. The best-performing ceramic scintillator was GLuGAG:Ce due to its higher optical transmittivity relative to the other evaluated ceramics; however, due to their high density, the ceramic scintillators all offered a higher achievable sensitivity compared to the nanocomposites. Each of these materials could potentially be used in PET applications, however the trade-off between sensitivity and

the accuracy in determining the endpoints of the lines of response is different in each case and must also be balanced against the cost of each material.

The developed technique can be extended to any new nanocomposite or ceramic scintillator material, provided the physical and optical properties can be accurately measured.

The following Chapters of this Thesis explore the application of these materials in the construction of a continuous monolithic cylindrical shell PET scanner, and the development of the line of response endpoint localisation and coincidence detection algorithms needed to acquire meaningful projection data and reconstruct an image.

Chapter 4

Localisation of the Lines of Response in a Continuous Cylindrical Shell PET Scanner

4.1 Introduction

One of the challenges in increasing the availability of clinical and research positron emission tomography (PET) is the substantial capital expense of the scanner. A major fraction of these costs is due to the scintillator crystals, used for the detection of coincident 511 keV photons emitted from the annihilation of positrons within the subject [5, 6, 4]. There is growing interest in new scintillator materials with less-stringent manufacturing requirements and greater geometric flexibility compared to the discrete monocrystalline materials presently used in PET. These materials include the polycrystalline transparent ceramic garnets and scintillator-polymer nanocomposites discussed in Chapter 3. The lower cost of these materials must be weighed against their typically inferior physical properties, which include lower optical transmittivity and, in the case of nanocomposites, lower density and effective atomic number. A PET scanner utilising such scintillator materials therefore offers a fundamentally different set of engineering trade-offs compared to those employing monocrystalline scintillators.

The geometric flexibility offered by these new materials includes the potential for creating novel structures and geometries which would be difficult or expensive

to fabricate with monocrystalline materials. One such geometry is a continuous monolithic cylindrical shell, with photodetectors tiled both on the inner and outer surface. In a monolithic scintillator, the optical photon distribution detected on one or both sides of the scintillating layer is used to estimate the 3D location of the endpoints of the line of response (LOR) between both halves of a coincidence pair. Compared to a traditional pixellated detector design, a continuous cylindrical shell offers numerous advantages, including uniform gap-free angular coverage around the centre of the field of view (FOV) and intrinsically high-resolution estimation of depth of interaction (DOI), which is expected to provide good uniformity of spatial resolution.

Several authors have proposed methods for localising the point of interaction of a gamma photon in a planar scintillator slab, including error-minimising optimisation approaches based on an analytic model of photon distribution within the slab, and neural network-based approaches which are adept at dealing with the non-uniformity of scintillator response near the edge of the slab [63, 77, 78]. In this Chapter, we describe an adaptation of one of these methods to a continuous cylindrical shell PET scanner, and present the first quantitative simulation results for a continuous-shell cylindrical PET system. The methods proposed in Chapter 3 are applied to optimise the thicknesses of the best-performing ceramic and nanocomposite scintillator materials identified in that Chapter - GLuGAG:Ce and LaF_3:Ce-PS, respectively. A Monte Carlo simulation model of a cylindrical-shell PET scanner utilising these materials is then created in the Geant4 Application for Tomographic Emission (GATE; [160, 161]), in which a point source is positioned at three different locations within the scanner field of view (at the centre of scanner, at an offset of 50% of the inner radius and at an offset of 75% of the inner radius). The error in locating the endpoints of the line of response in the radial, axial, tangential dimensions, together with the overall error and the error in placement of the line of response itself, is evaluated.

Section 4.2 briefly describes the optimisation method used to determine the scanner geometry; it also discusses the localisation technique and lists the key properties of the simulated scintillator materials. Section 4.3 presents the results of the simulation study, with the key implications discussed in Section 4.4. Section 4.5 sum-

Material	GLuGAG:Ce	LaF_3:Ce-PS
Type	Ceramic	Nanocomposite
Peak λ (nm)	550	334
Primary decay time (ns)	84	30
Light yield (ph/MeV)	48200	4500
ρ	6.9	3.47
$n(\lambda_p)$	1.92	1.65*

Table 4.1: Scintillator properties. All values are taken from the literature unless indicated with *, in which case the parameter was theoretically calculated based on other previously-published material properties [110, 111, 112].

marises the findings from this work and their implications for the image acquisition and reconstruction work to be performed in the subsequent Chapters.

4.2 Materials and methods

4.2.1 Materials

The scintillator materials used in this study have been identified as excellent candidates for monolithic scintillators in PET systems due to their combination of good optical transmittivity at the emission wavelength and moderate to high linear attenuation coefficient for 511 keV gamma photons. GLuGAG:Ce is a synthetic garnet, which can be fabricated as a polycrystalline ceramic with similar physical properties to the crystalline form [167]. LaF_3:Ce-PS is one of the best-performing nanocomposite scintillator materials, since the close match between the refractive index of its constituent components results in good optical transmittivity at its emission wavelength, even with a high loading factor (50% in this work) [104, 168, 169]. The key optical properties of the scintillators are listed in Table 4.1.

4.2.2 Optimisation of scanner geometry

The scanner is designed for small animal or human head imaging. To allow the simulated photodetectors to be tiled to the inner and outer surface of the scintillating

Material	GLuGAG:Ce	LaF_3:Ce-PS
Length (mm)	296	296
Inner radius r_{in}(mm)	233.3145	233.3145
Inner faces	104	104
Inner face width (mm)	14.442	14.442
Outer radius r_{out} (mm)	258.2385	276.1885
Average thickness (mm)	24.919	42.874
Outer faces	116	124
Outer face width	14.2	14.2
Detection efficiency (%)	67.82	48.83
Photoelectric fraction (%)	24.33	9.95

Table 4.2: Scanner dimensions and expected detection efficiency

cylinder, the cylindrical shell is approximated as the difference between two polygonal prisms. The geometry is shown in Figure 4.1. Each inner and outer face can accommodate an axial row of 21 square pixellated silicon detectors, each comprising a 14×14 array of 1 mm×1 mm pixels.

For each material, the specific thickness of the scintillator shell has been determined using an approach which maximises the efficiency of accurate endpoint localisation. In summary, a small number of Monte Carlo simulations are conducted in which 511 keV photons were directed perpendicularly into a slab of the material under test, and localisation was performed by parametrically fitting an analytic model of the expected optical photon distribution to the observed photon maps (a simpler version of the method described in Section 4.2.3). The probability of estimating the location of the point of interaction to within a threshold of 5 mm was computed (total error, in three dimensions), and a polynomial fit performed to identify the thickness which will maximise this probability.

For GLuGAG:Ce and LaF_3:Ce-PS, this resulted in the average thicknesses listed in Table 4.2; the expected detection efficiency (expressed as a percentage of incident normal 511 keV gamma photons) and percentage of interactions which are purely photoelectric for the given dimensions is also listed.

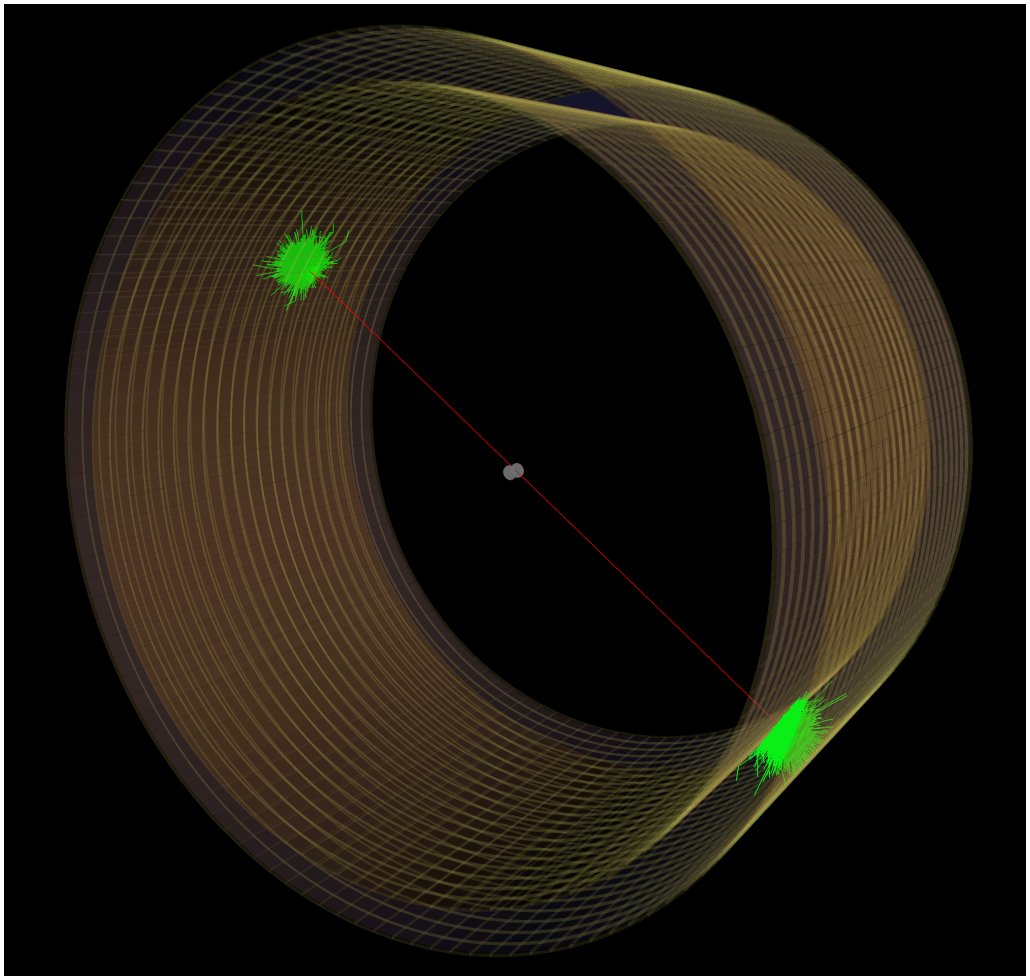

Figure 4.1: Geometry of the simulated scanners (GLuGAG:Ce is shown; the approximated cylindrical shell is slightly thicker with LaF_3:Ce-PS. Optical photons are shown in green.

4.2.3 Localisation method

The localisation technique described in this work assumes all optical photon events can be detected and timestamped with temporal resolution of the order of 10 ns or better (easily achievable with digital SiPM detectors [170]), and logged in list mode. The localisation method is a cylindrical-shell extension to the methods introduced by Li et al., which aim to fit an analytic model of optical photon distribution within a planar monolithic scintillator slab to the observed optical photon distribution [63, 77].

A suspected gamma interaction with the scintillator is considered for coincidence analysis if a spatio-temporal cluster of more than N_{min} optical photons are detected on both the inner and outer detector arrays ($N_{min} \geq 10$ is sufficient for satisfactory localisation for almost all detected events) within a timing window τ_d (inner and outer peak photon detection should be almost simultaneous; τ_d may be of the order of half the decay time constant of the scintillator). A potential coincidence is two double-sided clusters occurring within a coincidence timing window $\tau_c > \tau_d$ (in this work, τ_d is set to the primary decay time constant of the scintillator, which is much greater than the maximum cross-scanner time of flight of approximately 1.84 ns). Figure 4.1 shows a typical detected coincidence and the resulting showers of optical photons.

The polar coordinates $(r_{out}, \theta_{out}, z)$ of each pixel on the outer surface are converted to Cartesian coordinates $(r_{out}, y = r_{out}\theta_{out}, z)$, where z and y are the axial and tangential displacements, respectively. The polar coordinates of each pixel on the inner surface are similarly converted to Cartesian coordinates, with $y = r_{out}\theta_{in}$ scaled using the outer radius such that the cylindrical shell is 'unrolled' into a rectangular slab in which both inner and outer surfaces have the same tangential width. The computed y and z coordinates of each pixel are stored in a pair of look-up tables.

A coincidence event will appear as two approximately simultaneous clusters of non-zero pixels, with cluster peaks separated by a minimum angle related to the maximum size of the subject. Clusters will not physically overlap unless the coincidence is due to randoms or scattering of an emitted photon; such cases are rejected. The localisation algorithm requires the cylindrical shell to be cut in two places to

separate each half of the coincidence pair. To do this, the inner and outer pixel arrays are first added together, then summed axially, resulting in a one-dimensional signal featuring two peaks. The higher of the two peaks is first located, and then excised from the 1D signal based on the maximum theoretical radius of the cluster. Then, the smaller peak is located in the residual signal. The unrolled pixel maps are then cut half-way between the smaller and larger angles separating these two peaks, resulting in a pair of two-sided images of the pixel clusters. The size of each of these arrays is reduced by shrinking a rectangular region around each cluster, excluding all contiguous rectangular regions with no optical photon detections from the arrays. The remaining cluster regions and their corresponding axial and tangential coordinates are then passed to the fitting algorithm.

Analytic expressions for the expected inner and outer photon distributions are given by the attenuated Cauchy distributions in (3.1) and (3.2), respectively.

$$J_o(z_d, y_d) = \frac{J_0(r_{out} - r_s)\Delta z \Delta y e^{-\frac{\sqrt{(z_s - z_d)^2 + (y_s - y_d)^2 + (r_{out} - r_s)^2}}{\lambda}}}{4\pi \left((z_s - z_d)^2 + (y_s - y_d)^2 + (r_{out} - r_s)^2\right)^{\frac{3}{2}}} \tag{4.1}$$

$$J_i(z_d, y_d) = \frac{J_0(r_s - r_{in})\Delta z \Delta y e^{-\frac{\sqrt{(z_s - z_d)^2 + (y_s - y_d)^2 + (r_s - r_{in})^2}}{\lambda}}}{4\pi \left((z_s - z_d)^2 + (y_s - y_d)^2 + (r_s - r_{in})^2\right)^{\frac{3}{2}}} \tag{4.2}$$

where y_d and z_d are the a point on the respective detector surfaces, the point of scintillation is (r_s, y_s, z_s), Δz and Δy are the (scaled) pixel dimensions, J_0 is the number of emitted scintillation photons, λ is the radiation attenuation length, and r_{in} and r_{out} are the inner and outer radius of the cylindrical shell, respectively.

To account for total internal reflection within the scintillator slab[1], J_b is set to zero anywhere outside a circle of radius

$$R_o = z_s \frac{n_{mm}}{n_s^2 - n_{mm}^2} \tag{4.3}$$

where n_{mm} is the refractive index of Meltmount (the optical coupling compound) and n_s is the scintillator's refractive index. Similarly J_f is set to zero outside of a circle of radius

[1]Only a small minority of scintillation photons are internally reflected; most of these are absorbed by the scintillator before reaching a detector.

$$R_i = (T - z_s)\frac{n_{mm}}{n_s^2 - n_{mm}^2} \tag{4.4}$$

The estimated coordinates of the endpoints of the line of response are calculated by jointly minimising the error between (3.1) and (3.2) and the observed photon map using the Levenberg-Marquardt algorithm. Finally, the endpoints of the LOR are converted back into cylindrical coordinates and logged.

Energy windowing is straightforward with this detection model as the number of optical photons emitted by the interaction may be estimated from the observed photon maps; detection of scattered photons may be discarded if this number is below an arbitrary threshold.

4.2.4 Simulation

GATE 8.1/Geant4 10.4p02 are used for all simulations. GATE has been built with full optical photon tracking turned on. Optical properties of the materials are based on values obtained from the literature [167, 168, 169, 104]. The scintillator ring is optically coupled to the array of ideal silicon photodetectors with Meltmount optical epoxy [164].

A cylindrical ^{18}F source (radius = 1 mm, height = 2 mm) is placed at the centre of the field of view, encased in a cylindrical water phantom (radius = 5 mm, height = 10 mm). Simulations have been conducted with 50000 decays for each scintillator material. For each interaction with the scintillator, the true coordinates of the endpoints were logged together with the coordinates of each interaction of the optical photons with the photodetectors. The optical photon coordinates are rebinned to 1 mm×1 mm pixels and processed with the coincidence logic, and the error in each dimension together with the overall error for accuracy of endpoint estimation computed. Finally, the distance of the LOR from the centre of the true source location is computed for each detected coincidence.

4.3 Results

The accuracy of LOR endpoint localisation is visualised using hexagonal-cell heatmaps of the error scatterplots in the radial, axial and rotational dimensions, plus an overall

Error	Source Centre			Source 50% Inner Radius			Source 75% Inner Radius		
	Q1	Median	Q3	Q1	Median	Q3	Q1	Median	Q3
$\Delta\theta$ (Deg.)	-0.15	-0.0082	0.13	-0.14	-0.0063	0.13	-0.15	-0.0074	0.13
Δr (mm)	-1.66	-0.40	0.02	-1.66	-0.40	0.02	-1.64	-0.40	0.02
Δz (mm)	-0.29	0.0009	0.29	-0.29	0.0003	0.29	-0.29	-0.00001	0.27
Δd (mm)	0.68	1.40	3.44	0.68	1.42	3.62	0.68	1.42	3.91
ΔLoR (mm)	0.60	1.27	4.17	0.71	1.48	5.18	0.77	1.62	6.59

Table 4.3: GLuGAG:Ce error statistics summary

error and the error in placement of the line of response, as a function of increasing depth of interaction for both evaluated materials.

4.3.1 GLuGAG:Ce

Figure 4.2(a), 4.2(b) and 4.2(c) illustrate the errors in each dimension for GLuGAG:Ce. Overall error in endpoint location is shown in Figure 4.2(d), while Figure 4.2(e) shows the minimum distance from the estimated LOR to the nominal centre of the radioactive source. Figure 4.2(f) shows three slices through the LOR error heat-map (Figure 4.2(e)); the first at 10% of the scintillator thickness (measured from the inner detector surface, R $\approx$ 237.8 mm), the second at 50% of the scintillator thickness (R $\approx$ 247.8 mm) and the third at 90% of the scintillator thickness (R $\approx$ 257.8 mm). A Gaussian function has been fitted to each slice to indicate the accuracy of the LOR at these positions. The Gaussians have been offset in Y to account for baseline noise. The R position on the horizontal axis of each figure is the absolute radial distance from the centre of the scanner; the range shown in the plots begins at the inner detector surface and ends at the outer detector surface. Results for the offset source are very similar.

A summary of the statistical range of the errors (first quartile, median and third quartile) for GLuGAG:Ce with the source at the centre and at radial offsets of 50% and 75% of the inner radius of the scintillator shell are presented in Table 4.3. An additional metric is introduced in the table; total spatial error (Δd).

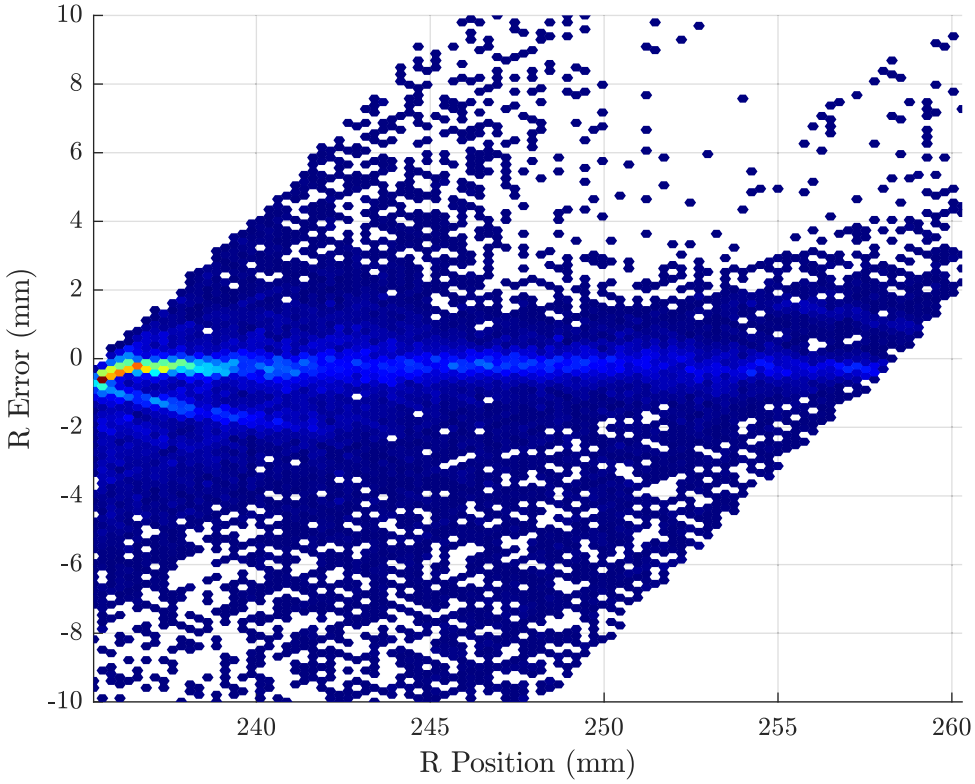

(a) GLuGAG:Ce: radial endpoint error vs. depth of interaction

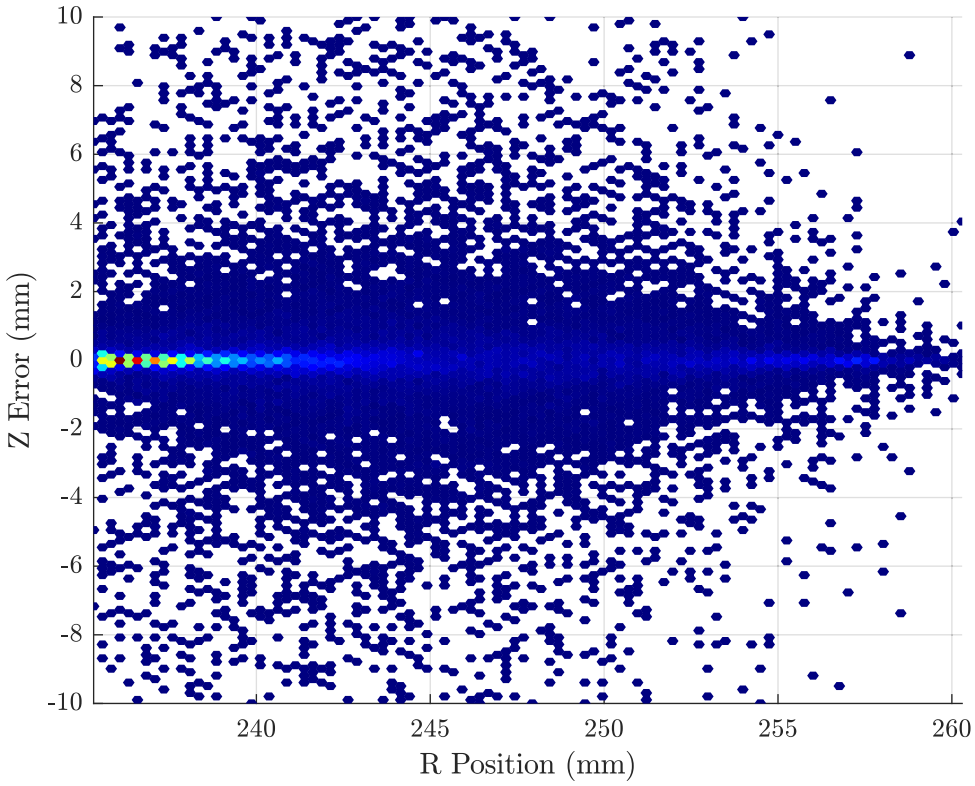

(b) GLuGAG:Ce: axial endpoint error vs. depth of interaction

Figure 4.2: GLuGAG:Ce: endpoint errors in each dimension and overall vs depth of penetration.

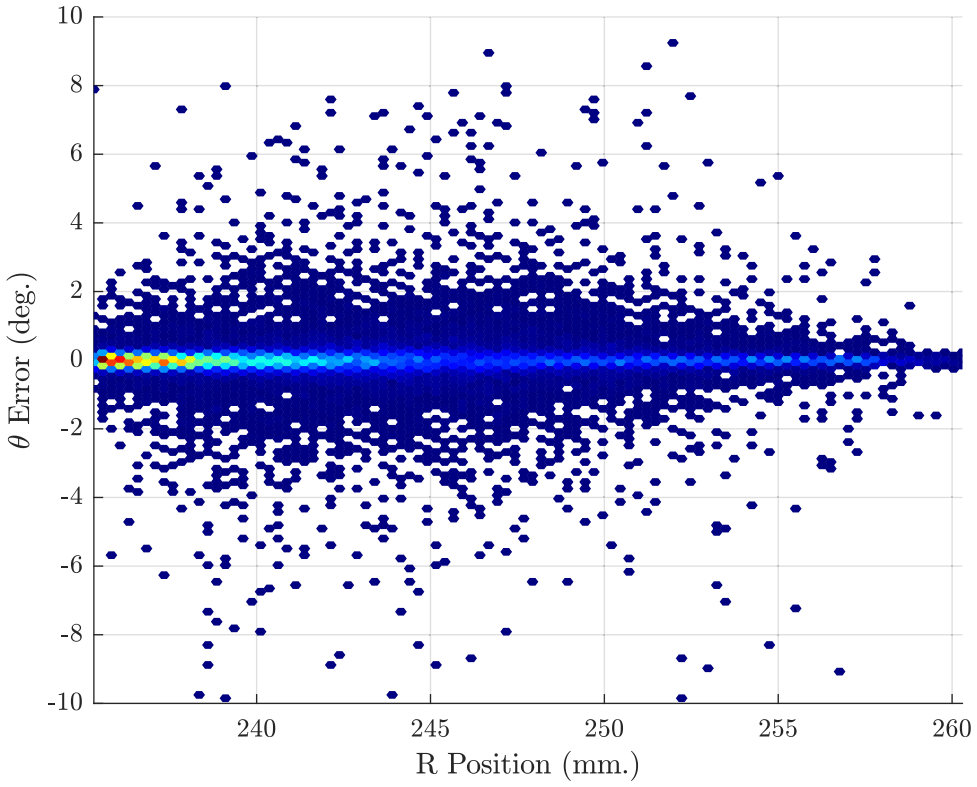

(c) GLuGAG:Ce: rotational endpoint error vs depth of interaction

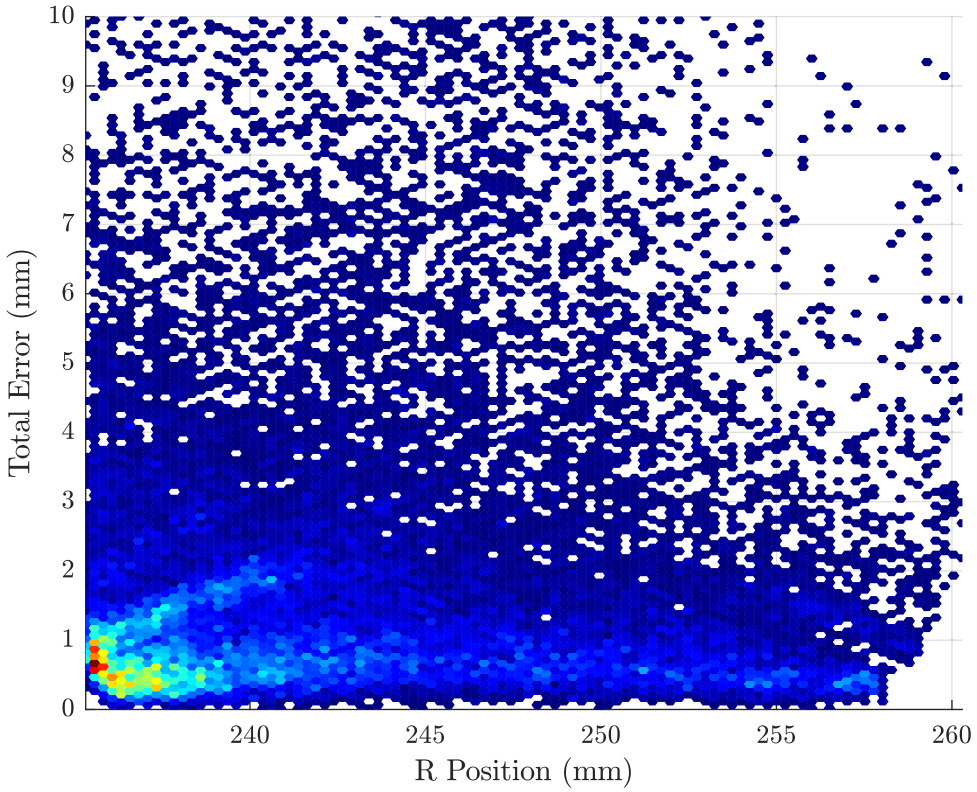

(d) GLuGAG:Ce: total endpoint error vs depth of interaction

Figure 4.2: (Continued from previous page).

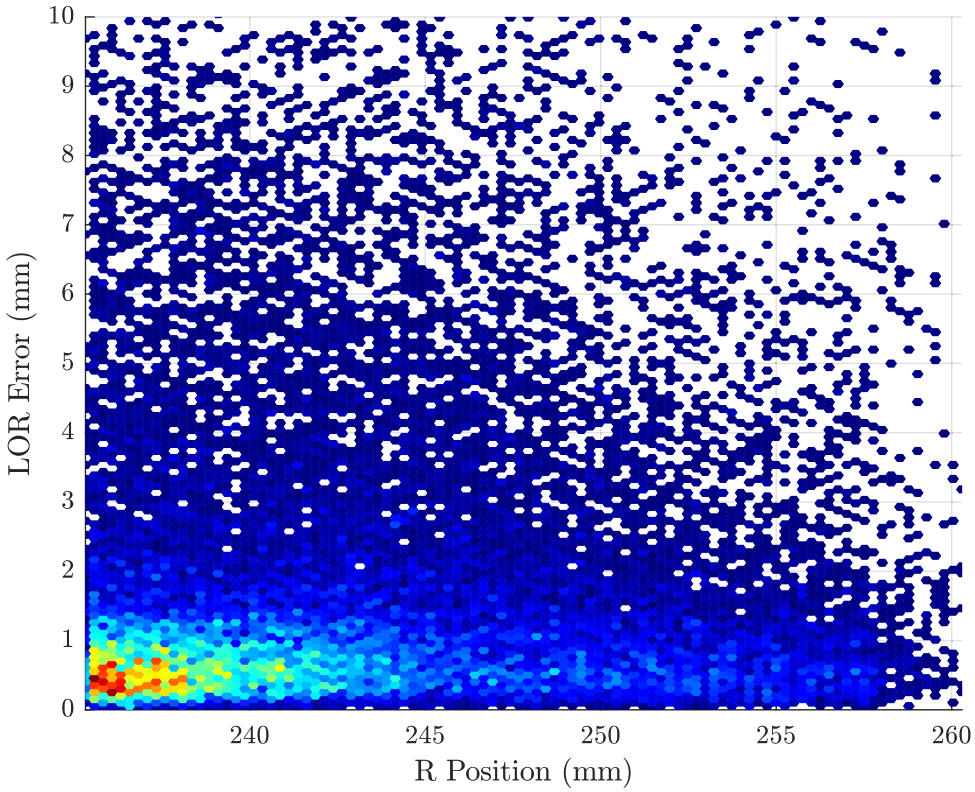

(e) GLuGAG:Ce: LoR offset error vs depth of interaction

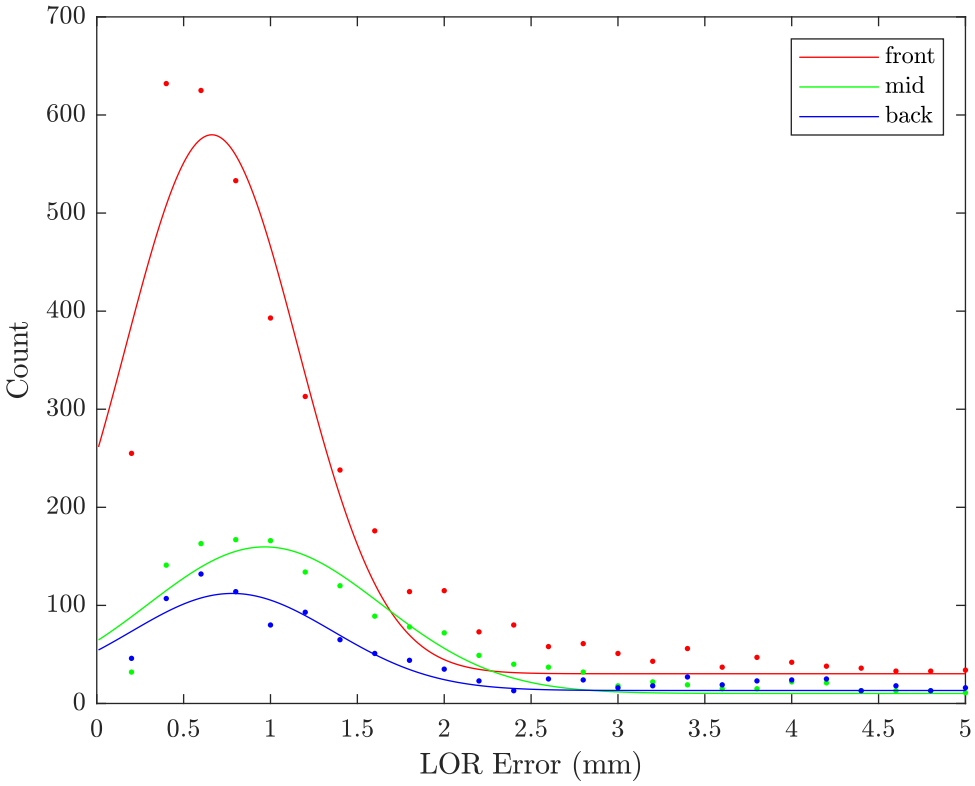

(f) GLuGAG:Ce: LOR error along histogram slices

Figure 4.2: (Continued from previous page). Figure 4.2(f) shows 3 slices through the heatmap in Figure 4.2(e). A Gaussian has been fit to each.

Error	Source Centre			Source 50% Inner Radius			Source 75% Inner Radius		
	Q1	Median	Q3	Q1	Median	Q3	Q1	Median	Q3
$\Delta\theta$ (Deg.)	-0.26	-0.0019	0.25	-0.27	-0.0038	0.26	-0.28	-0.0029	0.27
Δr (mm)	-3.07	0.33	1.22	-3.06	-0.33	1.21	-2.84	-0.31	1.11
Δz (mm)	-0.92	-0.0050	0.93	-0.93	0.0038	0.99	-1.02	-0.0030	0.97
Δd (mm)	1.35	3.52	8.33	1.34	3.57	9.26	1.23	3.49	10.87
ΔLoR (mm)	1.22	3.12	11.78	1.43	3.59	16.60	1.50	4.13	24.10

Table 4.4: LaF_3:Ce-PS error statistics summary

4.3.2 LaF_3:Ce-PS

Figure 4.3(a), 4.3(b) and 4.3(c) illustrate the error in radial, axial and rotational dimensions for LaF_3:Ce-PS. Overall error in endpoint location is shown in Figure 4.3(d), while Figure 4.3(e) shows the minimum distance from the estimated LOR to the nominal centre of the radioactive source. Figure 4.3(f) shows three slices through the LOR error heat-map (Figure 4.3(e)); the first at 10% of the scintillator thickness (measured from the inner detector surface, R $\approx$ 239.4 mm), the second at 50% of the scintillator thickness (R $\approx$ 256.7 mm) and the third at 90% of the scintillator thickness (R $\approx$ 274.5 mm). A Gaussian function has been fitted to each slice to indicate the accuracy of the LOR at these positions. The Gaussians have been offset in Y to account for baseline noise. The R position on the horizontal axis of each figure is the absolute radial distance from the centre of the scanner; the range shown in the plots begins at the inner detector surface and ends at the outer detector surface. Again, results for the offset source location are very similar.

A summary of the statistical range of the errors (first quartile, median and third quartile) for LaF_3:Ce-PS with the source in the same three positions (centre and offset at 50% and 75% of inner shell diameter) is presented in Table 4.4. Statistics for the total spatial error (Δd) have also been included.

4.3.3 Detector Sensitivity and Detection Accuracy

Table 4.5 presents a summary of the overall sensitivity of the two designs for each source position, expressed as a fraction of positron annihilations which result in detection of both endpoints, and the fraction of estimated endpoint locations which

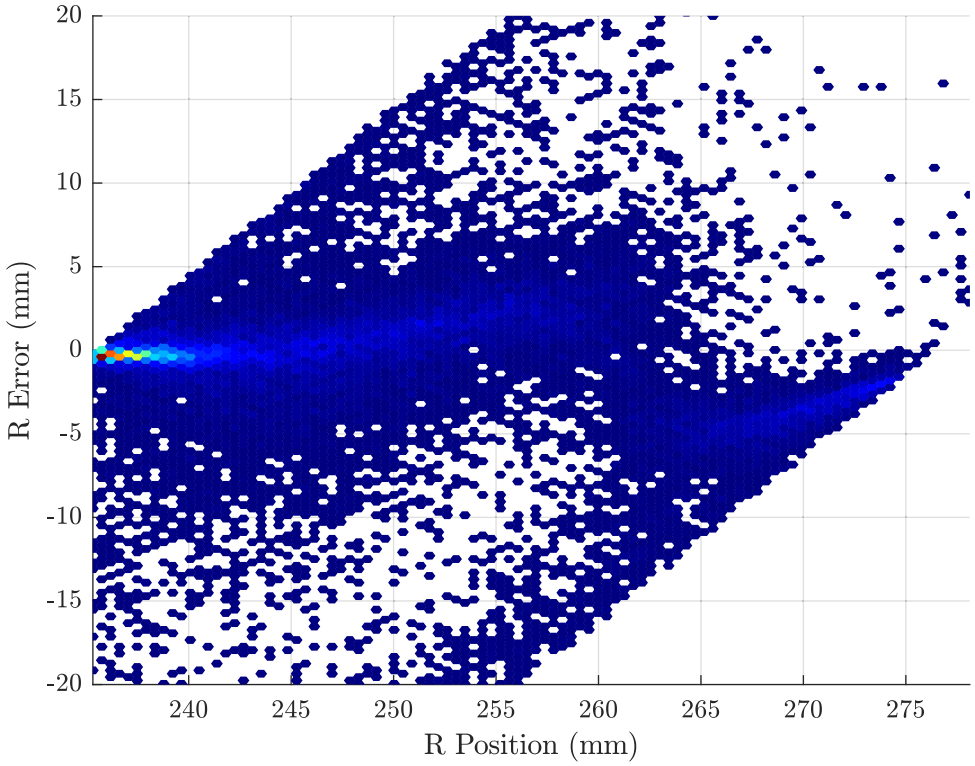

(a) LaF_3:Ce-PS: radial endpoint error vs depth of interaction

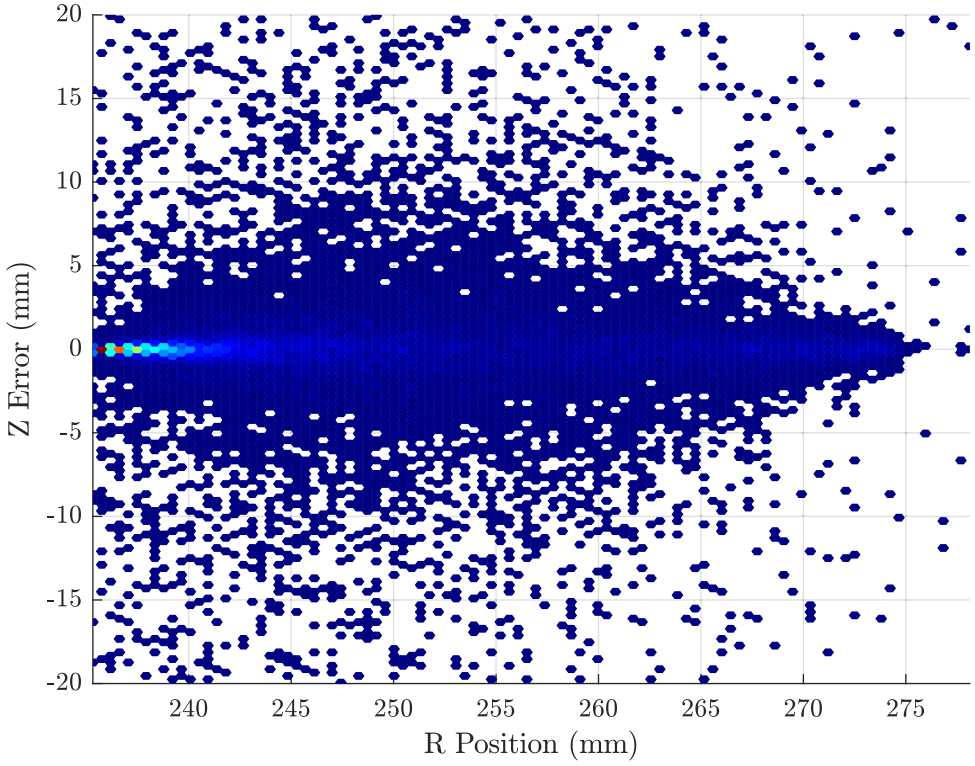

(b) LaF_3:Ce-PS: axial endpoint error vs depth of interaction

Figure 4.3: LaF_3:Ce-PS: endpoint errors in each dimension and overall vs. depth of penetration.

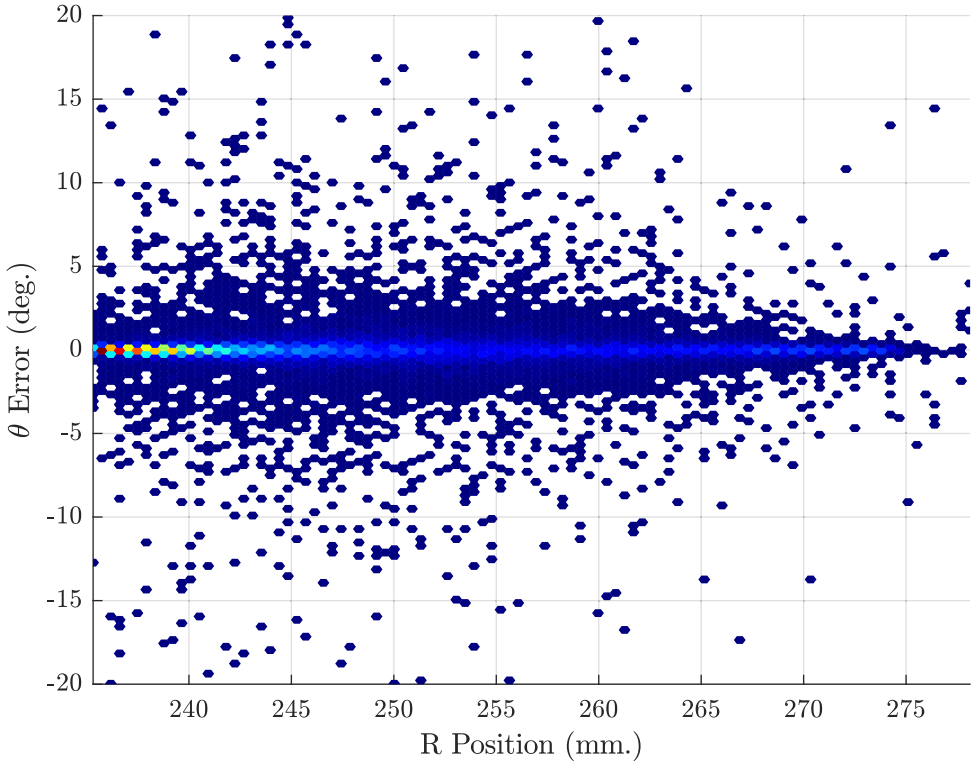

(c) LaF_3:Ce-PS: rotational endpoint error vs depth of interaction

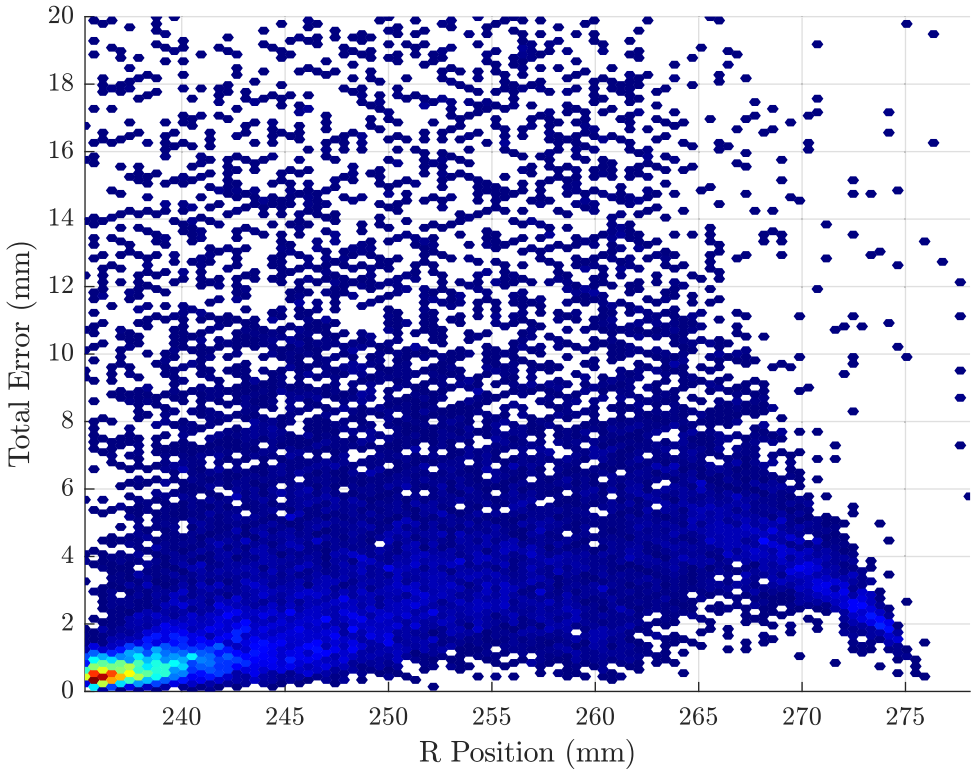

(d) LaF_3:Ce-PS: Total endpoint error vs depth of interaction

Figure 4.3: (Continued from previous page).

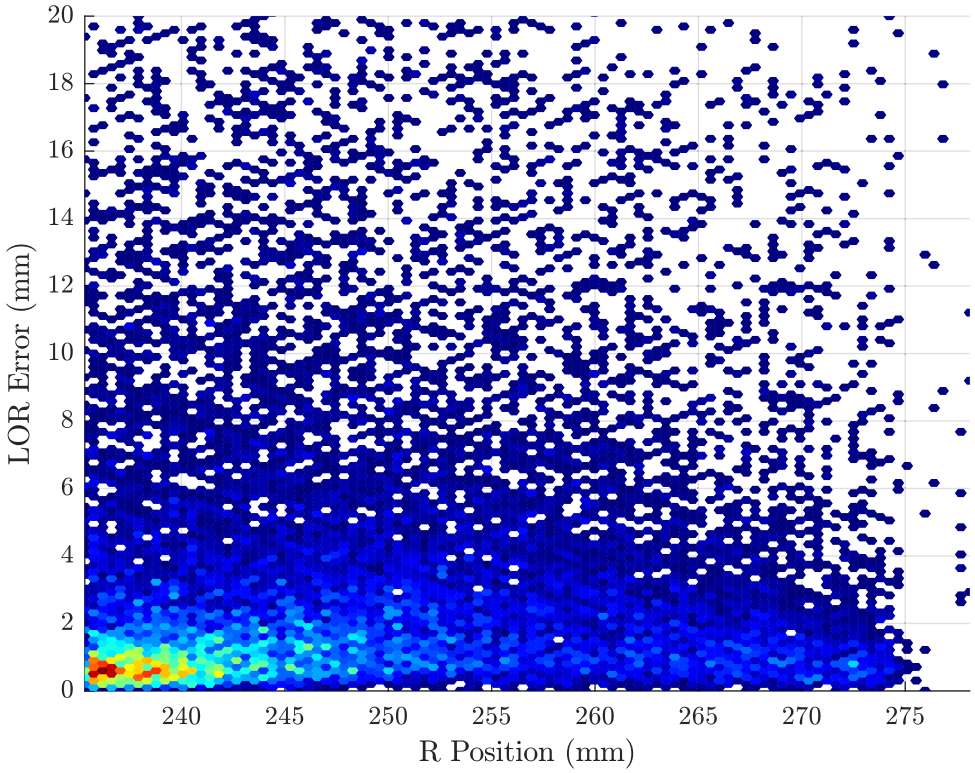

(e) LaF_3:Ce-PS: LOR offset error vs depth of penetration

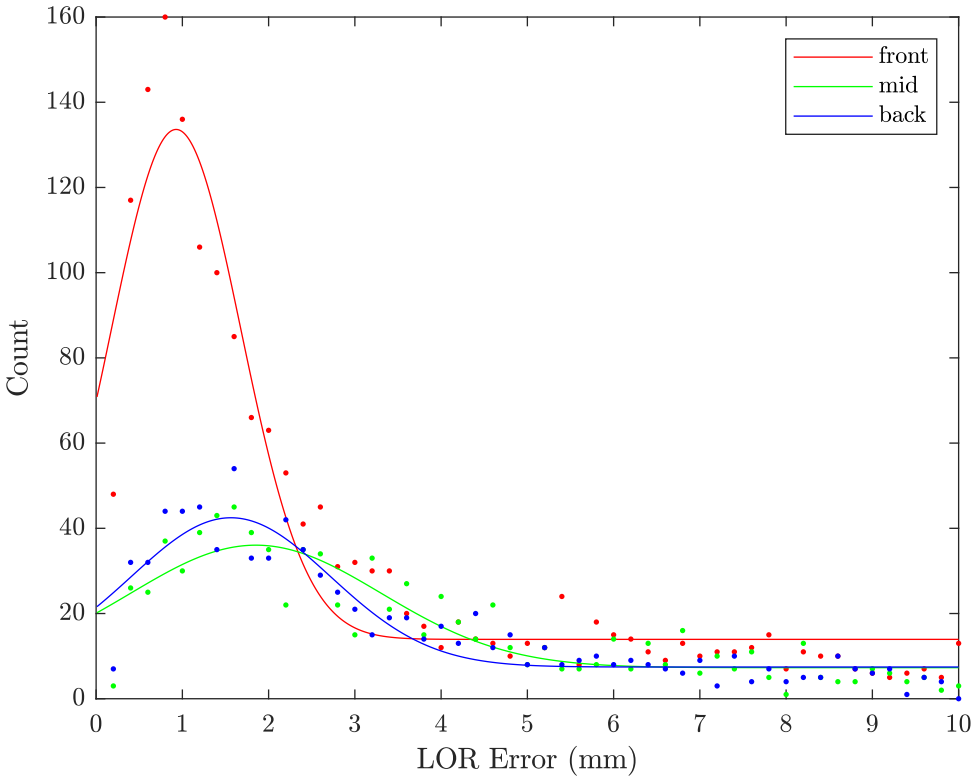

(f) LaF_3:Ce-PS: LOR error along histogram slices

Figure 4.3: (Continued from previous page). Figure 4.3(f) shows 3 slices through the heatmap in Figure 4.3(e). A Gaussian has been fit to each.

	Sensitivity (%)		% < 2 mm error		% < 5 mm error	
Source Location	GLuGAG:Ce	LaF3:Ce-PS	GLuGAG:Ce	LaF3:Ce-PS	GLuGAG:Ce	LaF3:Ce-PS
Centre	29	22	61.82	33.49	81.60	62.14
50% Inner Radius	28	21	61.22	33.62	80.43	60.91
75% Inner Radius	31	24	60.71	35.07	78.79	60.14

Table 4.5: Fractions of decays yielding usable LORs (both detected as a percentage of total positron annihilations) and accuracy of detected endpoints as a percentage detected within the specified error margin.

are within 2 mm and 5 mm of their ground-truth locations.

4.4 Discussion

There are some significant differences between the behaviour of the two scintillator materials. The high density of GLuGAG:Ce results in most photons stopping within the first 10 mm of the material, whereas they penetrate more deeply into the LaF_3:Ce-PS. For LaF_3:Ce-PS, all error metrics have quite long-tailed distributions - particularly in the ΔLOR metric. The largest component of the error is from the estimation of the depth of interaction in the cylindrical shell. Despite this, more than half of the detected gamma photons are localised in depth to an accuracy of better than 5 mm for LaF_3:Ce-PS and 2 mm for GLuGAG:Ce (Table 4.5) (with little variation with respect to radial offset), which compares well with most depth-of-interaction capable PET scanners of this size. Overall sensitivity of both variants of scanner geometry is very high, due to a combination of high scintillator thickness and geometric efficiency.

Figure 4.2(a) exhibits some interesting features - although the majority of errors at all depths are within +/-1 mm, a significant minority of errors exhibit a depth-dependent near linear positive AND negative increase in error with respect to increasing depth (essentially a dominant mode around zero with two minor modes whose values increase linearly with depth). This is most likely due to a number of different modes of interaction contributing to the total dataset - specifically, the split between photoelectric, single-Compton and multiple-Compton events. Photoelectric events should not introduce a bias in the error with respect to increased

depth, however, Compton-scattered events arriving at an oblique angle will tend to scatter in approximately the angle of incidence. Therefore, if multiple energy depositions occur they will tend to skew the estimated location, either positively or negatively, depending on the precise nature of the scatter event.

A large part of the error is due to the implicit assumption that all detected events are purely photoelectric, which is not true in practice. For both materials, our simulations show that more than three quarters of all interactions between incident gamma photons and the scintillator will be Compton-scattered, some more than once (see Table 4.2). However, some of the scattered photons go on to entirely escape the scintillator, while the subsequent interactions of many others often occur close to the initial interaction. In these cases, if a non-trivial amount of energy is deposited, the fitting process will still work very well, since the total energy deposition is one of the degrees of freedom of the optimiser. For multi-Compton interactions, since scattering is biased towards the forward direction, it is more probable than not that further interactions with the scintillator occur more deeply in the scintillator shell, leading to more optical attenuation of the resulting scintillation photons than for those produced during the initial interaction. This results in the observed optical photon pattern being typically dominated by the first and shallowest interaction. The parametric fit to the analytic model is therefore quite similar to the pure photoelectric case in many instances.

As expected for a PET system with high resolution DOI estimation capabilities, degradation in localisation performance with increased radial displacement is quite moderate, with the median error in LOR placement increasing from 1.27 mm to 1.62 mm between the centre and 75% of the inner radius of the cylindrical shell for GLuGAG:Ce, and 3.12 mm to 4.13 mm in the case of LaF_3:Ce-PS.

A direct comparison of the two materials suggests that GLuGAG:Ce is the superior material. However, this does not account for economic factors which also influence scanner design. The nanocomposite material has many desirable physical and mechanical properties. If the performance is adequate for the targeted application, it may very well be the more attractive material.

4.5 Conclusions and future work

This work established the feasibility of a continuous cylindrical shell PET scanner based on either optically transparent ceramic garnet or inorganic scintillator/polymer nanocomposite materials. Initial simulations for a point source located at three positions within the scanner's field of view are presented, yielding promising results for the accuracy of detection of the endpoints of the line of response.

In the following chapters, we will develop a coincidence detection algorithm for the proposed monolithic cylindrical shell scanner, and build a complete simulation and STIR-based image reconstruction pipeline. We will evaluate the coincidence detection sensitivity of the system and perform image reconstructions with point sources at several different locations within the scanner's field of view. The median LOR displacement errors of 1.27-1.62 mm for GLuGAG:Ce and 3.12-4.13 mm for LaF_3:Ce-PS obtained in this study are suggestive of good performance in the next phase of the project.

Chapter 5

Efficient spatio-temporal deconvolution-based pulse pile-up correction for coincidence detection in monolithic-scintillator PET systems

5.1 Introduction

In PET scanners utilising a continuous cylindrical shell of scintillator material, the task of coincidence detection is necessarily very different to that in classical PET. Rather than a situation in which most or all optical photons resulting from gamma photon energy deposition will be collected by a small subset of pixels in the photodetector array (depending on the optical coupling between scintillator and photodetectors), where a simple time-windowed binary AND-gate approach can be used for coincidence detection, coincidences in a continuous cylindrical shell scanner manifest as near-simultaneous bursts of optical photons which are detected on the inner and outer surface of the scintillator shell across a variable number of pixels. The production of these photons is not instantaneous; rather, following the interaction, they are progressively emitted with an emission intensity that rapidly rises and slowly decays according to a a multi-exponential function of time. The onset of these photon bursts

is determined by the time of flight of each half of the coincidence; depending on the activity in the object being imaged and the decay time of the scintillator, unrelated individual optical photon showers have a certain probability of overlapping, both in space and time. If it is possible to isolate and cluster individual photon showers as belonging to a single annihilation based on the spatio-temporal relation of the arriving optical photons, then it should be possible to utilise the methods presented in Chapter 4 to localise the endpoints of the line of response and incorporate it into the projection sinogram [171].

The problem of resolving individual photon showers in monolithic PET systems is analogous to the one-dimensional problem of pulse pile-up in classical nuclear spectroscopy, which has previously been addressed via temporal deconvolution of the composite signal by the impulse response of the scintillator to resolve the piled-up pulses as a string of quasi-instantaneous impulses (Dirac delta functions) [172]. In fact, if the signals from multiple individual photodetectors are added together, the ensemble can be thought of as a large single-channel detector. Due to the limited scintillator thickness (typically less than 30 mm), the specific depth of the point of interaction within the slab has a minimal impact on the pulse shape (since the maximum realistic optical photon path in the scintillator will be traversed in about 100-200 ps, compared to a minimum decay time in LSO of 20-50 ns [173, 174]). The pulse amplitude depends on the amount of energy deposited by the interaction, but the *shape* is always essentially the same. Therefore, it should be possible to successfully deconvolve the summation signal by a representative temporal impulse response to achieve good temporal pulse resolution.

This Chapter introduces a deconvolution-based method for identifying coincidences in continuous-shell cylindrical PET scanners. Statistical results from the application of this method to a Monte Carlo simulation are calculated and compared to the ground truth coincidence data obtained directly from the simulation. By implementing this method for coincidence detection in combination with the line-of-response endpoint localisation algorithm described in the previous Chapter, all of the essential infrastructure required for constructing PET lines of response and hence generating data for image reconstruction is available for a continuous-shell cylindrical PET system.

5.2 Materials and Methods

The methods described in this Section can be applied to any scanner with a continuous cylindrical shell and two-sided (inner and outer surface) optical detection. The specific geometry used for the Monte Carlo simulation evaluation of the proposed technique, and the simulation parameters themselves, are described in detail in Section 5.2.5 and 5.2.6, respectively. It is assumed that the optical photon counts in each pixel (both on the inside and outside of the shell) are periodically read out digitally, logged and reset via a synchronous clock signal which is simultaneously distributed to all detector modules via equal-length transmission paths.

5.2.1 Coincidence Detection Technique

The inner and outer detector surfaces are each divided into an integral number of sectors, with equal angular coverage in each sector (see Figure 5.2). The identity of any photodetector pixel in which a non-zero number of optical photons is detected in each clock cycle is converted into a cylindrical coordinate system and assigned to one of these sectors; in the specific geometry evaluated in this work, 16 sectors, each of 22.5°, were used. To capture interactions which may fall along the edges of the angular sections, the same data was also assigned to a second set of "offset sectors", which are the same size but offset by half of the sector width. Photon showers which lie on a sector boundary in one sector set will therefore be in the centre of a sector in the alternate set.

5.2.2 Impulse Response Generation

A centrally located periodic 10 MBq ^{18}F-like pseudo-source was simulated, and a sample of 1000 decays was generated. Photoelectric interactions were then identified via the amount of energy deposited by primary gamma photons, and the optical scintillation photons resulting from these primaries were grouped together as they arrived at the photodetectors, summed and logged at each time sample, resulting in a single time-domain waveform for each. The depth of interaction was also recorded for each photoelectric interaction; the radial dimension of the ring in this case was quantised into five 5 bins, with the minimum and maximum allowable positions

being the apothem of the inner and the radius of the outer polygon surfaces. The resulting time-domain waveforms were separately averaged for each of the five depth ranges, resulting in a representative mean impulse response at each depth (see Figure 5.1). The impulse responses were also amplitude-normalised (since interactions in the middle of the cylindrical shell will tend to result in smaller-amplitude optical pulses compared to those interacting near the inner or outer surface of the shell).

As expected, due to the relatively short photon propagation time relative to the scintillator decay constants, little variation is observed between photoelectric impulse responses at different depths (Compton events where some part of the initial photon energy escapes will also have a similar shape, but lower amplitude). This impulse response is used as the deconvolution kernel for the coincidence detection algorithm.

5.2.3 Single, 2-Coincidence and Multiple-Coincidence Detection

Synchronous readout from any pixels registering hits is performed at 10 ns intervals (comparable to the typical timing window of 6-12 ns in conventional PET systems [10, 175, 176]) and summed in each sector and offset sector to yield a set of time-domain signals (32 signals for this specific geometry). Each signal is deconvolved with the mean scintillator impulse response (see Figure 5.3), greatly reducing the pulse pile-up and cleanly separating most of the impulses.

In each time slice, a threshold of 5% of the maximum amplitude of a single photoelectric impulse is applied to each of the deconvolved waveforms. The type of event may then be distinguished by the number of channels where the amplitude exceeds the threshold. If only a single channel exceeds the threshold, the event is logged for potential use in the randoms correction procedure. If exactly two channels register, then the event is considered a potential coincidence and logged for further analysis. If more than two channels exceed the threshold, the event is recorded as a 'multiple-interaction event' but not used for image reconstruction as it is not possible to determine which two events should be used as the endpoints of the line of response. The choice of 5% for the threshold is largely arbitrary, and the method still works over a wide range of threshold values; however, this is a tunable

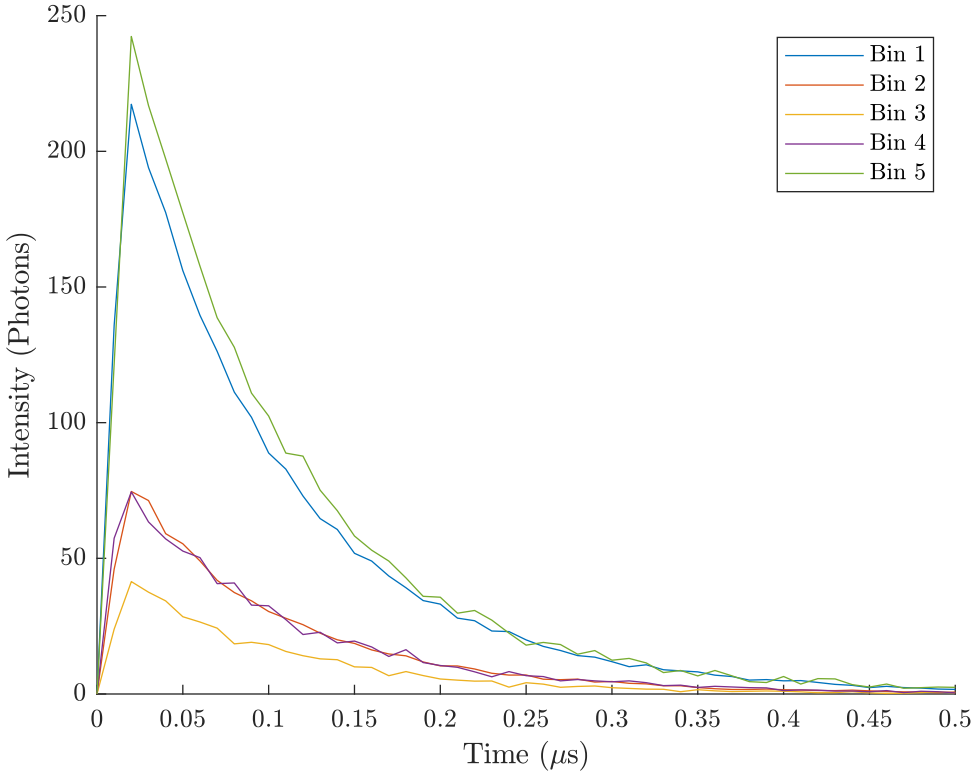

(a) Impulse response generation: raw intensity

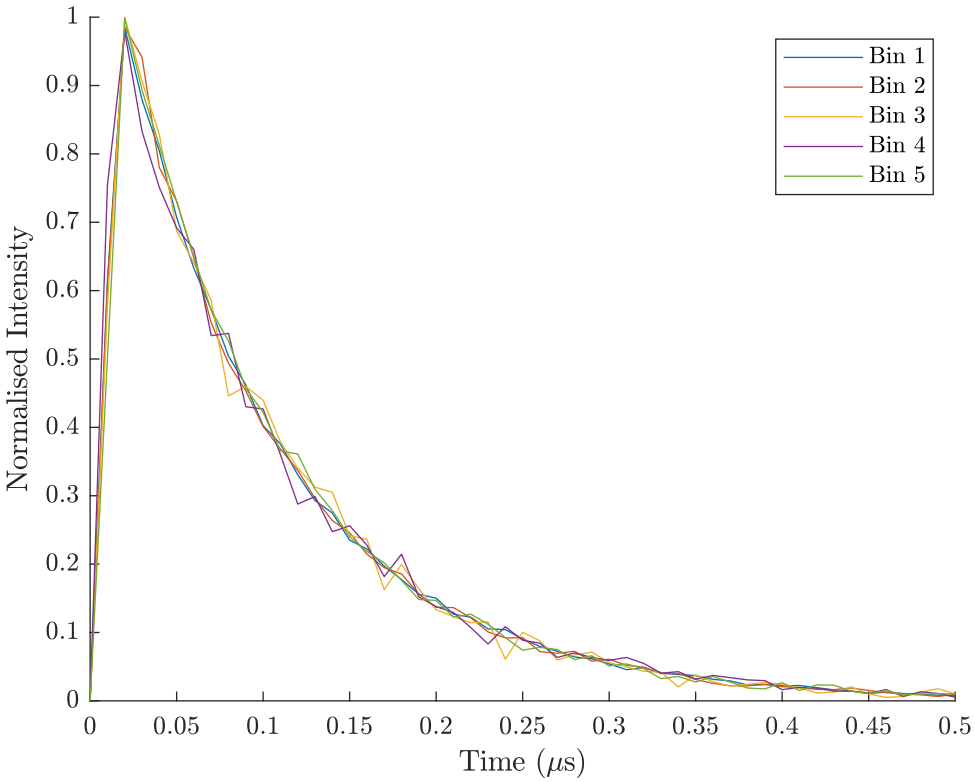

(b) Impulse response generation: normalised intensity

Figure 5.1: The generated impulse responses for five discrete radial bins. The bins are numbered 1 (closest to inner detector surface) to 5 (closest to outer detector surface).

parameter which may be adjusted if desired (a higher threshold will result in a lower rate of false positives, but lower overall sensitivity). Importantly, if one particular channel registers an event, and either (or both) of its immediate half-sector-offset neighbours also registers an event, the smaller event/events is/are ignored as it/they are assumed to be due to the same event (since the imaging object cannot fill the entire field of view, and it would need to almost touch the ring if it were to register a true coincidence in adjacent half-sectors).

The time samples in which a potential coincidence event has been identified signify the onset of the event, since the deconvolution process fully equalises the impulse response of the scintillation process - ideally, concentrating the energy of the event into a single instant (the time of arrival of the original gamma photon). The next step is temporal segmentation of the original optical photon arrival signals to the interval surrounding each event, and spatial segmentation to identify the location of the point of interaction.

Following identification of the onset of an event in the deconvolved waveforms at time t_c, the original (i.e. not deconvolved) signals from each detector are extracted between $t_c \leq t \leq t_c + \tau$, where τ is the duration of the impulse response (time to fall to 5% of the maximum value; approximately 3 time constants) and summed in the time dimension, resulting in a two-layered cylindrical image of all photons captured within the emission timing window. The global maximum is located, and the circular (or part-circular, for maxima near the axial extrema of the image) region surrounding this maximum with a radius determined by (4.3) and (4.4) is copied and then masked out (zeroed) on both layers. This process is then repeated (post-masking) as required, depending on the number of simultaneous events which have been identified as occurring within this sample period (i.e. based on the number of deconvolved signal channels exceeding the threshold), since the only remaining maximum should correspond to the other end of the line of response. The mask is also applied to the complete dataset, preventing the decaying pulses which commenced in the current sample from registering again in the samples immediately following, since the decaying pulse may still exceed the amplitude of these subsequent pulses. Depending on the number of photon clusters thus identified, the image subsets are copied into one of the time-ordered vectors of either single, coincidence and multiple

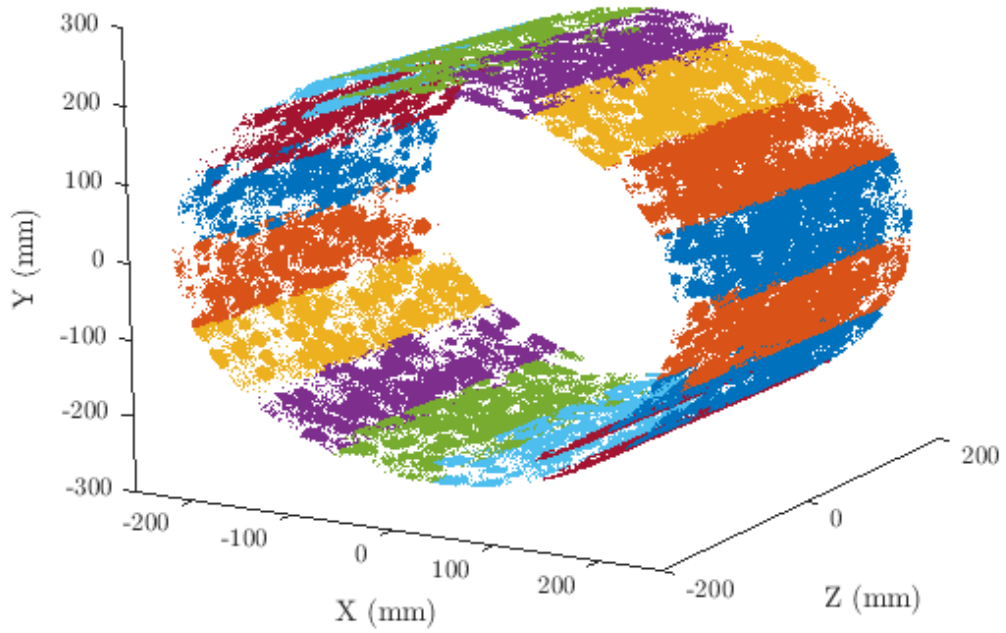

Figure 5.2: The scanner geometry is split up into 16 equal sectors. The sectors are shown here with different interactions shown in different colours. Note: some colours have been reused for the illustration; they are not the same sector.

coincidence events. As a simple heuristic to avoid double-counting any marginal events which straddle a sample interval (or which, due to poor SNR, do not deconvolve cleanly), if a coincidence is logged with either of its endpoints within 5 mm of the endpoints of the preceding coincidence, the second coincidence is discarded (as the probability of this occurring due to chance is vanishingly small).

5.2.4 Line of Response Position Estimation

The position localisation algorithm used here is the same as that described in Section 4.2.3, supplied with pairs of optical photon clusters identified via the previously-described deconvolution and spatio-temporal segmentation coincidence detection algorithm. The unique event identifier assigned to the coincidence events is used to group the data, before the analytic models of the inner and outer surface image projections, (4.1) and (4.2), are fitted to the images and the 3D position of each of the gamma interactions estimated. This process is shown in Figure 5.4.

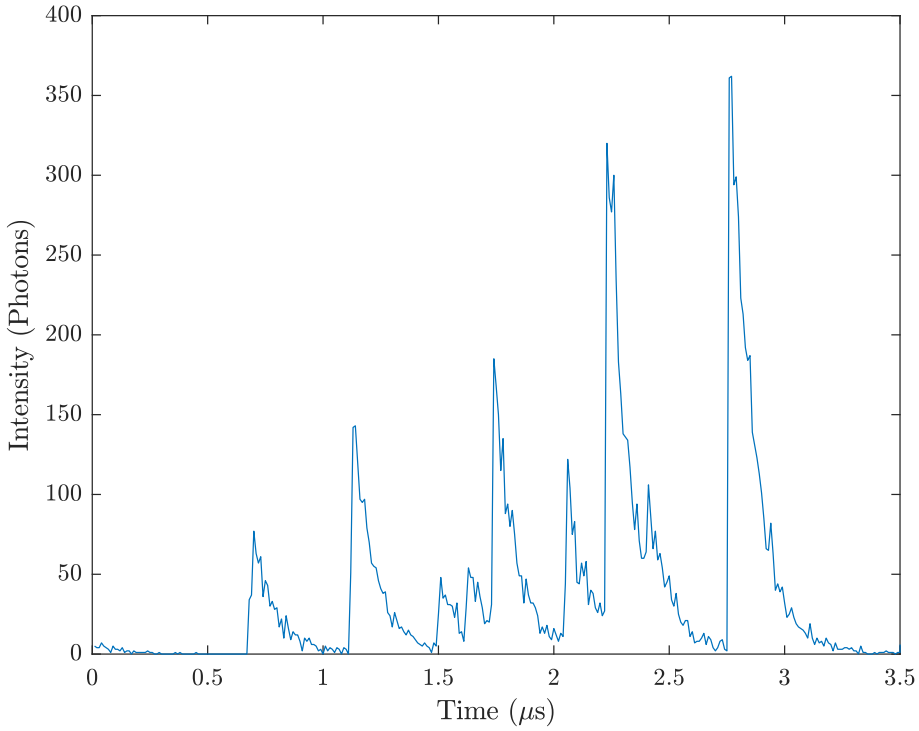

(a) Coincidence detection: unprocessed signal

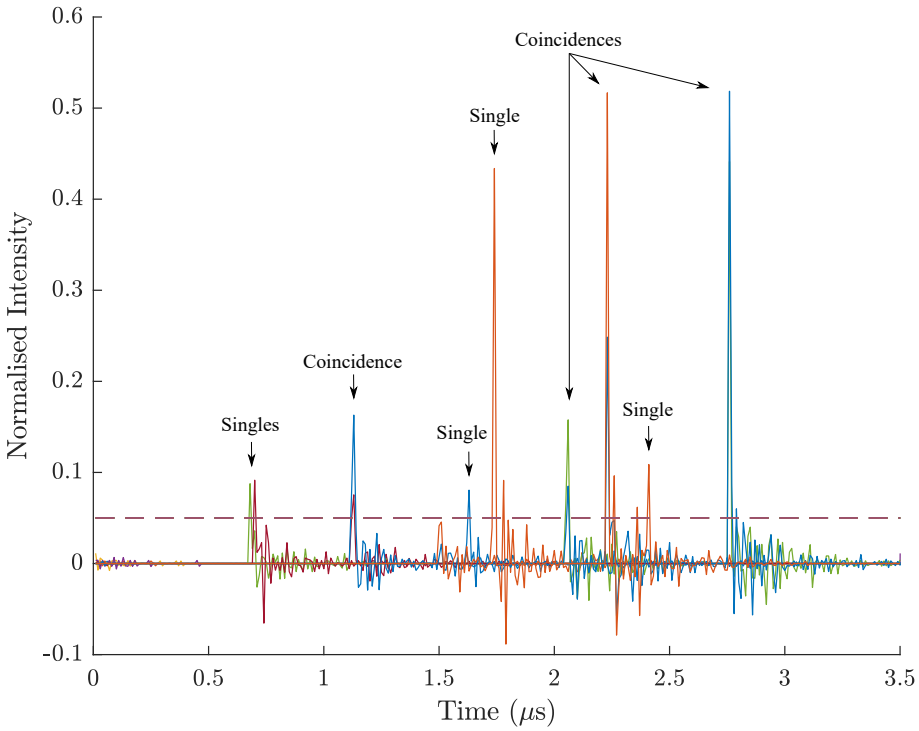

(b) Coincidence detection: deconvolved signal

Figure 5.3: Deconvolution is used to reduce pulse pile-up between events and properly resolve coincidence pairs. A coincidence pair is recorded if two peaks are within the same 10 ns sample interval and intensity is above 5%-of-maximum threshold (dashed line). The different colours correspond to different sections of the cylinder.

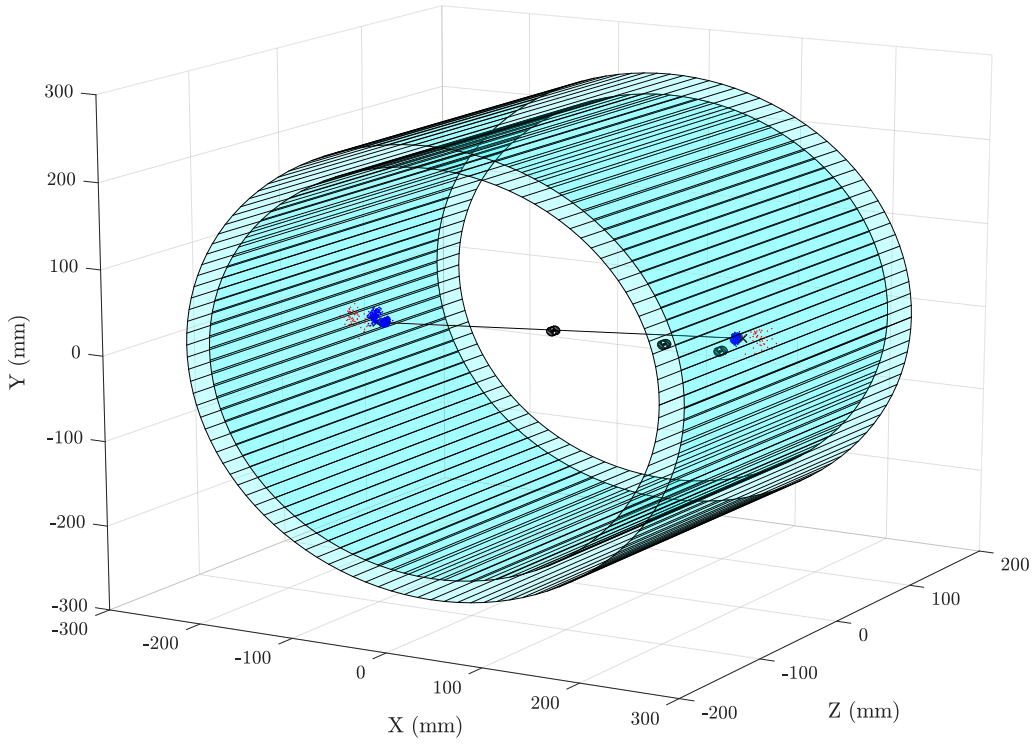

Figure 5.4: Line of response generated from a single coincidence detection, using optical photon distributions captured on the inner and outer detector surfaces. Each face of the inner and outer surfaces of these pseudo-cylindrical polyhedral shells represents a row of 21 SiPM detectors, with scintillator material sandwiched between the inner and outer detectors. The dark blue and orange points correspond to the annihilation photons detected on the inner surface and outer surfaces, respectively. The three small black cylinders inside the ring represent ^{18}F sources and water phantoms. The source generating the LOR is positioned at the centre of the field of view, while the other two are offset in the radial dimension by 50% and 75% of the inner surface radius.

5.2.5 Geometry

The geometry of the scanner is the same as that which is described in Section 4.2.2. Only the GLuGAG:Ce ceramic scintillator is used in these simulations, since this material was previously shown to offer the best performance amongst the evaluated scintillators - however, a scanner can be designed with an optimal scintillator thickness using any of the ceramic or nanocomposite materials. In summary, the scintillator is a polygonal (pseudo-cylindrical) shell, where the inner polygon has 104 14.442 mm faces and the outer polygon has 110 14.2 mm faces. Each of the polygon faces is optically coupled to a row of 21 12×12 pixel SiPM arrays (the geometry is shown in Figure 4.1). The pixel pitch of the SiPM arrays is 1 mm in both dimension (with an assumed 100% fill factor in the array), while a 1 mm insensitive area surrounds the array, with an additional axial separation between SiPMs of 0.1 mm, resulting in a total axial length of 296 mm.

3 MBq ^{18}F sources were placed at three positions inside the scanner: one in the centre of the field of view, and two more offset in the radial dimension by 50% and 75% of the inner surface radius. The axial position in each case was at the centre of the scanner. The sources were each cylindrical with a radius of 1 mm and height of 2 mm, and were each placed within a cylindrical water phantom of radius 5 mm, height 10 mm.

Separate simulations were performed for scanner normalisation; these are described in Chapter 6.

5.2.6 GATE Simulation Parameters

GATE version 8.1 [160, 161] and Geant4 version 10.4p02 [162] are used for all simulations. Full optical photon tracking was enabled on all simulations.

The polyhedral prismatic scintillator shell was designed in OpenSCAD and exported as a stereolithography (STL) file. It was then included in the GATE simulation using the "tessellated" volume option, which allows an STL file to be used as a geometric object. Optical properties for GLuGAG:Ce and meltmount optical coupling epoxy were taken from the literature [118, 167, 164]. Other physical components in the simulation employed standard GATE materials and surface properties.

The simulation was performed with the scintillator as a 'sensitive volume', so that

True Detections (%)	17.42 ± 0.13
Random Detections (%)	2.08 ± 0.07
Missed Detections (%)	15.37 ± 0.30
Total Interactions (%)	32.79 ± 0.21

Table 5.1: The proportion of true (true positive), random (false positive) and missed (false negative) detections as a percentage of the total number of decays. Results are expressed as the mean and standard error of the mean, after five repeats of the simulation.

the exact location and type of each interaction between the gamma photons and the scintillator could be absolutely determined. This allows the number of apparent coincidences (as detected by the coincidence detection algorithm) to be compared against the ground truth (cases where both photons interacted with the scintillator volume) such that false positives (randoms) and false negatives (missed true coincidences) can be quantified. An event (identified by a unique event ID) is classified as a true coincidence if two primaries are produced with different "track IDs" but with a "parent ID" equal to 1 (the ID of the original positron particle). Coincidences may also be classified as photoelectric-photoelectric (PE-PE), photoelectric-Compton scattered (PE-CS) or Compton scattered-Compton scattered (CS-CS) to determine the impact of the interaction type on the accuracy of the classification algorithm. Due to the resources involved in tracking optical photons in such a large sensitive volume, the number of primary decays is limited to 9000, and the simulation was repeated five times.

5.3 Results

5.3.1 Algorithm Detection Efficiency

Table 5.1 shows the proportion of true, random and missed coincidence detections as a percentage of the total number of positron decays.

True coincidences detected are 53.13% of the total number of interactions which actually occur. The random fraction is 0.1062.

	PE-PE	PE-CS	CS-CS
Type of Interaction (%)	6.24 ± 0.22	37.71 ± 0.50	56.04 ± 0.36
Interactions Detected (%)	52.71 ± 1.38	53.27 ± 0.80	53.06 ± 0.57

Table 5.2: The proportion of each detection type as a percentage of the total number of true detections and the detection percentage. Random events are not included.

5.3.2 Detection Efficiency by Interaction Type

Table 5.2 shows the proportion of coincidence detections which are photoelectric-photoelectric (PE-PE), photoelectric-Compton scattered (PE-CS) and Compton scattered-Compton scattered (CS-CS), by ground truth knowledge from GATE. The detection rate of each type is also calculated. All three types of events are quite similar (certainly within the error margin of each other), with PE-PE being the lowest at 52.71% and PE-CS the highest at 53.27%.

5.4 Discussion

The shape of the scintillator impulse response is very consistent, regardless of the depth of interaction within the crystal. However, the amplitude strongly depends on the nature of the interaction (either deposition of all of the gamma photon energy via photoelectric interactions, or partial energy deposition via Compton interactions) and the depth at which the energy is deposited (due to scattering and attenuation in the scintillator). The amplitude of the impulse response is a minimum for interactions whose depth is half the thickness of the cylindrical shell. These observations confirm the basic validity of the proposed approach.

The solid angle coverage of the simulated scanner geometry limits the proportion of decays which can be detected as a true coincidence to ∼32%, which is in close agreement with the results presented in table 4.5. Of this fraction of potentially detectable coincidences (which could be improved with increased solid angular coverage), including coincidences in which one or both interactions scatter following Compton interactions in the scintillator and which only deposit a small fraction of the incident photon's energy there, a little over half are classified as coincidences by the proposed algorithm, and hence will contribute to the sinogram, while the

others deposit too little energy in one or both halves of the coincidence to register. In a comparable discrete-crystal PET system, most coincidences which fail to be detected here would also be outside of the scanner's energy window and therefore not contribute to the sinogram.

In Chapter 3 the proportion of interactions which were photoelectric was ∼24% for the GLuGAG:Ce ceramic scintillator, so figures quoted in the first row of table 5.2 are close to the expected values (PE-PE coincidences are expected to occur with a probability of 0.24×0.24 or about 6%, PE-CS or CS-PE coincidences $0.24 \times (1 - 0.24) \times 2$ or about 36% and CS-CS coincidences $(1 - 0.24)^2$ or about 58%). The probability of detecting a true coincidence is better than 50% for all types of interaction. The failed detections usually correspond to cases in which either there was a multiple interaction at one endpoint (and hence the event was discarded, as would be the case in a classical pixellated-scintillator system), or one or both interactions near one end of the cylindrical scintillator shell, in which case too many photons may be lost for reliable classification.

5.5 Conclusion

This work introduced a spatio-temporal deconvolution and segmentation algorithm for PET systems based on large monolithic scintillators. When applied to a novel cylindrical-shell monolithic PET architecture, it was found that more than half of the potentially detectable true coincidence events could be correctly identified detected, with a random fraction of 10.62%. It was also found that both Compton-photoelectric and Compton-Compton coincidence pairs could be detected with a sensitivity approximately equivalent to that for photoelectric-photoelectric interactions.

The proposed algorithm identifies a sufficient fraction of true LORs to enable practical image reconstruction; the next Chapter will describes how these LORs are used to reconstruct a 3D image using a range of analytic techniques and image reconstruction algorithms.

Chapter 6

Design and Simulation of a Brain PET Scanner with a Continuous Cylindrical Shell Monolithic Scintillator

6.1 Introduction

Clinical PET scanners currently in use tend towards a common design structure - they use rectangular blocks of discrete scintillator crystal arrays, optically coupled to either photomultiplier tubes or silicon photomultipliers (SiPMs), completely surrounding the patient in a ring. This configuration has worked well for decades, although a major limitation still exists: the spatial resolution of the system is fundamentally tied to the dimensions of the elements in the scintillation detector array. A "hit" is recorded on a detector element if an interaction triggers a light yield above a certain energy threshold, though there is no way to explicitly determine exactly where the interaction occurred within the scintillator volume, only that it did occur. If two detector elements are triggered at approximately the same time, then a coincidence is said to occur and a line of response can be drawn between the two elements. A typical system might contain scintillation crystals approximately 4 mm×4 mm×22 mm [2], hence most modern systems achieve a spatial resolution somewhere in the vicinity of 3-5 mm for full body systems and 1-2 mm for small

animal systems [23].

A high spatial resolution is important in both diagnostic imaging and biological research applications of PET, since more image detail in fine structures is revealed, allowing for more conclusive diagnoses and stronger scientific conclusions to be drawn from an image. A key hypothesis for the development of a fully monolithic, cylindrical PET detector architecture, was that the design would allow for the spatial resolution to be improved because it is no longer limited by the dimensions of the scintillator crystal; rather it is based on the statistical methods which estimate the position at which the emitted gamma photon interacts with the detector (as described in Chapter 3.2). Each location is estimated by analysing an optical photon map and fitting an analytic function to the data to find the most likely three dimensional position for the location of the interaction. After exploring solutions to coincidence detection and LOR determination for such a radical architecture in the previous two Chapters, it is now possible to combine each of the proposed methods with several standard image reconstruction techniques to generate a complete image, with all necessary corrections applied.

In this Chapter a full optical simulation of three 3 MBq ^{18}F radioactive sources is performed using the Geant4 Application for Tomographic Emission (GATE) [160, 161]. For the first time, image reconstruction is achieved using several image reconstruction methods implemented in the well-known Software for Tomographic Image Reconstruction (STIR) package [156]. A number of standard corrections were first applied before the spatial resolution is estimated via measurement of the FWHM for each source in each dimension. This work aims to provide a basic proof of concept and validate the entire end-to-end signal processing pathway for the proposed scanner design.

Section 6.2 describes the methodology used for image reconstruction and correction, as well as the specific parameters and algorithms used; the parameters used in the optical simulation, which has generated the data for the reconstruction, are also discussed. Section 6.3 presents the results of the image reconstructions, with important observations discussed in Section 6.4. Finally, Section 6.5 concludes the chapter by summarising the key findings and outlining possible next steps for the continuation of the study.

6.2 Materials and Methods

6.2.1 Simulation Parameters

The fully monolithic continuous cylindrical shell scanner geometry is exactly the same as previously described in Section 4.2.2 and Section 5.2.5. GLuGAG:Ce ceramic garnet is again used as the scintillation material and meltmount has been modelled as the material used for optical coupling to the silicon photomultiplier arrays. Physical properties of the scintillator and other optical components have been obtained from the literature [118, 167, 164].

The simulation has again been performed in GATE version 8.1 [160, 161] with Geant4 version 10.4p02 [162]. Full optical tracking was enabled for all simulations, with the exception of the simulation used to generate normalisation data. In the main simulation, three 3 MBq ^{18}F sources were used, each modelled as a short cylindrical source with a diameter of 2 mm and height of 2 mm, positioned at the centre of the scanner FOV and offset in the radial dimension by 50% and 75% of the inner surface radius. Each of these sources were contained in a cylindrical water phantom with a radius of 5 mm and a height of 10 mm, to ensure all emitted positrons would annihilate but without inducing significant amounts of scattering. List-mode data was acquired with these sources over a period of 3 seconds of simulation time, giving a total of approximately 27 million decays.

For normalisation, a phantom of radius 233.315 mm and height 296 mm filled with a solution of ^{18}F in water is situated in the centre of the FOV of the scanner. Five billion events were simulated as primaries only (data collection and storage for an optical system is much too great for such a large number of events). The reasons for this approach will be discussed in detail in subsequent sections.

6.2.2 Image Reconstruction

STIR version 3.0 [156] was used for all image reconstructions. Since the geometry of the scanner is quite different to that normally used with STIR, some additional preprocessing steps are needed to convert the listmode data into a format which can be read by STIR and properly processed. The first tool [177] generates a pixellated cylindrical map of virtual detector locations within the scanner, based upon

input geometrical specifications, using a similar approach to that of Li et al., and Scheins et al. [52, 178]. The map is essentially a zero-thickness virtual cylinder; the two intersection points of each LOR are calculated, quantised and then mapped to the pixels of each virtual detector surface. This approach enables the continuous depth of interaction (DOI) estimate produced by the LOR endpoint estimator to be mapped to a single layer for image reconstruction, speeding up image reconstruction and greatly reducing memory consumption compared to a multi-layer DOI quantisation approach. The pixel dimensions in the virtual cylinder are arbitrarily chosen according to the desired trade-off between spatial resolution and signal to noise ratio (and image reconstruction time - a higher resolution virtual cylinder will greatly extend the time and memory required for image reconstruction, particularly for iterative algorithms).

In this work, the size of the virtual ring is equal to the length of the scanner (296 mm), with radius equal to the inner face of the detector ring (apothem of the inner polygon = 233.31 mm). There were 77 virtual rings along the axial length of the scanner, each containing 384 detector elements around the circumference. The number of voxels used in image space was 245×245×153 (in x, y, and z dimensions, respectively). The dimensions of each voxel are 1.922 mm×1.922 mm×1.922 mm.

Once mapped, the data is converted from ASCII text into **SAFIR** listmode format- a custom binary format which has been integrated into the STIR library for conversion into Interfile sinogram format [179, 180]. Re-sampling the LOR data in this manner requires an input sinogram header, which specifies the scanner parameters. The parameters used for this scanner geometry are listed in Table 6.1, and have been generated via STIR's inbuilt *create_projdata_template* function. Once the sinogram was produced, both analytic and iterative reconstruction algorithms were applied; specifically 2-D Filtered Back Projection (with single-slice rebinning), 3-D Filtered Backprojection with Reprojection and the Ordered Subsets Maximum A Posteriori - One Step Late (OSMAPOSL) algorithm, configured as simple OSEM (i.e. there was no a priori image and instead a flat image of zeros was used). OSEM was configured to operate with 8 subsets and 30 sub-iterations. The ramp filter used in FBP2D had an alpha parameter of 1 and cut-off frequency of 0.5. The Colsher filter used in FBP3DRP similarly used an alpha value of 1 and cut-off frequency of

0.5 in both the axial and planar dimensions.

All images presented in this Chapter have been produced using AMIDE to display image-domain Interfile data. AMIDE was also used to produce line profiles and measure the full width at half maximum (FWHM) from the point source images. The FWHM is measured for all sources in three dimensions, using zero as a reference point for the measurement (the analytic reconstructions produced small negative values in some instances).

6.2.3 Image Correction

Various corrections have been applied to the reconstructed images. Most of these operations are performed in the projection (sinogram) space, then the selected reconstruction algorithm is applied to the corrected sinogram afterwards. Equation (6.1) details the process by which the raw sinogram is generated and which should be corrected to restore the forward-projected emission sinogram as accurately as possible (and hence enable proper image reconstruction in the spatial domain):

$$sinogram\,(uncorrected) = \frac{fwd(emission) + (norm \times ACF \times (random + scatter))}{norm \times ACF} \tag{6.1}$$

where $fwd(emission)$ is the exact forward projection of the emission image, $norm$ is the attenuation-corrected sinogram acquired from a uniformly-filled phantom (or equivalently, generated using a component-based normalisation scheme), ACF is the attenuation correction factor sinogram, and $random$ and $scatter$ are the uncorrected sinograms resulting from random coincidences and scatter events, respectively.

To recover an accurate estimate of the forward-projected emission sinogram, the uncorrected sinogram is first multiplied element-by-element by a smoothed normalisation sinogram which encompasses the entire FOV of the scanner, and the ACF sinogram (which, in practice, is computed by converting the Hounsfeld units of a CT image into an estimated attenuation coefficient at 511 keV). The additive contributions from random and scattered events are then corrected by subtracting their normalised and attenuation-corrected sinograms; random correction is normally performed using a delayed coincidence channel (which can completely exclude

Material	GLuGAG:Ce
Number of detectors per ring	384
Number of rings	77
Default tangential Positions	245
Inner ring radius (mm)	234.97
Average DOI (mm)	0.01
Ring spacing (mm)	3.84
Tangential bin size (mm)	1.92
Intrinsic tilt (degrees)	0
Transaxial blocks per bucket	1
Axial blocks per bucket	1
Axial crystals per block	1
Transaxial crystals per block	1
Axial crystals per singles unit	1
Transaxial crystals per singles unit	1
Detector layers per block	1
Mash factor	1
Arc corrected	No*
Tangential positions	245
Span value	1
Max. ring difference	76

Table 6.1: Parameters used in STIR's *create_projdata_template*. * indicates that arc correction will be done later as part of the FBP2D or FBP3DRP algorithms. The Interfile code used for this particular scanner is included in Appendix A.2.

the possibility of any true coincidences being present) while scatter correction can be performed by performing a tail-fitting procedure on the image or by energy windowing to restrict the photons used in image reconstruction to non-scattered photons).

The sinograms used for normalisation, attenuation and randoms correction and their reconstructed images are shown in Figure 6.1. Each have been reconstructed using FBP3DRP. For the specific point-source simulations performed in this work, only a very small volume of water surrounds each point source (to ensure that the positrons annihilate); therefore, scattering is negligible and not included here (although the standard methods for scatter correction are applicable).

Each of the correction terms is discussed in more detail in the following sections, with the exception of scatter correction, which is not performed.

Random Correction

Random correction is performed on the data using a variation of the well-known delayed window technique [181]. Once single events, coincidence events and multiple events have been identified and classified into their own respective datasets using the coincidence identification technique discussed in the previous Chapter, the singles dataset is used to generate random coincidence data, using a variation of the coincidence detection method described previously in Section 5.2.1. To implement the delayed-coincidence method, we consider 'random' coincidences to be those where detected singles are separated by a number of timing bins equal to a time greater than the decay time of the scintillator. Specifically, the fixed separation time between pulses is equal to the time taken for the photoelectric impulse response to decay to less than 5% of its maximum energy; for GLuGAG:Ce this is 300 ns or 30 10 ns bins (rounded up to the nearest bin).

A logical array (with axes of sector number and timing bin) is once again used to identify coincidences. In the 'true' coincidence detection method, a coincidence was identified when two sections flagged an event in the same timing bin. Using a delayed window means that a single event in one timing bin must be paired with another which is both in a different sector and exactly delayed by a fixed interval of 300 ns. The method used was to duplicate the array, offset it by the decay time and then add the two arrays together, again looking for coincidences which were in

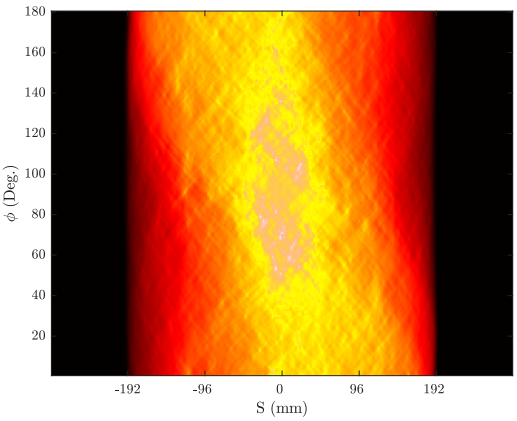

(a) Projection space: randoms correction.

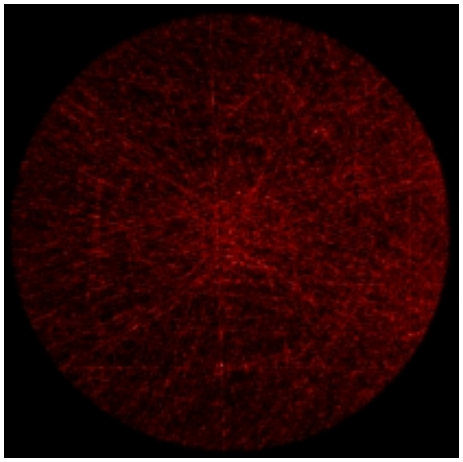

(b) Image space: randoms correction.

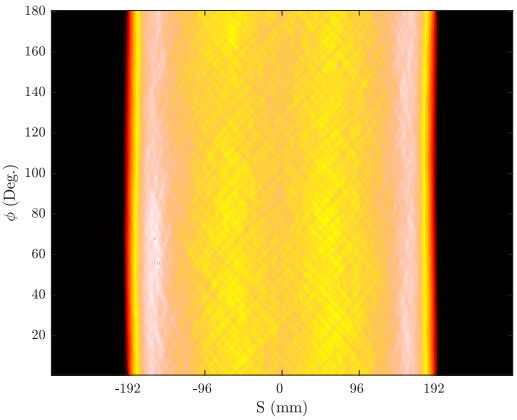

(c) Projection space: normalization correction.

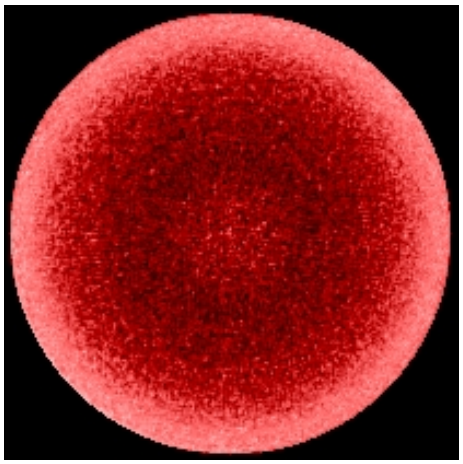

(d) Image space: normalization correction.

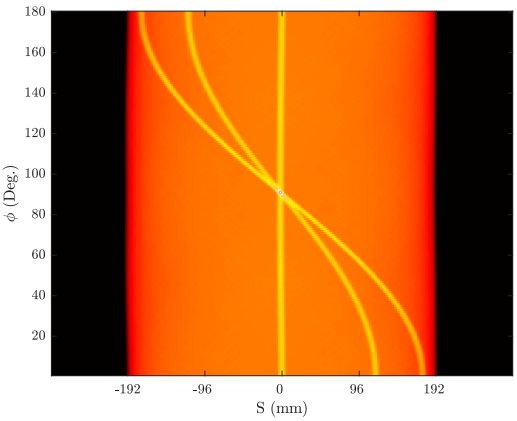

(e) Projection space: attenuation correction.

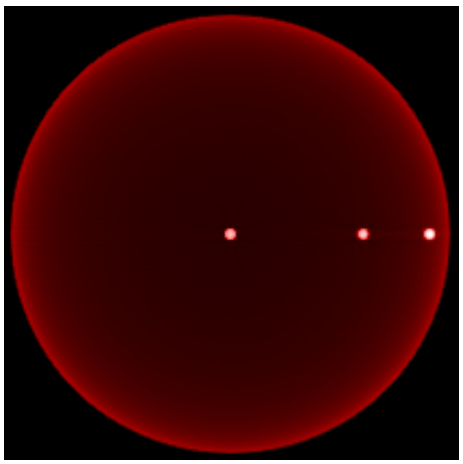

(f) Image space: attenuation correction.

Figure 6.1: Sinograms (a), (c), (e) and Transaxial image slices (b), (d), (f) of the correction factors. Images reconstructed using the FBP3DRP analytic algorithm.

different sectors. These may then be processed as normal with the LOR position estimation algorithm. The resulting LORs are then processed in the same manner as outlined in Section 6.2.2, to produce the required sinogram.

Attenuation Correction

An attenuation map (or mu-map) must be generated based on the structure and composition of the imaging object. This can be done entirely within the STIR environment by using the *generate_ image* function. Each of the three ^{18}F sources is completely contained within a compact cylindrical water phantom; the attenuation map equals 0.096 cm^{-1} within the water volume and 0 cm^{-1} everywhere else (for the air inside the FOV). The output image file contains voxels of size 245×245×153 (in x, y and z dimensions, respectively), which are each approximately 1.922 mm×1.922 mm×1.922 mm in size. Once the attenuation map is constructed, it is used as an argument in STIR's *calculate_attenuation _coefficients* function with the –ACF option flagged, to calculate the attenuation correction factor for each of the voxels on the attenuation map. This last step outputs a sinogram, in Interfile format, which is then used to perform attenuation correction on the image in the projection (sinogram) domain.

Normalisation

Due to the computational workload of conducting a simulation of sufficient fidelity of a flood-filled source with full optical photon tracking is not feasible. This would not be an issue for a physical scanner (where a normalisation scan must be performed periodically as a routine part of scanner maintenance); however, for this work, it is necessary to obtain the normalisation sinogram via an expedited simulation. Therefore, a cylindrical phantom, filled with an ^{18}F solution and encompassing almost the entire FOV of the scanner, is simulated in GATE with optical photon tracking disabled.

The exact locations of the first points of interaction between all 511 keV photons and the scintillator volume are recorded. Coincidences were identified by examining the "Event ID" number of these photons to identify pairs of annihilation photons originating from the same annihilation event. The two lowest "Track IDs" were used

to find the locations and times corresponding to the the first points of interaction (disqualifying cases where Track ID equalled the Parent ID of another interaction of the same event ID - these are subsequent interactions of the same photon). After the two endpoints of the LOR are found, they are recorded in a format which may be processed using the image reconstruction procedure outlined in Section 6.2.2. Following reconstruction, the normalisation sinogram essentially resembles that which would be obtained if a full optical simulation were performed, with the chief difference being that due to the exactness with which the points of interaction are known, the signal to noise ratio (SNR) of the resulting sinogram will be higher for the number of simulated decays. Since a normalisation sinogram should have as high an SNR as possible, this is beneficial to the image reconstruction process.

6.3 Results

6.3.1 Image Reconstruction

Figures 6.2, 6.3 and 6.4 are the reconstructed images of the three ^{18}F sources, using 2D-FBP, 3D-FBPRP and OSEM algorithms respectively. In each figure, subfigures (a), (c) and (e) are the raw (uncorrected) reconstructions in the transverse ($x-y$), coronal ($x-z$) and sagittal ($y-z$) planes, while subfigures (b), (d) and (f) are the corresponding images following normalisation and random and attenuation corrections.

6.3.2 Spatial Resolution Measurements

Figures 6.5 and 6.6 are line profiles taken from Figure 6.2. Figure 6.5 depicts an intensity profile of the line of voxels running horizontally through the centre of the transverse plane (x dimension), while the subfigures in Figure 6.6 correspond to pixels running through the centre of each source, vertically through the transverse plane (y dimension) and vertically through the coronal plane (z dimension). Similarly, Figures 6.7 and 6.8 are line profiles taken from Figure 6.3, and Figures 6.9 and 6.10 are line profiles taken from Figure 6.4. Profiles of both the raw (uncorrected) images as well as the corrected data sets (normalised, and corrected for randoms and

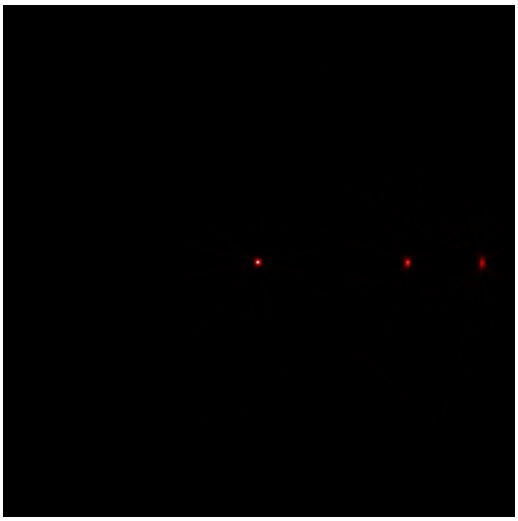

(a) Uncorrected transverse plane

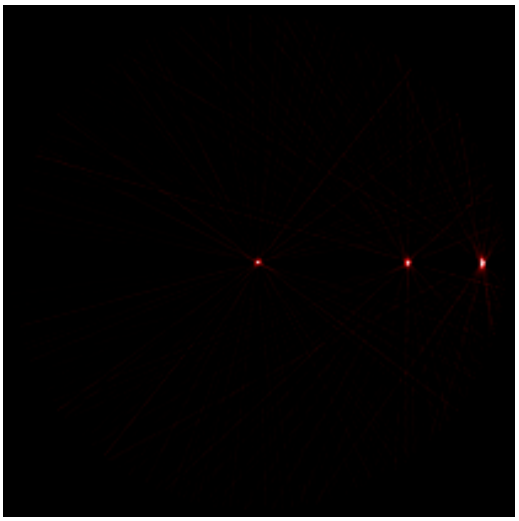

(b) Corrected transverse plane

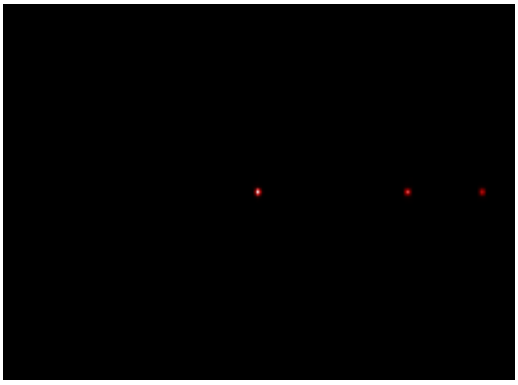

(c) Uncorrected coronal plane

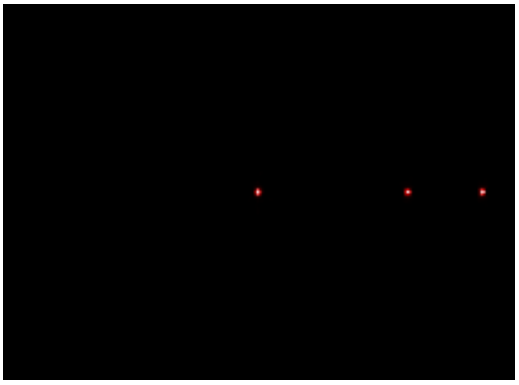

(d) Corrected coronal plane

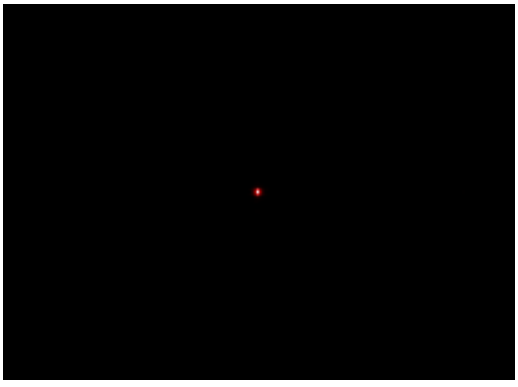

(e) Uncorrected sagittal plane

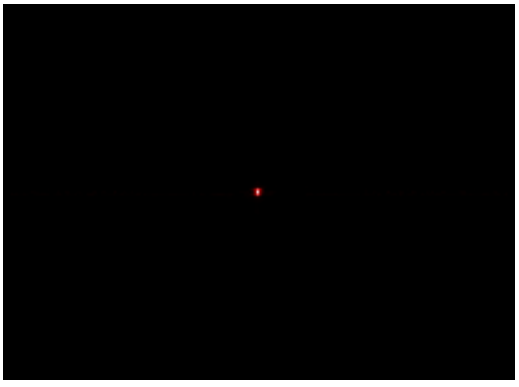

(f) Corrected sagittal plane

Figure 6.2: 2D analytic image reconstruction of three 3 MBq ^{18}F sources encapsulated in cylindrical water phantoms, using STIR's FBP2D algorithm.

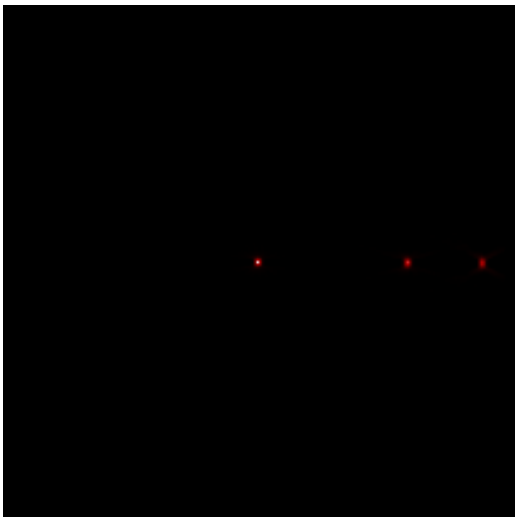

(a) Uncorrected transverse plane

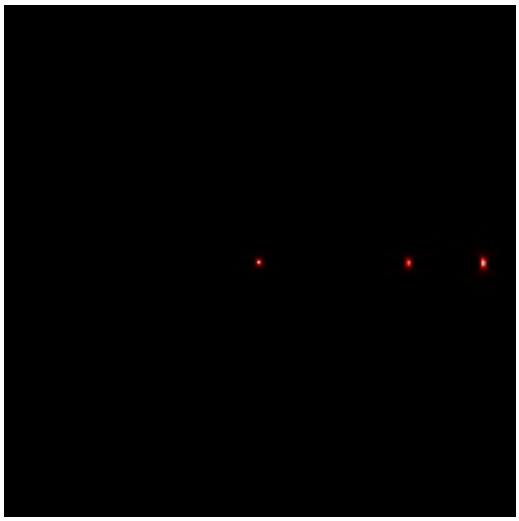

(b) Corrected transverse plane

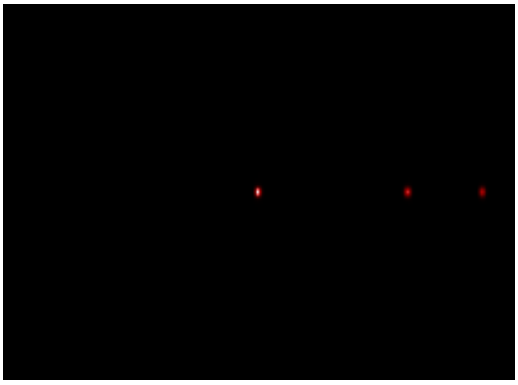

(c) Uncorrected coronal plane

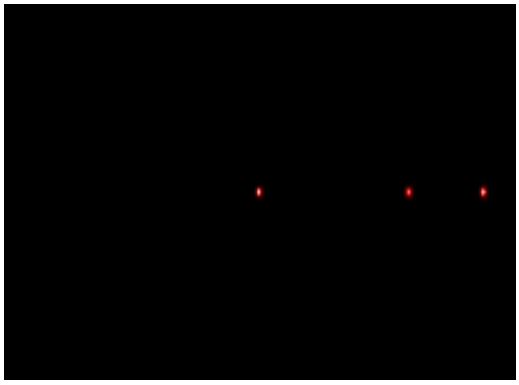

(d) Corrected coronal plane

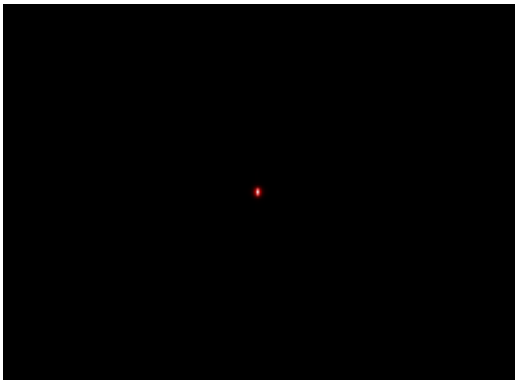

(e) Uncorrected sagittal plane

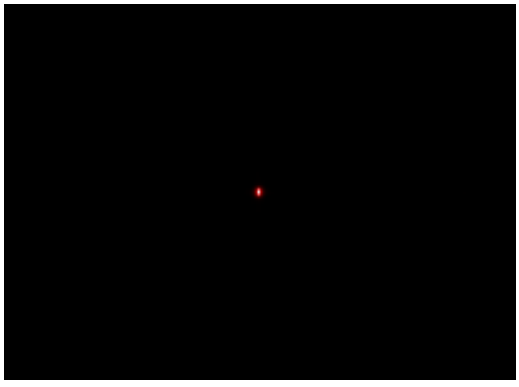

(f) Corrected sagittal plane

Figure 6.3: 3D analytic image reconstruction of three 3 MBq ^{18}F sources encapsulated in cylindrical water phantoms, using STIR's FBP3DRP algorithm.

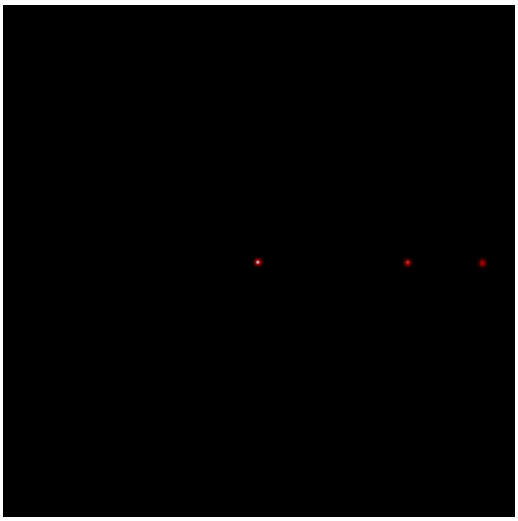

(a) Uncorrected transverse plane

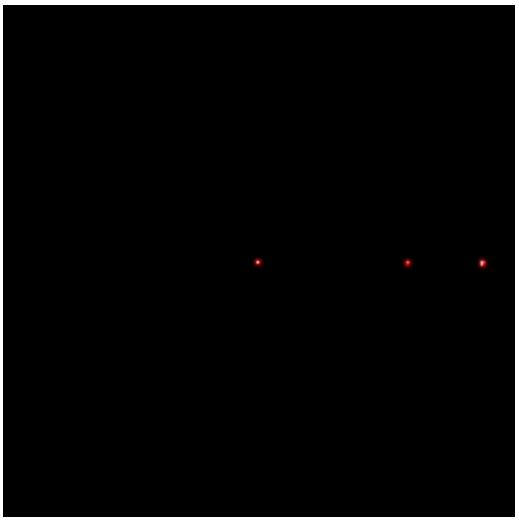

(b) Corrected transverse plane

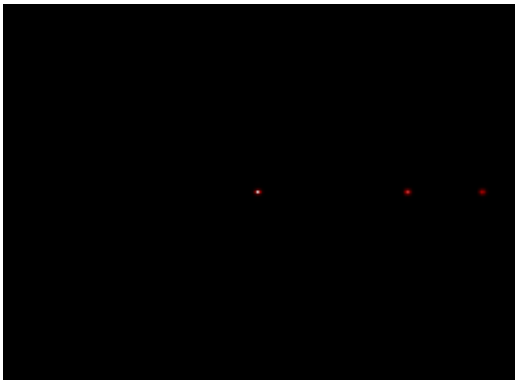

(c) Uncorrected coronal plane

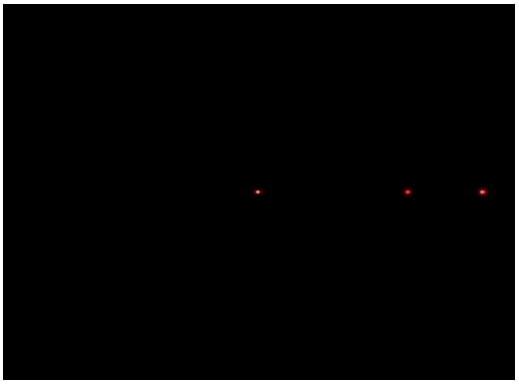

(d) Corrected coronal plane

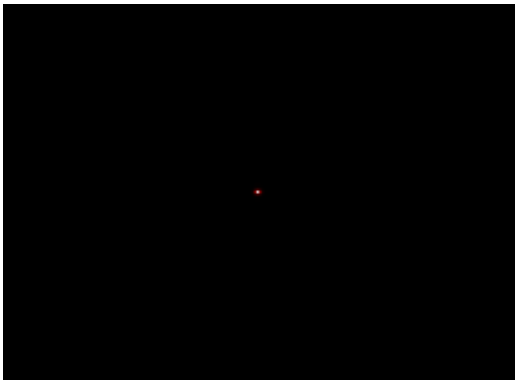

(e) Uncorrected sagittal plane

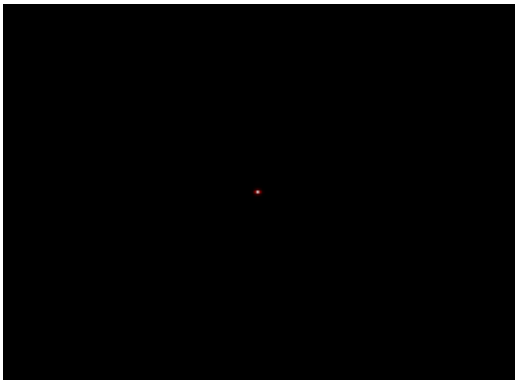

(f) Corrected sagittal plane

Figure 6.4: 3D iterative image reconstruction of three 3 MBq ^{18}F sources encapsulated in cylindrical water phantoms, using STIR's OSMAPOSL algorithm.

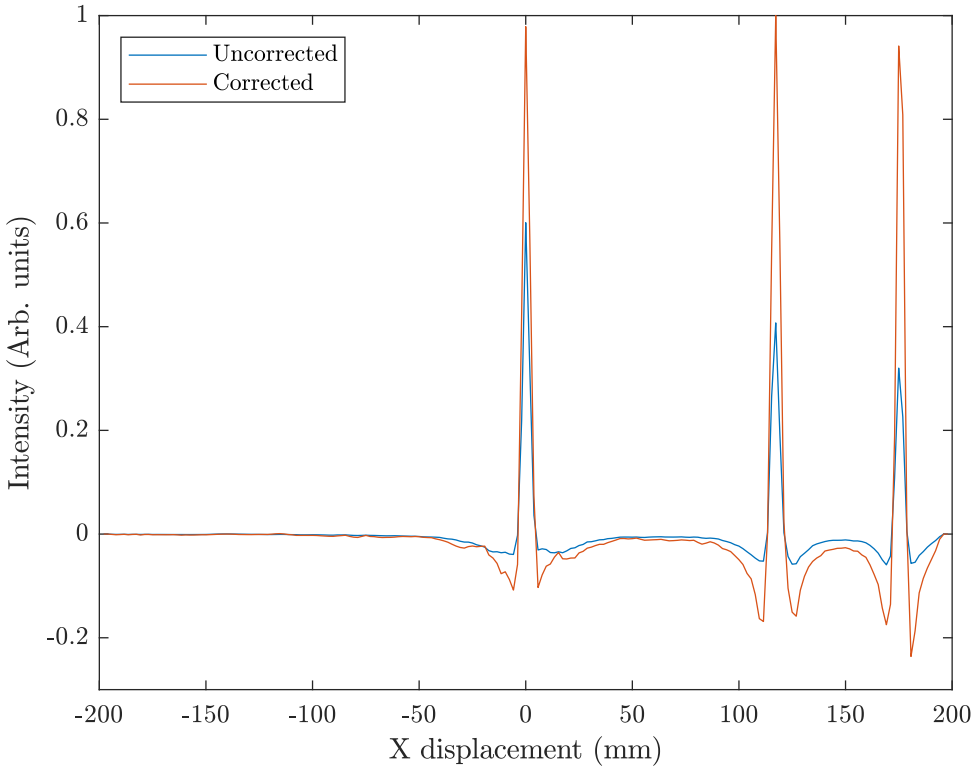

Figure 6.5: Intensity profile of the FBP2D-reconstructed image. The slice is taken along the x axis in the transverse plane of the scanner.

attenuation) have been overlaid for comparison. Tables 6.2, 6.3 and 6.4 summarise the FWHMs of each of the source intensities in x, y, and z dimensions, respectively. Each table compares all image reconstruction algorithms and the effect of image corrections on the results.

Recon. Algorithm	FWHM - Centre (mm)		FWHM - 50% Rad. (mm)		FWHM - 75% Rad. (mm)	
	Uncorr.	Corr.	Uncorr.	Corr.	Uncorr.	Corr.
2D-FBP	3.50 ± 0.52	3.71 ± 0.33	3.85 ± 0.81	3.88 ± 0.33	3.50 ± 0.99	3.10 ± 0.38
3D-FBP	3.29 ± 0.71	3.27 ± 0.50	4.09 ± 1.43	4.03 ± 0.76	3.69 ± 1.62	3.48 ± 0.61
OSEM	3.38 ± 0.32	3.36 ± 0.23	3.95 ± 0.59	3.95 ± 0.35	3.94 ± 0.75	3.84 ± 0.30

Table 6.2: Full width at half maximum (FWHM) of the intensity profiles at zero degrees in the transverse plane (x-axis of the system).

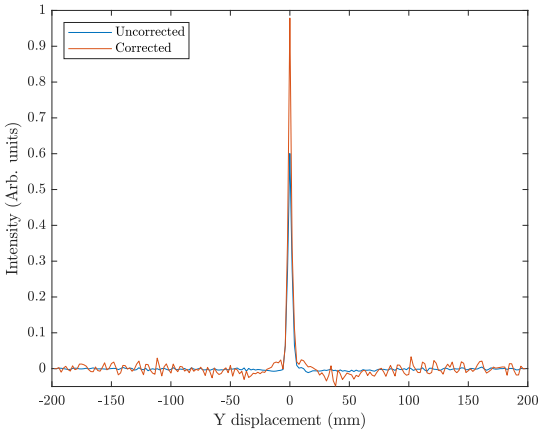

(a) Centre source (y-axis)

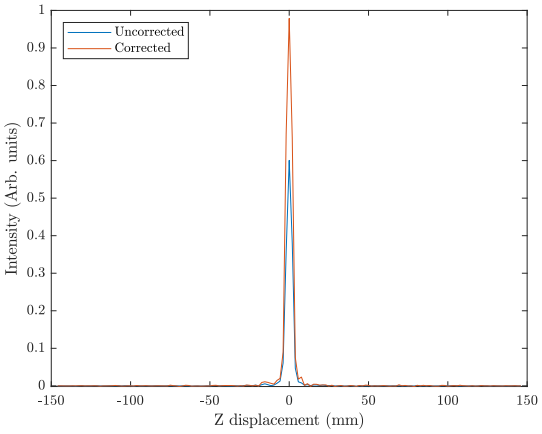

(b) Centre source (z-axis)

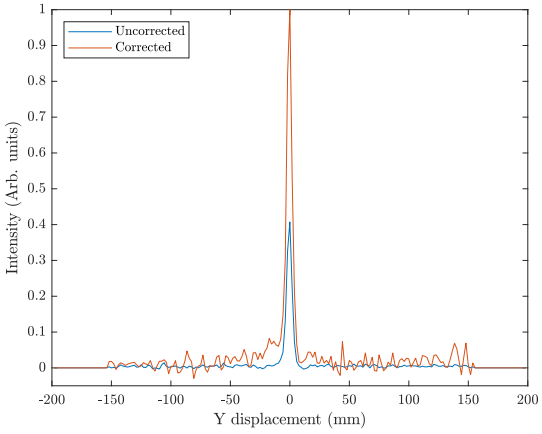

(c) 50% rad. source (y-axis)

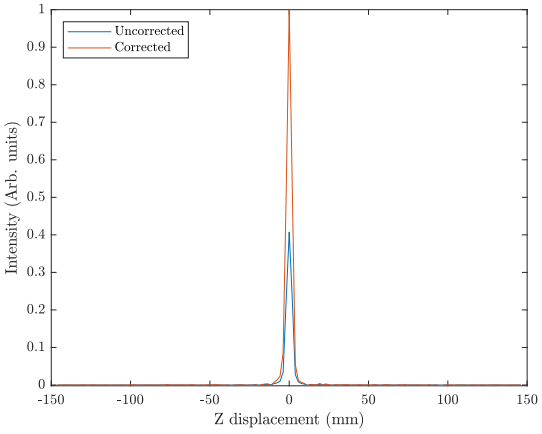

(d) 50% rad. source (z-axis)

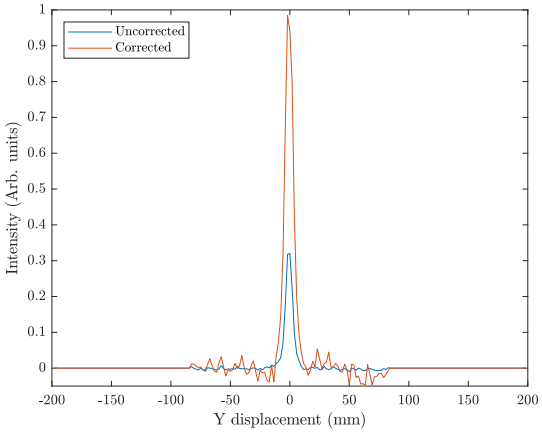

(e) 75% rad. source (y-axis)

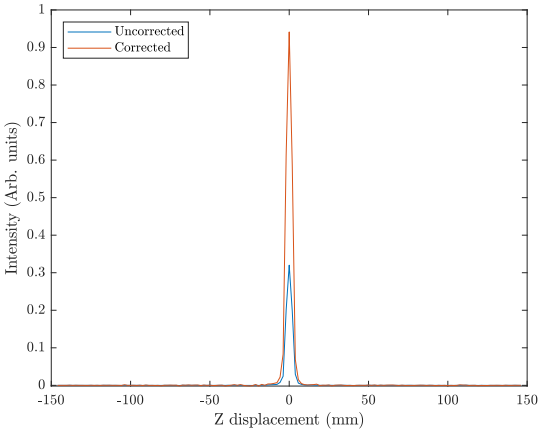

(f) 75% rad. source (z-axis)

Figure 6.6: Intensity profile of the FBP2D-reconstructed image. The slices are taken along the y and z axes, vertically, in the transverse and coronal planes of the scanner, respectively.

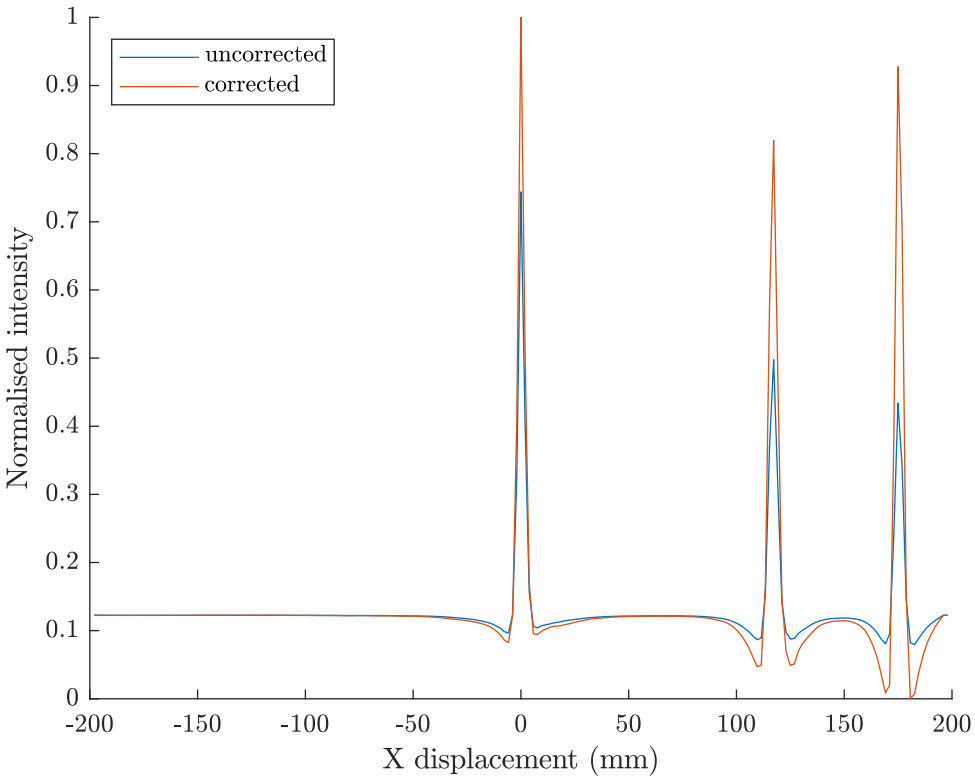

Figure 6.7: Intensity profile of the FBP3DRP-reconstructed image. The slice is taken along the x axis in the transverse plane of the scanner.

Recon. Algorithm	FWHM - Centre (mm)		FWHM - 50% Rad. (mm)		FWHM - 75% Rad. (mm)	
	Uncorr.	Corr.	Uncorr.	Corr.	Uncorr.	Corr.
2D-FBP	3.80 ± 0.52	3.23 ± 0.28	5.39 ± 1.04	5.51 ± 0.43	6.88 ± 1.43	8.32 ± 0.52
3D-FBP	3.82 ± 0.85	3.77 ± 0.59	5.61 ± 1.76	5.76 ± 0.97	6.35 ± 2.19	7.30 ± 0.93
OSEM	3.39 ± 0.32	3.31 ± 0.22	4.10 ± 0.61	3.99 ± 0.35	4.45 ± 0.76	4.41 ± 0.30

Table 6.3: Full width at half maximum (FWHM) of the intensity profiles at 90 degrees in the transverse plane (y-axis of the system).

Recon. Algorithm	FWHM - Centre (mm)		FWHM - 50% Rad. (mm)		FWHM - 75% Rad. (mm)	
	Uncorr.	Corr.	Uncorr.	Corr.	Uncorr.	Corr.
2D-FBP	4.35 ± 0.61	4.52 ± 0.38	4.11 ± 0.88	3.94 ± 0.35	4.36 ± 1.15	4.39 ± 0.39
3D-FBP	5.35 ± 1.04	5.31 ± 0.73	5.78 ± 1.79	5.75 ± 0.96	5.94 ± 2.19	5.89 ± 0.89
OSEM	2.45 ± 0.25	2.36 ± 0.18	3.17 ± 0.47	3.16 ± 0.27	3.25 ± 0.60	3.16 ± 0.23

Table 6.4: Full width at half maximum (FWHM) of the intensity profiles at 90 degrees in the coronal plane (z-axis of the system).

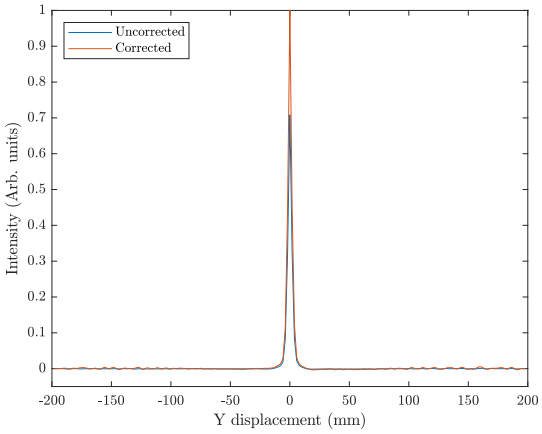

(a) Centre source (y-axis)

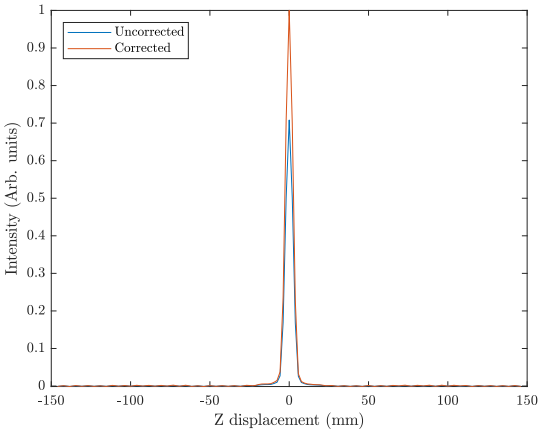

(b) Centre source (z-axis)

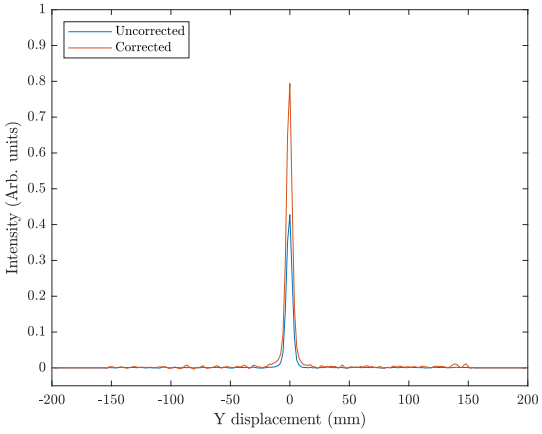

(c) 50% rad. source (y-axis)

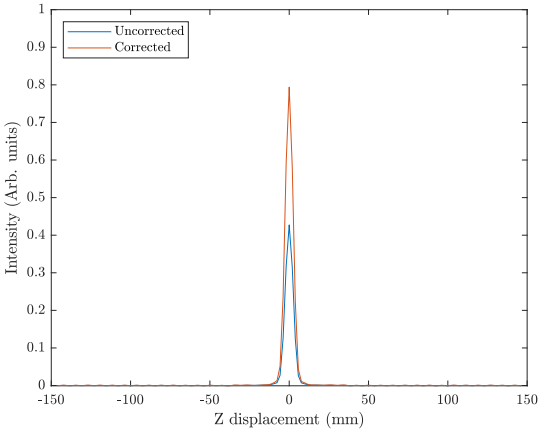

(d) 50% rad. source (z-axis)

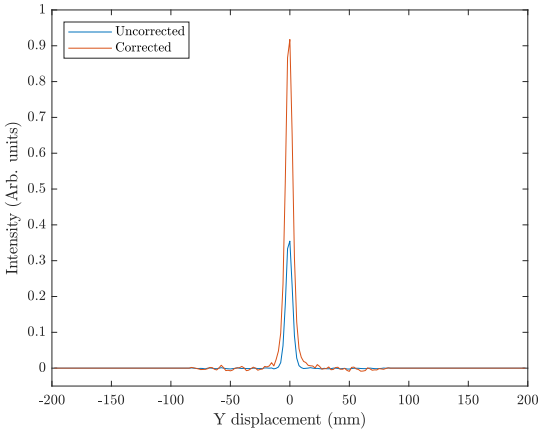

(e) 75% rad. source (y-axis)

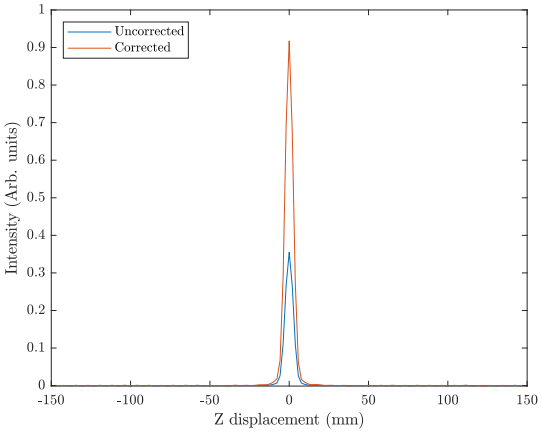

(f) 75% rad. source (z-axis)

Figure 6.8: Intensity profile of the FBP3DRP-reconstructed image. The slices are taken along the y and z axes, vertically, in the transverse and coronal planes of the scanner, respectively.

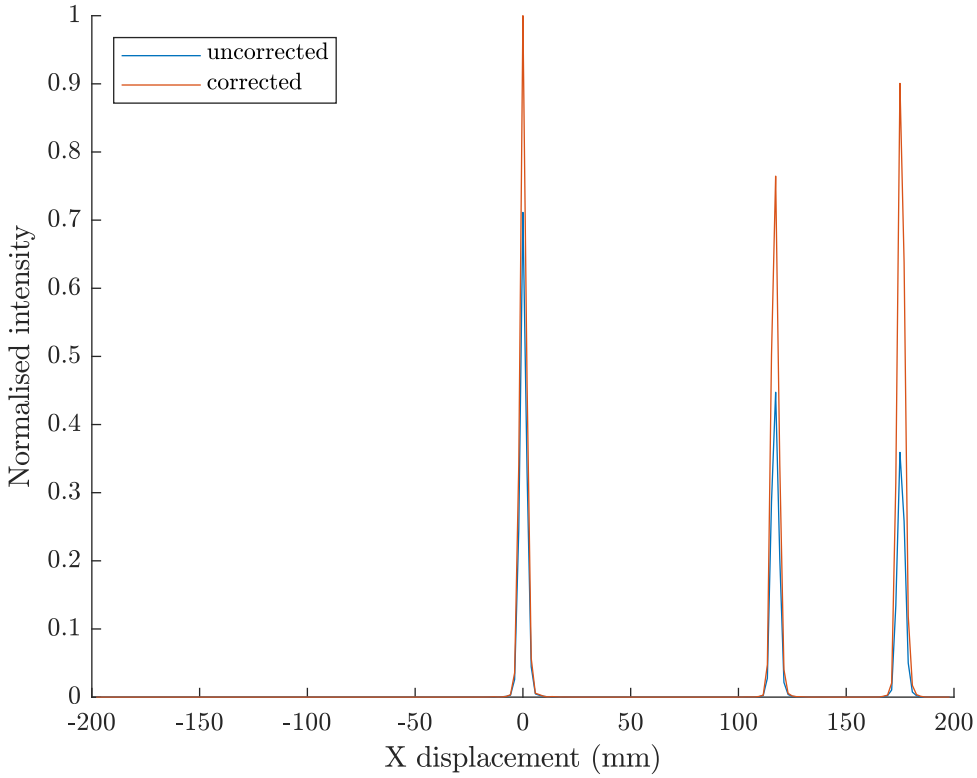

Figure 6.9: Intensity profile of the OSEM-reconstructed image. The slice is taken along the x axis in the transverse plane of the scanner.

6.4 Discussion

The uncorrected images exhibit a substantial variation in brightness from the inner to the outer point source. With corrections applied, the brightness of the sources has become much more uniform, with those positioned at 50% and 75% of the inner radius of the scanner more closely matching the brightness of the central point source. This is especially apparent when comparing Subfigures (a)-(b) or (c)-(d) in Figures 6.2, 6.3 or 6.4. In terms of brightness only, 2D FBP is almost perfectly normalised, although the 50% radius source is somewhat under-corrected in 3D FBP and OSEM (see Figures 6.5, 6.7 and 6.9). There is quite a large amount of noise present in the normalisation image (despite the simulation of 5 billion primaries), which may explain the non-uniformity to some degree. This may be able to be improved if resources were available to store and process a much larger number of events, which will be investigated further in future studies.

The two off-centre sources have become somewhat elongated in the y-dimension when analytically reconstructed. This is likely due to a geometric effect, caused by

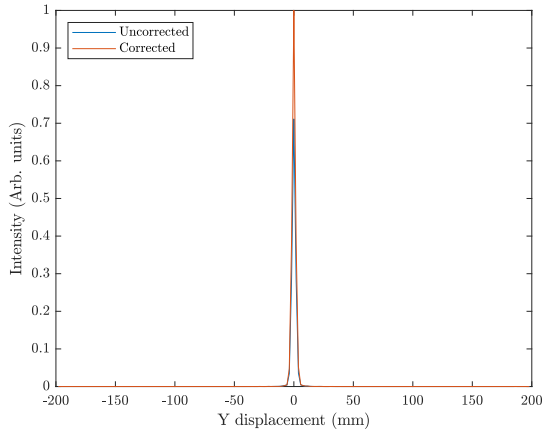

(a) Centre source (y-axis)

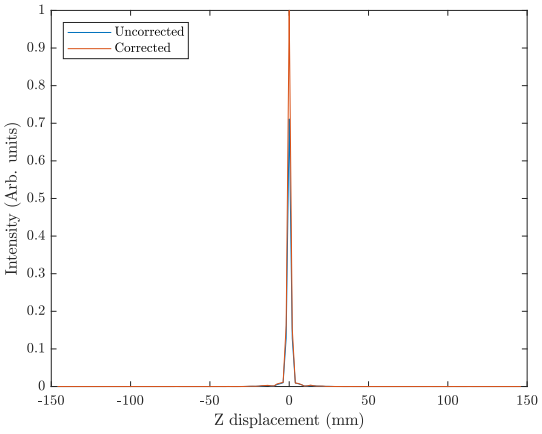

(b) Centre source (z-axis)

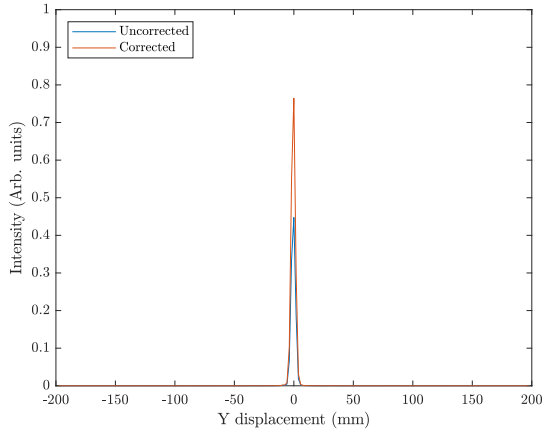

(c) 50% rad. source (y-axis)

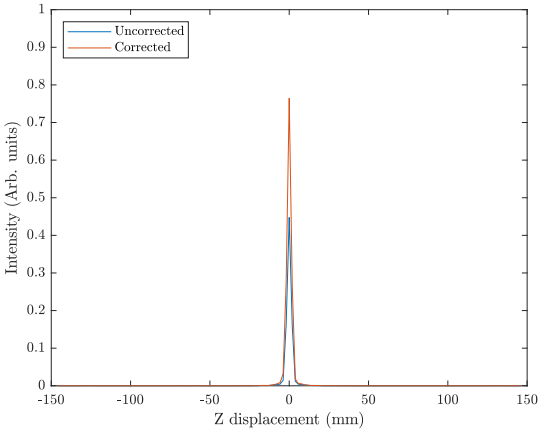

(d) 50% rad. source (z-axis)

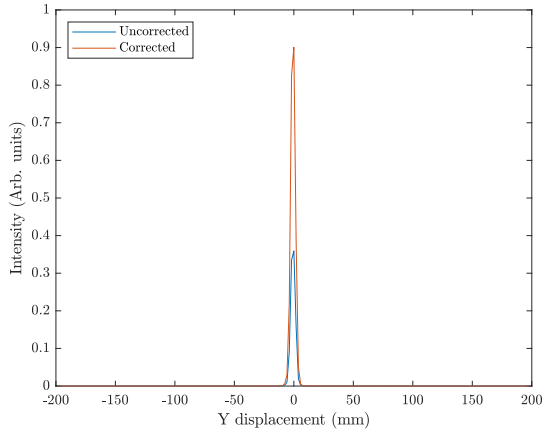

(e) 75% rad. source (y-axis)

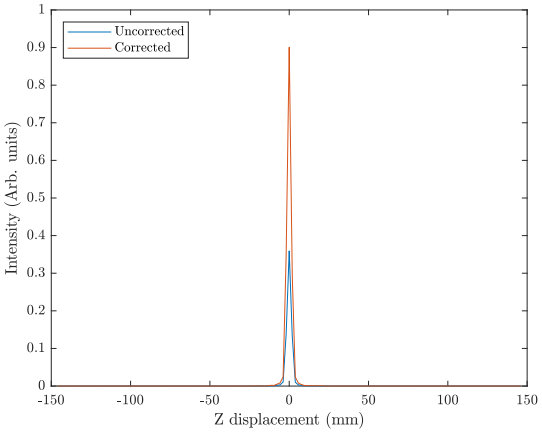

(f) 75% rad. source (z-axis)

Figure 6.10: Intensity profile of the OSEM-reconstructed image. The slices are taken along the y and z axes, vertically, in the transverse and coronal planes of the scanner, respectively.

under-sampling at the periphery (simulations had quite a short acquisition time due to computational load and sensitivity will be generally lower at these two sources, compared to the middle of the scanner). Artefacts, which can be predominantly observed along the y-dimension, are unfortunately exaggerated by normalisation (particularly for 2D-FBP), suggesting that the simplified approach to generation of the normalisation sinogram has introduced some systemic bias. It is substantially mitigated by the use of an iterative reconstruction algorithm. The effect is especially apparent in the results listed in Table 6.3 (FWHM in tangential direction), where the 75%-radius point source (with a physical diameter of 2 mm diameter) expands to 8.32 mm for the 2D-FBP reconstruction. By contrast, the tangential diameter of the point source in the image reconstructed via OSEM is 4.41 mm, which is much closer to the diameter in the radial direction (of 3.84 mm). The OSEM algorithm produced the most uniform reconstruction in all dimensions, with the majority of values for the FWHM well within 4 mm resolution (right down to 2.36 mm for the central source on the z axis). In almost all other cases, the applied corrections reduced the FWHM of the intensity curves and hence improved the spatial resolution of the system. The mean positron range for ^{18}F in water is approximately 0.8 mm with an absolute maximum of 2.4 mm; therefore, a reconstructed FWHM of the order of 4 mm for a 2 mm diameter source is quite reasonable.

OSEM clearly produces the best quality image of all reconstruction methods, although this comes at the cost of greatly increased reconstruction time. With all but one reconstructed point source having a FWHM of less than 4 mm, the spatial resolution is at least on par with, if not superior to current full body PET systems using discrete scintillation detectors. The voxel size used in this system was set as 1.922 mm$\times$1.922 mm$\times$1.922 mm (which is comparable to the diameter of the point sources), however, this choice is *fully configurable* depending on the parameters specified for the virtual ring used in reconstruction. With a larger number of recorded annihilation events it may possible to further reduce the virtual voxel size, although this will require a cleaner normalisation image to avoid degradation of the SNR of the corrected image. To fully evaluate this idea, one possible approach is simulating using primaries only and then introducing a deliberate error into the recorded position to properly model the localisation algorithm, using a statistical

model based on the error distributions presented in Section 3.3.3. This approach will be the subject of future work.

6.5 Conclusion

A continuous cylindrical shell PET system using the coincidence detection methods proposed in Chapter 5 and the LOR localisation techniques introduced in Chapter 4 was simulated with three point sources placed at different radial positions within the scanner's FOV. This work establishes the capability of the presented system in reconstructing a simple test image and thereby demonstrated the feasibility of the system. Three reconstruction algorithms were used to transform the image from sinogram space into image space; all three algorithms, 2D-FBP, 3D-FBP and OSEM, produced an image which clearly displayed the three sources with good spatial resolution, although artefacts produced by the analytic algorithms degraded the image somewhat along its y-axis. OSEM produced the highest-quality images, exhibiting good spatial resolution, with almost all measurements of the intensity profiles being less than <4 mm FWHM in width. This Chapter has demonstrated the basic process for image reconstruction; however, further work will be required to fully optimise the spatial resolution of the scanner design.

Chapter 7

Conclusion

At the beginning of this work, two critical aspects of PET were identified as potential opportunities for improvement: sensitivity to the high energy gamma photons produced during annihilation events and the spatial resolution of the reconstructed images. This work sought to develop an alternative pathway towards cost-effective improvements to both of these attributes.

The sensitivity of PET scanners is largely a function of both the solid angle coverage of the scintillation detectors as well as the thickness of the scintillator [23], while spatial resolution is based on a number of physical factors (chiefly positron range and acollinearity) as well as properties of the scanner architecture (e.g. dimensions of discrete crystal scintillators and the bore radius) [23, 24]. In this work, we hypothesised that a cylindrical-shell monolithic scintillator fabricated from either nanocomposite or transparent ceramic scintillator materials would enable the use of a thick scintillation layer with no dead space due to pixellation or block boundaries, which is able to capture a large fraction of emitted photons. Position estimation in the monolithic slab is accomplished by analysing scintillation photon distributions, rather than simply measuring the yield in a discrete detector. Consequently, spatial resolution is no longer limited by crystal dimensions - only by intrinsic physical properties of the positron annihilation process (range and acollinearity). In addition, a completely continuous ring would not suffer from the edge effects that can degrade position estimation in conventional flat monolithic scintillator slabs.

Section 7.1 of this Chapter briefly summarises how the aims of this Thesis were accomplished and lists the key findings of each step in the process, from initial

concept to architecture design, operation and finally performance characterisation. Section 7.2 discusses several potential future directions for this work.

7.1 Summary

Chapter 2 reviewed the underlying physics behind PET, and explored current developments in PET photodetectors, scintillator materials and image reconstruction techniques. It was apparent that inorganic scintillator / polymer matrix nanocomposites and transparent ceramic garnet scintillators have not previously been applied to any significant extent in PET, and that their flexible physical properties made them excellent candidates for application in a continuous cylindrical shell PET system. With many varieties and formulations of these materials available, the range of possible designs for a PET scanner utilising them was very large and quite different from those based on conventional scintillator materials. The physical properties of a nanocomposite could vary substantially based on scintillator loading factor, size of the nanoparticles, doping concentration and fabrication processes. These materials were also found to be highly susceptible to optical scattering due to Rayleigh effects and grain boundaries (for nanocomposites and ceramics respectively), which suggested that the usefulness of the materials for position-sensitive gamma detection (in monolithic scintillation detectors) may deteriorate if the slab thickness increased beyond some optimum value. Therefore, to effectively utilise these new materials in the proposed continuous cylindrical shell PET scanner, it was necessary to first model and simulate suitable materials, and then develop a systematic approach to optimising the slab thickness to maximise its usefulness in this application. The literature review also indicated that the most appropriate photodetectors for the proposed PET system would be silicon photomultipliers (SiPMs), which are fast, have high enough gain for accurate and sensitive photon counting, and are physically small enough to be used on both the inner and outer surfaces of the cylinder.

A critical question in the design of PET system is the choice of scintillation material. This question is even more complex if the choice is to be made amongst nanocomposite or transparent ceramic materials, as the optical scattering and attenuation of the scintillator cannot be ignored (particularly for designs using monolithic

scintillators) as it is for PET systems utilising discrete monocrystalline scintillators. In particular, it is necessary to determine the optimal thickness for each material, where 'optimal' is defined in terms of a metric specifically relevant to monolithic PET. A range of promising scintillation materials, including five nanocomposites and four transparent ceramic garnets, were simulated in Chapter 3 using GATE [160, 161]. A general method was developed for finding the optimal thickness - which we defined as *the thickness which enables the greatest fraction of incident photons to be localised to within a specified distance to the true point of interaction*. The method can potentially be adapted to any localisation algorithm and any nanocomposite / ceramic scintillator material (even regular crystal scintillators if desired) and allows the user to tune the process to the required level of accuracy. The position estimation algorithm used in this work is similar to other analytic algorithms which use least-squares fitting [63, 77], although for these materials it was necessary to introduce a scattering term to correctly model the photon distribution at the photodetector surface.

In general, the performance of the transparent ceramic garnet scintillators was superior to that of the nanocomposites due to their relatively high density and effective atomic number, despite having relatively short optical attenuation lengths. In particular, GLuGAG:Ce stood out as having the best overall characteristics. LaF_3:Ce with a polystyrene matrix was the best performing nanocomposite thanks to a high loading factor. It also had a good refractive index match between the nanoparticle and matrix materials, leading to better optical transmittivity compared to the other nanocomposites. These materials became the focus for the remaining simulation work in this Thesis.

The next stages of the project involved the design and simulation of the continuous cylindrical shell PET scanner in GATE, using the materials identified in Chapter 3 (GLuGAG:Ce and LaF_3:Ce / polystyrene), with the cylindrical shells modelled at the corresponding optimal thicknesses (optimised for maximum probability of interaction localisation to within 5 mm of the true position) and the inner and outer diameters adjusted to fit an integer number of photodetectors on each surface. Three point sources were simulated; one at the centre of the FOV and two others offset by 50% and 75% of the inner radius of the scanner. The general

principles used to localise the endpoints of the LORs is described in detail in Chapter 3, however, the method needs to be adapted for the cylindrical shell geometry. Therefore, in Chapter 4 the localisation technique was extended from a planar slab to a full cylindrical ring. The median error of the LOR position was 1.27-1.62 mm for GLuGAG:Ce (depending on the location of the source) and 3.12-4.13 mm for LaF_3:Ce / polystyrene indicating that the architecture is indeed feasible and the degradation of performance with increased radial displacement is moderate.

At practical activity rates, the likelihood of multiple temporally-overlapping events across the entire scintillator volume rapidly increases. Chapter 5 deals with this issue, introducing a deconvolution-based method for coincidence detection which aims to separate these overlapping events. Scintillation photons are released with a fast rise time and relatively slow decay, causing some uncertainty over the location of events which are produced in quick succession (i.e. the decaying photon burst from one event may overlap - either in space or time - with another event). To overcome this problem, Chapter 5 details how pixels are first grouped spatially to produce a reduced number of time-domain optical flux signals, which are then temporally deconvolved by the impulse response of the scintillator, resulting in an impulse train where each impulse indicates the onset of a scintillation event. Coincidences were identified when two of these impulses occurred in the same timing bin and different spatial regions of the cylinder. Photon maps were then gathered around the most highly populated areas in the potential coincidence event. The percentage of events able to be detected by the scanner architecture was 32.79%, which is a limitation imposed by the solid angle coverage of the geometry of the specific scanner that was simulated. After implementing the proposed coincidence timing algorithm, the proportion of true events (total positron annihilations) actually able to be detected was 17.42%, the percentage of missed detections (false negatives, typically due to insufficient energy deposition leading to a weak optical signal) was 15.37% , and the percentage of randoms (false positives) was 2.08% . From this, it is observed that the sensitivity of the scanner is quite good, considering that most 'whole body' scanners have a coincidence detection sensitivity of $\sim$2% [2]. The potential certainly exists for further reductions in the number of false negatives; however, the essential result of this work is that the algorithm is good enough to generate data for image

reconstruction.

Finally, in Chapter 6 the image reconstruction capabilities of the scanner architecture are demonstrated. The algorithms used are from STIR [156]. Several corrections are made on the output sinogram before reconstructing, including normalisation, attenuation and random correction. Good image reconstruction was achieved with two analytic algorithms (2D filtered backprojection and 3D FBP with reprojection (3DFBPRP)) and one iterative algorithm (OSEM). The FWHM of the 2 mm diameter sources was measured to be less than 4 mm in almost all cases for OSEM (in x, y, and z dimensions), but with a slight smearing evident in the y dimension for the analytic algorithms. It is expected that this could be significantly reduced if a deconvolution method was applied to correct for positron range.

These results indicate a clear improvement in sensitivity while achieving good spatial resolution compared to typical preclinical whole-body PET scanners. Simulating a PET system in GATE using full optical tracking produces a huge volume of data and requires a very large amount of computational resources over an extended period of time, which limits the number of events that could be used in the reconstructions presented in this Thesis. The reconstructed images shown in Chapter 6 are essentially a product of only 3 seconds of simulated scan time for three 3 MBq ^{18}F sources.

7.2 Recommendations & Future Work

This Thesis has established the basic premise that a continuous cylindrical shell monolithic-scintillator PET system utilising transparent ceramic garnet or nanocomposite scintillators is feasible. However, the problem is by no means completely solved, and considerable opportunities for further research and development remain.

The most logical next step in the evolution of this scanner would be a full performance characterisation using NEMA 2008 standard testing [182]. The primary reason this has not yet been done is due to the processing and storage resources needed for a fully optical simulation with the parameters outlined in the standard. It would perhaps be more manageable to perform this testing using primaries only. This could potentially be achieved using a statistical model of the localisation al-

gorithm performance with a particular scintillator material which can degrade the exact points of interaction with the scintillator as recorded by GATE, essentially by adding a random 3D vector generated using statistical distributions based on the tables in Section 3.3.3. This method could also be used to generate a much higher quantity of data for the image reconstruction, potentially allowing for the voxel size to be reduced (since it is reliant on a virtual cylinder only) and theoretically at least, a higher SNR and spatial resolution than what has been presented here. This approach would need to be validated against fully optical simulations to confirm that it does not introduce additional errors or result in an overestimation of the reconstructed image quality.

The deconvolution-based coincidence detection method presented in Chapter 5 was successful in minimising pulse pile-up in our detector architecture and allowed for a sufficient fraction of coincidences to be identified for image reconstruction. However, coincidence time-stamping is limited by our temporal sampling of the signal (with a relatively course 10 ns resolution) and is therefore not currently time-of-flight capable. Future work would potentially seek to enhance the algorithm to improve timing capability to sub-nanosecond resolution (and therefore become TOF capable); using fully 3D pulse shape analysis (2 dimensions spatial and 1 dimension temporal), to jointly estimate these parameters.

Chapter 6 only presented results for a single material (again, chiefly due to processing time). Evaluation of simulated scanners optimised to use other evaluated materials would also be of great value, since in practice economic considerations may dominate the material selection criteria rather than strictly technical considerations.

We have demonstrated the geometrical flexibility of the materials used with a fully monolithic cylindrical shell. An interesting alternative to the cylindrical shell geometry (especially for brain imaging) might be a partially truncated spherical shell system. Several spherical PET system designs based on discrete crystal scintillators or even liquid scintillators have been previously proposed [80, 131, 183, 82] however, few truly spherical PET systems have been actually implemented. Nanocomposites or ceramics may be a good solution for this geometry, as they can be formed into complex shapes relatively easily. A lot of the methods presented in this work may also be applied to a spherical geometry - the algorithms used for position estimation,

LOR determination and coincidence detection via deconvolution could all be adapted to a monolithic spherical shell and the most appropriate materials and corresponding thicknesses have already been discussed.

To date, this work has only been evaluated via simulations and would need to be experimentally validated. The first step would be to confirm that the materials evaluated in Chapter 3 perform as expected and that the optimal thickness of each agree with our modelling. The practical engineering aspects of a physical implementation of the proposed scanner design present significant technical challenges, but should be within the capabilities of modern non-planar circuit fabrication techniques; nevertheless, creating a physical embodiment of the proposed scanner would be a major research project in its own right.

7.3 Concluding Remarks

In summary, the feasibility of a continuous cylindrical shell PET scanner fabricated with nanocomposite or transparent ceramic scintillators has been established and shows great promise as a pathway towards high sensitivity whole-body or total-body PET with good spatial resolution. We believe that with the radically simplified scintillator fabrication enabled by this geometry, the costs of our proposed design will be substantially lower than for a conventional approach based on discrete crystal scintillators.

Bibliography

[1] Gordon L Brownell. "A history of positron imaging". In: *Physics Research Laboratory, Massachusetts General Hospital, MIT* (1999), p. 1.

[2] Piotr J Slomka, Tinsu Pan, and Guido Germano. "Recent advances and future progress in PET instrumentation". In: *Seminars in nuclear medicine*. Vol. 46. 1. Elsevier. 2016, pp. 5–19.

[3] Simon R. Cherry et al. "Total-Body PET: Maximizing Sensitivity to Create New Opportunities for Clinical Research and Patient Care". In: *Journal of Nuclear Medicine* 59.1 (Sept. 2017), pp. 3–12. DOI: 10.2967/jnumed.116.184028. URL: https://doi.org/10.2967/jnumed.116.184028.

[4] Simon R Cherry et al. "Total-body imaging: Transforming the role of positron emission tomography." In: *Science translational medicine* 9.381 (2017).

[5] S Surti, M E Werner, and J S Karp. "Study of PET scanner designs using clinical metrics to optimize the scanner axial FOV and crystal thickness". In: *Physics in Medicine and Biology* 58.12 (May 2013), pp. 3995–4012. DOI: 10.1088/0031-9155/58/12/3995.

[6] S Surti and J S Karp. "Impact of detector design on imaging performance of a long axial field-of-view, whole-body PET scanner". In: *Physics in Medicine and Biology* 60.13 (June 2015), pp. 5343–5358. DOI: 10.1088/0031-9155/60/13/5343.

[7] Stefaan Vandenberghe et al. "Recent developments in time-of-flight PET". In: *EJNMMI physics* 3.1 (2016), p. 3.

[8] Herman T Van Dam et al. "Sub-200 ps CRT in monolithic scintillator PET detectors using digital SiPM arrays and maximum likelihood interaction time estimation". In: *Physics in Medicine & Biology* 58.10 (2013), p. 3243.

[9] Habib Zaidi. *Quantitative analysis in nuclear medicine imaging*. Springer, 2006.

[10] Simon R Cherry, James A Sorenson, and Michael E Phelps. *Physics in nuclear medicine e-Book*. Elsevier Health Sciences, 2012.

[11] Dale L Bailey et al. *Positron emission tomography*. Springer, 2005.

[12] Oskar Klein and Yoshio Nishina. "The scattering of light by free electrons according to Dirac's new relativistic dynamics". In: *Nature* 122.3072 (1928), p. 398.

[13] T Ido et al. "Labeled 2-deoxy-D-glucose analogs. 18F-labeled 2-deoxy-2-fluoro-D-glucose, 2-deoxy-2-fluoro-D-mannose and 14C-2-deoxy-2-fluoro-D-glucose". In: *Journal of Labelled Compounds and Radiopharmaceuticals* 14.2 (1978), pp. 175–183.

[14] Hossein Jadvar and J Anthony Parker. *Clinical PET and PET/CT*. Springer Science & Business Media, 2005.

[15] S. Guhlke, A.M. Verbruggen, and S. Vallabhajosula. "Radiochemistry and Radiopharmacy". In: *Clinical Nuclear Medicine*. Ed. by H.J. Biersack and L.M. Freeman. Springer, 2007. Chap. 2, pp. 34–72.

[16] Anatoliy Granov, Leonid Tiutin, and Thomas Schwarz. *Positron emission tomography*. Springer Science & Business Media, 2013.

[17] Heinrich R Schelbert et al. "N-13 ammonia as an indicator of myocardial blood flow." In: *Circulation* 63.6 (1981), pp. 1259–1272.

[18] P L Jager et al. "Radiolabeled amino acids: basic aspects and clinical applications in oncology." In: *Journal of nuclear medicine* 42.3 (2001), pp. 432–445.

[19] Tom K Lewellen. "Recent developments in PET detector technology". In: *Physics in Medicine & Biology* 53.17 (2008), R287.

[20] Thomas K Lewellen. "The challenge of detector designs for PET". In: *American Journal of Roentgenology* 195.2 (2010), pp. 301–309.

[21] Wen Cai et al. “Synthesis of bulk-size transparent gadolinium oxide–polymer nanocomposites for gamma ray spectroscopy”. In: *Journal of Materials Chemistry C* 1.10 (2013), pp. 1970–1976.

[22] William W Moses and Marcus Ullisch. “Factors influencing timing resolution in a commercial LSO PET camera”. In: *IEEE Transactions on Nuclear Science* 53.1 (2006), pp. 78–85.

[23] Eric Berg and Simon R Cherry. “Innovations in instrumentation for positron emission tomography”. In: *Seminars in nuclear medicine*. Vol. 48. 4. Elsevier. 2018, pp. 311–331.

[24] Ciprian Catana. “Development of dedicated brain PET imaging devices: recent advances and future perspectives”. In: *Journal of Nuclear Medicine* 60.8 (2019), pp. 1044–1052.

[25] Stefano Del Sordo et al. “Progress in the development of CdTe and CdZnTe semiconductor radiation detectors for astrophysical and medical applications”. In: *Sensors* 9.5 (2009), pp. 3491–3526.

[26] Paul Lecoq, Alexander Gektin, and Mikhail Korzhik. “Inorganic scintillators for detector systems: physical principles and crystal engineering”. In: 2nd ed. Springer, 2016. Chap. 8, pp. 289–311.

[27] A. Gektin. “Bulk Crystal Growth of Electronic, Optical and Optoelectronic Materials”. In: John Wiley & Sons, 2005. Chap. 12, pp. 357–386.

[28] Eric Berg et al. “Development and evaluation of mini-EXPLORER: a long axial field-of-view PET scanner for nonhuman primate imaging”. In: *Journal of Nuclear Medicine* 59.6 (2018), pp. 993–998.

[29] Emilie Roncali and Simon R Cherry. “Application of silicon photomultipliers to positron emission tomography”. In: *Annals of biomedical engineering* 39.4 (2011), pp. 1358–1377.

[30] Simon R Cherry et al. “MicroPET: a high resolution PET scanner for imaging small animals”. In: *IEEE Transactions on Nuclear Science* 44.3 (1997), pp. 1161–1166.

[31] William W Moses and SE Derenzo. “Prospects for time-of-flight PET using LSO scintillator”. In: *IEEE Transactions on Nuclear Science* 46.3 (1999), pp. 474–478.

[32] Glenn F Knoll. *Radiation detection and measurement*. John Wiley & Sons, 2010.

[33] Gaspar Delso et al. “Performance measurements of the Siemens mMR integrated whole-body PET/MR scanner”. In: *Journal of nuclear medicine* 52.12 (2011), pp. 1914–1922.

[34] Melanie Bergeron et al. “Performance evaluation of the LabPET APD-based digital PET scanner”. In: *IEEE Transactions on Nuclear Science* 56.1 (2009), pp. 10–16.

[35] Yongfeng Yang et al. “A prototype PET scanner with DOI-encoding detectors”. In: *Journal of Nuclear Medicine* 49.7 (2008), pp. 1132–1140.

[36] Sibylle I Ziegler et al. “A prototype high-resolution animal positron tomograph with avalanche photodiode arrays and LSO crystals”. In: *European journal of nuclear medicine* 28.2 (2001), pp. 136–143.

[37] Kanai S Shah et al. “Position-sensitive avalanche photodiodes for gamma-ray imaging”. In: *IEEE Transactions on Nuclear Science* 49.4 (2002), pp. 1687–1692.

[38] A Tapfer et al. “Comparison of three approaches for timing optimization of a dual layer LSO-APD small animal PET scanner”. In: *World Congress on Medical Physics and Biomedical Engineering, September 7-12, 2009, Munich, Germany*. Springer. 2009, pp. 533–536.

[39] *Si APD (Avalanche Photodiode) Selection Guide - March 2019*. KAPD0001E08. Hamamatsu Photonics K.K. Mar. 2019.

[40] *Introduction to SiPM Technical Note*. Rev. 6.0. SensL Technologies, Ltd. Feb. 2017.

[41] Peter M Düppenbecker et al. “Development of an MRI compatible digital SiPM based PET detector stack for simultaneous preclinical PET/MRI”. In: *2012 IEEE Nuclear Science Symposium and Medical Imaging Conference Record (NSS/MIC)*. IEEE. 2012, pp. 3481–3483.

[42] B Dolgoshein et al. “Status report on silicon photomultiplier development and its applications”. In: *Nuclear Instruments and Methods in Physics Research Section A: Accelerators, Spectrometers, Detectors and Associated Equipment* 563.2 (2006), pp. 368–376.

[43] Marcelo F Di Carli et al. “Clinical myocardial perfusion PET/CT”. In: *Journal of Nuclear Medicine* 48.5 (2007), pp. 783–793.

[44] Claudio Piemonte et al. “Recent developments on silicon photomultipliers produced at FBK-irst”. In: *2007 IEEE Nuclear Science Symposium Conference Record*. Vol. 3. IEEE. 2007, pp. 2089–2092.

[45] William G Oldham, Reid R Samuelson, and Paolo Antognetti. “Triggering phenomena in avalanche diodes”. In: *IEEE Transactions on electron devices* 19.9 (1972), pp. 1056–1060.

[46] Claudio Piemonte. “A new silicon photomultiplier structure for blue light detection”. In: *Nuclear Instruments and Methods in Physics Research Section A: Accelerators, Spectrometers, Detectors and Associated Equipment* 568.1 (2006), pp. 224–232.

[47] Fabio Acerbi et al. “NUV silicon photomultipliers with high detection efficiency and reduced delayed correlated-noise”. In: *IEEE transactions on Nuclear Science* 62.3 (2015), pp. 1318–1325.

[48] Claudio Piemonte et al. “Performance of NUV-HD silicon photomultiplier technology”. In: *IEEE Transactions on Electron Devices* 63.3 (2016), pp. 1111–1116.

[49] Alberto Gola et al. “SiPM optical crosstalk amplification due to scintillator crystal: effects on timing performance”. In: *Physics in Medicine & Biology* 59.13 (2014), p. 3615.

[50] Marnix C Maas et al. “Monolithic scintillator PET detectors with intrinsic depth-of-interaction correction”. In: *Physics in Medicine & Biology* 54.7 (2009), p. 1893.

[51] K Li et al. “A feasibility study of PETiPIX: an ultra high resolution small animal PET scanner”. In: *Journal of Instrumentation* 8.12 (2013), P12004.

[52] K Li et al. “A new virtual ring-based system matrix generator for iterative image reconstruction in high resolution small volume PET systems”. In: *Physics in Medicine and Biology* 60.17 (Aug. 2015), pp. 6949–6973. DOI: 10.1088/0031-9155/60/17/6949. URL: https://doi.org/10.1088/0031-9155/60/17/6949.

[53] Craig S Levin. “Design of a high-resolution and high-sensitivity scintillation crystal array for PET with nearly complete light collection”. In: *IEEE Transactions on Nuclear Science* 49.5 (2002), pp. 2236–2243.

[54] Frances WY Lau et al. “Analog signal multiplexing for PSAPD-based PET detectors: simulation and experimental validation”. In: *Physics in Medicine & Biology* 55.23 (2010), p. 7149.

[55] A Vandenbroucke et al. “Performance characterization of a new high resolution PET scintillation detector”. In: *Physics in Medicine & Biology* 55.19 (2010), p. 5895.

[56] WW Moses et al. “A room temperature LSO/PIN photodiode PET detector module that measures depth of interaction”. In: *IEEE Transactions on Nuclear Science* 42.4 (1995), pp. 1085–1089.

[57] Yongfeng Yang et al. “Depth of interaction resolution measurements for a high resolution PET detector using position sensitive avalanche photodiodes”. In: *Physics in Medicine & Biology* 51.9 (2006), p. 2131.

[58] Junwei Du, Xiaowei Bai, and Simon R Cherry. “A depth-of-interaction encoding PET detector module with dual-ended readout using large-area silicon photomultiplier arrays”. In: *Physics in Medicine & Biology* 63.24 (2018), p. 245019.

[59] E Costa, E Massaro, and L Piro. "A BGO-CsI (Tl) phoswich: A new detector for X-and γ-ray astronomy". In: *Nuclear Instruments and Methods in Physics Research Section A: Accelerators, Spectrometers, Detectors and Associated Equipment* 243.2-3 (1986), pp. 572–577.

[60] J-B Mosset et al. "Development of an optimized LSO/LuYAP phoswich detector head for the Lausanne ClearPET demonstrator". In: *IEEE transactions on nuclear science* 53.1 (2006), pp. 25–29.

[61] Chen-Ming Chang, Joshua W Cates, and Craig S Levin. "Time-over-threshold for pulse shape discrimination in a time-of-flight phoswich PET detector". In: *Physics in Medicine & Biology* 62.1 (2016), p. 258.

[62] Marnix C Maas et al. "Experimental characterization of monolithic-crystal small animal PET detectors read out by APD arrays". In: *IEEE Transactions on Nuclear Science* 53.3 (2006), pp. 1071–1077.

[63] Zhi Li et al. "Nonlinear least-squares modeling of 3D interaction position in a monolithic scintillator block". In: *Physics in Medicine & Biology* 55.21 (2010), p. 6515.

[64] Peter Bruyndonckx et al. "Neural network-based position estimators for PET detectors using monolithic LSO blocks". In: *IEEE Transactions on Nuclear Science* 51.5 (2004), pp. 2520–2525.

[65] Valerio Tabacchini et al. "Improved image quality using monolithic scintillator detectors with dual-sided readout in a whole-body TOF-PET ring: a simulation study". In: *Physics in Medicine & Biology* 62.5 (2017), p. 2018.

[66] Nan Zhang et al. "Anode position and last dynode timing circuits for dual-layer BGO scintillator with PS-PMT based modular PET detectors". In: *IEEE Transactions on Nuclear Science* 49.5 (2002), pp. 2203–2207.

[67] Christopher Thompson et al. "Comparison of single and dual layer detector blocks for pre-clinical MRI–PET". In: *Nuclear Instruments and Methods in Physics Research Section A: Accelerators, Spectrometers, Detectors and Associated Equipment* 702 (2013), pp. 56–58.

[68] Andy LaBella et al. “Prism Mirror Light Guide for Enhanced Gamma Ray Localization in PET”. In: *2019 IEEE Nuclear Science Symposium and Medical Imaging Conference (NSS/MIC)*. IEEE, pp. 1–4.

[69] Andy LaBella et al. “High Resolution Depth-Encoding PET Detector Module with Prismatoid Light Guide Array”. In: *Journal of Nuclear Medicine* (2020), jnumed–119.

[70] Andy LaBella et al. “Prismatoid light guide array for enhanced gamma ray localization in PET: a Monte Carlo simulation study of scintillation photon transport”. In: *Physics in Medicine & Biology* (2020).

[71] Hao Peng and Craig S. Levin. “Recent Developments of High-Performance PET Detectors”. In: *Medical Imaging: Technology and Applications*. Ed. by Troy Farncombe and Kris Iniewski. Boca Raton: CRC Press, 2013. Chap. 12, pp. 301–333.

[72] P Bruyndonckx et al. “Performance study of a PET detector module based on a continuous scintillator”. In: *IEEE transactions on nuclear science* 53.5 (2006), pp. 2536–2542.

[73] D Clément et al. “Development of a 3D position sensitive scintillation detector using neural networks”. In: *Nuclear Science Symposium, 1998. Conference Record. 1998 IEEE*. Vol. 3. IEEE. 1998, pp. 1448–1452.

[74] Jinhun Joung, Robert S Miyaoka, and Thomas K Lewellen. “cMiCE: a high resolution animal PET using continuous LSO with a statistics based positioning scheme”. In: *Nuclear Instruments and Methods in Physics Research Section A: Accelerators, Spectrometers, Detectors and Associated Equipment* 489.1-3 (2002), pp. 584–598.

[75] T Ling, TK Lewellen, and RS Miyaoka. “Depth of interaction decoding of a continuous crystal detector module”. In: *Physics in Medicine & Biology* 52.8 (2007), pp. 2213–2228.

[76] Herman T van Dam et al. “Improved nearest neighbor methods for gamma photon interaction position determination in monolithic scintillator PET detectors”. In: *IEEE Transactions on Nuclear Science* 58.5 (2011), pp. 2139–2147.

[77] Jorge Cabello et al. “Simulation study of PET detector limitations using continuous crystals”. In: *Physics in Medicine & Biology* 60.9 (2015), pp. 3673–3694.

[78] P Conde et al. “Determination of the interaction position of gamma photons in monolithic scintillators using neural network fitting”. In: *IEEE Transactions on Nuclear Science* 63.1 (2016), pp. 30–36.

[79] LA Galin. “A point source of luminous radiation in a scattering medium”. In: *Journal of Applied Mathematics and Mechanics* 23.2 (1959), pp. 428–435.

[80] ZH Cho, KS Hong, and SK Hilal. “Spherical positron emission tomograph (S-PET) I-performance analysis”. In: *Nuclear Instruments and Methods in Physics Research* 225.2 (1984), pp. 422–438.

[81] David C Ficke, John T Hood, and Michel M Ter-Pogossian. “A spheroid positron emission tomograph for brain imaging: a feasibility study”. In: *Journal of Nuclear Medicine* 37.7 (1996), pp. 1219–1225.

[82] Nayerehalsadat Mortazavi Moghaddam et al. “Preliminary design and simulation of a spherical brain PET system (SBPET) with liquid xenon as scintillator”. In: *Nukleonika* 54.1 (2009), pp. 33–38.

[83] Siwei Xie et al. “LOR-PET: a novel PET camera constructed with a monolithic scintillator ring”. In: *2017 IEEE Nuclear Science Symposium and Medical Imaging Conference (NSS/MIC)*. IEEE. 2017, pp. 1–3.

[84] Suleman Surti and Joel S Karp. “Advances in time-of-flight PET”. In: *Physica medica* 32.1 (2016), pp. 12–22.

[85] Virginia Ch Spanoudaki and Craig S Levin. “Photo-detectors for time of flight positron emission tomography (ToF-PET)”. In: *Sensors* 10.11 (2010), pp. 10484–10505.

[86] Suleman Surti. “Update on time-of-flight PET imaging”. In: *Journal of Nuclear Medicine* 56.1 (2015), pp. 98–105.

[87] Brian F Hutton, Kjell Erlandsson, and Kris Thielemans. “Advances in clinical molecular imaging instrumentation”. In: *Clinical and Translational Imaging* 6.1 (2018), pp. 31–45.

[88] Maurizio Conti. “Why is TOF PET reconstruction a more robust method in the presence of inconsistent data?” In: *Physics in Medicine & Biology* 56.1 (2010), p. 155.

[89] Abolfazl Mehranian and Habib Zaidi. “Impact of time-of-flight PET on quantification errors in MR imaging–based attenuation correction”. In: *Journal of Nuclear Medicine* 56.4 (2015), pp. 635–641.

[90] Michel Defrise, Ahmadreza Rezaei, and Johan Nuyts. “Time-of-flight PET data determine the attenuation sinogram up to a constant”. In: *Physics in Medicine & Biology* 57.4 (2012), p. 885.

[91] Ahmadreza Rezaei, Michel Defrise, and Johan Nuyts. “ML-reconstruction for TOF-PET with simultaneous estimation of the attenuation factors”. In: *IEEE transactions on medical imaging* 33.7 (2014), pp. 1563–1572.

[92] Kengo Shibuya et al. “Timing resolution improvement using DOI information in a four-layer scintillation detector for TOF-PET”. In: *Nuclear Instruments and Methods in Physics Research Section A: Accelerators, Spectrometers, Detectors and Associated Equipment* 593.3 (2008), pp. 572–577.

[93] Stefan Seifert, Herman T van Dam, and Dennis R Schaart. “The lower bound on the timing resolution of scintillation detectors”. In: *Physics in Medicine & Biology* 57.7 (2012), p. 1797.

[94] Markus P. Hehlen et al. “Nanocomposite Scintillators”. In: *Nanocomposite, Ceramic, and Thin Film Scintillators*. Ed. by Martin Nikl. Singapore: Pan Stanford Publishing Pte. Ltd., 2017. Chap. 2, pp. 25–77.

[95] M Moszyński et al. “Properties of the new LuAP: Ce scintillator”. In: *Nuclear Instruments and Methods in Physics Research Section A: Accelerators, Spectrometers, Detectors and Associated Equipment* 385.1 (1997), pp. 123–131.

[96] CL Melcher et al. “Crystal growth and scintillation properties of the rare earth oxyorthosilicates”. In: *Proceedings of the International Conference on Inorganic Scintillators and their Applications SCINT95, Delft University Press, The Netherlands*. 1996, p. 309.

[97] Ludivine Pidol et al. “High efficiency of lutetium silicate scintillators, Ce-doped LPS, and LYSO crystals”. In: *IEEE Transactions on Nuclear Science* 51.3 (2004), pp. 1084–1087.

[98] *Saint-Gobain Crystals: Lanthanum Bromide and Enhanced Lanthanum Bromide*. 2017. URL: `https://www.crystals.saint-gobain.com/sites/imdf.crystals.com/files/documents/lanthanum-material-data-sheet.pdf` (visited on).

[99] M. Moszyński et al. “Properties of the YAG:Ce scintillator”. In: *Nuclear Instruments and Methods in Physics Research Section A: Accelerators, Spectrometers, Detectors and Associated Equipment* 345.3 (1994), pp. 461–467.

[100] Eugene Hecht. *Optics*. 4th ed. San Francisco: Addison Wesley, 2002.

[101] C Zorn. “A pedestrian’s guide to radiation damage in plastic scintillators”. In: *Nuclear Physics B-Proceedings Supplements* 32 (1993), pp. 377–383.

[102] Edward A. McKigney et al. “Nanocomposite scintillators for radiation detection and nuclear spectroscopy”. In: *Nuclear Instruments and Methods in Physics Research Section A: Accelerators, Spectrometers, Detectors and Associated Equipment* 579.1 (2007), pp. 15–18.

[103] M.J. Berger et al. *XCOM: Photon Cross Section Database (version 1.5)*. `https://physics.nist.gov/PhysRefData/Xcom/html/xcom1.html`. 2010. (Visited on).

[104] Russell K. Feller et al. “Large-scale synthesis of CexLa1-xF3 nanocomposite scintillator materials”. In: *Journal of Materials Chemistry* 21.15 (2011), pp. 5716–5722.

[105] C. F. Bohren and D. R. Huffmann. “Absorption and Scattering of Light by Small Particles”. In: Weinheim: WILEY-VCH Verlag GmbH & Co. KGaA, 1998. Chap. 5, pp. 130–157.

[106] Changli Lü and Bai Yang. “High refractive index organic–inorganic nanocomposites: design, synthesis and application”. In: *Journal of Materials Chemistry* 19.19 (2009), pp. 2884–2901.

[107] Walter Caseri. “Nanocomposites of polymers and inorganic particles: preparation, structure and properties”. In: *Materials Science and Technology* 22.7 (2006), pp. 807–817.

[108] Mei Chee Tan, Swanand D. Patil, and Richard E. Riman. “Transparent Infrared-Emitting CeF3 :Yb-Er Polymer Nanocomposites for Optical Applications”. In: *ACS applied materials & interfaces* 2.7 (2010), pp. 1884–1891.

[109] Tong Li, Chunlin Zhou, and Ming Jiang. “UV absorption spectra of polystyrene”. In: *Polymer bulletin* 25.2 (1991), pp. 211–216.

[110] Walter Caseri. “Nanocomposites”. In: *The Chemistry of Nanostructured Materials*. Ed. by Peidong Yang. Singapore: World Scientific Publishing Co. Pte. Ltd., 2003. Chap. 13, pp. 359–386.

[111] D.V. Szabó and T. Hanemann. “Polymer nanocomposites for optical applications”. In: *Advances in Polymer Nanocomposites - Types and Applications*. Ed. by Fengge Gao. Cambridge: Woodhead Publishing Ltd., 2012. Chap. 17, pp. 567–604.

[112] Tasoula Kyprianidou-Leodidou, Walter Caseri, and Ulrich W Suter. “Size variation of PbS particles in high-refractive-index nanocomposites”. In: *The Journal of Physical Chemistry* 98.36 (1994), pp. 8992–8997.

[113] YuanQiao Rao and Samuel Chen. “Molecular composites comprising TiO2 and their optical properties”. In: *Macromolecules* 41.13 (2008), pp. 4838–4844.

[114] Mustafa M Demir and Gerhard Wegner. “Challenges in the preparation of optical polymer composites with nanosized pigment particles: a review on recent efforts”. In: *Macromolecular Materials and Engineering* 297.9 (2012), pp. 838–863.

[115] Takayuki Yanagida et al. “Comparative study of ceramic and single crystal Ce: GAGG scintillator”. In: *Optical Materials* 35.12 (2013), pp. 2480–2485.

[116] Xianqiang Chen et al. “Preparation and optical properties of transparent (Ce, Gd) 3Al3Ga2O12 ceramics”. In: *Journal of the American Ceramic Society* 98.8 (2015), pp. 2352–2356.

[117] Takayuki Yanagida et al. “Scintillation properties of transparent ceramic Pr: LuAG for different Pr concentration”. In: *IEEE Transactions on Nuclear Science* 59.5 (2012), pp. 2146–2151.

[118] Yuntao Wu et al. “Single crystal and optical ceramic multicomponent garnet scintillators: A comparative study”. In: *Nuclear Instruments and Methods in Physics Research Section A: Accelerators, Spectrometers, Detectors and Associated Equipment* 780 (2015), pp. 45–50.

[119] N.J. Cherepy et al. “Comparative gamma spectroscopy with SrI 2 (Eu), GYGAG (Ce) and Bi-loaded plastic scintillators”. In: *Nuclear Science Symposium Conference Record (NSS/MIC), 2010 IEEE*. IEEE. 2010, pp. 1288–1291.

[120] N.J. Cherepy et al. “High energy resolution with transparent ceramic garnet scintillators”. In: *Hard X-Ray, Gamma-Ray, and Neutron Detector Physics XVI*. Vol. 9213. International Society for Optics and Photonics. 2014, p. 921302.

[121] NJ Cherepy et al. “Transparent ceramic scintillators for gamma spectroscopy and MeV imaging”. In: *Hard X-Ray, Gamma-Ray, and Neutron Detector Physics XVII*. Vol. 9593. International Society for Optics and Photonics. 2015, 95930P.

[122] Furukawa. *Datasheet on Ce:GAGG and Pr:LuAG scintillator crystal*. `http://www.furukawa-denshi.co.jp/cgi-bin/pdfdata/20140428162950.pdf`. 2015. (Visited on).

[123] Richard O Duda and Peter E Hart. *Use of the Hough transformation to detect lines and curves in pictures*. Tech. rep. SRI INTERNATIONAL MENLO PARK CA ARTIFICIAL INTELLIGENCE CENTER, 1971.

[124] Johann Radon. “On the determination of functions from their integral values along certain manifolds”. In: *IEEE transactions on medical imaging* 5.4 (1986), pp. 170–176.

[125] Adam Alessio, Paul Kinahan, et al. “PET image reconstruction”. In: *Nuclear medicine* 1 (2006), pp. 1–22.

[126] Lucas Parra and Harrison H Barrett. "List-mode likelihood: EM algorithm and image quality estimation demonstrated on 2-D PET". In: *IEEE transactions on medical imaging* 17.2 (1998), pp. 228–235.

[127] Andrew J Reader et al. "Fast accurate iterative reconstruction for low-statistics positron volume imaging". In: *Physics in Medicine & Biology* 43.4 (1998), p. 835.

[128] Reader A. *Medical image reconstruction techniques [Video file]*. The Biomedical & Life Sciences Collection, Henry Stewart Talks. 2010. URL: `https://hstalks.com/bs/1663/`.

[129] GN Ramachandran and AV Lakshminarayanan. "Three-dimensional reconstruction from radiographs and electron micrographs: application of convolutions instead of Fourier transforms". In: *Proceedings of the National Academy of Sciences* 68.9 (1971), pp. 2236–2240.

[130] Gopal B Saha. *Basics of PET imaging: physics, chemistry, and regulations*. Springer, 2015.

[131] Zang-Hee Cho. *Foundations of medical imaging*. Wiley-Interscience, 1993.

[132] J Fessler. "Analytical tomographic image reconstruction methods". In: *Image Reconstruction: Algorithms and Analysis* 66 (2009), p. 67.

[133] TH Farquhar et al. "An investigation of filter choice for filtered back-projection reconstruction in PET". In: *IEEE transactions on nuclear science* 45.3 (1998), pp. 1133–1137.

[134] Margaret E Daube-Witherspoon and Gerd Muehllehner. "Treatment of axial data in three-dimensional PET". In: *Journal of nuclear medicine* 28.11 (1987), pp. 1717–1724.

[135] Andrew J Reader and Habib Zaidi. "Advances in PET image reconstruction". In: *PET clinics* 2.2 (2007), pp. 173–190.

[136] Robert M Lewitt, Gerd Muehllehner, and Joel S Karp. "Three-dimensional image reconstruction for PET by multi-slice rebinning and axial image filtering". In: *Physics in Medicine & Biology* 39.3 (1994), p. 321.

[137] Michel Defrise et al. “Exact and approximate rebinning algorithms for 3-D PET data”. In: *IEEE transactions on medical imaging* 16.2 (1997), pp. 145–158.

[138] James G Colsher. “Fully-three-dimensional positron emission tomography”. In: *Physics in Medicine & Biology* 25.1 (1980), p. 103.

[139] Paul E Kinahan and JG Rogers. “Analytic 3D image reconstruction using all detected events”. In: *IEEE Transactions on Nuclear Science* 36.1 (1989), pp. 964–968.

[140] C Labbé et al. *Description of the STIR implementation of FBP 3DRP*. `http://stir.sourceforge.net/documentation/STIR-FBP3DRP.pdf`. Accessed: 2019-06-02. 2008.

[141] Philippe P Bruyant. “Analytic and iterative reconstruction algorithms in SPECT”. In: *Journal of Nuclear Medicine* 43.10 (2002), pp. 1343–1358.

[142] Jeffrey A Fessler. “Penalized weighted least-squares image reconstruction for positron emission tomography”. In: *IEEE transactions on medical imaging* 13.2 (1994), pp. 290–300.

[143] Damian Borys, Katarzyna Szczucka-Borys, and Kamil Gorczewski. “System matrix computation for iterative reconstruction algorithms in SPECT based on direct measurements”. In: *International Journal of Applied Mathematics and Computer Science* 21.1 (2011), pp. 193–202.

[144] Habib Zaidi. “Relevance of accurate Monte Carlo modeling in nuclear medical imaging”. In: *Medical physics* 26.4 (1999), pp. 574–608.

[145] Vladimir Y Panin et al. “Fully 3-D PET reconstruction with system matrix derived from point source measurements”. In: *IEEE transactions on medical imaging* 25.7 (2006), pp. 907–921.

[146] Andrew J Reader. “The promise of new PET image reconstruction”. In: *Physica Medica* 24.2 (2008), pp. 49–56.

[147] Richard Gordon, Robert Bender, and Gabor T Herman. “Algebraic reconstruction techniques (ART) for three-dimensional electron microscopy and X-ray photography”. In: *Journal of theoretical Biology* 29.3 (1970), pp. 471–481.

[148] Lawrence A Shepp and Yehuda Vardi. “Maximum likelihood reconstruction for emission tomography”. In: *IEEE transactions on medical imaging* 1.2 (1982), pp. 113–122.

[149] Jorge Llacer. “Tomographic image reconstruction by eigenvector decomposition: Its limitations and areas of applicability”. In: *IEEE transactions on medical imaging* 1.1 (1982), pp. 34–42.

[150] Ana Iriarte et al. “System models for PET statistical iterative reconstruction: A review”. In: *Computerized Medical Imaging and Graphics* 48 (2016), pp. 30–48.

[151] H Malcolm Hudson and Richard S Larkin. “Accelerated image reconstruction using ordered subsets of projection data”. In: *IEEE transactions on medical imaging* 13.4 (1994), pp. 601–609.

[152] Peter J Green. “Bayesian reconstructions from emission tomography data using a modified EM algorithm”. In: *IEEE transactions on medical imaging* 9.1 (1990), pp. 84–93.

[153] Guobao Wang and Jinyi Qi. “Penalized likelihood PET image reconstruction using patch-based edge-preserving regularization”. In: *IEEE transactions on medical imaging* 31.12 (2012), pp. 2194–2204.

[154] Bing Bai, Quanzheng Li, and Richard M Leahy. “Magnetic resonance-guided positron emission tomography image reconstruction”. In: *Seminars in nuclear medicine*. Vol. 43. 1. Elsevier. 2013, pp. 30–44.

[155] Kjell Erlandsson et al. “MR imaging–guided partial volume correction of PET data in PET/MR imaging”. In: *PET clinics* 11.2 (2016), pp. 161–177.

[156] Kris Thielemans et al. “STIR: software for tomographic image reconstruction release 2”. In: *Physics in Medicine & Biology* 57.4 (2012), p. 867.

[157] Thibaut Merlin et al. “CASToR: a generic data organization and processing code framework for multi-modal and multi-dimensional tomographic reconstruction”. In: *Physics in Medicine & Biology* 63.18 (2018), p. 185005.

[158] J Fessler. *Michigan Image Reconstruction Toolbox*. `https://web.eecs.umich.edu/~fessler/code/`. (Visited on).

[159] Takayuki Yanagida et al. “Evaluation of properties of YAG (Ce) ceramic scintillators”. In: *IEEE transactions on nuclear science* 52.5 (2005), pp. 1836–1841.

[160] Sébastien Jan et al. “GATE: a simulation toolkit for PET and SPECT”. In: *Physics in Medicine & Biology* 49.19 (2004), pp. 4543–4561.

[161] S. Jan et al. “GATE V6: a major enhancement of the GATE simulation platform enabling modelling of CT and radiotherapy”. In: *Physics in Medicine & Biology* 56.4 (2011), pp. 881–901.

[162] Sea Agostinelli et al. “GEANT4—a simulation toolkit”. In: *Nuclear instruments and methods in physics research section A: Accelerators, Spectrometers, Detectors and Associated Equipment* 506.3 (2003), pp. 250–303.

[163] Marnix C Maas et al. “Model of the point spread function of monolithic scintillator PET detectors for perpendicular incidence”. In: *Medical physics* 37.4 (2010), pp. 1904–1913.

[164] DJ Jan van der Laan et al. “Optical simulation of monolithic scintillator detectors using GATE/GEANT4”. In: *Physics in Medicine & Biology* 55.6 (2010), p. 1659.

[165] Dennis Wright and Sébastien Incerti. *A SHORT GUIDE TO CHOOSING PHYSICS LISTS*. 2011. URL: `http://geant4.in2p3.fr/IMG/pdf_PhysicsLists.pdf` (visited on).

[166] DJ Van Der Laan et al. “Using Cramér-Rao theory combined with Monte Carlo simulations for the optimization of monolithic scintillator PET detectors”. In: *IEEE Transactions on Nuclear Science* 53.3 (2006), pp. 1063–1070.

[167] Yimin Wang et al. “Properties of transparent (Gd, Lu)3(Al, Ga)5O12:Ce ceramic with Mg, Ca and Ce co-dopants”. In: *Medical Applications of Radiation Detectors V*. Ed. by H. Bradford Barber, Lars R. Furenlid, and Hans N. Roehrig. SPIE, Aug. 2015. DOI: 10.1117/12.2187123.

[168] R E Del Sesto et al. *Development of nanocomposite scintillators*. https://www.researchgate.net/profile/Ross_Muenchausen/publication/265669239_Development_of_nanocomposite_scintillators/links/566996aa08ae430ab4f72b73/Development-of-nanocomposite-scintillators.pdf. 2007. (Visited on).

[169] M. Osiński et al. “Lanthanide-halide-based nanoscintillators for portable radiological detectors”. In: *Optics and Photonics in Global Homeland Security V and Biometric Technology for Human Identification VI*. Vol. 7306. Proceedings of SPIE. May 2009, p. 730617. DOI: 10.1117/12.819018.

[170] Stefan Seifert et al. “First characterization of a digital SiPM based time-of-flight PET detector with 1 mm spatial resolution”. In: *Physics in Medicine and Biology* 58.9 (Apr. 2013), pp. 3061–3074. DOI: 10.1088/0031-9155/58/9/3061.

[171] Keenan J Wilson et al. “Localisation of the Lines of Response in a Continuous Cylindrical Shell PET Scanner”. In: *2019 41st Annual International Conference of the IEEE Engineering in Medicine and Biology Society (EMBC)*. IEEE. 2019, pp. 4844–4850.

[172] Weijun Guo, Robin P. Gardner, and Charles W. Mayo. “A study of the real-time deconvolution of digitized waveforms with pulse pile up for digital radiation spectroscopy”. In: *Nuclear Instruments and Methods in Physics Research Section A: Accelerators, Spectrometers, Detectors and Associated Equipment* 544.3 (June 2005), pp. 668–678. DOI: 10.1016/j.nima.2004.12.036. URL: https://doi.org/10.1016/j.nima.2004.12.036.

[173] M. Kapusta et al. “Comparison of the scintillation properties of LSO:Ce manufactured by different laboratories and of LGSO:Ce”. In: *IEEE Transactions on Nuclear Science* 47.4 (2000), pp. 1341–1345. DOI: 10.1109/23.872975. URL: https://doi.org/10.1109/23.872975.

[174] S. Gundacker et al. “Precise rise and decay time measurements of inorganic scintillators by means of X-ray and 511 keV excitation”. In: *Nuclear Instruments and Methods in Physics Research Section A: Accelerators, Spectrometers, Detectors and Associated Equipment* 891 (May 2018), pp. 42–52. DOI: 10.1016/j.nima.2018.02.074. URL: https://doi.org/10.1016/j.nima.2018.02.074.

[175] FD Popota et al. “Monte Carlo simulations versus experimental measurements in a small animal PET system. A comparison in the NEMA NU 4-2008 framework”. In: *Physics in Medicine & Biology* 60.1 (2014), p. 151.

[176] David Guez et al. “Counting rates modeling for PET scanners with GATE”. In: *IEEE Transactions on Nuclear Science* 55.1 (2008), pp. 516–523.

[177] R. Shopa. *Converting list mode of events to STIR (interfile) sinograms*. GitHub repository, https://github.com/rshopa/listmode-to-safir. 2017. (Visited on).

[178] J.J. Scheins, F. Boschen, and H. Herzog. “Analytical calculation of volumes-of-intersection for iterative, fully 3-D PET reconstruction”. In: *IEEE Transactions on Medical Imaging* 25.10 (Oct. 2006), pp. 1363–1369. DOI: 10.1109/tmi.2006.880679. URL: https://doi.org/10.1109/tmi.2006.880679.

[179] Robert Becker et al. “The SAFIR experiment: Concept, status and perspectives”. In: *Nuclear Instruments and Methods in Physics Research Section A: Accelerators, Spectrometers, Detectors and Associated Equipment* 845 (2017), pp. 648–651.

[180] J Fischer. *Custom input file format class for reading arbitrary crystal positions into STIR*. IEEE Satellite Workshop on Open Source Software in Medical Imaging. presentation. San Diego, CA, USA, Nov. 2015. URL: http://stir.sourceforge.net/MIC2015UsersMeeting/STIR_UM2015_Fischer_SAFIRInputFileFormat.pdf.

[181] Steven R Meikle and Ramsey D Badawi. “Quantitative techniques in PET”. In: *Positron Emission Tomography*. Springer, 2005, pp. 93–126.

[182] *NEMA Standard Publication NU4-2008: Performance Measurements of Small Animal Positron Emission Tomographs*. National Electrical Manufacturers Association. Rosslyn, VA, 2008.

[183] Han Shi et al. "Design study of dedicated brain PET with polyhedron geometry". In: *Technology and Health Care* 23.s2 (2015), S615–S623.

[184] G Bean. *bean-matlab-toolkit*. `https://github.com/brazilbean/bean-matlab-toolkit`. (Visited on).

Appendix A

Code Documentation

A.1 Nanocomposite & Transparent Ceramic Optimal Thickness Code

A.1.1 Code Availability

All GATE and MATLAB scripts used in Chapter 3 for simulation and analysis of the optimal thickness experiments are available here:
`https://bitbucket.org/keenanwilson/nanocomposite_ceramic_thickness_optimisation.git`

A.1.2 Software Requirements

- GATE scripts are confirmed working with GATE version 8.0 and Geant4 version 10.2.2 (Below version 8.0 may require rearrangement of the code). GATE is required to be built with optical tracking turned ON.
- MATLAB code is confirmed working with version 2019b.

A.1.3 GATE Code - How to Run

The repository has been set up so that each material and thickness combination used in the experiments has its own directory which has everything needed to run it. These include:

- **.mac file**: The actual GATE script specifying parameters for the simulation.

- **GateMaterials.db**: the materials database containing physical information for the simulation (e.g. density, atomic number, state of matter).

- **Surfaces.xml**: containing information for optical interactions between mediums.

- **Materials.xml**: containing optical information properties of each material (e.g. refractive index, optical attenuation length, scintillation yield.)

Currently these are all symbolically linked to master files in `nanocomposite_ceramic_thickness_optimisation/GATE_sim_scripts`, so should be altered there if required. Two parameters which I would suggest playing with in the *.mac* are firstly, *setTotalNumberOfPrimaries* (the second last line), which should be set to a small number if initially testing the system. Secondly, visualisation can be enabled by commenting out */vis/disable* at the beginning of the script.

GATE should be run via command line, with all of these scripts available in the same path, via:

```
Gate scriptName.mac
```

It will output a *.root* file, which can be analysed as is (using ROOT software), or as in our case, converted to ASCII format using a program called *read_root*, for input into the MATLAB scripts.

read_root

The *read_root* program requires compilation first (instructions can be found inside the actual C++ script). For conversion of the output data use:

```
read_root_v4 rootOutput.root
```

This will output a *Hits.dat* file, which logs information on all photon interactions within the sensitive detector region of the system (i.e. the scintillator and pixel volumes).

A.1.4 MATLAB Code - How to Run

All scripts required to run the MATLAB code are in `nanocomposite_ceramic_thickness_optimisation/MATLAB_analysis_code`. All *Hits.dat* files will need to be in the same location. The main script is the function *concatData_SD_twosided* and requires a numerical input for the number of primaries in the simulation. Other parameters have been hardcoded into the script and need to be changed depending on the material and thickness under test. These include:

- **det_dim_pix**: number of pixels in X and Y dimensions. Written as a vector [x y], e.g. [20 20] is a 20 pixel × 20 pixel detector.
- **det_dim_mm**: size of the pixel array in mm. Written as a vector [x y], e.g. [20 20] is an array of 20 mm × 20 mm.
- **atten_length**: optical attenuation length of the scintillation material (see Materials.xml).
- **slab_thickness**: thickness of scintillator slab. Will usually add 0.3 mm to include the thickness of the meltmount / epoxy layer.
- **fastmode**: set as 0/1 depending on whether visualisation is required (1 = no visualisation).
- **n_scint**: refractive index of the scintillator (see Materials.xml).
- **n_epoxy**: refractive index of the epoxy (see Materials.xml).
- **yield**: scintillation yield of the scintillator material (see Materials.xml).

The *concatData_SD_twosided* script will cycle through each *Hits.dat* file in the directory, apply the *photonfit_smallDetector_twosided* function to it and then concatenate all of the output text files. Without going in to too much detail, the photonfit algorithm will estimate the position of the first primary interaction using optical photon maps captured by the pixellated detector array. We can then find the error in this position from the ground truth interaction position, as recorded by GATE. Additional (sub-)functions needed for photonfit to operate include:

- *pointsourceattenuative_twosided*: the function fit to the data to estimate the position of the primary.
- *gen_psa_twosided*: a function handle for *pointsourceattenuative_twosided*.
- *curvefitting*: function used to actually fit *pointsourceattenuative_twosided* using least squares.
- *plot_PS*: visualisation function.

Finally, *locationError_SD_twosided* will output a scatter plot visualisation of the error in X, Y, Z dimensions as well as a "total error", D. A histogram of primary particle first hit location error is also returned. A second script called *locationError_SD_hexscatter* has been included which has a slightly different visualisation for the scatter plots (this requires *hexscatter* to run [184]). Additional utility functions have also been included (but are not required):

- *detectorstats*: provides some statistical analysis on the output.
- *scatterCount*: script to add 2 extra variables to the table output by *concatData_SD_twosided*; the number of primary interactions for each event and the amount of energy deposited.

A.2 Continuous Cylindrical Shell PET Code

A.2.1 Code Availability

All GATE, MATLAB and STIR scripts used in Chapters 4, 5 and 6 for simulation, coincidence detection, LOR determination and image reconstruction of the continuous cylindrical shell PET system are available here:
`https://bitbucket.org/keenanwilson/cylindrical_monolithic_PET.git`

A.2.2 Software Requirements

- GATE scripts are confirmed working with GATE version 8.0 and Geant4 version 10.2.2 (Below version 8.0 may require rearrangement of the code). GATE is required to be built with optical tracking turned ON.

- MATLAB code is confirmed working with version 2019b.
- STIR scripts confirmed working with version 3.0.
- listmode-to-safir, available at `https://github.com/rshopa/listmode-to-safir` [177].

A.2.3 GATE Code - How to Run

Optical Simulations

Similar to Section A.1.3, each particular experiment has been set up with all of the necessary scripts present in each directory. In addition to all of the scripts listed in Section A.1.3 an *.stl* file is also required to describe the geometry of the scintillator volume. This file may be generated with the python scripts found in `cylindrical_monolithic_pet/GATE/optical/scint_template`. The main script (*polygonPET_optical.py*) requires input variables which are currently hard-coded at the beginning of the script; these need to be changed depending on the desired configuration of the scanner. These are:

- **SiPM_dim**: SiPM dimensions in mm. [Width, length, thickness]
- **num_sides_in**: number of sides on the inner surface of the polygon volume.
- **num_sides_out**: number of sides on the outer surface of the polygon volume.
- **num_SiPM_Z**: number of SiPMs along axial length of scintillator.
- **min_SiPM_spacing**: spacing on each side of SiPM.
- **scint_material**: String. Must match entries in GateMaterials.db and Materials.xml files.
- **epoxy_thickness**: thickness of epoxy between scintillator volume and SiPM volume.

Two templates are present in the directory: *polygonPET_template.scad* and *polygonPET_template_optical.mac*, which are used by the python scripts to auto-generate an *.stl* file for the scintillator volume (depending on the input parameters) and a

corresponding GATE *.mac* file. All other volume in GATE *.mac* file will vary depending on the size and shape of the scintillator volume.

Three *.mac* scripts exist for each optical simulation, each with a different source position; at the centre, 50% of the distance to the inner radius of the cylinder and 75% of the inner radius of the cylinder. These have been run separately with the output being concatenated afterwards. Note that in `cylindrical_monolithic_pet/GATE/optical/timingWindow/GLuGAGCe/` there are two mac files in each directory; one contains *sensitiveScint*, which means that the scintillator volume is a sensitive detector and is able to record the true point of interaction of the gamma photon. The other script containing *10kbq3sec* forgoes the sensitive volume for faster simulation, allowing for the high event count simulations used in image reconstruction.

Normalisation Scripts

Normalisation has been performed without optical photon tracking in GATE. Separate python scripts and templates have been included for this as well.

read_root

Each *read_root* program requires compilation first (instructions can be found inside the actual C++ script). There are four scripts each with a different output, depending on what is required by the MATLAB code.

- *read_root_bin*: outputs to binary. Used in `cylindrical_monolithic_pet/MATLAB/timingWindow/non-sensitive_detector_scripts` MATLAB scripts for image reconstruction in Chapter 6.

- *read_root_compt*: outputs to binary. Used in `cylindrical_monolithic_pet/MATLAB/timingWindow/sensitive_detector_scripts(compton)` MATLAB scripts for coincidence detection in Chapter 5.

- *read_root_norm*: outputs to binary. Used in `cylindrical_monolithic_pet/MATLAB/normalisation` MATLAB scripts for normalisation of the image in Chapter 6.

- *read_root_v5*: outputs to ASCII. Used in `cylindrical_monolithic_pet/`

`MATLAB/LOR_determination` MATLAB scripts for LOR determination in Chapter 4.

A.2.4 MATLAB Code - How to Run

LOR Determination Scripts

The code used for LOR determination in Chapter 4 may be found in `cylindrical_monolithic_pet/MATLAB/LOR_determination`. Again, ensure that the relevant *Hits.dat* files are located in the same directory (from *read_root_v5*). Run the code using the main script *concatData_polygonPET.m*. Currently, the variables used in the script are hard-coded at the beginning and need to be changed manually, depending on the type of material used and the geometry of the scanner. These include:

- **fastmode**: set as 0/1 depending on whether visualisation is required (1 = no visualisation).
- **num_pix_Z**: number of pixels on each SiPM along the axial dimension of the scanner (in Chapter 4 we call this z).
- **num_pix_C**: number of pixels on each SiPM along the tangential dimension of the scanner (in Chapter 4 we call this y).
- **dim_pix**: dimensions of each SiPM pixel in mm, written as a vector [y, z].
- **num_sipm_Z**: number of SiPMs in axial (z) dimension.
- **num_sipm_out**: number of SiPMs on the outer surfaces of the ring (equals the number of outer faces of the polyhedron).
- **num_sipm_in**: number of SiPMs on the inner surface of the ring (equals the number of inner faces of the polyhedron).
- **border_wdth**: thickness of the passive area, bordering the active pixel area of the SiPM, in mm.
- **sipm_space_out**: gap between SiPMs on the outer surface of the scintillator volume, in mm.

- **sipm_space_in**: gap between SiPMs on the inner surface of the scintillator volume, in mm.
- **n_1**: refractive index of the scintillator (see Materials.xml).
- **n_2**: refractive index of the epoxy (see Materials.xml).
- **thickness_scint**: scintillator thickness (the difference between radius of the inner and outer polygons). This should be output by the python scripts mentioned in Section A.2.3.
- **atten_length**: optical attenuation length of the scintillator, in mm (see Materials.xml).
- **yield**: scintillation yield (see Materials.xml).
- **wavelength**: wavelength of the scintillation photons.

The structure of the script hierarchy is very similar to the code in Section A.1.4. Each *.dat* file will be called in sequentially and processed by *photonfit_polygonPET*, which executes the fitting algorithms discussed in Chapter 4. The function structure is basically as follows:

- *concatData_polygonPET*
  - *SiPM_binning*
  - *gen_psa_twosided_cylindrical*
    - *pointsourceattenuative_twosided_cylindrical*
  - *photonfit_polygonPET*
    - *coinMidpoint*
    - *histoSplit*
    - *dataSubset*
    - *curvefitting_cylindrical*

The basic hierarchy is: main script (•) which contains the experimental parameters and calls in the data, second level functions (−) are executed automatically by the main function and third level functions (∗) which are automatically executed by

the second layer. Since it is not really necessary to explain exactly how each function works to run the scripts, we will keep the explanation at a high level. In reality, *photonfit_polygonPET* will output a text file containing (among other things) the endpoints of the LOR for each coincidence event, as well as the error in the LOR from the ground truth recorded by GATE . The other second level functions are only needed to calculate input data for *photonfit_polygonPET*. The main script will then concatenate all of the output data.

Other scripts have been included as utilities:

- *polygonPET_errorStats_GLuGAGCe*: for statistical analysis and visualisation (requires *hexscatter*). Specific to the GLuGAG:Ce scanner.
- *polygonPET_errorStats_LaF3CePS*: for statistical analysis and visualisation (requires *hexscatter*). Specific to the LaF_3:Ce-polystyrene scanner.

Deconvolution Coincidence Detection Scripts

The scripts used for coincidence detection in Chapters 5 and 6 are slightly different, but are essentially run using the same methodology, so they will be covered together. The scripts are located in `cylindrical_monolithic_pet/MATLAB/timingWindow`. Input binary files with a *.dat* extension are required; particular *read_root* programs used to produce these are explained in SectionA.2.3.

The first step is to run *rearrangeDataTimeSlice_bin* (non-sensitive detector) or *rearrangeDataTimeSlice_compton* (sensitive detector). This is splitting the data up into a format which is manageable for system memory, splitting it into time bins. it requires three inputs:

- **time_step**: length of time allocated to a single output file. Controls the number of files output.
- **max_time**: stop time of the GATE simulation (i.e. total simulation time).
- **set_num**: unique integer if running multiple sets of data in parallel (to make sure event ID is not duplicated).

If there were multiple sets of data processed in parallel (giving multiple sets of the same timing bins), then they need to be combined via concatenation. This

can be done with *combineTimeSliceData_binary* (it may need to be altered slightly depending on the number of data sets), or just in the shell command line.

The output is another binary file which is then input into the next function: *coincidenceSorting_polygonPET_binary/compton*. Note that the files must be processed sequentially in terms of timing bin, so they need to be named accordingly (e.g. name data2 as data02, so it is processed before data10).

Both functions essentially have the same hierarchy:

- *coincidenceSorting_polygonPET*
  - *SiPM_binning*
  - *impulseResponse*
  - *findTimeSection*
    - *fdeconv*
    - *coincidence_sorting*
  - *groupRandoms*
  - *coincidence_sorting*

The algorithm will process the input binary files, sorting them into separate output files of coincidences, singles and randoms using the procedure outlined in Chapter 5. There are a number of inputs required for the script:

- **filename_impulse**: Impulse response data. Can use *Hits_10MBq_cleaned_impulseRef.dat* provided.
- **fastmode**: set as 0/1 depending on whether visualisation is required (1 = no visualisation).
- **num_pix_Z**: number of pixels on each SiPM along the axial dimension of the scanner (in Chapter 4 we call this z).
- **num_pix_C**: number of pixels on each SiPM along the tangential dimension of the scanner (in Chapter 4 we call this y).
- **dim_pix**: dimensions of each SiPM pixel in mm, written as a vector [y, z].

- **num_sipm_Z**: number of SiPMs in axial (z) dimension.
- **num_sipm_outer**: number of SiPMs on the outer surfaces of the ring (equals the number of outer faces of the polyhedron).
- **num_sipm_inner**: number of SiPMs on the inner surface of the ring (equals the number of inner faces of the polyhedron).
- **border_wdth**: thickness of the passive area, bordering the active pixel area of the SiPM, in mm.
- **sipm_space_out**: gap between SiPMs on the outer surface of the scintillator volume, in mm.
- **sipm_space_in**: gap between SiPMs on the inner surface of the scintillator volume, in mm.
- **n_1**: refractive index of the scintillator (see Materials.xml).
- **n_2**: refractive index of the epoxy (see Materials.xml).
- **thickness_scint**: scintillator thickness (the difference between radius of the inner and outer polygons). This should be output by the python scripts mentioned in Section A.2.3.
- **wavelength**: wavelength of the scintillation photons
- **num_bins_DOI**: number of bins used for characterising the impulse response. Default 5.
- **bin_size_time**: time sample size for histogram binning, in ns. Used in the deconvolution algorithm.
- **num_sections**: number of spatial sections / sectors we are splitting the cylinder into. Used in the deconvolution algorithm
- **thresh_peak_frac**: peak threshold for system to detect an event, as a percentage of the maximum peak.
- **time_slice**: time slice corresponding *time_step* in *rearrangeDataTimeSlice*.

The output binary files containing coincidences or randoms may then be input into the next function, *concatData_polygonPET_timingWindow*, in order to determine the endpoints of the LORs, producing a list mode text file as output. A number of variables for this function have been hard-coded (at the beginning as before); all of these have been previously discussed. The argument **dataType** is a string and can be specified as either 'coincidences' or 'randoms', corresponding to the input data. The functions needed for *concatData_polygonPET_timingWindow* are as follows:

- *concatData_polygonPET_timingWindow*
  - *gen_psa_twosided_cylindrical*
    - *pointsourceattenuative_twosided_cylindrical*
  - *photonfit_polygonPET_timingWindow*
    - *coinMidpoint*
    - *histoSplit*
    - *dataSubset*
      - *findBoundaries*
    - *curvefitting_cylindrical*

The final step is to convert the output text file of listmode LOR data into a format which can actually be read by STIR, using the aptly named *convertToSTIRListMode*, which also requires *intersectLineCylinderVec*. This will basically draw a virtual cylinder of zero thickness within the centre of the cylinder and calculate the point of interaction of each LOR with that cylinder. The logged positions will be used in the **SAFIR** STIR scripts. Make sure that the name of the input file and the parameters for the detector geometry correctly reflect your own scanner.

Normalisation Scripts

Normalisation scripts are somewhat simpler, as they don't require any optical fitting algorithms, but they essentially will perform the same task as the scripts described in the last section. Though in this case we are simply finding the location of the first interaction points of known coincidences and then recording these in list mode.

The script has been set up to make use of parallel computing where possible. The arguments for *coincidence_sorting_norm* are:

- **filename**: binary file name (string).
- **num_events**: total number of events simulated in individual data file.
- **num_subsets**: how many times we want to split up the main data file (to run faster) e.g. for 50M events, we might split the data into 50 blocks to be processed.
- **num_workers**: used for a parallel pool. Set depending on number of cores available.
- **fastmode**: set as 0/1 depending on whether visualisation is required (1 = no visualisation).

Upon completion, *convertToSTIRListMode* must again be used to convert the output text file into a format which can be read by STIR.

A.2.5 STIR Code - How to Run

All STIR files may be found in the following directory `cylindrical_monolithic_pet/stir`. Required input files are the "coincidences", "randoms" and "normalisation" data, output by the MATLAB function *convertToSTIRListMode*. Firstly, a crystal map of the scanner architecture must be generated. We have included one in the repository, though if the geometry is to be changed (with new values in *polygonPET_geometry*), then run the following with the updated *.par* file:

```
GenerateCrystalMapJPET -p polygonPET_geometry.par -o
    crystal_map_polygonPET.txt
```

This creates a virtual ring inside the scanner geometry and maps a grid of virtual detector surfaces in Cartesian space. In the next step, we will map our own list-mode data to these virtual detectors. Navigate to each of the directories - `stir/true_random`, `stir/randoms` and `stir/normalisation` and run the following process in each:

```
ConvertToMUPET -i stir_table_GLuGAG.txt -p
    polygonPET_geometry.par -o output_polygonPET_GLuGAG.clm.
    safir

lm_to_projdata lm_to_projdata_polygonPET.par
```

The first command converts the list mode data to **SAFIR** form and the second converts to interfile format; producing sinogram files, .hs (header) and .s (data). The parameter file in this last step also points to another interfile pair (*polygonPET.hs/.s*), which specifies the parameters of the scanner (this can be created with STIR's create_projdata_template).

At this point, any of these generated sinogram files can be reconstructed using STIR's image reconstruction algorithms. For example, the following code will produce an interfile image (*.hv/.v*) - raw data which may be viewed using AMIDE software.

```
FBP2D FBP2D.par
```

Though any algorithm could be used with the corresponding *.par* file. To generate the attenuation image, change directory to `stir/attenuation` and run

```
./generate_image.sh
```

This is a shell script to generate an interfile image of three attenuation maps, corresponding to the three water phantoms encompassing the ^{18}F sources, using STIR's *generate_image*. To correct the raw coincidence sinogram data, all generated sinogram files will need to be moved to the `stir/correction` directory. From this directory run:

```
./run_correction.sh
```

This will perform a number of *stir_math* operations using Equation 6.1, to produce a final corrected interfile sinogram called *output_precorrected.hs/.s*. Any of STIR's image reconstruction algorithms (e.g. FBP2D, FBP3DRP, OSMAPOSL) may then be used to reconstruct the image, provided that the .par file is present, producing a final corrected image.